Effect of a Prior Plastic Deformation during Heat Treatments on the Mechanical Properties of Ni-Based Superalloys for Turbine Blade Application

Satoshi Utada

THESE

Pour l'obtention du Grade de
DOCTEUR DE L'ECOLE NATIONALE SUPERIEURE DE MECANIQUE ET D'AEROTECHNIQUE
(Diplôme National – Arrêté du 25 mai 2016)

Ecole Doctorale :
Sciences et Ingénierie en Matériaux, Mécanique, Energétique

Secteur de Recherche :
Mécanique des Solides, des Matériaux, des Structures et des Surfaces

Présentée par :

Satoshi UTADA

****

Effect of a prior plastic deformation during heat treatments on the mechanical properties of Ni-based superalloys for turbine blade application

****

Directeur de thèse : Patrick VILLECHAISE
Co-encadrants : Jonathan CORMIER et Jérémy RAME

****

Soutenue le 17 Décembre 2020

devant la Commission d'Examen

****

JURY

Rapporteurs :
VIGUIER Bernard, Professeur, ENSIACET, CIRIMAT, Toulouse
REED Roger, Professeur, University of Oxford, Oxford, UK

Membres du jury :
PORTELLA Pedro, Professeur, BAM, Berlin, Germany
PETTINARI-STURMEL Florence, Professeur, Université de Toulouse, CEMES, Toulouse
RAME Jérémy, Ingénieur, Safran Aircraft Engines, Gennevilliers
CORMIER Jonathan, Maître de conférences, ISAE-ENSMA, Institut P', Futuroscope-Chasseneuil
VILLECHAISE Patrick, Directeur de Recherche, ISAE-ENSMA, Institut P', Futuroscope-Chasseneuil

ACKNOWLEDGMENTS

This thesis research was organized in a collaborative project between the Department of Physics and Mechanics of Materials in Institute Pprime/ISAE-ENSMA and Safran Aircraft Engines in the framework of CIFRE. I would like to show my gratitude to Safran Aircraft Engines for the financial support and experimental material supply. Keidanren Ishizaka Memorial Foundation is greatly acknowledged for choosing me as an Industrial Leader HR Development Scholarship student and provided me the financial support necessary for traveling and starting life in France.

I would like to express my exceptional gratitude and appreciation for my supervisor, Jonathan Cormier, who has supported and guided me throughout this research project, both professionally and privately. Working with a person with such a strong passion for superalloys and aviation was always exciting. I am delighted to have this continuous relationship with Jonathan since the CREEP2015 conference in Toulouse.

I am grateful for the discussions and experiences with my thesis director Patrick Villechaise on EBSD analyses and various scientific topics. I disturbed Patrick a lot in his office when he looked very busy with the lab director's work, but he was always polite and helpful.

The thesis jury committees Professor Bernard Viguier (CIRIMAT, INP-ENSIACET, Toulouse), Professor Roger C. Reed (University of Oxford, UK), Professor Pedro Dolabella Portella (Federal Institute for Materials Research and Testing (BAM), Germany), and Professor Florence Pettinari-Sturmel (Université de Toulouse, CEMES, Toulouse) are gratefully acknowledged for accepting this responsibility of examination under the complicated situation. Discussions with this member during the thesis defense were of very high quality and genuinely constructive ones. I appreciate that all the committee members had gone deep into my manuscript. It is my honor to have such an outstanding member for the culmination of my thesis research.

This project would not have proceeded smoothly without the help and understandings of the industry team from the Safran group. Dr. Sarah Hamadi (Safran Aircraft Engines) and Christophe Audic (formerly at Safran Aircraft Engines) are greatly acknowledged for their sincere support, which removed all obstacles at the beginning and eased my entry to the YQGC team. I would like to appreciate significantly Dr. Jérémy Rame (Safran Aircraft Engines) for inheriting the role of an industrial advisor and for his continuous support that helped me concentrate on the research works. Dr. Sandrine Charles, Dr. Elodie Drouelle, Dr. Nicolas Leriche, Damien Ponsen, Dr. Aurélien Vattré (all at Safran Aircraft Engines) and Joël Delautre, Sébastien Blas, Anaïs Götzfried (all formally at Safran Aircraft Engines) and Dr. Lorena Mataveli Suave (Safran Tech) are all acknowledged for fruitful discussions both scientifically and from an industrial standpoint. I would also like to appreciate Julien Dauchez, Nabila Pacaud (both at Safran), and Guillaume Lapy (Safran Aircraft Engines) for handling the patent application works.

My sincere appreciation goes to the supporting staff at Institut Pprime. My study was highly dependent on the creep testing bench and the FEG-SEM which were taken care of by Florence Hamon. Sample preparation equipment was always available through seamless management by Guillaume Benoit and Médéric Morriset.

It was not possible to design and perform VHCF tests without the assistance of Jacques Lefort and Florent Mauget. Gérald Sailly and Cédric Djossinou were very quick and efficient in responding to my requests regarding IT issues. Brigitte Vigner, Karine Lombard, and Francine Bayle were always warm and welcome at the secretary's office whenever I needed administrative help, which was especially important during the first year. I would also like to thank other technical staffs and electrical/machining atelier for the supports out of my sight, which enabled me to carry out the experiments very smoothly. I learned the importance of these professionals always being there to build up a dynamic and sustainable research team.

Other members of Institut Pprime, Dr. Samuel Hémery, Dr. Maxime Perrais, Dr. Alice Cervellon, Dr. François Bourdin, and Dr. Nicolas Mrozowski, are appreciated for technical support and discussions. Dr. Vincenzo Caccuri is acknowledged for developing the in-house software RIM-X that enabled me to perform microstructure characterization very rapidly in a unique way. Thanks to the Team Superalloy in Pprime for interesting scientific exchanges. I look forward to seeing the beautiful results you will present in the future.

A special thanks go to my excellent colleague and friend Luciana Maria Bortoluci Ormastroni (Institut Pprime). I really like our works that become Superalloys 2020 proceedings and the VHCF characterization chapter. It was incredibly efficient to work with Luciana, thanks to her devotion to supporting my experiments and open-minded way of thinking. I also feel relaxed when we shared our common situation being extremely far away from home.

I am grateful for the invitation from Professor Michael J. Mills (the Ohio State University, OH, USA) for collaboration on the TEM analyses and providing me an opportunity for a great experience during my stay at the OSU. I would like to thank Dr. Milan Heczko and Ashton J. Egan (both at the Ohio State University) for the sample preparation and analytical works. Although it is just one observation site, the TEM image provided by Milan is inspirational and becomes a very important part of my thesis.

I would like to thank my external colleagues for engaging experiences from other collaborations outside my thesis. The work on MarM-246 modifications with Professor Carlos Angelo Nunes and Dr. Luciano Braga Alkmin (both at University of São Paulo, Brazil) had shown very good completion. Investigating the non-isothermal creep damaging mechanism of cast superalloys with Dr. Stoichko Antonov (Max-Planck-Institut für Eisenforschung, Germany) and Professor Qiang “Charles” Feng and Wenrui An (both at University of Science and Technology Beijing, China) has been an exciting project.

I would like to express my gratitude to my former supervisor Professor Shinsuke Suzuki (Waseda University, Japan), for encouraging me to dive into the academic society and his help on scholarship applications. Dr. Hiroshi Harada and Dr. Kyoko Kawagishi (both at National Institute for Materials Science (NIMS), Japan) are highly acknowledged for our continuing relationship and TMS-238 characterization project. It is my pleasure to be involved in this very special material developed in Japan.

My B001 colleagues are an important part of my research life in Pprime. I was never bored being a member of this most diverse office. Since my arrival, 14 people took a seat in this office: Selim (Thanks for helping me with many things just after arrival), Marina (I know you were balancing the atmosphere of the office), François (Thanks for technical help, discussions, geek talks, and welcoming me with your parents), Ravi (I miss those

video game days and non-sense. Thanks for invited me to your wedding, it was a strange and interesting journey which I will probably never experience again.), Nico (You were my first choice to ask for help. I enjoyed thinking with you about celebrations for our colleagues. And, of course, Muse.), Giuseppe (We have developed a quite unique friendship. I really appreciate you organized volleyball, which was always fun.), Mahak (Endless talk... bad when I had something else to do, but very good when I wanted to forget about something. I liked to see you debating with Giuseppe.), Adèle (Started together, finished together, my thesis companion. Dealing with the same difficulties at the same time made it much more comfortable than working alone.), Mélanie (You being in the office makes me feel at home.), Tiphaine (Your hard work motivates me a lot. I love the new petit-dej Friday tradition.), Natan (Thanks for being patient when I tried to communicate in French.), Julien and Salvador (I like a festive atmosphere you make, which is different from old members.), and Marjolaine (I wished if there were more time to know each other. Good luck.). Thank you again for all of you.

I sincerely appreciate Tomoki-san, a fantastic Japanese friend who supported me in starting life in France and taught me many things. I cannot imagine how difficult it would have been without him.

All other members of Institut Pprime added color to my life as a Ph.D. candidate, through breaktime, repas d'axe, ATEM activities, and so on. Thank you all for this unforgettable experience in France.

Finally, my sincere thanks go to my parents and younger brother Tetsuya for their precious support and encouragement. They were always in my heart even though we were far away. Influence from my father, formerly a JASDF officer, and my English language background from my days in the US are significant for me to reach this point. I am forever indebted to my parents for giving me the opportunities and experiences that have made me who I am.

皆様に心より感謝申し上げます。

Satoshi UTADA

宇多田 悟志

TABLE OF CONTENTS

General Introduction 1

Chapter 1: Literature review and research background 5

Résumé : Revue de la littérature et contexte des travaux de recherche 7

1. 1. Cast Ni-based superalloys for turbine blade application 9

1. 1. 1. Blade alloy development 9

1. 1. 2. Ni-based single crystal superalloy 11

1. 1. 3. Manufacturing processes 13

A) Casting and solidification 13

B) Solution and aging heat treatments 14

C) Porosity and hot-isostatic pressing (HIP) 16

1. 2. High-temperature deformation and durability of superalloys 17

1. 2. 1. Strengthening mechanism of γ/γ′ Ni-based superalloys 17

1. 2. 2. Tensile deformation 18

1. 2. 3. Creep 19

A) High-temperature/low-stress creep 19

B) Low-temperature/high-stress creep 22

1. 2. 4. Very high cycle fatigue 23

1. 3. Pre-straining effect 24

1.3.1. Pre-straining before solution treatment 24

1.3.2. Microstructure behavior after pre-straining 25

1.3.3. Mechanical properties of pre-deformed superalloys 26

1.3.4. Rejuvenation treatment 28

1. 4. Previous experimental results 33

1.4.1. Microstructure after pre-deformation and following aging treatments 34

1.4.2. Creep properties of pre-deformed AM1 SX superalloy 35

1.4.3. Tensile tests and low cycle fatigue tests 38

1. 5. Research objectives 40

References 40

Chapter 2: Experimental procedures 49

Résumé : Les procédures expérimentales 51

2. 1. Materials 52

2. 2. Specimen preparation 52

2. 3. Tensile plastic deformation (pre-deformation) 53

2. 4. Heat treatment 54

2. 5. Creep tests 56

2. 6. Very high cycle fatigue tests 58

2. 7. Microstructure characterizations 59

References 59

Chapter 3: Microstructure evolution after pre-deformation, and rejuvenation treatment 61

Résumé : Évolution de la microstructure après la pré-déformation, et traitement thermique de restauration 63

3. 1. Introduction 65

3. 2. Tensile pre-deformation of experimental materials 65

3. 3. Microstructure evolution during aging treatments of AM1 after pre-deformation at room-temperature 67

3. 3. 1. Standard aging treatments 67

3. 3. 2. Aging treatments at different temperatures 71

3. 3. 3. Effect of inheriting internal strain from room-temperature pre-deformation on the microstructural behavior during high-temperature exposure 75

3. 4. Microstructures of AM1 after higher-temperature pre-deformation 80

3. 5. Effect of chemical compositions on the microstructure evolution behavior 87

3. 6. Rejuvenation treatment on the pre-deformed materials 92

3. 6. 1. Determination of rejuvenation treatment conditions 92

3. 6. 2. Effects of deformation methods on the rejuvenation capability 98

3. 7. Summary 99

References 100

Chapter 4: Creep damaging mechanisms of pre-deformed Ni-based single crystal superalloys 105

Résumé : Mécanismes de dégradation par fluage des superalliages monocristallins base-Ni avec pré-déformation 107

4. 1. Introduction 110

4. 2. Creep damaging mechanisms of SX superalloys with pre-deformation at RT 110

4.2.1. Creep results on AM1-RTPD-HT1 at higher temperatures (1050 °C, 950 °C) 110

4.2.2. Microstructure characterizations on AM1 after creep tests at higher temperatures (1050 °C, 950 °C) 113

A) AM1 without PD 113

B) AM1 with PD, creep test at 1050 °C / 140 MPa 115

C) AM1 with PD at 1050 °C / 200 MPa 117

D) AM1 with PD at 950 °C / 300 MPa 118

4.2.3. Local lattice misorientation in the microstructure coarsened band 121

4.2.4. Creep results on 4P-RTPD-HT1 and 4P-RTPD-HT2 at higher temperatures (1150 °C, 1050 °C) 122

4.2.5. Microstructure characterizations of CMSX-4 Plus after creep tests at higher temperatures (1150 °C and 1050 °C) 124

A) CMSX-4 Plus at 1150 °C / 110 MPa 124

B) CMSX-4 Plus at 1050 °C / 200 MPa 129

4.2.6. Void nucleation and growth during heat treatment and creep 131

A) Stereological analyses of voids 131

B) Void nucleation and growth mechanism 134

4.2.7. Localized shearing and damage accumulation mechanisms during high temperature creep 136

A) γ′-rafting regime (volume fraction ~50%) 136

B) Topological inversion regime (volume fraction >50%) 139

4.2.8. Effect of pre-deformation at RT on creep properties at lower temperatures 141
A) AM1 at 850 °C / 500 MPa and 750 °C / 800 MPa 141
B) CMSX-4 Plus at 950 °C / 390 MPa and 850 °C / 650 MPa 145
4.2.9. Ultra-high temperature creep (≥ 1200 °C) 148
4. 3. Examination of damage localization using different material histories and test conditions 151
4.3.1. Pre-deformation at higher temperature and rejuvenation effect 151
4.3.2. Pre-deformation after aging treatment 155
4.3.3. Thermal cycling creep tests 159
4. 4. Summary 161
References 163

Chapter 5: VHCF properties of pre-deformed AM1 SX superalloy 167

Résumé : Propriétés VHCF du superalliage monocristallin AM1 avec pré-déformation 169
5. 1. Introduction 170
5. 3. Fractographic observations 170
5. 4. Microstructure characterization of specimen's longitudinal section 173
5. 5. Effect of pre-deformation in fully reversed condition $R = -1$ 175
5. 6. Enhanced shearing and recrystallization at positive stress ratio condition, $R = 0.5$ 177
5. 7. VHCF life restoration by rejuvenation heat treatment 179
5. 8. Summary 179
References 180

General conclusions and perspectives 183

GENERAL INTRODUCTION

Ni-based single crystal (SX) superalloys are heat-resistant structural materials mainly used for blades and vanes of gas turbine systems such as aero-engines (Figure i(a)) and power generators (Figure i(b)) [1–4]. Modern civil aero-engines are designed with large high by-pass ratio turbofan and small/light core section to maximize efficiency. Simultaneously, turbine inlet temperature (TIT) of combustion gas is increasing to improve the thermal efficiency of the gas turbine systems. To meet the requirement of increasing the thermal efficiency of gas turbine systems, the first stages of low-pressure turbine (LPT) blades (Figures ii and iii) are expected to be replaced from conventionally cast or directionally solidified superalloys to SX superalloys in a very near future. Furthermore, the geometrical designs of the components are becoming more complex to ensure better aerodynamic properties. Either in application of SX superalloys for large LPT blades or geometrically complex designed components, introduction of minor plastic deformation (PD) may occur during different stages of the component production, such as the cooling process after solidification and the demolding process [5,6]. This PD can also be a result of manipulation shocks or thermal shock by differences in local cooling rate for larges blades during solution heat treatment [7].

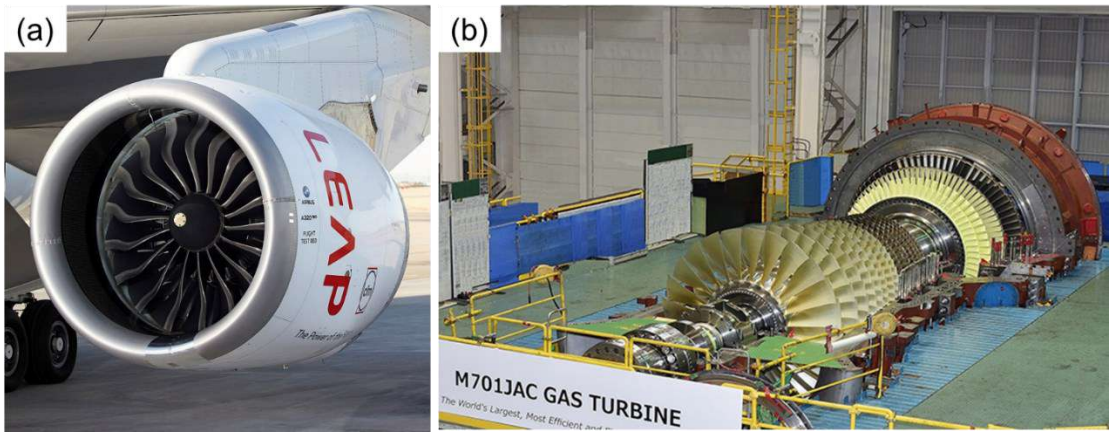

Figure i. (a) LEAP-1A turbofan engine powering Airbus A320neo developed by CFM International (50/50 joint venture between GE Aviation and Safran Aircraft Engines). (b) M701 JAC land-based power generating gas turbine developed by Mitsubishi Hitachi Power Systems (MHPS).

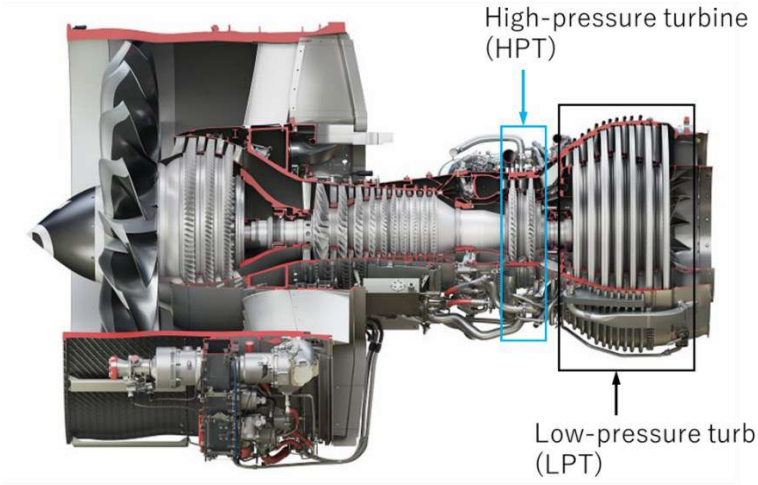

Figure ii. Cutaway model of LEAP-1A turbofan engine showing different sections of gas turbine system.

Figure iii. An example of a non-cooled first stage LPT blade

PD during cooling from solidification increases the risk of recrystallization risk during subsequent solution treatment step [8–10]. Various types of pre-straining after full heat treatment have also been studied to mimic complex temperature/stress operating condition of turbine blades [11–15]. On the other hand, researches on the consequences of production originated unintentional deformation on the mechanical properties of Ni-based SX superalloy are limited at this point. In the turbine blade foundry of Safran Aircraft Engines, manipulation related deformation that can induce unexpected microstructure evolution was reported and this naturally decreases production yield. However, the effect of PD introduced during different stages of turbine blade production is not well known and questions still remain whether such components are serviceable or not with respect to creep and fatigue design criteria. Comprehensive scientific research is hence necessary to understand the actual behavior of the material with irregular microstructure created during production.

To understand the effect of PD during production, microstructure and mechanical properties of the first-generation Ni-based SX superalloy AM1, one of the most practical alloys used in Safran engines, after different pre-deformations and heat-treatment procedures were examined. The additional supersolvus rejuvenation heat-treatment was applied to the SX superalloy with different tensile plastic damage before aging treatments to verify rejuvenation capability. In addition, effect of pre-deformation and rejuvenation capability were similarly evaluated in the third-generation Ni-based SX superalloy CMSX-4 Plus, which is a possible candidate for non-cooled LPT blades.

This thesis manuscript is divided into the following chapters to present and discuss the effect of pre-deformation on the mechanical properties of Ni-based SX superalloys.

- **Chapter 1**: Literatures related to this research is reviewed in this chapter. Production procedures, general mechanical properties of the Ni-based SX superalloys, other researches on pre-straining effects, basics of

rejuvenation treatment, and precedent experimental results before thesis research are introduced.

- **Chapter 2**: Basic experimental procedures are presented. Material preparation, heat treatments, specimen geometries, tensile test for pre-deformation, creep tests, very high cycle fatigue tests, and microstructure characterization methods are introduced.
- **Chapter 3**: Effect of different pre-deformations on the microstructural behavior during subsequent heat treatments are presented. Pre-deformation was applied from room-temperature up to 950 °C on AM1 and microstructures are compared. Different microstructure evolution in AM1 and CMSX-4 Plus are discussed with their intrinsic properties came from chemical compositions. Rejuvenation treatment conditions are determined for both alloys.
- **Chapter 4**: Creep properties of the pre-deformed materials at different temperature/stress conditions are examined. Mechanism of creep life debit caused by pre-deformation is presented. Situations causing intense creep damage localization is discussed.
- **Chapter 5**: Very high cycle properties of pre-deformed AM1 are presented with unique microstructural features caused by pre-deformation. Damaging mechanisms are discussed in accordance with the previous chapter.
- Concluding remarks and perspectives are presented at the end.

References

[1] H. Harada, High temperature materials for gas turbines: the present and future, in: Proc. Int. Gas Turbine Congr. 2003 Tokyo, Tokyo, 2003: pp. 1–6.

[2] T.M. Pollock, S. Tin, Nickel-Based Superalloys for Advanced Turbine Engines: Chemistry, Microstructure and Properties, J. Propuls. Power. 22 (2006) 361–374. doi:10.2514/1.18239.

[3] R.C. Reed, The Superalloys: Fundamentals and Applications, Cambridge University Press, Cambridge, 2006. doi:10.1017/CBO9780511541285.

[4] H. Long, S. Mao, Y. Liu, Z. Zhang, X. Han, Microstructural and compositional design of Ni-based single crystalline superalloys — A review, J. Alloys Compd. 743 (2018) 203–220. doi:10.1016/j.jallcom.2018.01.224.

[5] C. Panwisawas, H. Mathur, J.-C. Gebelin, D.C. Putman, P. Withey, N. Warnken, C.M.F. Rae, R.C. Reed, Prediction of Plastic Strain for Recrystallisation during Investment Casting of Single Crystal Superalloys, in: Superalloys 2012, John Wiley & Sons, Inc., Hoboken, NJ, USA, 2012: pp. 547–556. doi:10.1002/9781118516430.ch60.

[6] C. Panwisawas, J.-C. Gebelin, R.C. Reed, Analysis of the mechanical deformation arising from investment casting of directionally solidified nickel-based superalloys, Mater. Sci. Technol. 29 (2013) 843–853. doi:10.1179/1743284712Y.0000000197.

[7] S. Pierret, T. Etter, A. Evans, H. Van Swygenhoven, Origin of localized rafting in Ni-based single crystal turbine blades before service and its influence on the mechanical properties, Acta Mater. 61 (2013) 1478–1488. doi:10.1016/j.actamat.2012.11.024.

[8] R. Bürgel, P.D. Portella, J. Preuhs, Recrystallization in single crystals of nickel base superalloys, in: Superalloys 2000, 2000: pp. 229–238. doi:10.7449/2000/Superalloys_2000_229_238.

[9] D.C. Cox, B. Roebuck, C.M.F. Rae, R.C. Reed, Recrystallisation of single crystal superalloy CMSX-4, Mater. Sci. Technol. 19 (2003) 440–446. doi:10.1179/026708303225010731.

[10] Z. Li, X. Fan, Q. Xu, B. Liu, Influence of deformation temperature on recrystallization in a Ni-based single crystal superalloy, Mater. Lett. 160 (2015) 318–322. doi:10.1016/j.matlet.2015.07.120.

[11] M. Sakaguchi, M. Ike, M. Okazaki, Microstructural changes in a single crystal Ni-base superalloy induced by plastic straining, Mater. Sci. Eng. A. 534 (2012) 253–259. doi:10.1016/J.MSEA.2011.11.066.

[12] M. Sakaguchi, M. Okazaki, Distinctive role of plastic and creep strain in directional coarsening of a Ni-base single crystal superalloy, Mater. Sci. Eng. A. 710 (2018) 121–128. doi:10.1016/j.msea.2017.10.085.

[13] H. Long, S. Mao, Y. Liu, H. Wei, Q. Deng, Y. Chen, Z. Zhang, X. Han, Effect of pre-straining treatment on high temperature creep behavior of Ni-based single crystal superalloys, Mater. Des. (2019) 107633. doi:10.1016/j.matdes.2019.107633.

[14] R. Giraud, J. Cormier, Z. Hervier, D. Bertheau, K. Harris, J. Wahl, X. Milhet, J. Mendez, A. Organista, Effect of the Prior Microstructure Degradation on the High Temperature/Low Stress Non-Isothermal Creep Behavior of CMSX-4® Ni-Based Single Crystal Superalloy, Superalloys 2012. (2012) 265–274. doi:10.1002/9781118516430.ch29.

[15] A. Epishin, T. Link, H. Klingelhöffer, B. Fedelich, P. Portella, Creep damage of single-crystal nickel base superalloys: mechanisms and effect on low cycle fatigue, Mater. High Temp. 27 (2010) 53–59. doi:10.3184/096034009X12603595726283.

CHAPTER 1
LITERATURE REVIEW
AND
RESEARCH BACKGROUND

Table of contents

Résumé : Revue de la littérature et contexte des travaux de recherche 7

1. 1. Cast Ni-based superalloys for turbine blade application 9

1. 1. 1. Blade alloy development 9

1. 1. 2. Ni-based single crystal superalloy 1 1

1. 1. 3. Manufacturing processes 1 3

A) Casting and solidification 1 3

B) Solution and aging heat treatments 1 4

C) Porosity and hot-isostatic pressing (HIP) 1 6

1. 2. High-temperature deformation and durability of superalloys 1 7

1. 2. 1. Strengthening mechanism of γ/γ′ Ni-based superalloys 1 7

1. 2. 2. Tensile deformation 1 8

1. 2. 3. Creep 1 9

A) High-temperature/low-stress creep 1 9

B) Low-temperature/high-stress creep 2 2

1. 2. 4. Very high cycle fatigue 2 3

1. 3. Pre-straining effect 2 4

1.3.1. Pre-straining before solution treatment 2 4

1.3.2. Microstructure behavior after pre-straining 2 5

1.3.3. Mechanical properties of pre-deformed superalloys 2 6

1.3.4. Rejuvenation treatment 2 8

1. 4. Previous experimental results 3 3

1.4.1. Microstructure after pre-deformation and following aging treatments 3 4

1.4.2. Creep properties of pre-deformed AM1 SX superalloy 3 5

1.4.3. Tensile tests and low cycle fatigue tests 3 8

1. 5. Research objectives 4 0

References 4 0

RÉSUMÉ : REVUE DE LA LITTÉRATURE ET CONTEXTE DES TRAVAUX DE RECHERCHE

Les superalliages monocristallins à base de Ni sont des alliages structuraux résistants aux hautes températures, généralement utilisés pour les aubes et les distributeurs des turbines à gaz comme les turboréacteurs d'avions et les turbines à gaz industrielles [1–4]. Ils sont constitués d'une matrice désordonnée γ (soluté de Ni) durci par une forte fraction volumique (60 à 70 %) de précipités γ′ (Ni_3Al : réseau de type $L1_2$). L'interface cohérente γ/γ′ limite le mouvement des dislocations, ce qui permet aux superalliages base-Ni de présenter des propriétés mécaniques plus élevées que l'alliage monophasé γ ou γ′ [2,5]. En général, des traitements thermiques de mise en solution et de revenu sont appliqués aux superalliages coulés pour optimiser leur microstructure qui présente des propriétés supérieures à haute température.

Afin d'améliorer l'efficacité thermique des turbines à gaz, les superalliages coulés conventionnels ou à solidification dirigée employés de nos jours dans les premiers étages d'aubes de turbines basse pression seront remplacés par des superalliages monocristallins dans un futur proche. De plus, les profils aérodynamiques des pièces se complexifient afin de garantir de meilleures propriétés aérodynamiques.

Une faible déformation plastique peut être introduite dans une pièce monocristalline au cours de différentes étapes de la production, lors du refroidissement après solidification ou lors du démoulage [6,7]. Cette déformation plastique peut également être le résultat de chocs de manipulation ou de chocs thermiques dus à des différences de vitesse de refroidissement locales lors de mise en solution [8]. Une déformation plastique inattendue peut se produire plus fréquemment dans les grandes aubes de turbine et/ou les aubes de turbine ayant des profils aérodynamiques complexes.

Certaines études se sont focalisées par le passé sur l'effet de la déformation plastique sur l'évolution de la microstructure γ/γ′ au cours des vieillissements suivants cette déformation [9–12]. En raison de la relaxation des contraintes internes introduites par la déformation plastique, une évolution de la microstructure semblable à celle d'une mise en radeaux [9–11] et/ou la précipitation en phase TCP (topologically closed packed) [12] peuvent se produire pendant le vieillissement. Par ailleurs, une seule étude s'est focalisée sur l'effet des contraintes résiduelles introduites dans une aube de turbine au cours des processus de production, contraintes résiduelles qui provoquent une évolution de la microstructure et une relaxation des contraintes internes [8]. Les études sur l'impact d'une déformation plastique en cours de production sur la durabilité du matériau sont ainsi très limitées.

Une étude préalable à ce travail de thèse a reproduit une déformation accidentelle de pièces monocristallines en cours de production via l'introduction d'une faible déformation plastique à température ambiante entre la mise en solution et les traitements de revenu. Des essais de fluage sur le superalliage monocristallin AM1 pré-déformé ont montré une réduction de la durée de vie en fluage, en particulier à des températures supérieures à 950 °C. Néanmoins, les mécanismes exacts conduisant à une recristallisation et à la chute de la durée de vie en fluage n'ont pas été déterminés. Par conséquent, certaines questions sont à éclaircir :

- Comment la microstructure évolue-t-elle au cours des traitements de revenu après la pré-déformation ?
- Comment la microstructure dégradée affecte-t-elle la durabilité à haute température de l'AM1 et d'autres superalliages monocristallins base-Ni de compositions chimiques différentes, dans des conditions de fluage différentes ?
- Quelles sont les causes et les origines de la recristallisation au cours de la déformation par fluage ?
- Comment d'autres trajets de pré-déformation peuvent-ils affecter la microstructure et les propriétés mécaniques des superalliages monocristallins ? (Pré-déformation à des températures plus élevées, à différents étapes comme après un traitement thermique complet).

D'un point de vue industriel :

- Les matériaux pré-déformés sont-ils utilisables pour les conditions de service des turboréacteurs ?
- Existe-t-il un moyen de réutiliser les matériaux pré-déformés ?

L'objectif de ces travaux de thèse est d'obtenir une compréhension plus détaillée des questions mentionnées ci-dessus. Une étude complète sur l'effet de la déformation liée aux questions de production n'a jamais été réalisée ailleurs. En outre, le concept de traitement thermique de restauration est appliqué aux matériaux pré-déformés pour démontrer la possibilité de les remettre en production/en service. Le traitement de régénération (deuxième mise en solution) des superalliages monocristallins avec déformation plastique par traction est également un sujet nouveau.

1. 1. Cast Ni-based superalloys for turbine blade application

Ni-base superalloys have superior high temperature properties such as creep, fatigue, thermomechanical fatigue, oxidation resistance, corrosion resistance [2,3,13]. By taking advantage of these characteristics, they are mainly applied for hot section materials of various gas turbine systems such as aero-engines, gas turbine engines for ships, and land-based power generating gas turbines. Modern gas turbines are using Brayton thermal cycle for the conversion of thermal energy to mechanical energy and the most effective way to improve thermal efficiency in the system is to increase turbine inlet temperature (TIT) of combustion gas. Nowadays, the TIT of the newest military jet-engine Pratt & Whitney's F135 is reaching 1982 °C (3600 °F) [14] which is above the melting point of many structural metals. Some components are using ceramic matrix composites (CMC) which has properties capable of application at much higher temperatures. However, Ni-based superalloys are still the first choice for the turbine blade applications due to their robustness and maturity in processing operations. Turbine blade, especially one in the high-pressure turbine (HPT) section just after combustion chamber, is a rotating component in the turbine that is exposed at the highest temperature and mechanical loads during operation. Advanced thermal barrier coatings, internal cooling gas, and external gas film cooling protects the turbine blades from exceeding durable temperature (Figure 1.1). In order to improve specific fuel consumption of gas turbines, not only to increase TIT, but also decreasing amount of cooling air are important. High performance cast superalloys have been developed to answer this demand of increasing temperature capability on structural materials.

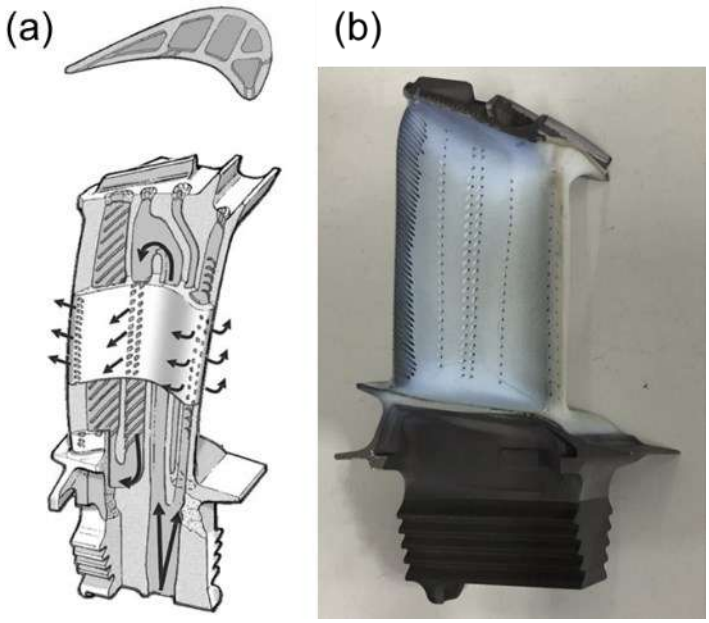

Figure 1.1. Schematic illustration of cooling path of a turbine blade (a) [3] and HPT blade with thermal barrier coatings overlaid on the aerofoil section (b).

1. 1. 1. Blade alloy development

Ni-base superalloys for turbine blade applications are composed of disordered γ (Ni solute) matrix and coherent cubic γ′ (Ni_3Al: $L1_2$ type lattice) precipitates (Figure 1.2). Coherent γ/γ′ interfaces interfere with the dislocation movement, which enables the Ni-base superalloys to exhibit higher creep performance than either γ or γ′ single phase alloy [2,5]. Creep properties are considered as one of the most important properties that determines elongation of the turbine rotor blade after the operation under centrifugal forces. Because turbine blades with

excessive creep deformation will be eliminated during engine maintenance, creep properties can be critical for operation lifetime of the turbine blade.

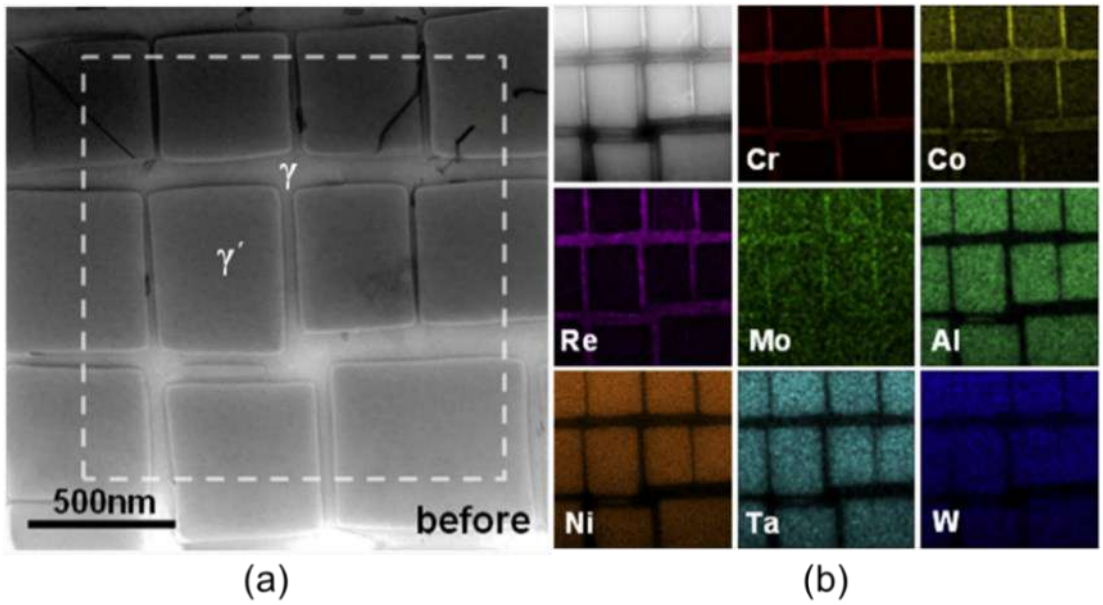

Figure 1.2. Typical microstructure of Ni-based SX superalloy consist of disordered γ phase matrix and cuboidal γ′ phase coherent precipitate (a). Elemental distribution maps of the area indicated by dashed rectangle in (a) obtained by energy-dispersive X-ray spectrometry (EDS) (b). [15]

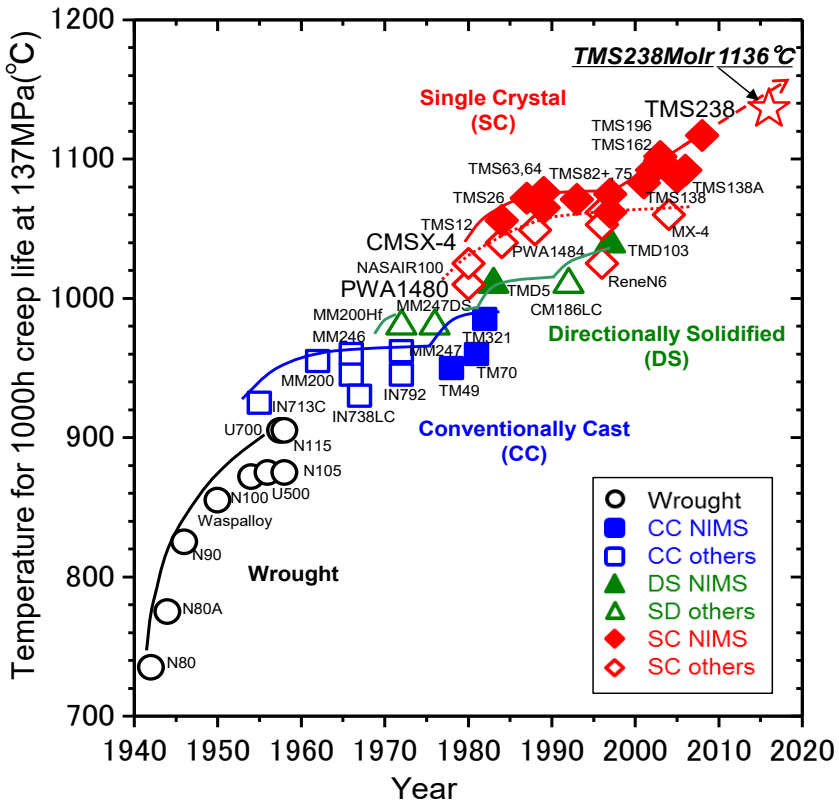

Figure 1.3. The history of improvement in temperature capability of turbine blade alloys. [16]

Figure 1.3 presents the history of increasing temperature capability of the blade alloys [16]. The turbine blade alloys have been developed first from cast and wrought Nimonic alloys such as Nimonic 80A and 90, and they were used in early turbo jet engines in the 1940s. After development of vacuum induction melting (VIM) and precision lost-wax casting methods, improved quality of casting product enabled the application of

polycrystalline cast (conventionally cast, CC, Figure 1.4(a)) alloys such as IN713C, Rene125 and MarM-247. Then, directional solidification process that creates columnar grain boundaries along solidifying direction drastically improved creep properties of the blades. Those are called directionally solidified (DS) alloys (Figure 1.4(b)) and their examples are Mar-M200 + Hf (DS200+Hf/PWA1422), CM186LC, and GTD111. Improved casting technique allowed to remove grain boundaries from the cast component to create single-crystal (SX, SC, monocrystalline) superalloys (Figure 1.4(c)).

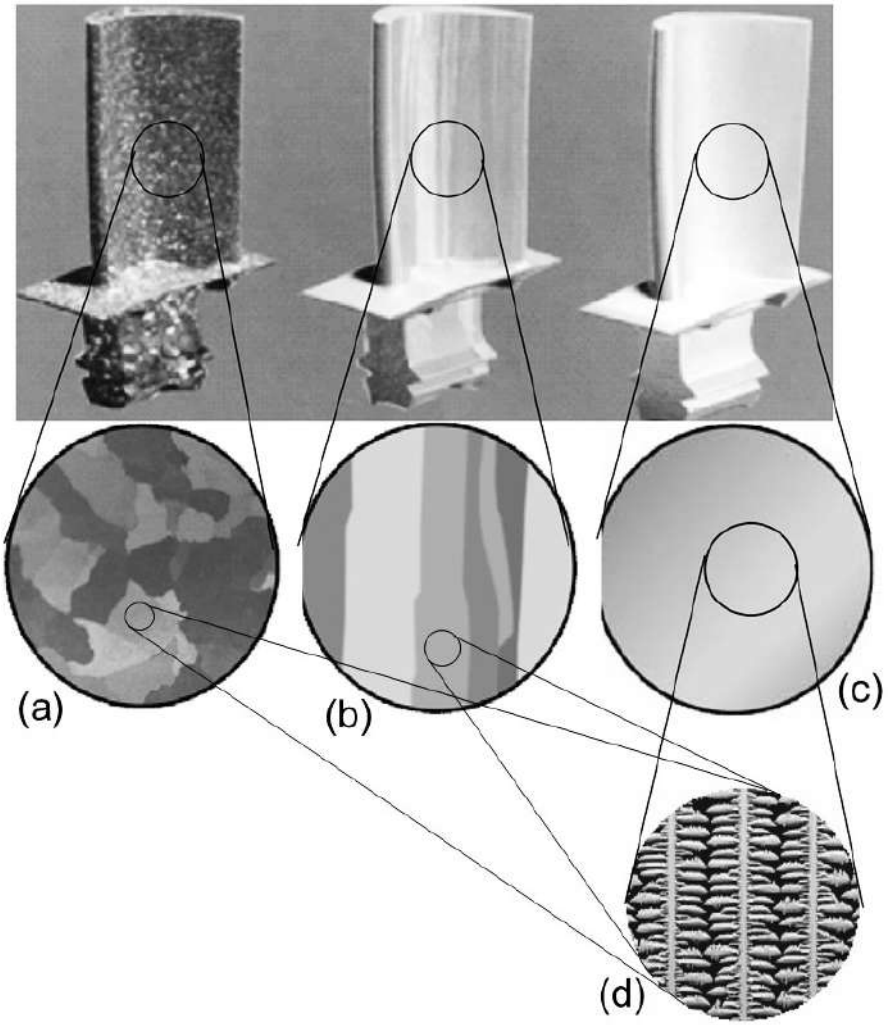

Figure 1.4. Ni-base superalloy turbine blades solidified as (a) equiaxed morphology, (b) columnar grains, (c) single crystal, (d) an enlarged view of the single crystal blade showing detailed dendritic structure calculated using CAFD solidification software. [17]

1. 1. 2. Ni-based single crystal superalloy

The grain boundaries are the weakest part of the alloy under creep loading because they can easily initiate cracks and grain boundary sliding. Complete solution treatment is difficult in polycrystalline alloys because of strong chemical segregation at grain boundaries and the existence of some grain boundary strengthening elements such as C, B, and Zr. Elimination of the grain boundaries in a superalloy enabled the alloy design to extract these minor elements and to increase concentration of refractory elements.

Commercial SX-specialized superalloys started from the 1st generation PWA1480 (Alloy 454) developed in 1970s [18], AM1, CMSX-2, and SRR99, followed by the 2nd generation which contains around 3wt% of Re

such as PWA1484, CMSX-4, and Rene N5 [19,20]. Further increase in temperature capability was achieved by 5-6wt% Re containing 3rd generation alloys such as Rene N6, CMSX-10, and TMS-75 [21,22]. Increasing the content of strengthening elements (Re and W) has inverse effect to the stability of γ/γ′ equilibrium, which can result in alloy strength degradation by undesirable intermetallic precipitations known as topologically close-packed (TCP) phase [23–25]. To improve phase stability with increased amount of strengthening elements, Ru was added in 4th generation alloys such as TMS-138, MX-4/PWA1497, and MC-NG [26]. The 5th generation alloy TMS-196 improved creep temperature capability by adjusting composition to control the lattice misfit and microstructural behavior [27]. To overcome lower oxidation resistance of strength-focused 3rd and 4th generation superalloys, TMS-238 has increased Cr content to have comparable oxidation resistance as 2nd generation alloys, achieving the best compromise between creep and environmental resistance [28]. Recent alloy design studies are adding new platinum group metals such as Ir (phase stabilizer in place of Ru) and Pt (increasing γ′ volume fraction at ultra-high temperature above 1200°C) [29–32]. Re-free new 1st generation alloys RenéN500 and TMS-1700/MGA1700 or low-Re content 3rd generation CMSX-4 Plus were also developed to decrease alloy cost [33–35]. List of various SX superalloys are presented in Table 1.1.

Ni-based SX superalloys have one of most complicated alloy systems that consist of up to 19 elements in the chemical composition [2,3]. This is related to the severe operating condition of the component and complex strengthening mechanism that realizes the demand. Table 1.2 explains basic functions of each alloying elements in the superalloys.

Table 1.1 List of Ni-based SX superalloys

Superalloys	Nominal composition (wt %, Ni bal.)													Gen	Development
	Co	Cr	Mo	W	Al	Ti	Nb	Ta	Hf	Re	C	B	Others		
PWA1480	5.0	10.0	-	4.0	5.0	1.5	-	12.0	-	-	-	-	-	1st	P&W
Rene N4	8.0	9.0	2.0	6.0	3.7	4.2	0.5	4.0	-	-	-	-	-		GE
CMSX-2	4.6	8.0	0.6	8.0	5.6	1.0	-	9.0	-	-	-	-	-		Cannon Muskegon
TMS-6	-	9.2	-	8.7	5.3	-	-	10.4	-	-	-	-	-		NIMS
AM1	6.7	7.6	2.0	5.6	5.2	1.2	-	8.0	0.05	-	-	-	-		ONERA/Snecma
MC2	5.0	8.0	2.0	8.0	5.0	1.5	-	5.0	-	-	-	-	-		ONERA
SRR99	15.0	10.0	3.0	-	5.5	4.0	-	-	-	-	-	-	-		Rolls-Royce
MDSC-7M	4.5	10.0	0.7	6.0	5.4	2.0	-	5.4	-	0.1	-	-	-		M&C/CRIEPI
Rene N500	7.5	6.0	1.6	6.25	6.25	-	-	6.5	0.2	-	0.04	0.004	-		GE
CMSX-7	10.0	6.0	0.6	9.0	5.7	0.8	-	9.0	0.2	-	-	-	-		Cannon Muskegon
TMS-1700/MGA1700	-	9.0	0.6	7.6	5.4	-	-	10.0	-	-	-	-	-		NIMS/MHI
PWA1484	10.0	5.0	2.0	6.0	5.6	-	-	8.7	-	3.0	-	-	-	2nd	P&W
Rene N5	8.0	7.0	2.0	5.0	6.2	-	-	7.0	0.2	3.0	-	-	-		GE
CMSX-4	9.0	6.5	0.6	6.0	5.6	1.0	-	6.5	0.1	3.0	-	-	-		Cannon Muskegon
TMS-82+	7.8	4.9	1.9	8.7	5.3	0.5	-	6.0	0.1	2.4	-	-	-		NIMS/Toshiba
YH61	1.0	7.1	0.8	8.8	5.1	-	0.8	8.9	0.26	1.4	0.07	0.02	-		Hitachi
Rene N515	7.5	6.0	2.0	6.25	6.25	-	0.1	6.5	0.6	1.5	0.035	0.004	-		GE
CMSX-8	10.0	5.4	0.6	8.0	5.7	0.7	-	8.0	0.2	1.5	-	-	-		Cannon Muskegon
TMS-286	-	9.0	-	8.0	5.4	-	2.3	5.8	-	1.2	-	-	0.15Si		NIMS
Rene N6	12.5	4.2	1.4	6.0	5.75	-	-	7.2	0.15	5.4	0.05	0.004	0.01Y	3rd	GE
CMSX-10	3.0	2.0	0.4	5.0	5.7	0.2	0.1	8.0	0.03	6.0	-	-	-		Cannon Muskegon
CMSX-10N	3.1	1.7	0.5	5.5	5.9	0.1	0.1	8.5	-	6.8	-	-	-		Cannon Muskegon
TMS-75	12.0	3.0	2.0	6.0	5.0	-	-	6.0	0.1	5.0	-	-	-		NIMS
CMSX-4 Plus	10.0	3.5	0.6	6.0	5.7	0.85	-	8.0	0.1	4.8	-	-	-		Cannon Muskegon
MX-4/PWA1497	16.5	2.0	2.0	6.0	5.6	-	-	8.3	0.15	6.0	-	-	3.0 Ru	4th	GE/P&W/NASA
MC-NG	< 0.2	4.0	1.0	5.0	6.0	0.5	-	5.0	0.1	4.0	-	-	4.0 Ru		ONERA
TMS-138	5.8	3.2	2.8	5.9	5.9	-	-	5.6	0.1	5.0	-	-	2.0 Ru		NIMS/IHI
TMS-138A	5.8	3.2	2.8	5.6	5.7	-	-	5.6	0.1	5.8	-	-	3.6 Ru		NIMS
TMS-196	5.6	4.6	2.4	5.0	5.6	-	-	5.6	0.1	6.4	-	-	5.0 Ru	5th	NIMS
TMS-238	6.5	4.6	1.1	4.0	5.9	-	-	7.6	0.1	6.4	-	-	5.0 Ru	6th	NIMS
TMS-238MoIr	6.2	4.4	3.1	3.8	5.3	-	-	7.2	0.1	6.1	-	-	4.7Ru, 5.8Ir		NIMS
TROPEA	9.0	6.5	0.6	6.0	5.6	1.0	-	9.0	0.1	1.0	-	-	2.0Pt	-	Pprime/Safran

Table 1.2. Functions of elements used in Ni-based SX superalloys

	Ni	Co	Cr	Mo	W	Al	Ti	Nb	Ta	Hf	Re	Ru	Ir	Pt	C, B	Zr	Si
γ matrix	X	X	X	X							X	X					
γ′ precipitate						X	X	X	X				X				
Carbide former							X	X	X	X					X	X	
Negative lattice misfit			-	+		+			-		+		-	-			
Solid solution strengthning		+			+			+	+		+	+	+				
Precipitation strengthening						+	+		+								
Grain boundary strengthening															+		
Environmental resistance	+		+	-		+				+	+				-	+	+
Precipitate stability (γ/γ′)					+				+		+			+			
Phase stability (avoid TCP)		+	-	-	-		-	-	-		-	+	+	+			-
Castability							-		+	-							

(X: preferential distribution, +: positive effect, -: negative effect)

1. 1. 3. Manufacturing processes

A) Casting and solidification

Superalloy turbine blades are nowadays produced by the investment lost-wax casting that enables to obtain hollow aerofoils with complicated but high-precision form. This formability is essential to the design of turbine blades with good aerodynamic properties. This casting method also helped to control the solidification process that is important to eliminate grain boundaries. After pouring the melt from crucible into the mold, the casting is moved from heating chamber to the cooling chamber at a controlled withdrawal rate. In other words, moving speed of solid/liquid interface and temperature gradient at the interface are controlled so that the crystals can continue to grow in one direction, so called directional solidification.

In the directional solidification, either grain-selector or SX seed are used to determine original grain to grow and to obtain SX casting products. The pig-tail-shaped spiral grain-selector is popularly used for SX turbine blade casting because it is relatively easier to build a casting mold. During the directional solidification, grains will be eliminated as the angle of the pig-tail spiral changes, and eventually only the crystal in <001> preferential growth direction reaches the main cavity of the casting mold (Figure 1.5). Advantage of SX seed is that the crystal growth direction can be determined, and hence, this is applied for very complex or large component, or to control secondary orientation of the cast product.

Practically, the Bridgman-Stockberger casting method (high-rate solidification) that consists of baffle, radiation cooling chamber, and water-coolant chill plate for creating temperature gradient, is selected for turbine blade casting (Figure 1.6(a)). A possible alternative is liquid metal cooling (LMC) method using direct contact of liquid metal with the mold that enables faster cooling and higher temperature gradient compared to the Bridgman method (Figure 1.6(b)). The LMC cast SX product has better metallurgical characteristics and capable of casting bigger components compared to the Bridgman cast product. However, the process cost makes the Bridgman method more popular choice in foundry for aero-engine turbine blades.

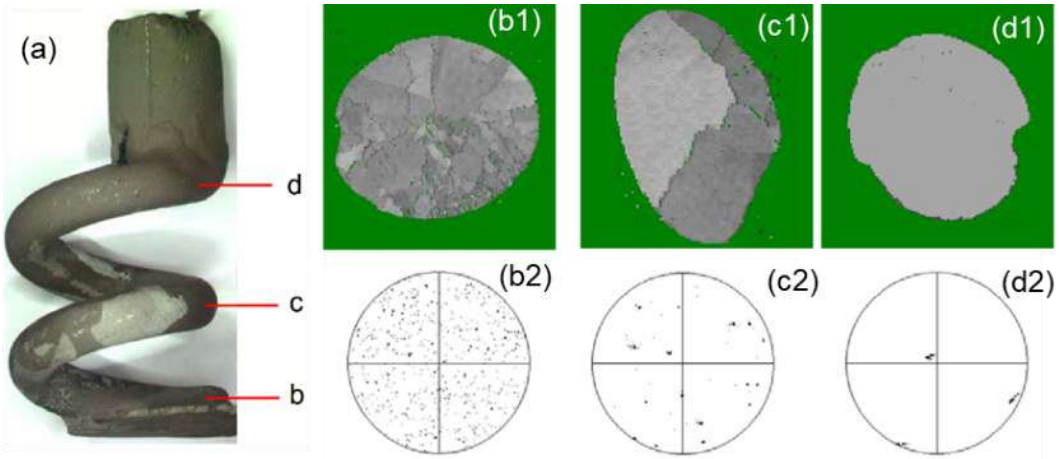

Figure 1.5. (a) Spiral grain-selector. (b1-d1) Grain textures at different heights of the spiral. (b2-d2) ⟨001⟩ pole figures at various heights corresponds to (b1-d1). [17]

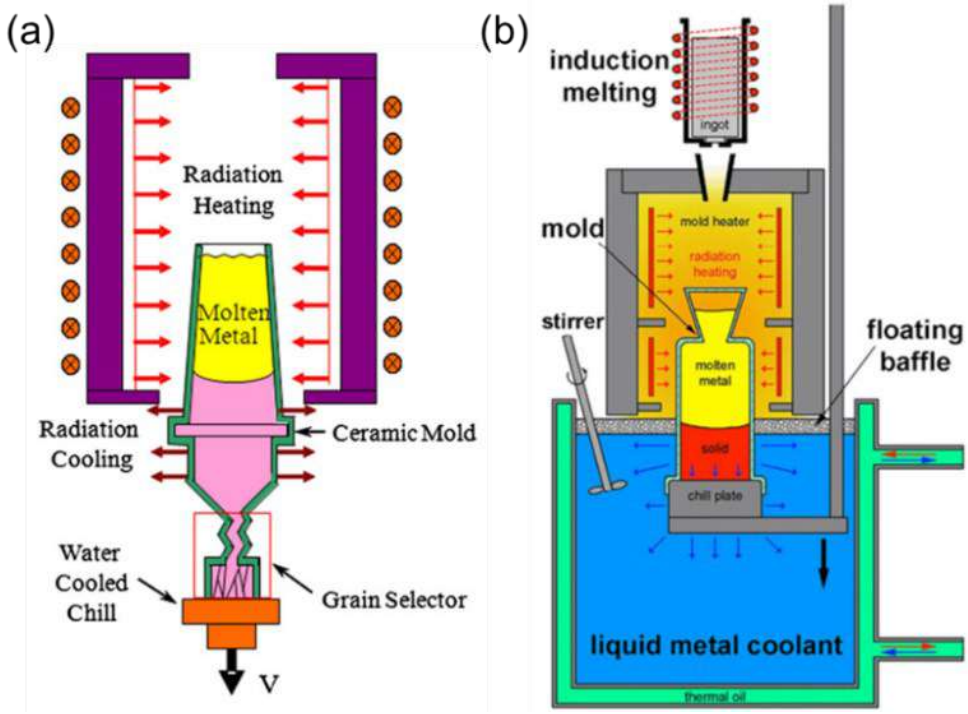

Figure 1.6. Schematic illustration of Bridgman-Stockberger (high-rate solidification) (a) [36] and liquid metal cooling (b) [37].

B) Solution and aging heat treatments

Directional solidification is accompanied by dendritic growth and hence, strong segregation is created in the cast product. As mentioned previously, the Ni-based SX superalloys have design base of Ni-Ni_3Al system (60-70% of γ′ phase) which is shown as tie-line in the Ni-Al phase diagram (Figure 1.7). During solidification, each alloying element have preferential solid/liquid distribution that changes local chemistry at the solidification line as the line moves from bottom to top. This creates dendritic microsegregation with γ′-rich eutectic at the interdendritic areas in the as-cast material (Figure 1.8(a)). In order to reduce microsegregation and remove eutectics, the material has to be solution treated at supersolvus temperature of γ′ phase. Above the solvus temperature, γ′ phase dissolves into γ phase and this high temperature exposure proceeds homogenization of the segregated elements. Because local solution window (difference between solvus and liquidus temperatures) is controlled by the magnitude of segregation, some alloys with higher refractory

contents (especially alloys after 3rd generation with small solution window) must take stepwise solution treatment to avoid incipient melting (Figure 1.8(b)). Mechanical properties of superalloys can be improved by avoiding chemical segregation and reducing volume fraction of the eutectic pool [38–40].

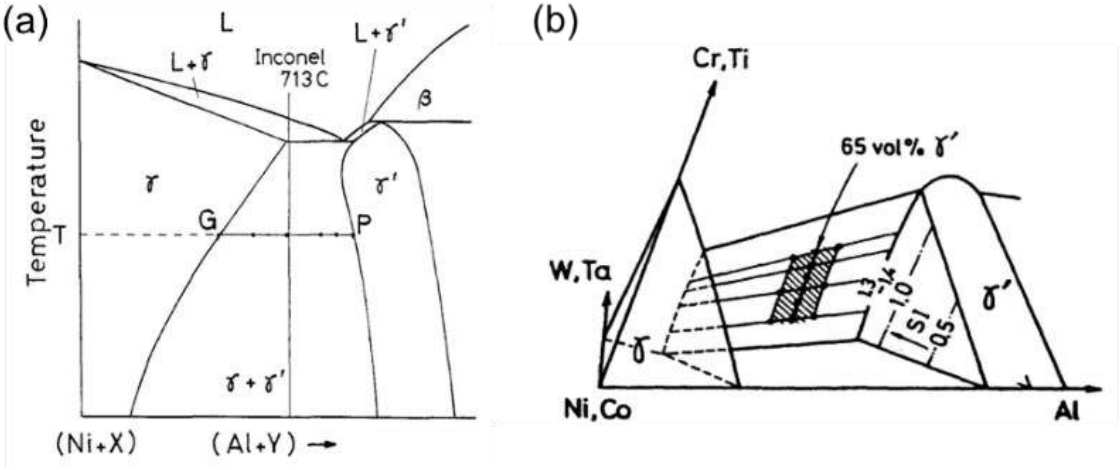

Figure 1.7. Pseudo-binary phase diagram of (Ni+X)-(Al+Y) system at 1000 °C (a), Y is a substitutional element for an Al site in γ′ and X is an element for an Ni site [41]. Schematic phase diagram used for alloy design having the composition range with 65% γ′ volume fraction (b) [42].

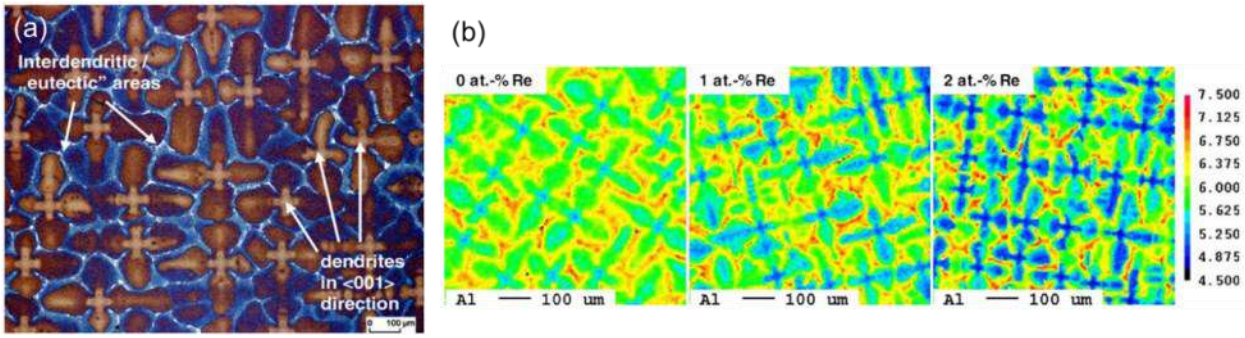

Figure 1.8. Optical micrograph of as-cast structure showing the evolved dendritic structure with the eutectics in the interdendtiric areas (a). EPMA (electron probe microanalysis) composition map of Al (scale in wt%) for as-cast experimental alloys showing increasing segregation of Al with increasing Re content (b). [43]

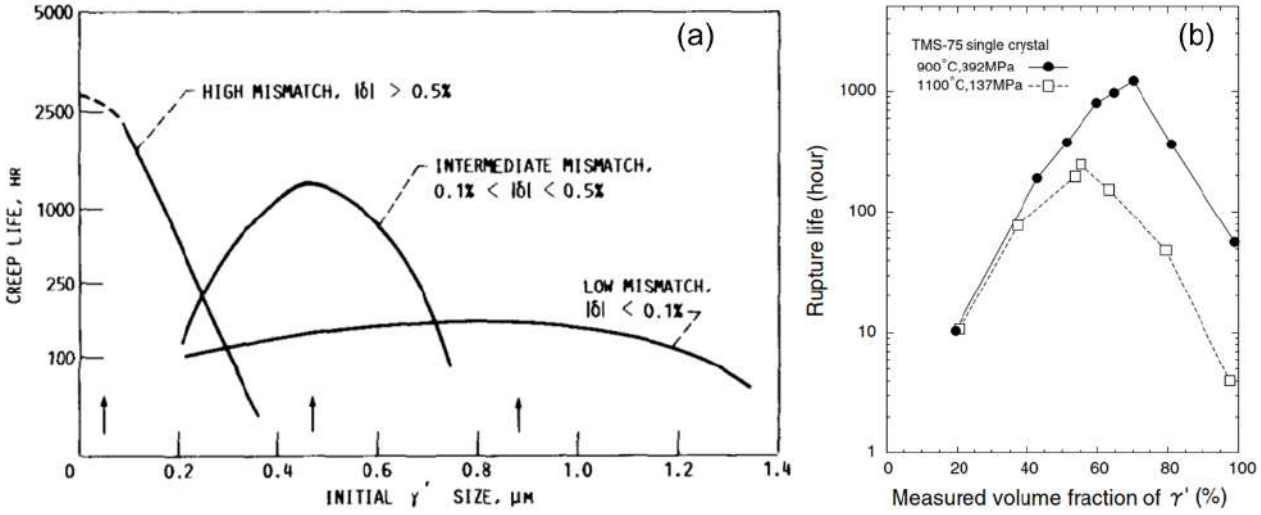

Figure 1.9. (a) Relationship of initial γ′ precipitate size and creep rupture life of SX superalloys with various lattice mismatch under directional coarsening condition [44]. (b) Relationship between measured γ′ volume fraction and creep rupture life of TMS-75 SX superalloy [5].

After the solution treatment, at least two aging treatments are generally applied to the SX superalloys. Because most of the γ′ precipitates have already formed during the cooling of the solution treatment, aging treatments intend to modify microstructure characteristics [45,46]. The first aging treatment is performed at the range of 1000-1170 °C that affects precipitate size and morphology. It is generally operated at the temperature with the highest (or intended) absolute γ/γ′ lattice misfit to form cuboidal γ′ precipitates in the γ matrix channels. The γ/γ′ lattice misfit (δ), difference of lattice parameter between γ (α_γ) and γ′ ($\alpha_{\gamma'}$) phases, is defined as $\delta = 2(\alpha_{\gamma'}-\alpha_\gamma)/(\alpha_{\gamma'}+\alpha_\gamma)$. The cuboidal precipitates can be achieved if the absolute lattice misfit range at the aging temperature is $0.1\% < |\delta| < 0.5\%$. Size of the precipitates are typically set to 0.3-0.5 μm in cube edge length, which is ideal for various mechanical properties (tensile/compressive loading and fatigue) of [001] oriented material at wide range of temperatures (Figure 1.9(a)) [39,44,47–49]. The secondary aging treatment between 700-900 °C is applied to control the γ′ volume fraction (from 40-50% at first aging temperature to 60-70%) and to have thin γ matrix channels. This volume fraction is known to have best creep performance and thinner matrix channel prevents the accumulation of dislocations during deformation (Figure 1.9(b)) [5].

C) Porosity and hot-isostatic pressing (HIP)

The microsegregation is an issue in the directional coarsening that has chemical composition gradient in the liquid/solid interface region, or the mushy zone. In this zone, local concentration of elements with lower melting point creates the trapped melt between solidified dendrite arms. Due to the solidification shrinkage of the trapped liquid with no more melt supply, cavitation forms in the inter-dendritic area known as solidification-pores (S-pores, Figures 1.10(a, b)) [50–52]. S-pores in the Bridgman-processed SX superalloys generally have a size of 100-150 μm and their size is a critical parameter for determining fatigue properties. One solution for the S-pore issue is to apply hot-isostatic pressing (HIP). In the HIP process, materials are exposed in high temperature and isostatic gas pressure to densify and to reduce the porosity. This process effectively improves fatigue life of SX superalloys by the reduction of S-pores [53–56].

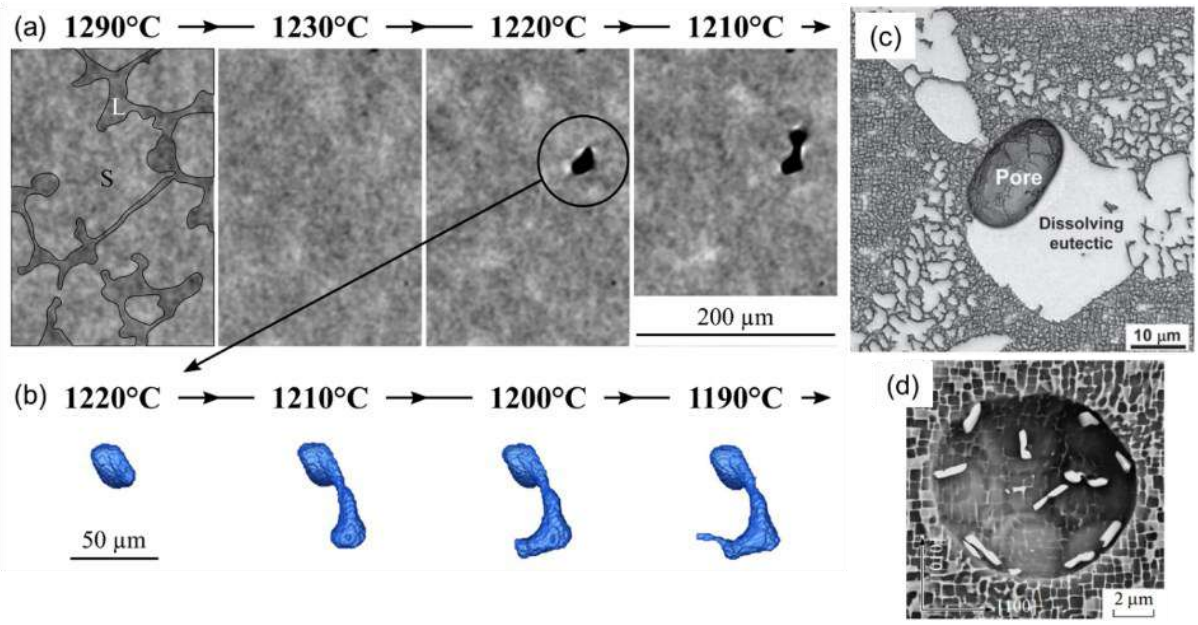

Figure 1.10. Formation of S-pore in the interdendritic area during cooling (L: liquid, S: solid) in cross section (a) and 3D rendering (b) obtained by in-situ microtomography [52]. H-pores in CMSX-10 nucleated at the eutectic/matrix interface (c) [57] and spherical one in the matrix (d) [58].

During subsequent homogenizing solution heat treatment, dissolution of eutectics and differences in interdiffusion rates of alloying elements cause Kirkendall-Frenkel effect [59] leading to the nucleation and growth of homogenization-pores (H-pores, Figures 1.10(c, d)) [50,57]. Very fast Al diffusion from eutectics and migration of vacancies to the interface of dissolving eutectic in exchange generate the H-pores. Therefore, volume fraction of H-pores correlates with the volume fraction of non-equilibrium γ/γ′-eutectic in as-cast state [57]. Compared to the S-pores, size of the H-pore is relatively smaller and has minor effect on the fatigue life of the SX superalloys. Nonetheless, all types of pores affect crack initiation at the beginning of creep failure.

If SX superalloys are cast by LMC method, higher temperature gradient at the solidification front (thinner mushy zone) compared to the Bridgman method reduces dendritic segregation. Because of mild segregation and very fine dendritic structure can be created in LMC, both the S-pores and eutectics are less and smaller, or even they can be eliminated from as-cast structure.

1. 2. High-temperature deformation and durability of superalloys

1. 2. 1. Strengthening mechanism of γ/γ′ Ni-based superalloys

As introduced, Ni-based superalloys are generally designed to have FCC γ phase matrix and ordered $L1_2$ γ′ phase precipitates. Elements are randomly distributed in the ordered γ phase and it is reinforced by solid solution strengthening of refractory elements, such as Co, Cr, W, and Re. Addition of these elements will decrease stacking fault energy of γ matrix which facilitates full 1/2⟨110⟩ dislocation decompose into partial dislocations in a {111} plane. Recombination of the partial dislocations is necessary to proceed deformation in this plane. Therefore, lowering energy to introduce stacking fault help increasing deformation resistance of the material.

Ordered $L1_2$ γ′ precipitates contribute to material's strength in two different ways. First way is the precipitation being obstacles for deformation that proceeds by coupled dislocations shearing smaller particles and by Orowan loops by-passing larger particles [60–62]. These processes are determined by precipitate distribution and size [62]. Second is the intrinsic characteristics of deformation in $L1_2$ structure and the interaction with alloying elements distributing in Al site, such as Ta and Ti. Because of secondary element exists in ordered structure, full dislocation in FCC structure is equivalent to Burger's vector of 1/2⟨110⟩ in $L1_2$, which forms anti-phase boundary (APB) with two neighboring planes with higher bonding energy. This increases energy required for nucleation and movement of dislocation in γ′ phase compared to γ phase. To decrease activation energy, dislocations split into pairs that first one proceeds with APB formation and trailing one restores ordered structure (b_1 in Figure 1.11(b)). If the deformation proceeds with dislocations with Burger's vector 1/3⟨112⟩ or 1/6⟨112⟩, different types of stacking faults are created which also requires formation energy higher than that in FCC (b_2 and b_3 in Figure 1.11(b)). Higher bonding energy of the system and requirement of paired dislocation movement are contributing to the strengthening of γ′ phase. To improve shear resistance of the superalloys, Ta and Ti fraction in their composition is considered since these alloying elements increase APB energy of the γ′ phase by replacing Al site.

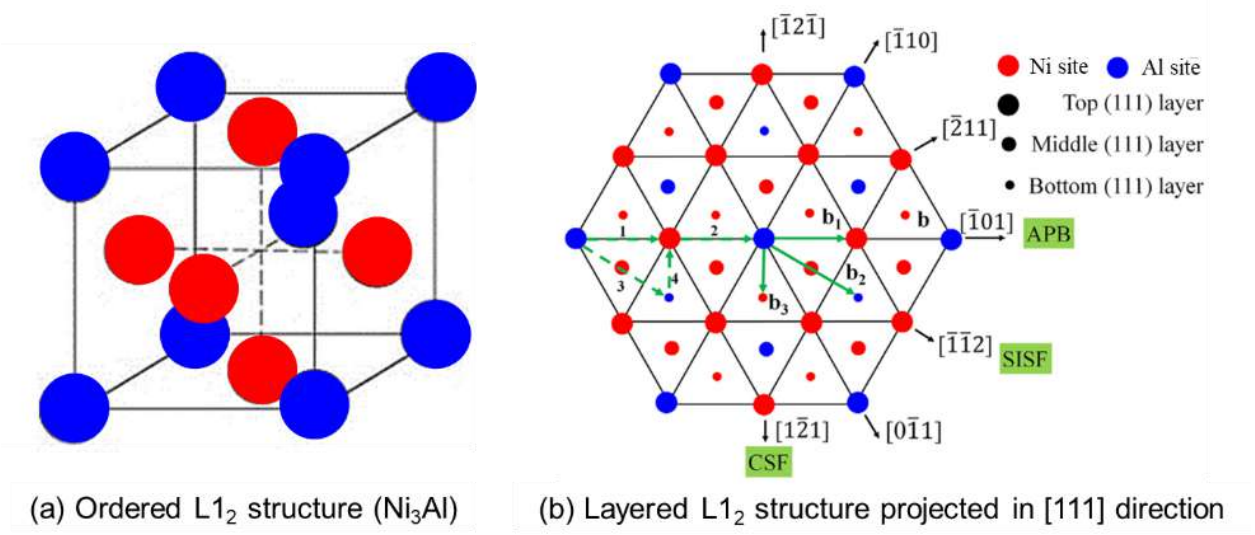

Figure 1.11. Unit cell arrangement of ordered $L1_2$ structure Ni_3Al γ′ phase (a) and its projection in [111] direction (b) [4].

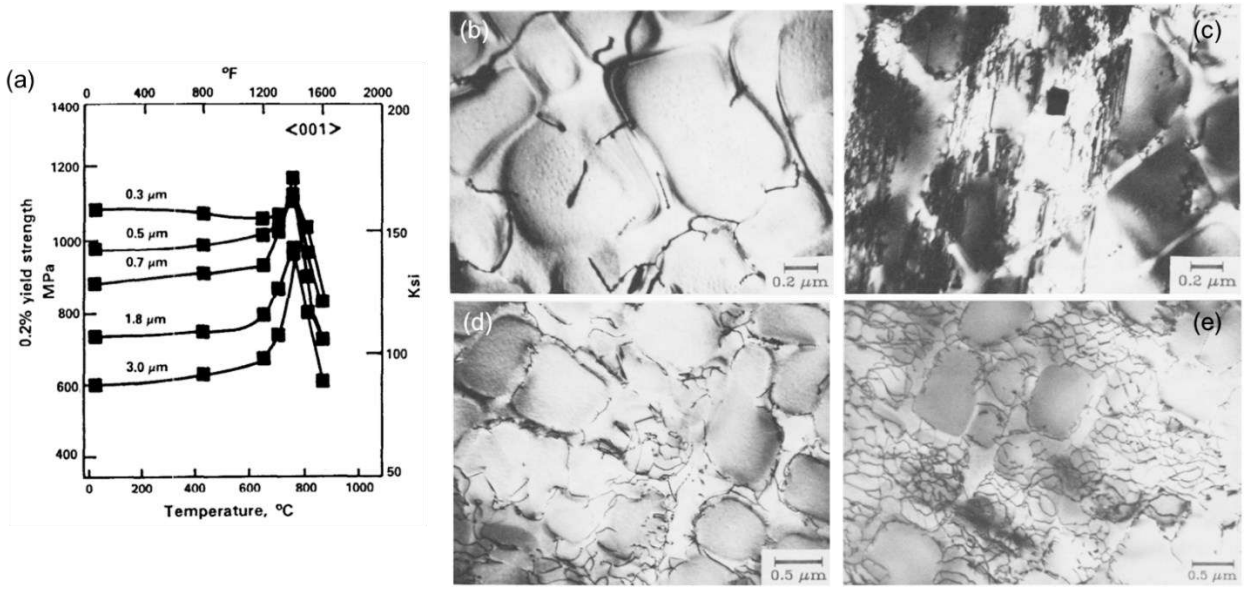

Figure 1.12. Effect of temperature and precipitation size on 0.2% offset yield strength of oriented <001> PWA1480 (a) [49]. Dislocations observed after tensile tests on PWA1480 at 20 °C (b), 705 °C (c), 982 °C (d), and 1093 °C (e), g = <200> [63].

1. 2. 2. Tensile deformation

Ni-based superalloys are known for temperature anomaly that yield stress increases with increasing temperature, typically up to 750-800 °C [48,49,63–66]. Example of PWA1480 SX superalloy exhibiting temperature anomaly is shown in Figure 1.12(a). This is owing to another feature of alloy with $L1_2$ intermetallic structure [64]. At higher-temperature, thermally activated cross-slip of dislocation from {111} slip plane onto {100} occurs in order to decrease APB energy. In this Kear-Wilsdorf locking mechanism, dislocations are locked on the {100} plane that cannot move without trailing pair dislocation [67]. Figures 1.12(b) and 1.12(c) are dislocations observed in PWA1480 after yielding at 20 °C and 705 °C, respectively. Although the yield stresses were similar for these temperatures, more homogeneous and higher density of dislocation is present in Figure 1.12(c) which is result of the thermally activated mechanism. At the higher temperatures, dislocations

are by-passing γ/γ′ interfaces (at 982 °C in Figure 1.12(d)) and their density increases with formation of dislocation networks (at 1093 °C in Figure 1.12(e)).

1. 2. 3. Creep

When the deformation strain rate is very small, strengthening mechanism of superalloys totally changes and yield strength drastically decreases. In low-temperature/high-stress creep, deformation is mainly driven by dislocation glide on the active slip systems. In high-temperature/low-stress condition, diffusion and dislocation climb become main rate controlling processes. Creep properties of SX superalloys are sensitive to the temperature/stress conditions. Creep characteristics of ⟨001⟩ oriented SX are mainly introduced here.

A) High-temperature/low-stress creep

Creep of SX superalloys at high temperatures (>1000 °C) is typically called as "rafting" regime because of microstructure evolution that occurs at the early stage of deformation [68]. The "rafting" word is used to describe directional coarsening of γ' phase as shown in Figure 1.13. The original cuboidal structure coarsens transverse to the loading direction after the primary creep stage for negative misfit alloys. The formation of γ'-raft first start by dislocation glide and climb in γ channels (Figure 1.14(b)) and dislocation density increases with formation of networks as deformation proceeds (Figure 1.14(c)). During steady secondary stage, fine networks of dislocations are formed, and matrix channels disappear (Figures 1.13(d) and 1.14(a)). Because lattice misfit creates interfacial strain, local stresses are modified to have anisotropic coherency stresses when external stress is applied (Figure 1.15). Dislocations are preferentially introduced in the vertical channel which exhibits higher elastic strain field at the primary creep stage. This accelerates solute exchange by dislocation pipe diffusion and coarsens γ' precipitates in horizontal direction, ultimately creates plate-like structure perpendicular to the loading axis. Because more dislocations are introduced to relax interfacial strain, alloy with higher absolute misfit generally forms finer dislocation networks (compare TMS-75(+Ru) and TMS-138 in Figure 1.14). The rafted structure with finer dislocation networks has been proved to increase the creep resistance of superalloys in lower stress condition by effectively hindering mobile dislocations from bypassing the γ' precipitates (Figure 1.16).

At the transition period from secondary to tertiary creep stages, dislocations shearing from γ/γ' interface into γ' phase occurs [69,70]. This further enhances coarsening of γ'-rafts (Figure 1.13(e)), but also make rafts into disrupted wavy form. Associated with dislocation climb, vacancy transportation become active. Creep void nucleates and grows, which typically called deformation-pores (D-pores) [51,58,71,72]. Growth of creep voids and crack propagation from the voids occur at the very steep tertiary stage and become source of creep failure [73–75].

At intermediate temperature/stress condition, directional coarsening also occurs but it does not develop with primary creep stage, and sometimes, the primary creep stage does not appear. Instead, creep curve consists of very short and small primary stage followed by monotonic increasing creep rate until rupture [76–78]. Increasing creep strain correlates to increase in dislocation density. Because γ' volume fraction is higher than 50% at the intermediate temperatures 850-1000 °C, evolution of the rafted microstructure leads to topologically inverted structure [78]. Topological inversion is the state that γ' phase become matrix by having

volume fraction superior to γ phase. It appears that γ' phase is covering isolated γ phase, but in three dimensions, both phases are connected all over the volume in very complex mesh-like structure. It has been recently proposed that dislocation shearing in the γ' phase with γ phase solute transportation as the mechanism of evolution into this complex structure (Figure 1.17) [79].

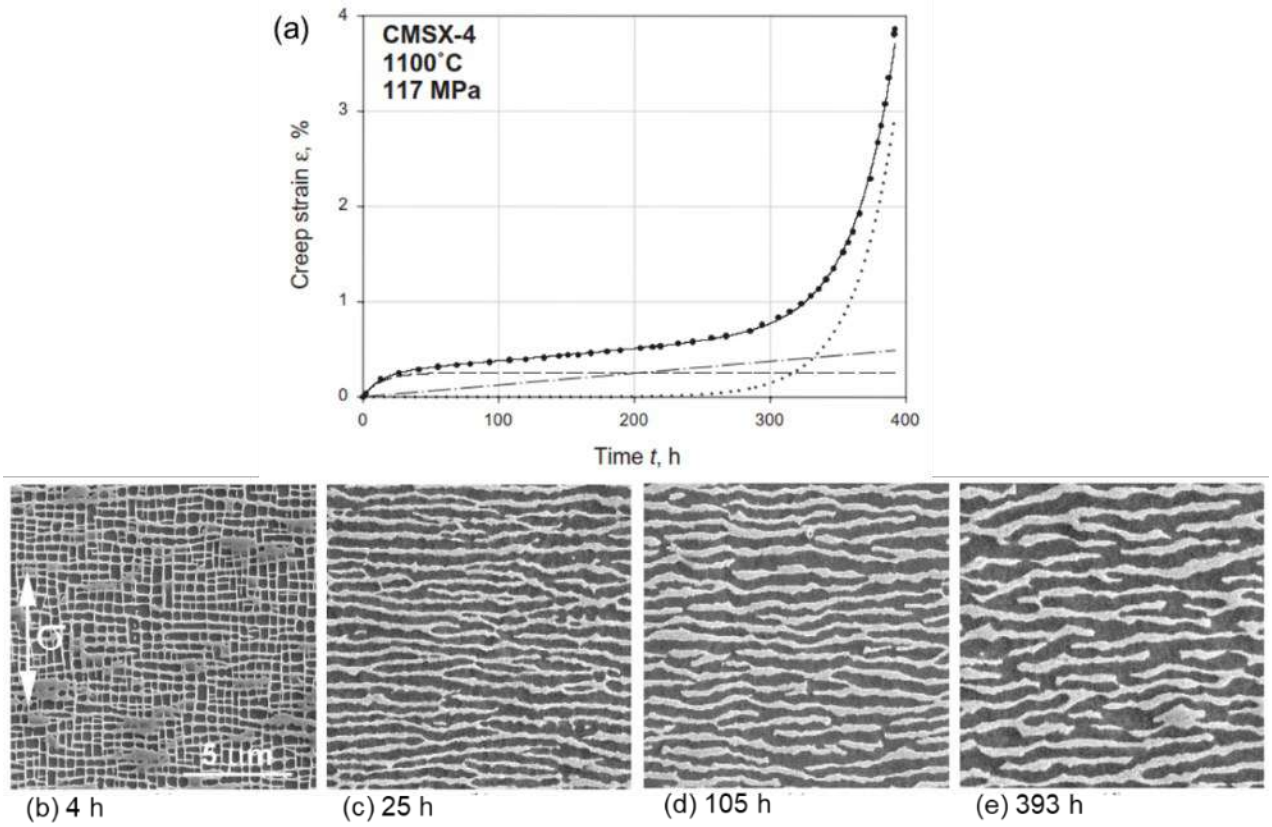

Figure 1.13. Typical creep curve of CMSX-4 at 1100 °C / 117 MPa (a). Microstructures were obtained from interrupted specimens at primary creep (b), transition from primary to secondary (c), middle of steady state creep, and after rupture far from rupture surface (d). [75]

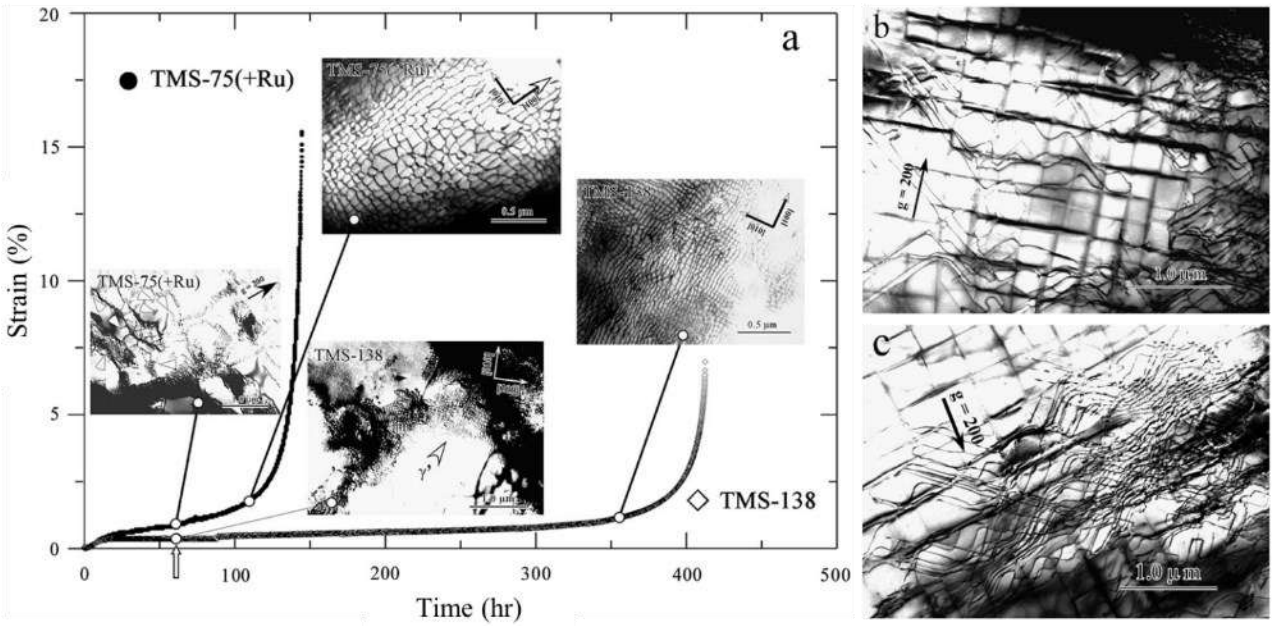

Figure 1.14. Creep curve of TMS-75(+Ru) and TMS-138 at 1100 °C / 137 MPa with TEM images at different creep stages (a). (b) and (c) are TMS-138 at 2 h and 5 h, respectively. [80]

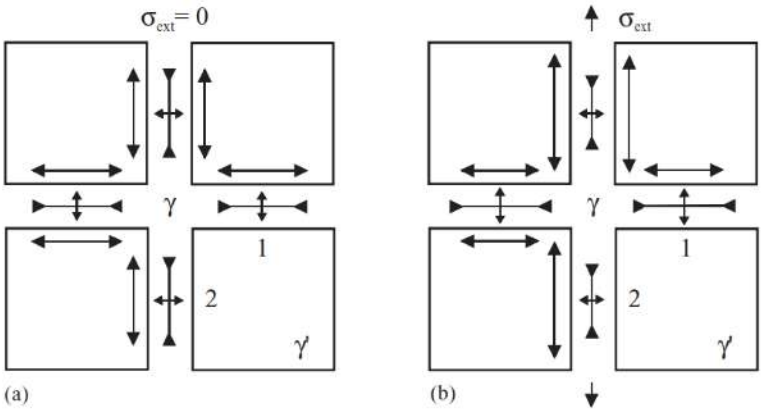

Figure 1.15. Schematic illustration of internal stress components in γ/γ' structure without (a) and with (b) external stress. [81]

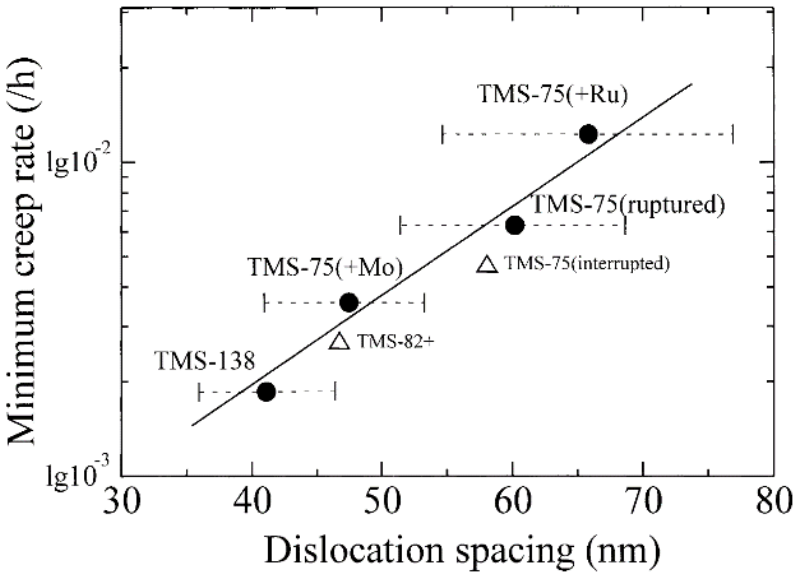

Figure 1.16. Relationship between minimum creep rate of SX superalloys at 1100 °C / 137 MPa and dislocation network spacing. [82]

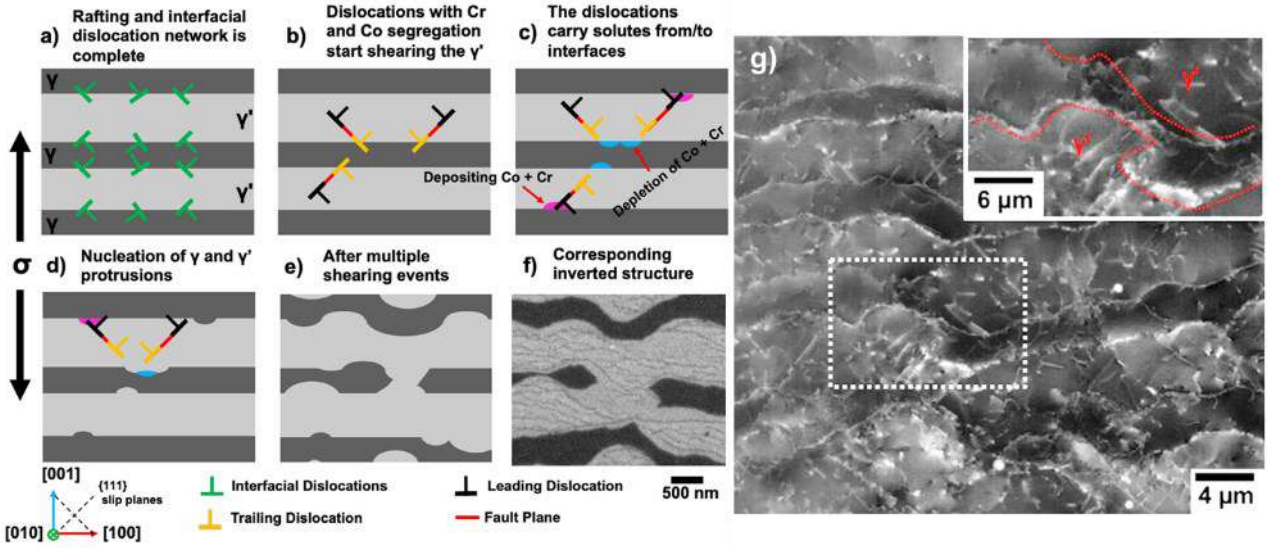

Figure 1.17. (a-f) Schematic illustration of inverted structure formation proceeds by solute transporting dislocation shearing. (g) Electron channeling contrast image (ECCI) showing two adjacent γ/γ' interface (red dotted line) about to coalesce in MC2 SX superalloy crept at 850 °C / 400 MPa. [79]

B) Low-temperature/high-stress creep

At lower temperatures where diffusion is relatively less active, and with higher stresses, very large primary creep strain is introduced to SX superalloy. Due to higher stress, deformation in this condition is driven by slip and hence strongly dependent on specimen's crystallographic alignment [83,84]. Figures 1.18 and 1.19 are examples of low-temperature creep behavior in relation to the specimen's longitudinal orientation. When the specimen is oriented with small Schmid factor of highly stressed ⟨112⟩{111} slip system, ⟨110⟩{111} become only active slip system during the primary creep stage which is the case for N specimen in Figure 1.19. Otherwise, stacking fault ribbons developed in ⟨112⟩{111} slip system can shear through γ/γ' interface, leading to large primary strain [85]. Transition from primary to secondary creep is result of a lattice rotation with increasing creep strain which leads to favored activity of ⟨110⟩{111} system compared to ⟨112⟩{111}. Because shearing by ⟨112⟩{111} slip system is associated with stacking faults, primary creep is very sensitive to the chemistry and γ' precipitate size of the alloy [86–88].

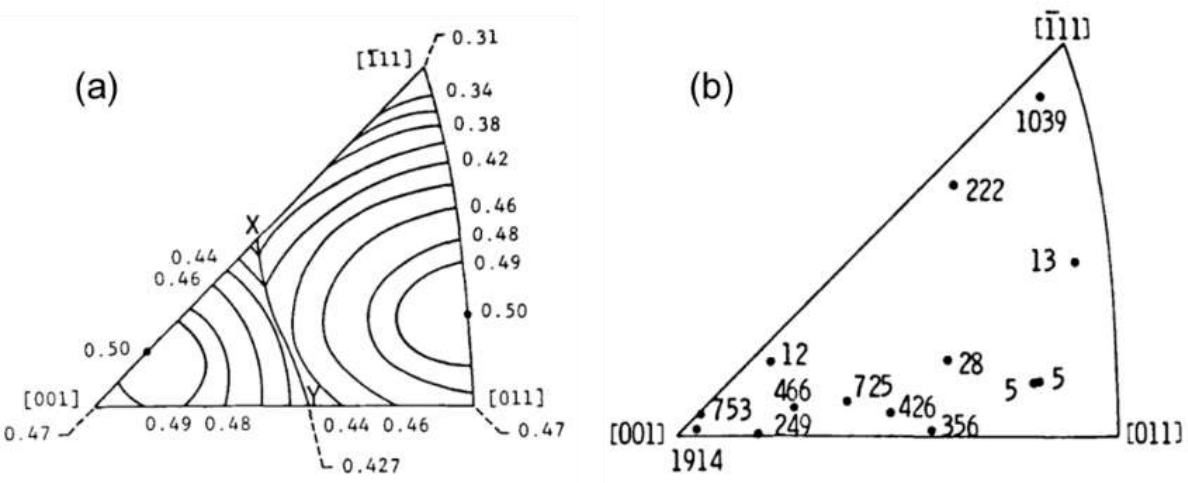

Figure 1.18. (a) Schmid factor contours for ⟨112⟩{111} slip systems. (b) Creep lives of MarM200 SX specimen tested at 750 °C / 689 MPa, creep duration in h associated with orientation. [83]

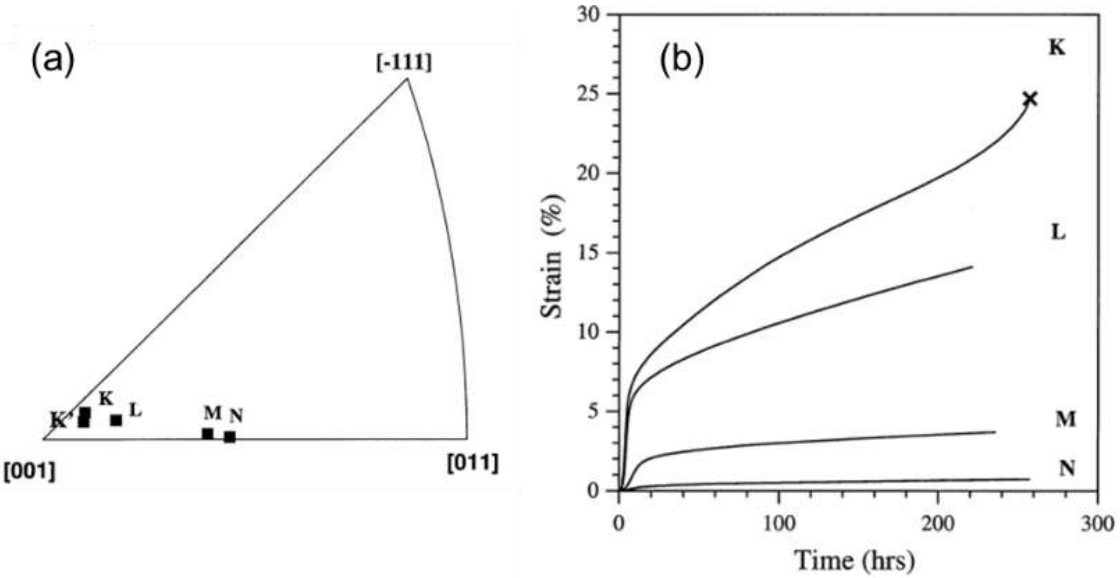

Figure 1.19. CMSX-4 specimen orientation (a) and creep curves of the specimens tested at 850 °C / 400 MPa (b). [84]

1. 2. 4. Very high cycle fatigue

Very high cycle fatigue (VHCF) life of Ni-based SX superalloys in fully reversed stress condition ($R = -1$) is generally determined by the size and position of the largest pore located in the specimen's loaded volume [55,89–92]. This is due to a higher stress concentration in the vicinity of pore that activates shearing of γ/γ' microstructure by slip bands [91]. The largest pores tend to be S-pores located in the interdendritic area [50,51]. In the recent article by Cervellon et al., fatigue crack initiation mechanism in VHCF (>> 10^7) under fully reversed conditions at 1000 °C has been proposed [91]. It was described that stress concentration near a large S-pore induces localized intense shearing of γ' precipitates and then activates recrystallization and associated interacting solute segregation at dislocations [79,91,93]. Local crack propagation threshold decreases as recrystallization proceeds, which corresponds to the "rough zone" observed in a fractography of a fatigue failed specimen (Figure 1.20).

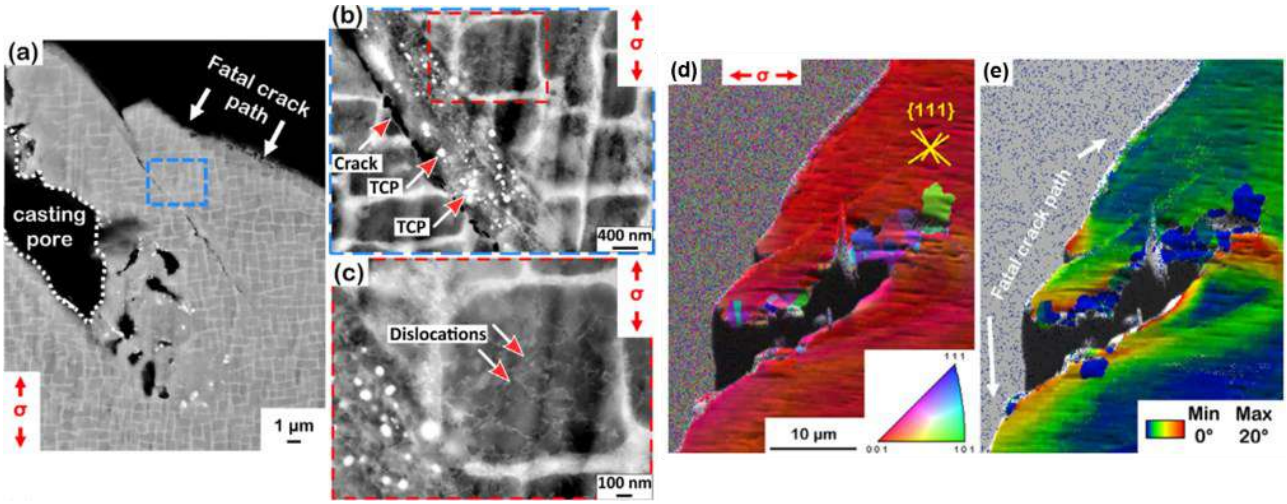

Figure 1.20. (a) Longitudinal section of crack initiating pore in CMSX-4 Plus specimen tested at 1000 °C with alternating stress of 210 MPa, failed at 4.7 × 10^7 cycles. (b) ECCI of the rectangle in (a). (c) magnified image of rectangle in (b). (d) Inverse pole figure (IPF) map and (e) grain reference orientation deviation (GROD) map at the crack initiation site of the same specimen. [91]

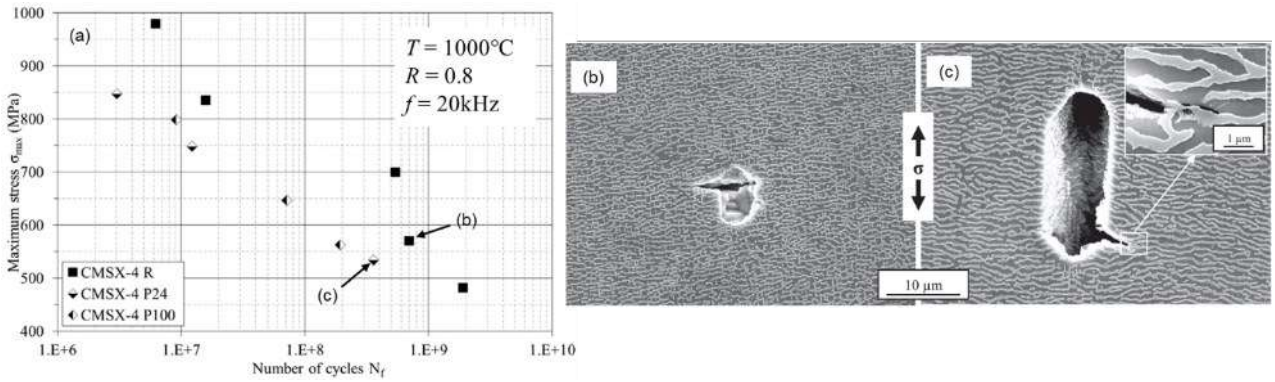

Figure 1.21. (a) S-N diagram at 1000 °C, $R = 0.8$, $f = 20$ kHz on CMSX-4 R (regular cuboidal structure), P24 (pre-rafted for 24 h), and P100 (pre-rafted for 100 h). Pre-rafting performed at 1100 °C / 120 MPa. Internal pores with mode-I crack propagation are shown for R (b) and P24 (c) specimens tested at similar stress conditions as labeled in (a). [89]

On the other hand, VHCF life at positive stress ratio condition ($R > 0$) is affected by the γ/γ' microstructure and intrinsic creep strength of Ni-based SX superalloys [55,89]. Overaged and coarsened microstructures are

known to have lower creep durability and lower yield stress especially at higher stress or with higher strain rate [46,89]. Therefore, since specimen is in tensile loading during all period of positive stress ratio condition with very fast strain rate (in the order of 10^2 /s), creep damages such as microstructure coarsening and cracks initiating from creep voids take place in the VHCF regime (Figure 1.21).

1. 3. Pre-straining effect

Previous efforts on pre-straining effects were made to understand recrystallization risks of SX superalloys during solution treatment, to understand γ'-rafting mechanisms, and to create pre-rafting microstructure for demonstrating complex operating condition of the turbine blades. Rejuvenation heat treatment procedure for microstructure restoration after creep is also introduced in this section.

1.3.1. Pre-straining before solution treatment

PD during solidification process is known to increase the risk of recrystallization during subsequent solution heat treatment [94–99]. Therefore, the motivation of pre-straining in as-cast SX material is to understand the recrystallization mechanism during solution treatment. In these studies, PD was introduced in a wide range of temperatures from room temperature (RT) to 1250 °C by tensile, compression, indentation, and grit-blasting to mimic thermomechanical plastic strains introduced during solidification and demolding processes. Recrystallization probability increases with increasing applied plastic strain, increasing deformation temperature, and increasing subsequent aging temperature/time (Figure 1.22) [95,97]. Higher recrystallization sensitivity after deformation at higher temperature is due to the higher dislocation density compared to the deformation at RT (Figure 1.23) [95]. In these cases, the recrystallization is activated by the dislocations introduced by PD and it starts from free surface [94,98,99] or primary dendrite core [97,100] (Figure 1.24). Especially at temperatures near solvus, introduced dislocations become diffusion path and enhance dissolution of γ′ phase and consequently recrystallization. Because the volume fraction of γ′ phase is lower in the primary and secondary dendrite arms, the dissolution triggered recrystallization starts from these areas.

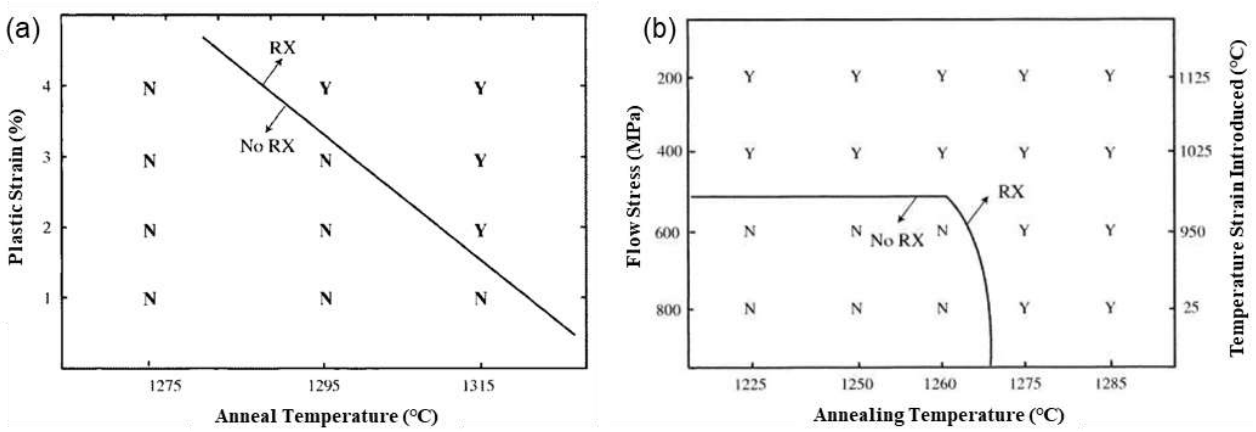

Figure 1.22. Recrystallization sensitivity of as-cast CMSX-4. (a) Applied plastic strain vs. subsequent annealing temperature. (b) Deformation temperature vs. subsequent annealing temperature on specimen with 4% applied plastic strain. [95]

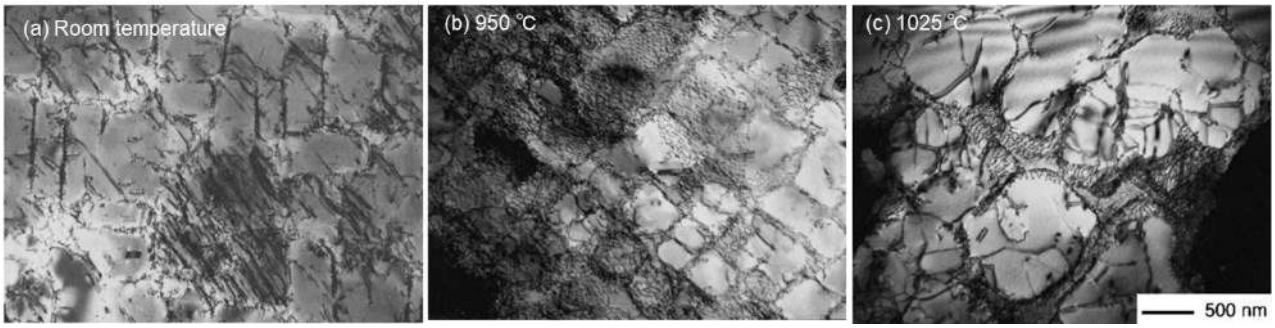

Figure 1.23. Dislocation structures of as-cast CMSX-4 specimens after tensile deformation (4% plastic strain) at different temperatures. [95]

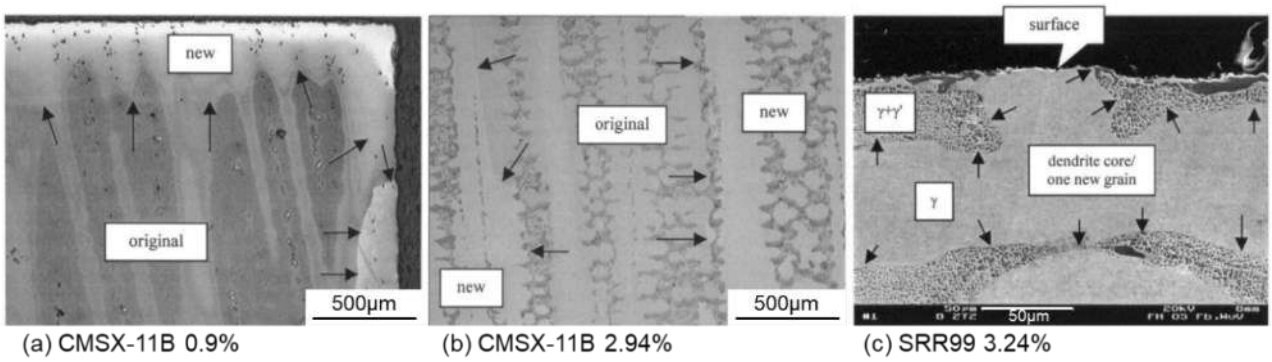

Figure 1.24. Recrystallization from surface and dendrite core on specimens deformed by compression in as-cast state. (a) CMSX-11B with 0.9% strain, solution heat treated at 1260 °C for 6 h. (b) CMSX-11B with 2.94% strain, heat treated at 1230 °C for 10 h. (c) SRR99 with 3.24% strain, heat treated at 1250 °C for 10 h under vacuum. Arrows are pointing at recrystallized grain boundaries. [94]

1.3.2. Microstructure behavior after pre-straining

Some studies have been focusing on the effect of PD on the γ/γ′ microstructure evolution during subsequent aging treatments [9–12,101]. In these studies, PD was applied at RT or at higher temperatures up to 1050 °C after solution and aging treatments. If PD is introduced after aging treatments, subsequent exposure at high temperature (>1000 °C) accelerates microstructure evolution to decrease internal elastic strain [9,12]. During aging, microstructure shows anisotropic coarsening similar to the γ′-rafting, which means that the coarsening direction is dependent on the type of deformation, tensile or compressive, and distribution of dislocations (Figure 1.25(a-c)) [9–11,102]. If tensile PD is applied at RT, PD proceeds by γ/γ′ shearing with practically no dislocation introduced outside of the slip bands. Therefore, microstructure coarsens only in the vicinity of slip bands, the region with intense elastic strain, and creates the band of coarsened microstructure (Figure 1.25(a, d)) [9,11]. Liu et al. showed that if the applied plastic strain exceeds a certain magnitude, even aging at 1000 °C can trigger recrystallization [11]. Recrystallization at the deformation bands introduced during out-of-phase thermomechanical fatigue tests is a similar case that dislocation density at the band exceeding tolerance for recrystallization to be triggered during heating sequence above 850 °C [103–105]. On the other hand, aging at 1080 °C after higher temperature (900 °C) pre-straining resulted in typical N-type rafting structure (Figure 1.25(c)) [9,10]. This behavior is well known from many experiments that intended to obtain pre-rafted microstructure [106,107]. In the study by Strunz et al., compressive pre-strain of 2% was applied at RT, 700 °C, and 950 °C to a Ni-based SX superalloy and aging at 950-1050 °C was subsequently applied. γ′-rafting was detected on a specimen with PD at 950 °C plus aging at 1050 °C for 6.5 h and not in a specimen pre-deformed

at RT [101]. Moreover, TCP phase can precipitate in pre-deformed material during aging treatments [12,108].

1.3.3. Mechanical properties of pre-deformed superalloys

The mechanical behavior of polycrystalline [109–114] and SX [89,107,115–119] Ni-based superalloys with a prior PD has also been studied. In these studies, plastic strain was applied after full heat-treatment including solution and aging treatments either by RT tensile PD or high-temperature creep deformation.

In polycrystalline Ni-based superalloys, PD applied at RT creates decohesion and increases residual stress of nearby grains. Thus, creep life of the pre-deformed material decreases due to the grain boundary cavitation and particle (carbide in grain boundary) cracking enhanced by the residual stresses (Figure 1.26(b)) [109–112,114]. Creep life and ductility of polycrystalline superalloy decreases with increasing pre-strain (Figure 1.26(a)) [112,114]. In the work by Stöcker et al., tensile pre-deformation at RT decreased subsequent VHCF lifetime of Nimonic alloys because of surface roughness [113].

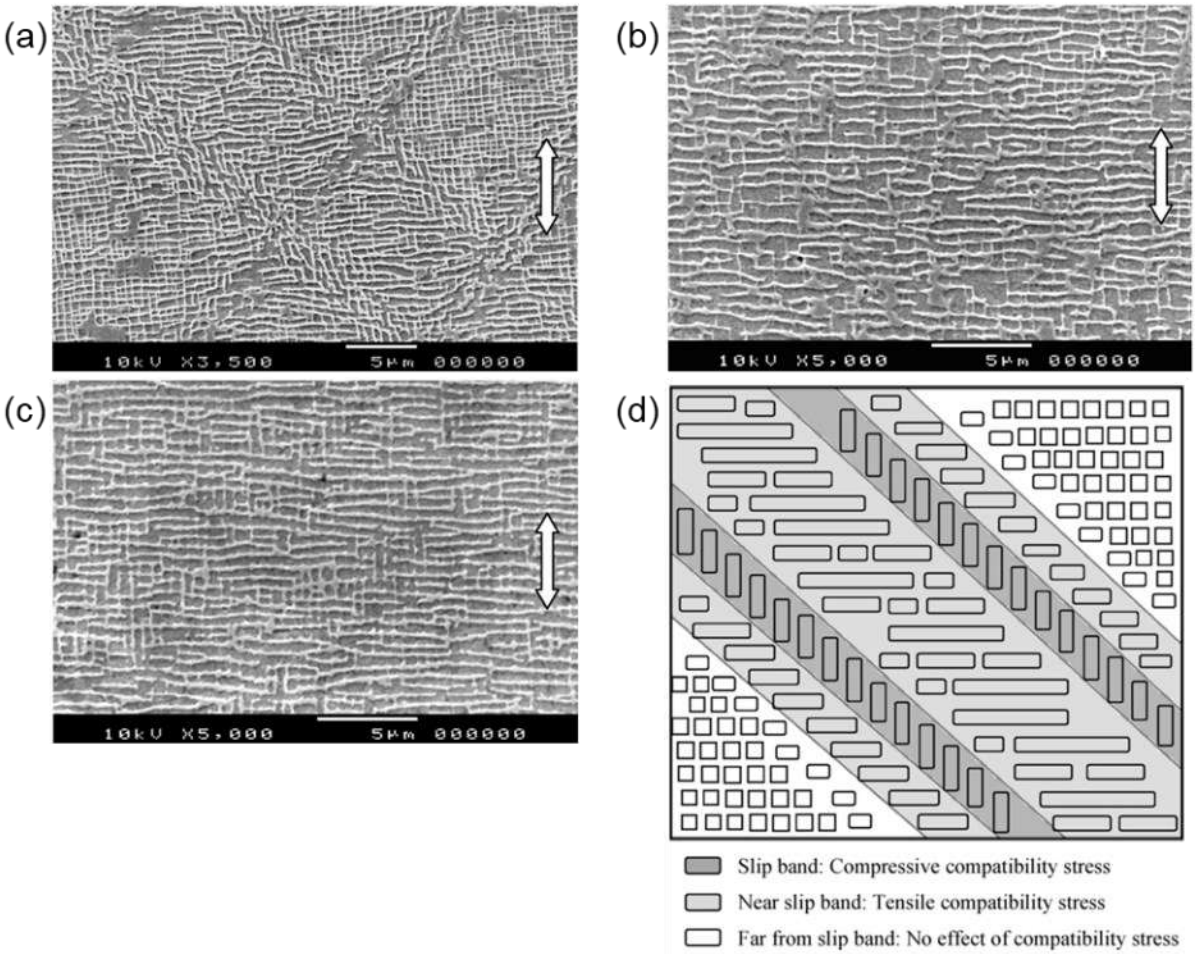

Figure 1.25. Scanning electron microscope (SEM) images of CMSX-4 specimens with 0.8% plastic strain applied by tensile deformation at RT (a), 700 °C (b), and 900 °C (c) after subsequent aging at 1080 °C for 20h. (d) Schematic illustration of the compatibility stress build up in the slipped and the un-slipped region in the specimen deformed at RT. [9]

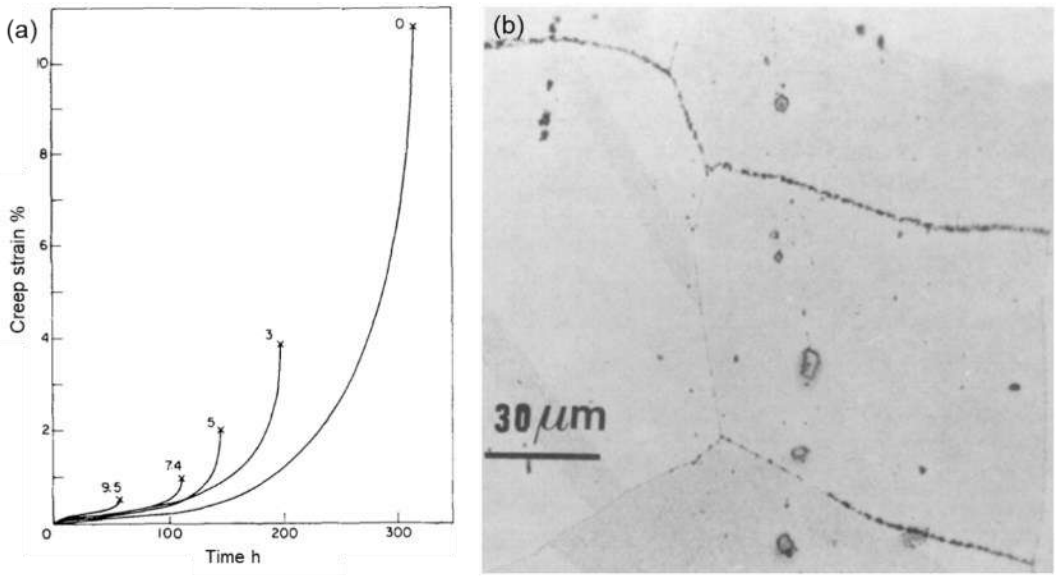

Figure 1.26. Creep curves of Inconel Alloy X-750 at 700 °C / 400 MPa (a). Pre-strained at RT and strain is labeled next to each curve. An example of cavities widely distributed in grain boundaries of the creep tested specimen with 9.5% pre-strain (b). [114]

The objectives of previous studies on pre-strained SX superalloys were mainly to evaluate the mechanical properties of pre-rafted SX superalloys. Therefore, prior PD was intended to obtain an anisotropic γ′-rafted microstructure. It was originally aimed at understanding the advantage of the γ′-rafting on the mechanical properties [47,115,120,121]. In recent studies, pre-rafting is introduced for understanding the interaction of different temperature and loading conditions that may occur during service conditions of gas turbines [89,107,117]. With the same motivation, the study by Long et al. investigated effect of creep-type pre-straining at 750 °C on the Ni-based SX superalloy's creep properties at 1100 °C / 137 MPa and 750 °C / 750 MPa [119]. The initial dislocation structure decreased creep life at 1100 °C / 137 MPa with TCP phase precipitation during creep of Re-containing SX superalloy (Figure 1.27(a)) [119]. Creep life of Re-free alloy at 750 °C / 750 MPa also decreased with absence of primary creep stage (Figure 1.27(b)) [119], which is consistent with the study by Drew et al [116]. In the study by Drew et al. in CMSX-4 at 750 °C / 750 MPa, γ/γ′ interfacial dislocations and dislocations in γ channels inherited from prior creep at 950 °C interrupted stacking fault in shorter segment of two precipitates (Figure 1.28(b, c)); therefore, primary creep strain was smaller in pre-strained material (Figure 1.28(a)) [116].

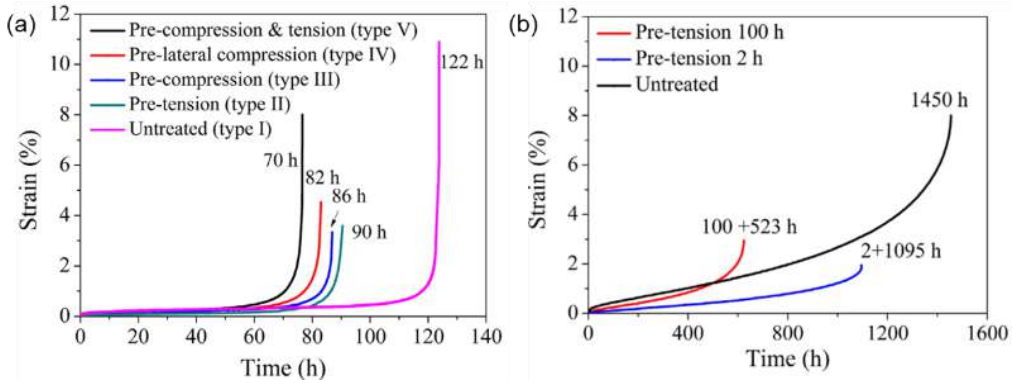

Figure 1.27. Creep curves of Re-containing second generation (a) and Re-free first generation (b) Ni-based SX superalloys with different temperature/load histories. Creep test performed at 1100 °C / 137 MPa with prior straining of 750 °C / 750 MPa for 1 h (a). Creep test performed at 750 °C / 750 MPa were interrupted at 2 h and 100 h and resumed for 1095 h and 523 h until rupture, respectively (b). [119]

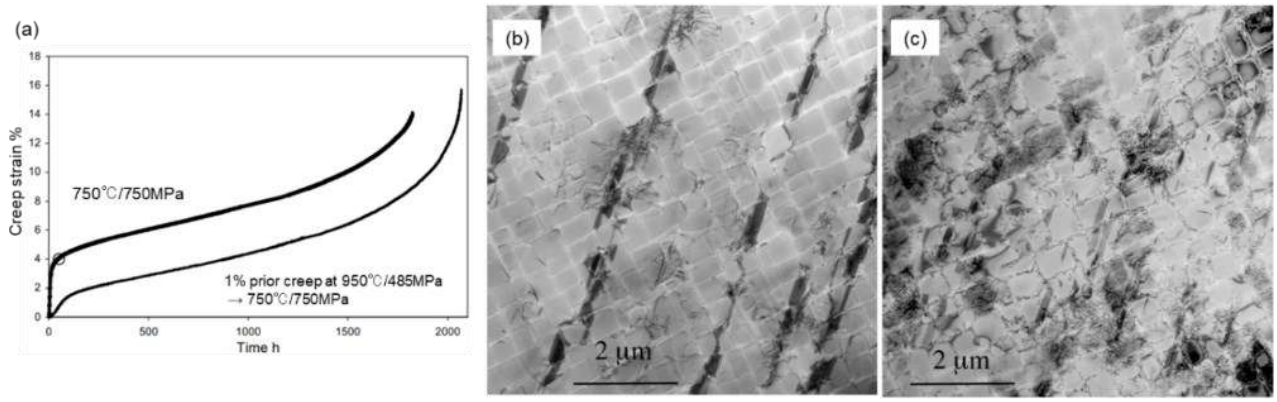

Figure 1.28. Creep curves of CMSX-4 from two stage tests (a). TEM images after creep test at 750 °C / 750 MPa interrupted at 1% creep strain on CMSX-4 without pre-strain (b) and CMSX-4 with prior 1% creep strain introduced at 950 °C / 485 MPa (c). [116]

1.3.4. Rejuvenation treatment

Rejuvenation is a process to restore microstructural characteristics of a turbine component after geometrical refurbishment processes. The process was first established for polycrystalline turbine components [122–125] and has been continuously developed for SX application [126–133]. The technique is usually a combination of near solution heat treatment and HIP, trying to avoid possible recrystallization during such a process. A turbine blade suffers from internal microstructural damages during long-duration high-temperature exposure and creep loading under operation [14–18]. Over-aging precipitation coarsening, creep void formation, precipitation of brittle TCP phase, and changes in carbide types are the main damages in SX superalloys [117,134–136]. Additionally, changes in grain-boundaries occur in polycrystalline alloys. The types of damage and the changes of microstructure differs depending on the area of the component due to the variety of temperature/stress conditions. An example of serviced microstructure in a turbine blade is shown in Figure 1.29 [137]. Generally, over-aged coarsening decreases creep resistance under low-temperature/high-stress conditions, and creep void formation occurs and become a failure source under high-temperature/low-stress conditions. Rejuvenation that refurbishes bulk mechanical properties of SX superalloy is an effective process to extend service life of a turbine component as shown in Figure 1.30 [127].

The main idea of re-heating up to solvus temperature is to dissolve γ′ precipitates into γ phase and to regenerate nearly optimal γ matrix and γ′ cuboids by following precipitation aging treatments just like original solution + aging treatments. As shown in Figure 1.31, microstructure of SX superalloy CMSX-4 can be restored by rejuvenation heat treatment after over-age coarsening at 1050 °C for 1000 h [128,138]. During re-solution stage, dislocations introduced during deformation will be annihilated or rearranged since there are almost no remaining γ/γ′ interfaces that block movement of dislocations and due to the very high temperature that enhances diffusion for rearrangement. Dissolution of TCP phase [129,133] and partial decomposition of carbides [126,127] also occur during re-solution with higher solubility of γ phase at such high temperature. When precipitation aging treatments are applied, γ′ phase precipitates and grows from γ phase as normal aging treatment. This rejuvenation heat treatment is known to effectively extend creep life of SX superalloys (Figure 1.32) [130,132] and extended service life can be achieved if the process is applied before the accumulation of microstructural damages [127,131,132], which mainly occur during creep acceleration stage after slower creep rate period. Figure 1.33 shows the accumulation of creep damage that is exposed after second creep loading

on the rejuvenated SX samples. Faster coarsening was observed after second creep loading in the sample with 5.0% creep strain during first creep loading [132].

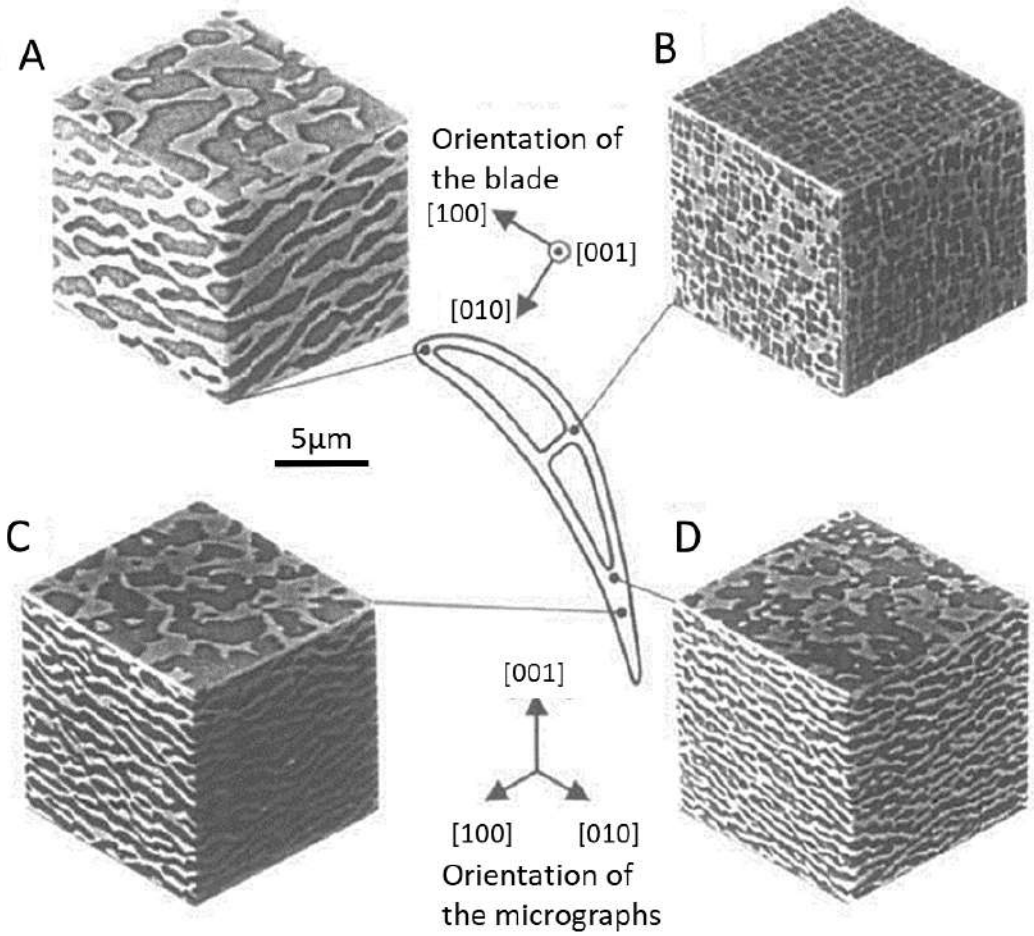

Figure 1.29. Schematic drawing of the cross-section with SEM images of the typical microstructures for different positions after an accelerated simulation mission endurance test (ASMET). [137]

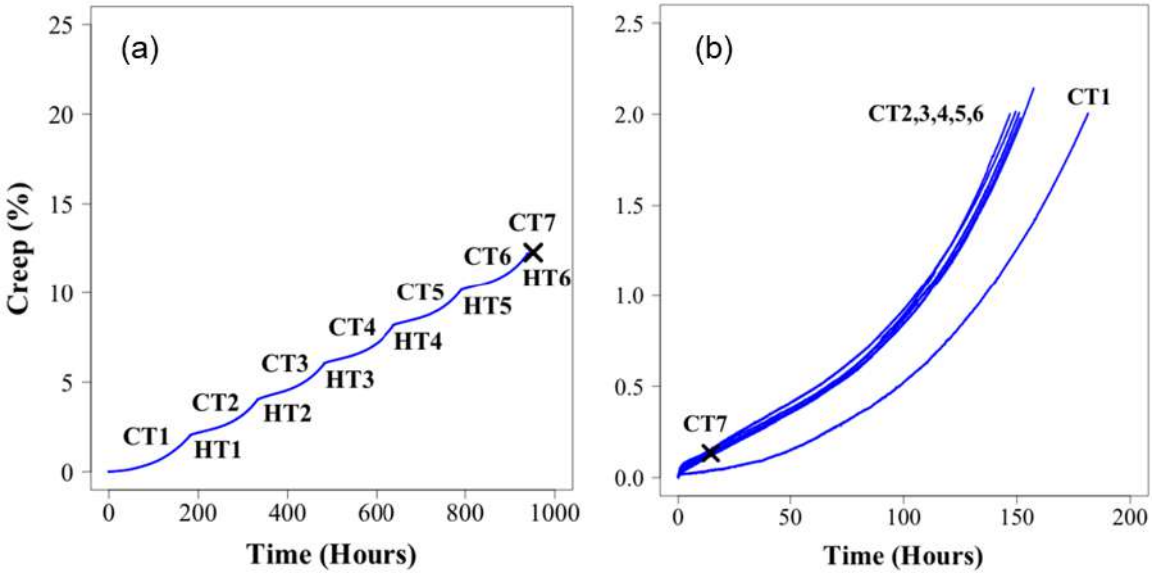

Figure 1.30. (a) Multiple rejuvenation creep curves tested at 982 °C / 206 MPa for Rene N5 with a creep strain threshold of 2% strain. HT1-HT6 are rejuvenation treatments between creep tests (CT1-CT7) performed at 28 °C below solvus temperature followed by standard aging treatments. (b) Creep curves for each test (CT1-CT7) with the same reference point. [127]

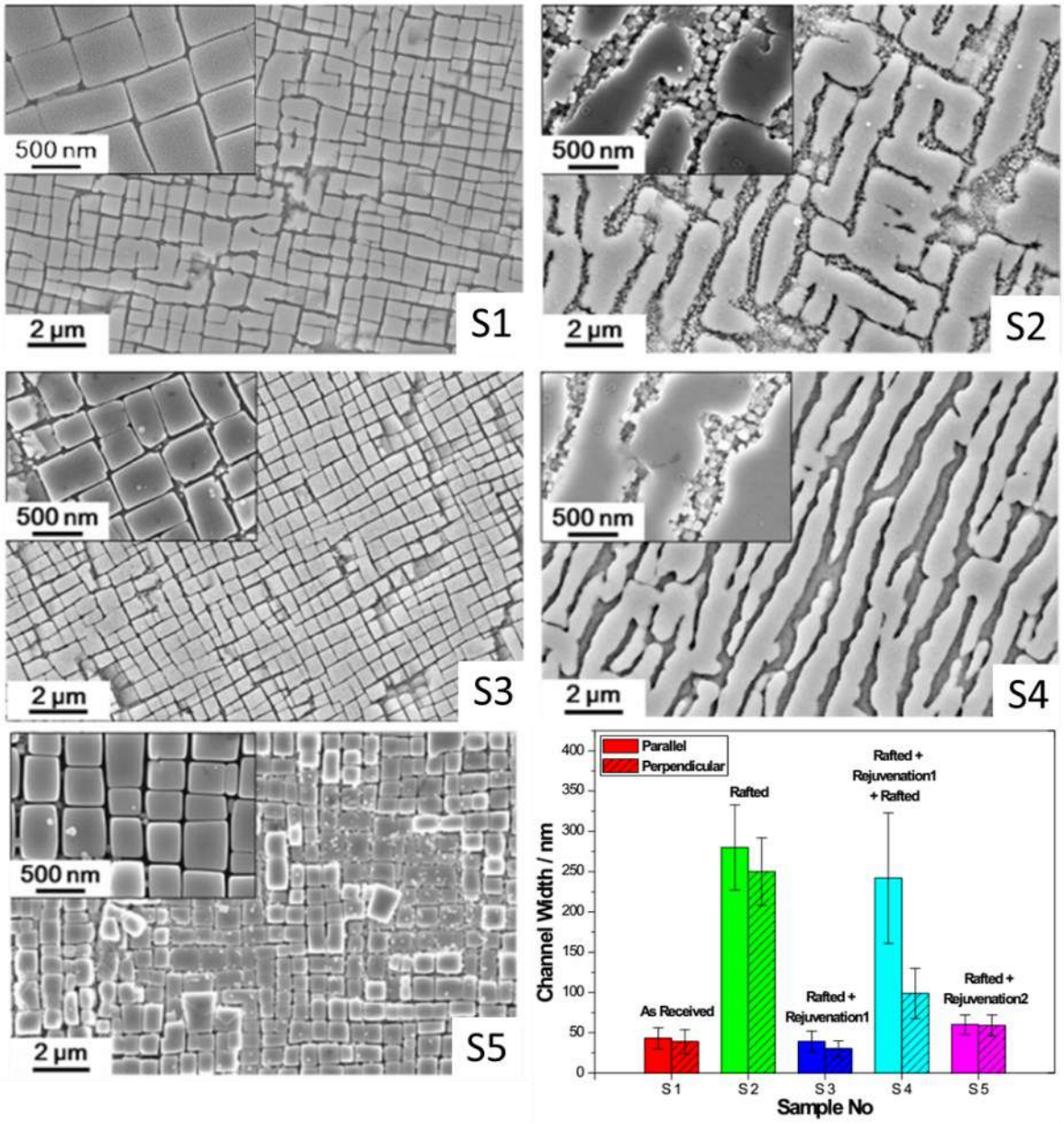

Sample No	Heat Treatments	γ Channel Width / nm		Rafting Parameter
		Parallel	Perpendicular	
S 1	As-received	43±13	39±11	0.56
S 2	Rafted	280±53	250±42	1.64
S 3	Rafted + Rejuvenation 1	58±19	54±17	0.55
S 4	Rafted + Rejuvenation 1 + Rafted	242±81	99±31	2.65
S 5	Rafted + Rejuvenation 2	60±12	59±13	0.53

Figure 1.31. SEM images of the CMSX-4 samples after different heat treatment conditions. Rafted microstructure was obtained by aging at 1050 °C for 1000 h. [138]

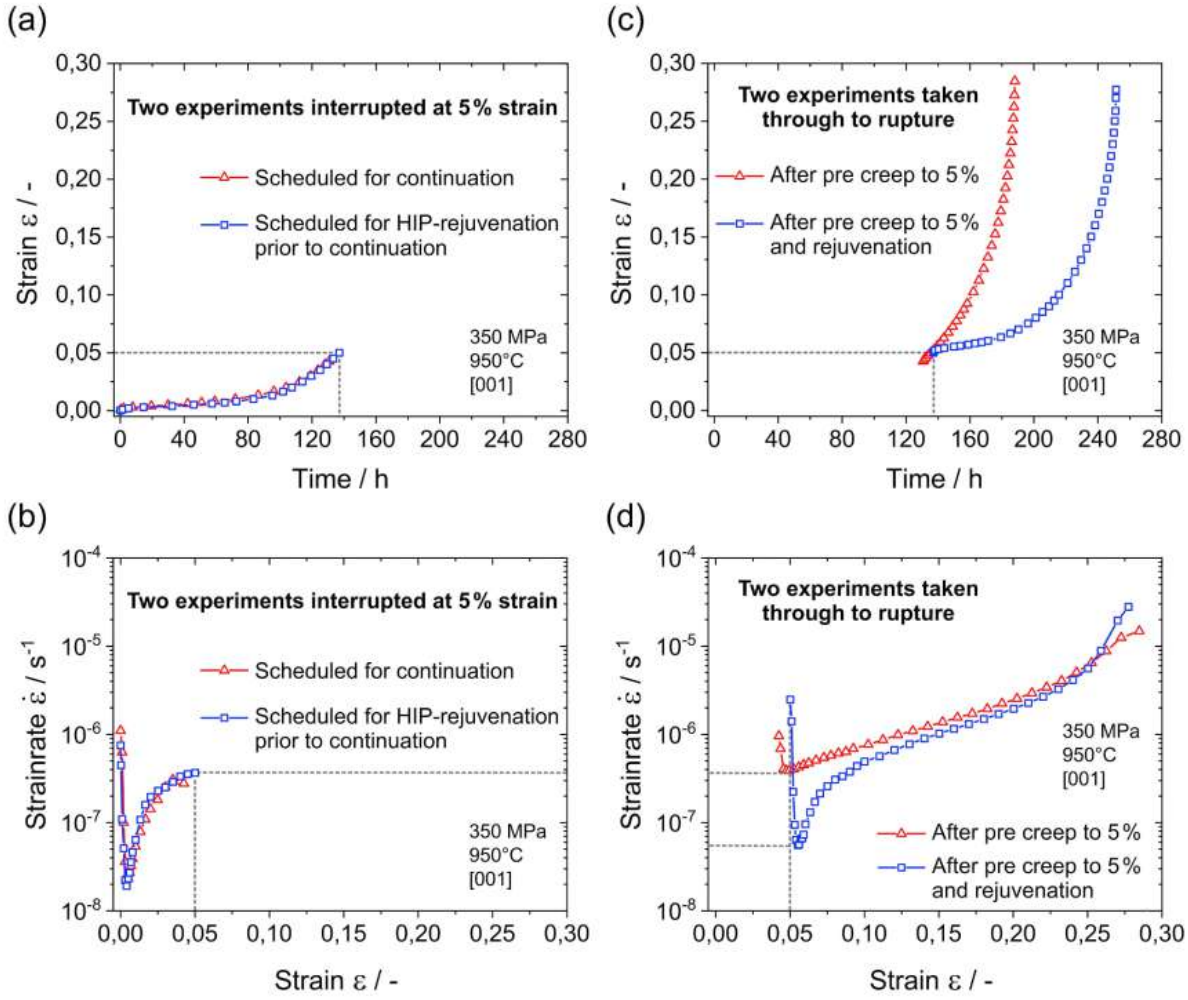

Figure 1.32. Creep curves of two experiments on ERBO/1 SX superalloy. Red triangle: interrupted at 5.0% strain, fast cooling to RT, and then continued at same condition. Blue square: interrupted at 5.0% strain, fast cooling to RT, HIP-rejuvenation treatment, continued at the same condition. (a, b) Creep and creep strain rate curves for first creep loading. (c, d) Creep and creep strain rate curves for second creep loading. [132]

Re-solution treatment can only restore over-aged precipitates into original form, but creep voids cannot be eliminated. Creep voids in damage concentrating area can limit high cycle fatigue life of SX component [55,139] as well as creep life [54,73,134,140]. Since HIP procedure is known for its advantage of increasing mechanical properties of superalloys by densifying and removing casting voids [54,55], this method is also useful for solving creep void issue if it is applied in the refurbishment process. Therefore, ideally, HIP treatment is processed at the rejuvenation temperature so that precipitate restoration can proceed simultaneously. Example of SX superalloy after creep deformation followed by rejuvenation treatment consist of re-solution and HIP is shown in Figure 1.34.

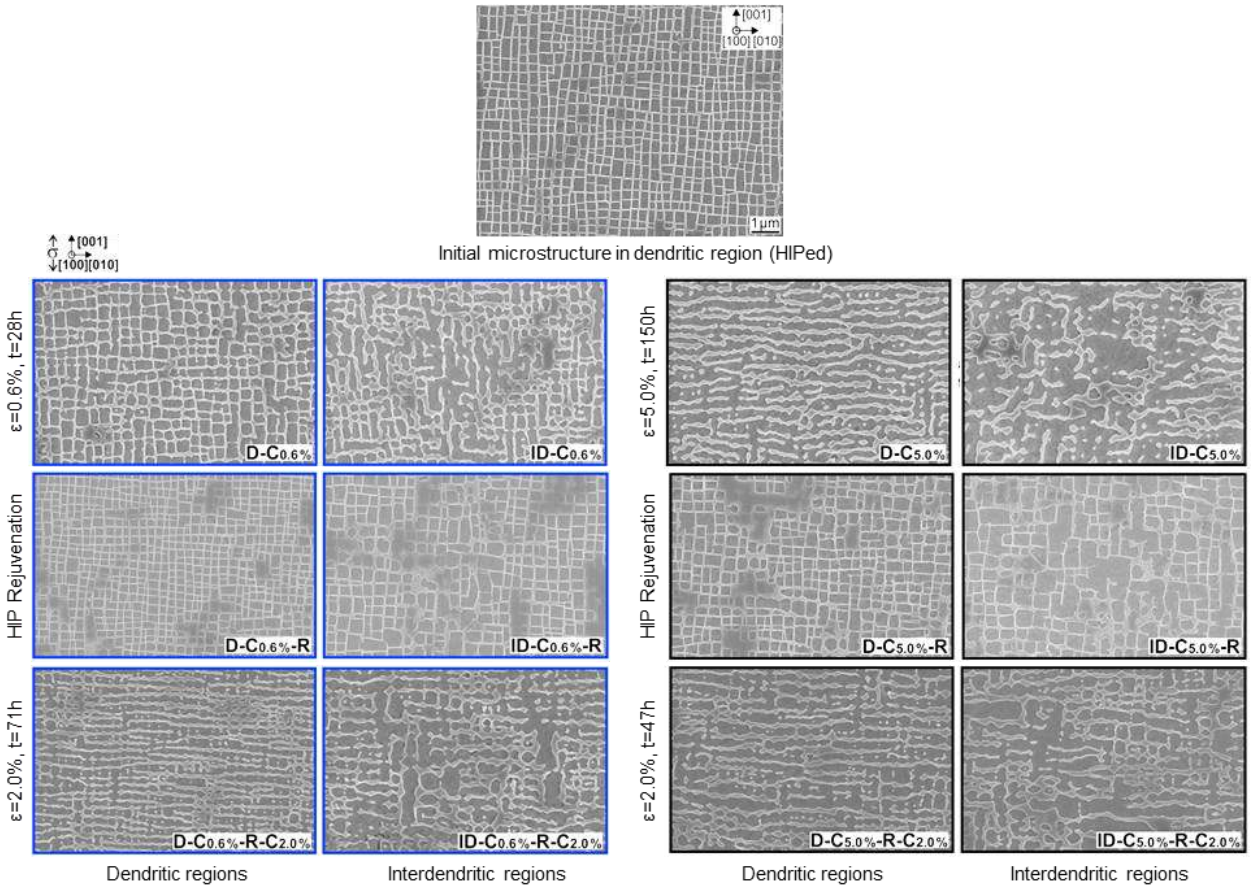

Figure 1.33. Microstructures of ERBO/1 SX superalloy at different stages. Initial microstructure in a dendritic region is on the top. 6 images on the left and 6 images on the right are after creep test (950 °C / 350 MPa) interrupted at 0.6% and 5.0% strain, respectively. After creep interrupting test, samples are treated by HIP Rejuvenation and applied creep load again at the same condition until they reach 2.0% strain, then interrupted. [132]

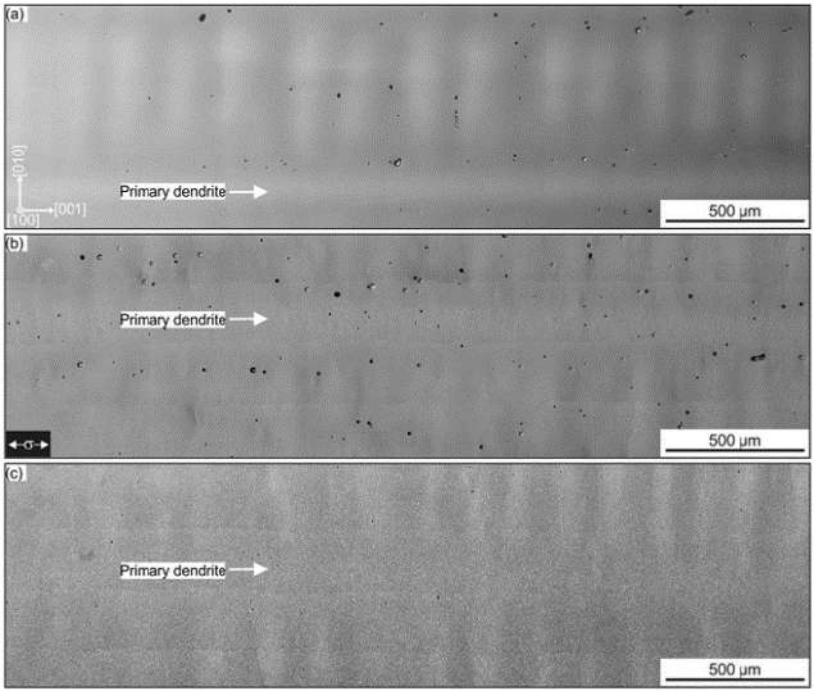

Figure 1.34. SEM-BSE (backscatter electron) images of the same region of the ERBO/1C SX creep testing sample. (a) the initial state prior to creep, (b) after creep test at 1050 °C / 160 MPa interrupted at 5% creep strain, and (c) after HIP rejuvenation treatment. [130]

1. 4. Previous experimental results

Previous studies reviewed in section 1.3 were motivated by questions regarding; recrystallization probability caused by residual stress during solidification, surface recrystallization induced by grid blasting, cold deformation after full heat treatment, simulating thermo-mechanical damage, complex creep damage history, and HIP rejuvenation treatment for microstructure restoration after creep. Meanwhile, effect of pre-deformation between solution treatment and aging treatments on the material's mechanical properties has never been investigated before the precedent experiments performed in the collaborative project by Institut Pprime and Safran Aircraft Engines. The motivation of the project came up from non-conforming turbine blades from Safran Aircraft Engines' foundry. For this case, only one literature is available, study by Pierret et al. that reported microstructure evolution within a turbine blade caused by plastic deformation during cooling from solution treatment (Figures 1.35 and 1.36) [8]. This section provides review of the previous results that have been performed in advance to the PhD research. In the following chapters, results in this section will be discussed together with the main experimental results of this dissertation.

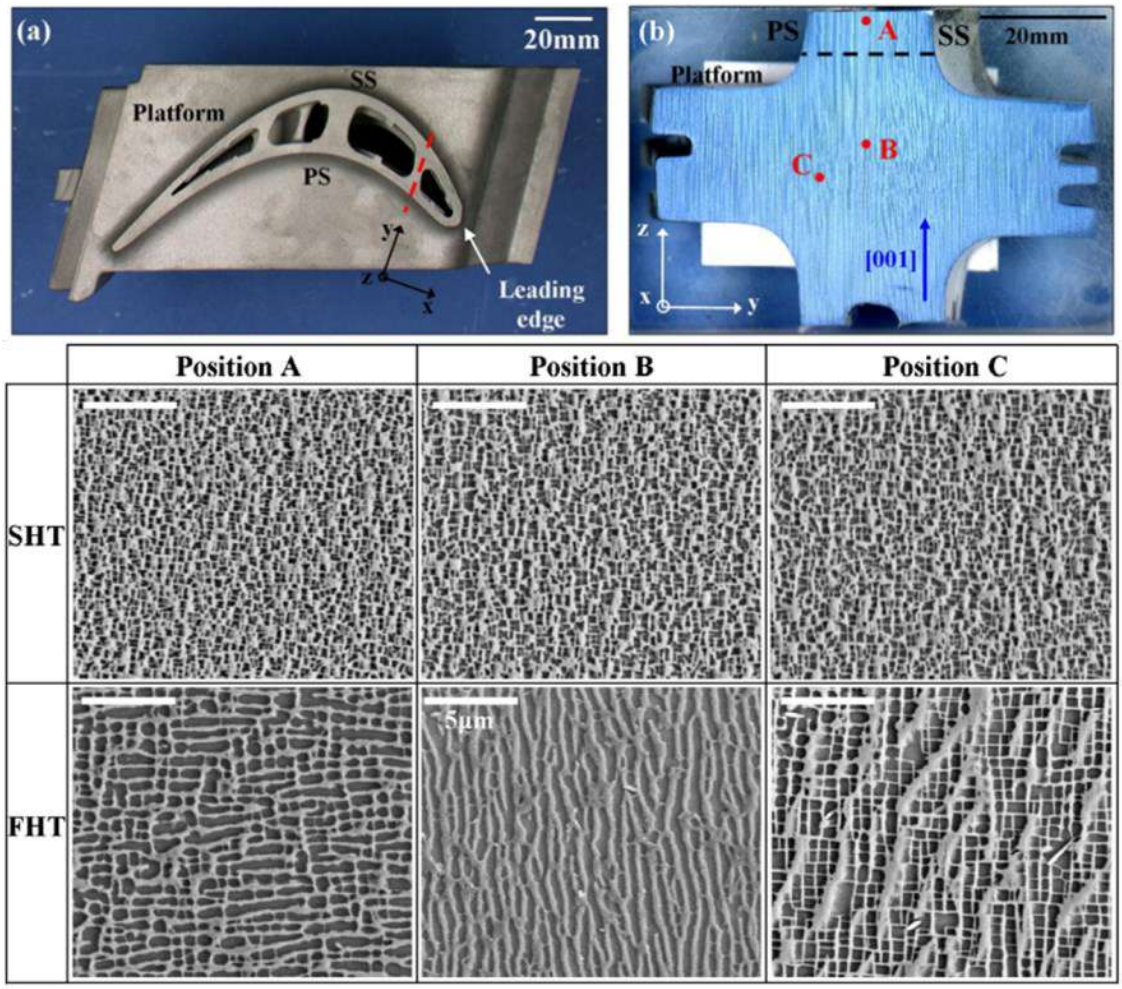

Figure 1.35. Turbine blade's cross section 5 mm above platform (a) and image of sliced surface with observed position labeled A-C (b). Microstructures were observed after solution (SHT) and full (FHT) heat treatment (scale is 5 μm). Plastic deformation must have been introduced between solution and aging in order to have microstructure evolution in FHT specimens. [8]

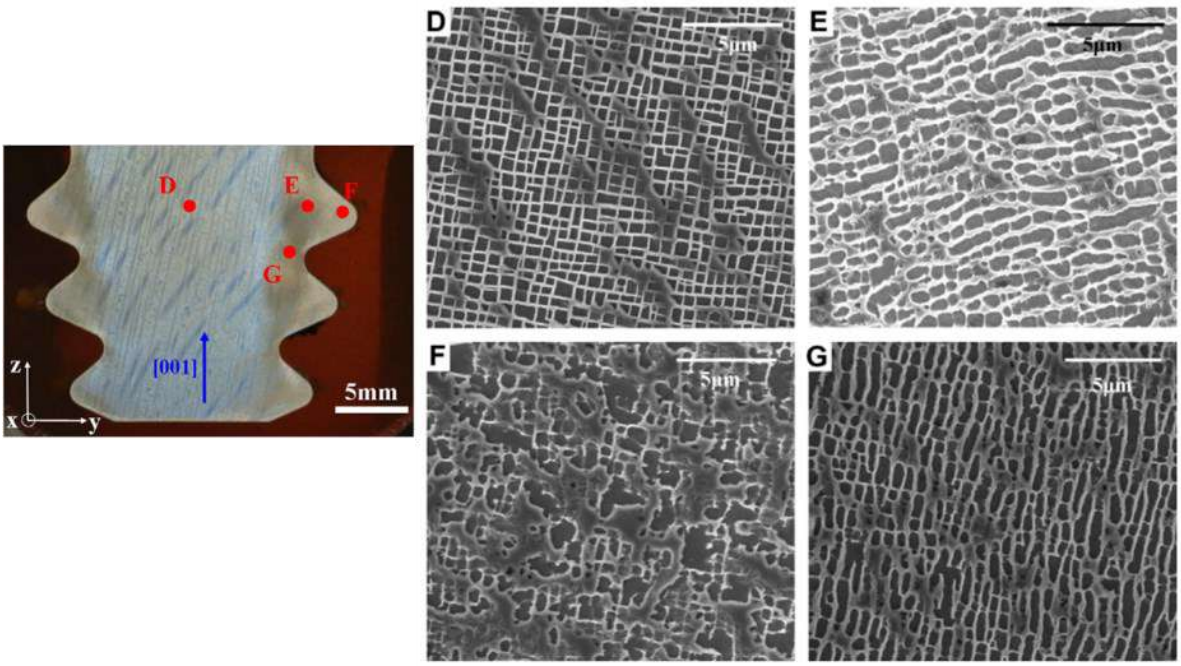

Figure 1.36. Observed areas D-G are labeled on the image of the blade root cross-section after full heat treatment. [8]

1.4.1. Microstructure after pre-deformation and following aging treatments

In the first experiment in this study, plastic deformation was introduced to the AM1 Ni-based SX superalloy after the solution treatment, before the aging heat-treatments (Figure 1.37). Instead of ideal γ matrix and γ′ cuboidal structure in Figure 1.38(a), the microstructure of AM1 had the band-shaped affected zone as a consequence of plastic deformation applied in between the heat-treatments (Figures 1.38(b, c)).

By electron backscatter diffraction (EBSD) characterizations after plastic deformation and two aging treatments, neither measurable lattice rotation nor localized recrystallization have been observed (Figure 1.39). The misorientation profiles are also plotted in Figure 1.39 across γ′ coarsened bands both within a primary dendrite arm and within an interdendritic spacing. Rotation angles in the range 0.5-0.6° are corresponding to the angular resolution of the EBSD technique within the applied setup.

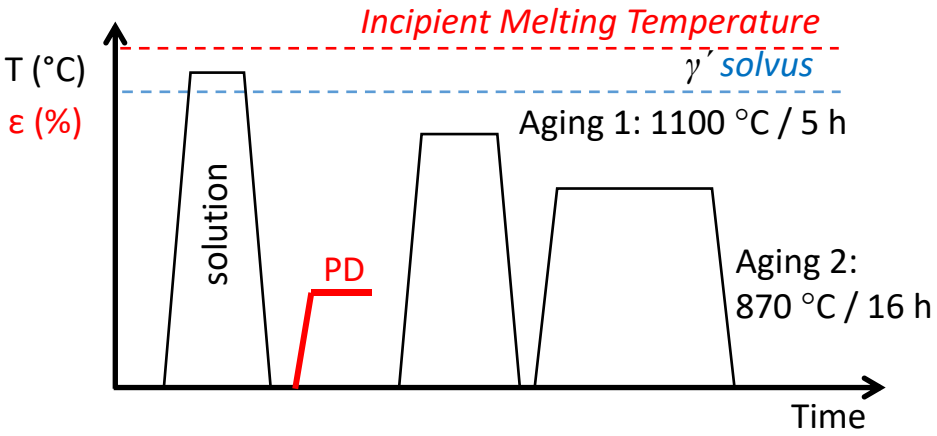

Figure 1.37. Temperature-time diagram of plastic deformation and heat-treatment procedures of AM1 performed in the precedent research.

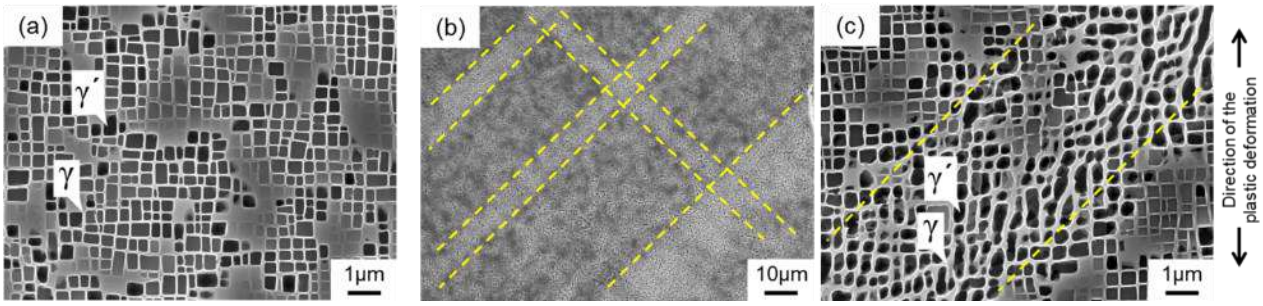

Figure 1.38. Microstructure of AM1 Ni-based SX superalloy. Typical γ/γ′ structure (a), and evolution of γ′ phase can be observed in the band-shaped affected zone in lower (b) and higher magnifications (c).

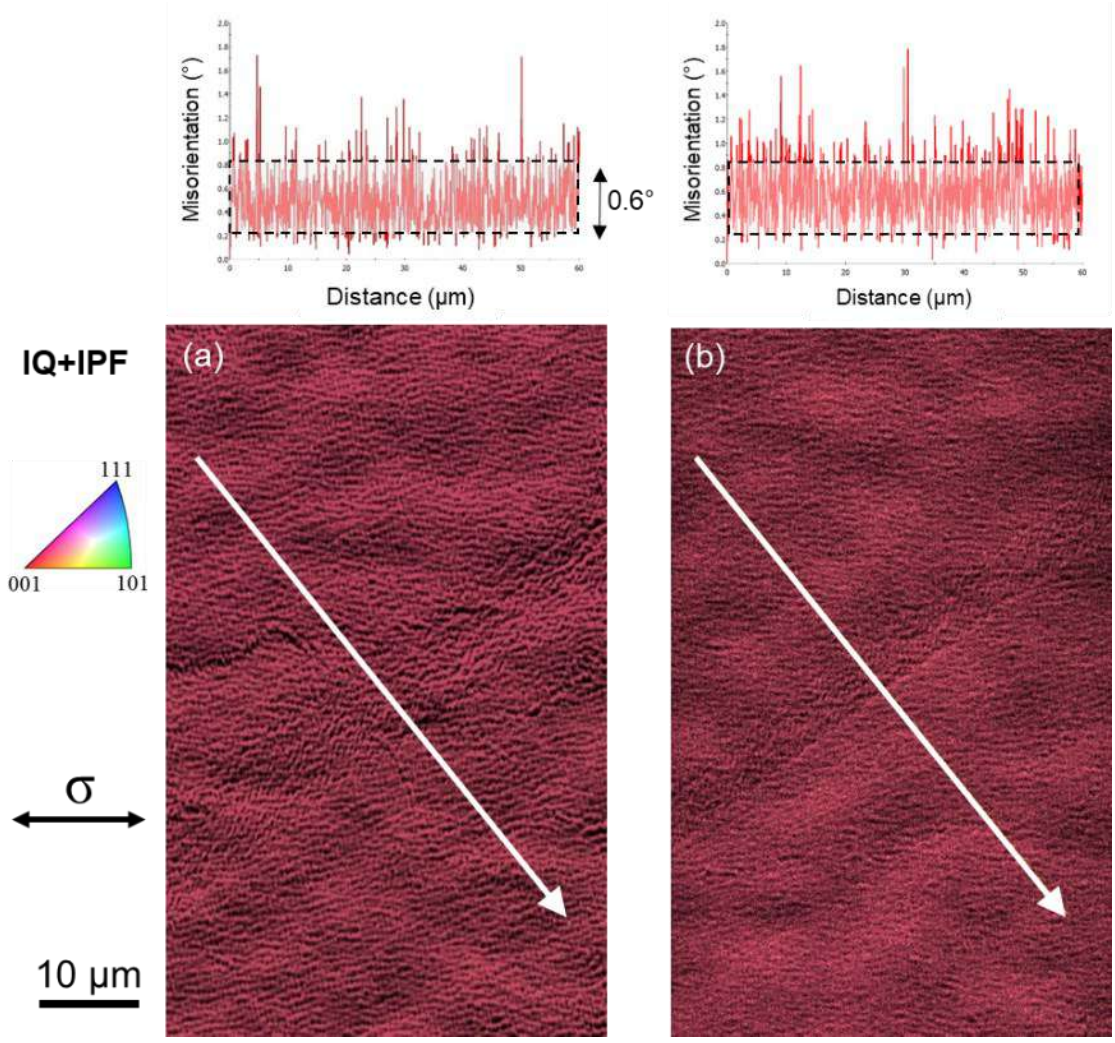

Figure 1.39. IPF (coded along tensile axis) superimposed to Image Quality maps in a primary dendrite arm (a) and in an interdendritic spacing (b) of AM1 alloy after solution treatment + 0.8% PD + 1100 °C / 5 h / quenched in air + 870 °C / 16 h / quenched in air. Misorientation profiles (white arrows) are presented above each map.

1.4.2. Creep properties of pre-deformed AM1 SX superalloy

In order to investigate the effect of such microstructure evolution on the high-temperature durability, creep tests at various conditions (1050 °C / 140 MPa, 950 °C / 300 MPa, 850 °C / 500 MPa, 750 °C / 800 MPa) have been performed on the plastically pre-deformed samples and compared with the material without plastic deformation in the preparation. The results obtained from these creep tests are shown in Figure 1.40. The pre-

deformed samples have decreased its creep life compared to the non-deformed samples by 30 to 50%. Since planar fracture surface of the ruptured specimens is in same plane of the band-shaped zone (Figure 1.41), it can be clearly said that creep failure of the pre-deformed samples was related to the local microstructure evolution induced by the pre-deformation. By the SEM and EBDS analyses, the initiation of cavities and recrystallization in the band are revealed to be reasons of early rupture and planar fracture in the creep at higher temperature such as 1050 °C / 140 MPa (Figure 1.42). Atom probe tomography reconstructed 3D image and line concentration profile in Figure 1.43 are showing solute segregated dislocations in γ′ phase in the vicinity of recrystallized band. Characteristic creep damage in the band is definitely involved in the recrystallization and consequently early failure of pre-deformed material.

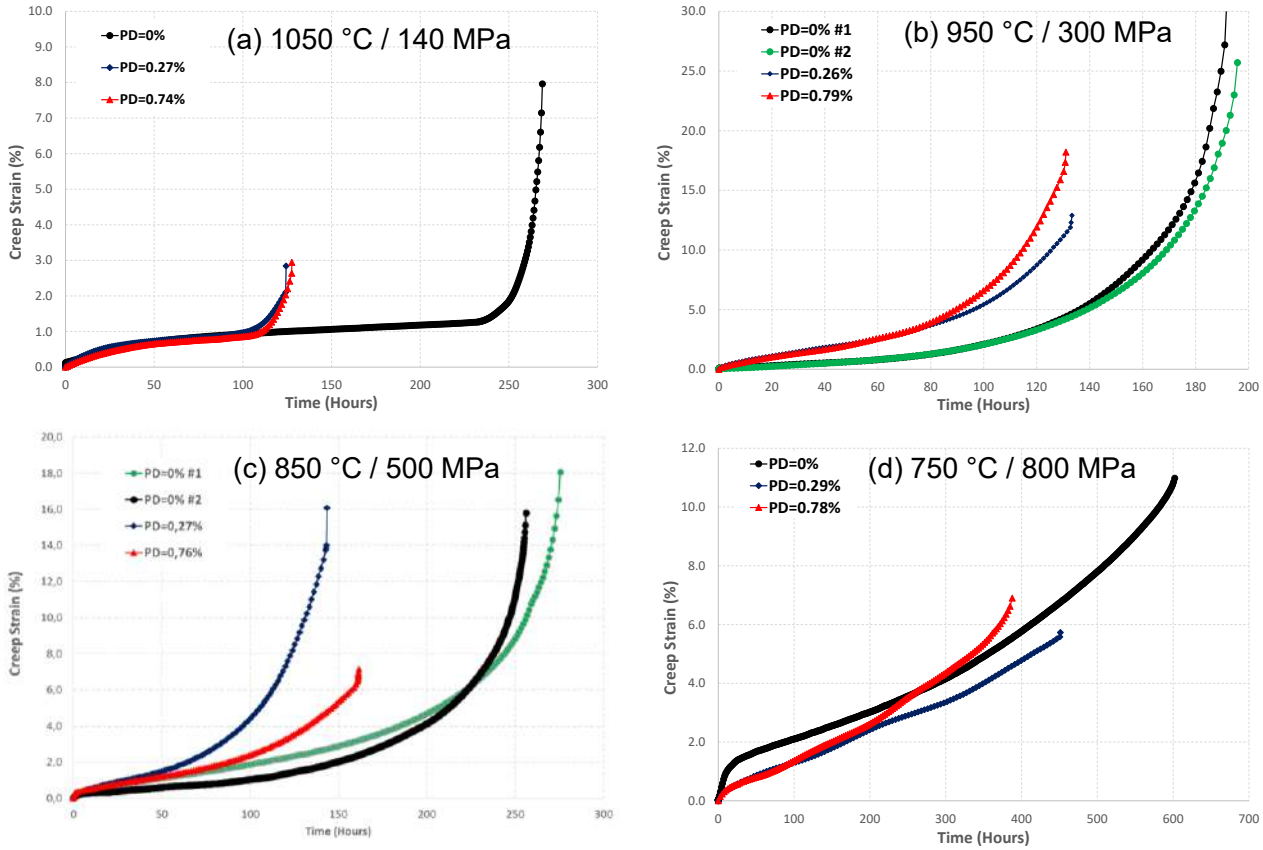

Figure 1.40. Creep curves without PD and with PD of about 0.3% and about 0.8% at (a) 1050 °C / 140 MPa, (b) 950 °C / 300 MPa, (c) 850 °C / 500 MPa, and (d) 750 °C / 800 MPa.

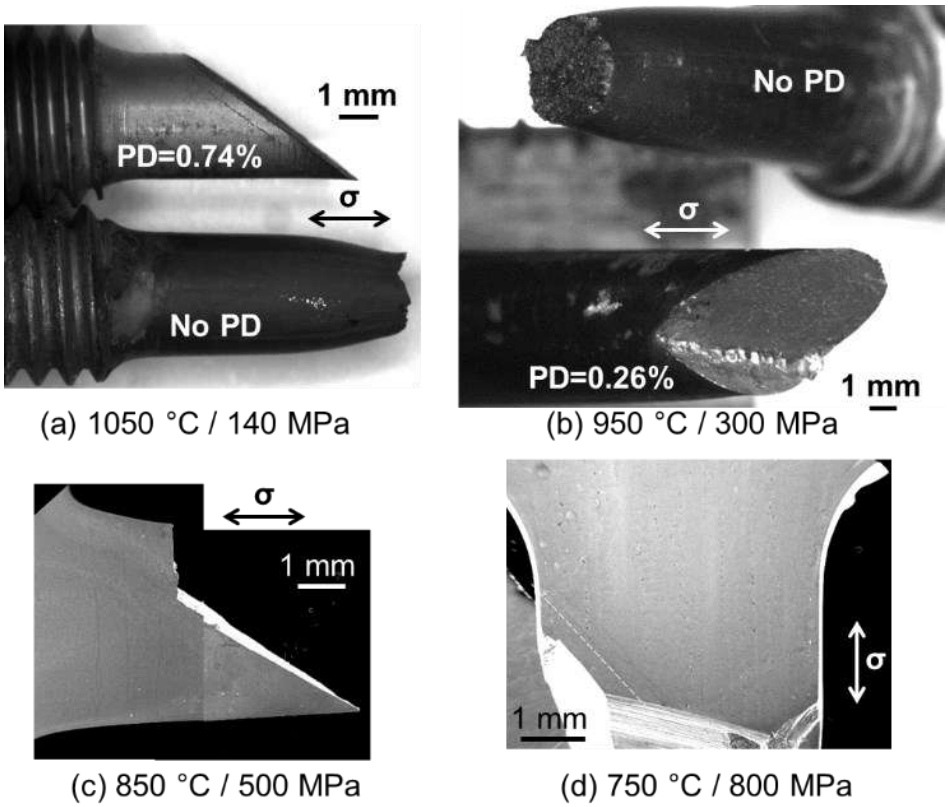

Figure 1.41. Observed images of specimens' fracture surfaces after the creep rupture tests.

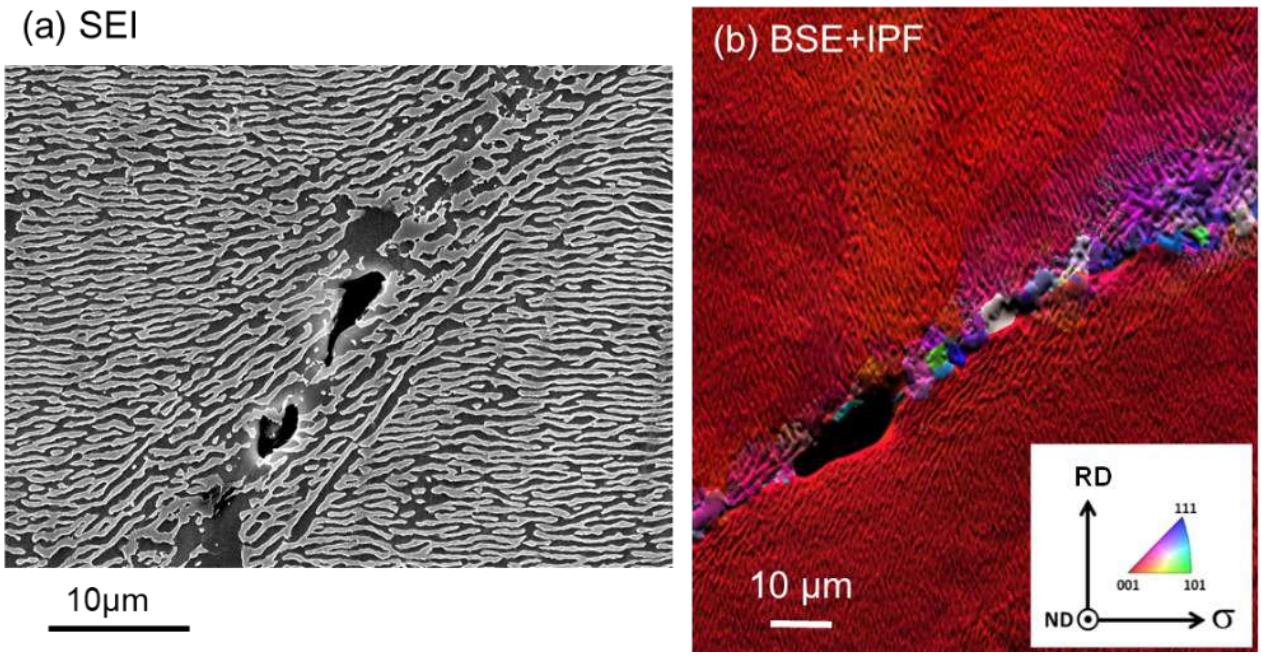

Figure 1.42. (a) Crack initiation and cavitation along coarsened microstructure in the band. (b) Inverse Pole Figure color-coded orientation maps referring to the tensile direction after creep rupture test at 1050 °C / 140 MPa / PD=0.74%.

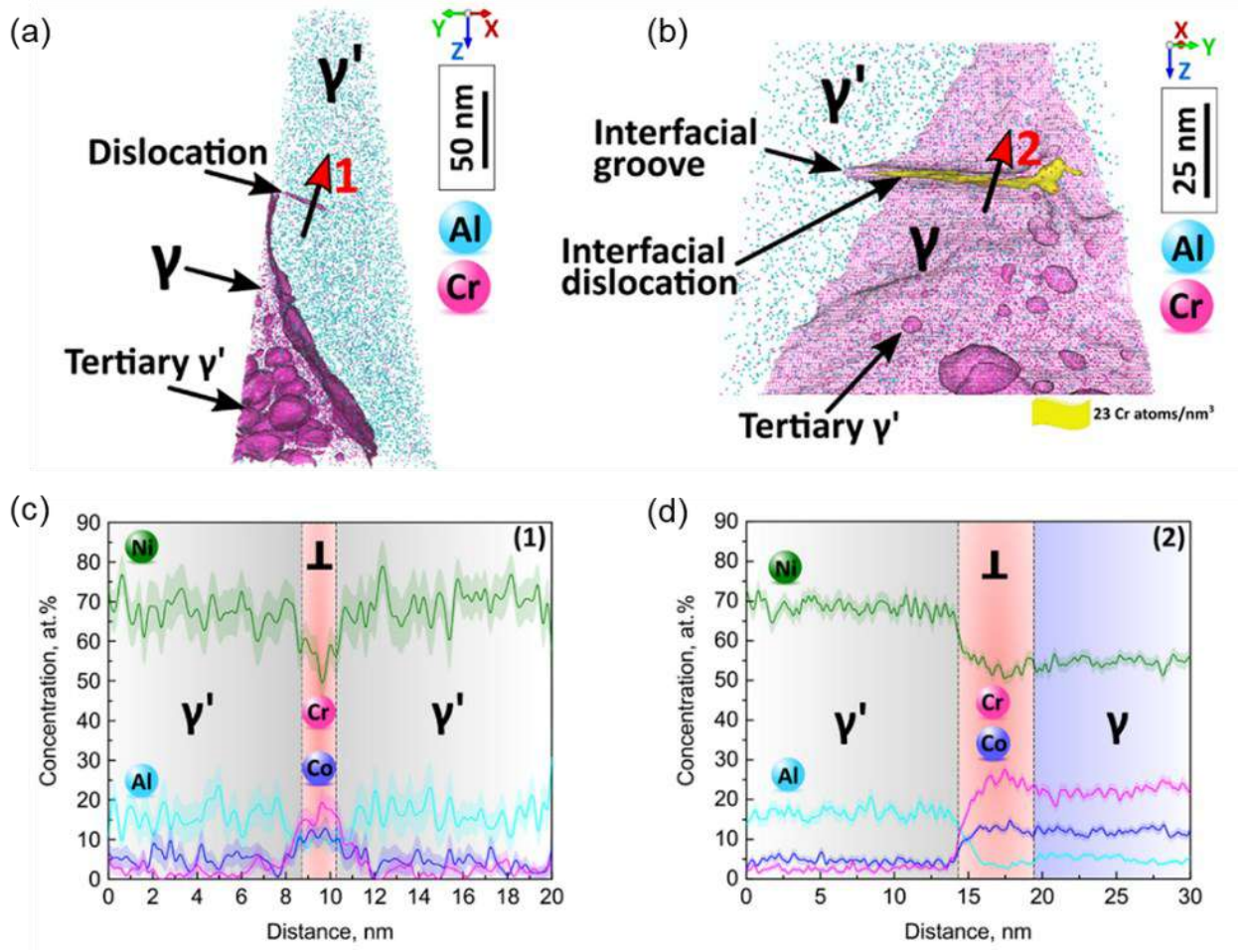

Figure 1.43. Atom probe reconstruction at the γ/γ′ interface of a rafted γ′ precipitate in the immediate vicinity of a recrystallized band after creep rupture test on pre-deformed AM1 specimen at 1050 °C / 140 MPa showing a dislocation within the γ′ phase (a). The dislocation and the γ/γ′ interface are shown with an iso-compositional surface at 8.0 at% Cr. (b) is a detail of the atom probe reconstruction from (a), showing the position of the cylindrical region of interest focusing on an interfacial dislocation groove within the γ′ precipitate. (c) and (d) are 1D concentration profiles perpendicular to the dislocation denoted by the red arrow (1) in (a) and to the interfacial dislocation groove denoted by red arrow (2) in (b), respectively. Error bars are shown as lines filled with color and correspond to the 2σ counting error.

1.4.3. Tensile tests and low cycle fatigue tests

In addition to the creep tests, tensile tests (Figure 1.44) and low cycle fatigue (LCF) tests (Figures 1.45 and 1.46) have been performed at 750 °C and 950 °C. Although the tensile property is not the same, pre-deformed specimens had higher tensile strength and ductility at 750 °C and comparable yield strength at 950 °C compared to the reference data. Dislocations formed during aging treatment after pre-deformation possibly interacted with slip bands introduced during tensile deformation at 750 °C, creating strong strain hardening. At 950 °C, yield strength was not affected, however, ductility decreased because of higher initial dislocation density. Also, the LCF lives were not affected severely by the evolved microstructure if the surface of specimens was polished to remove stresses inherited from machining. Since LCF behaviors of SX superalloys can be described by their tensile properties, fatigue results in Figures 1.45 and 1.46 are reasonable outcome.

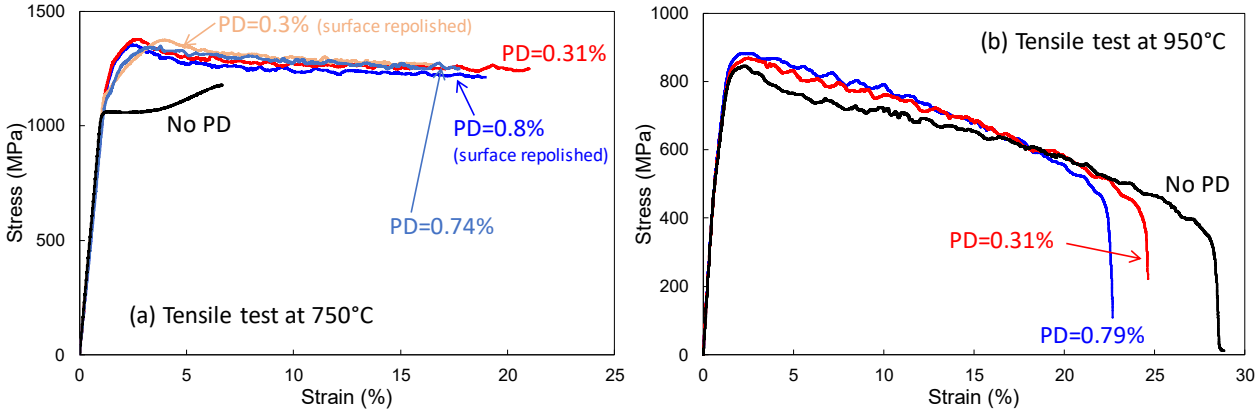

Figure 1.44. Results of high-temperature tensile tests at 750 °C (a) and 950 °C (b) on the specimens without and with pre-deformation. Strain rate = 3×10^{-4} /s

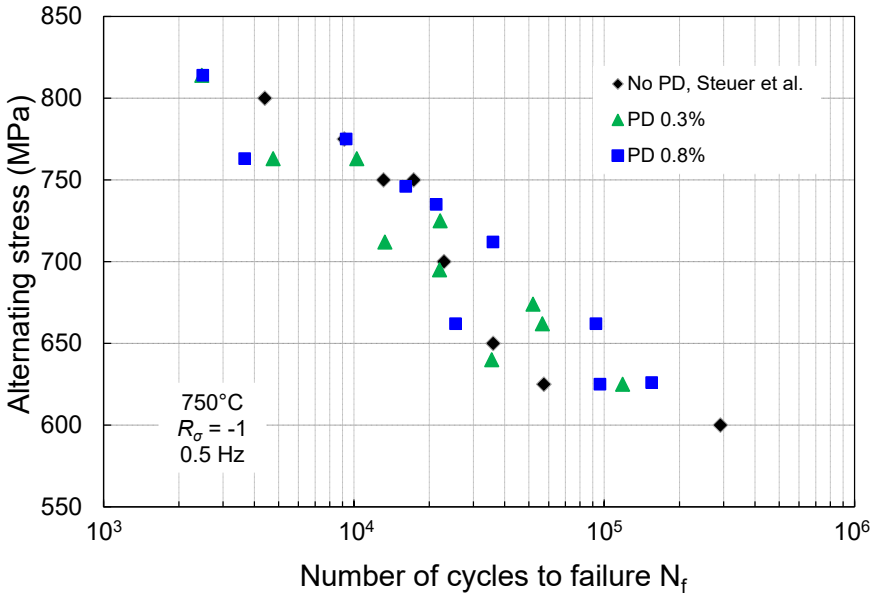

Figure 1.45. Results of high-temperature low cycle fatigue tests at 750 °C on the AM1 specimens without and with pre-deformation. R = -1, frequency = 0.5 Hz. Reference data are taken from [141].

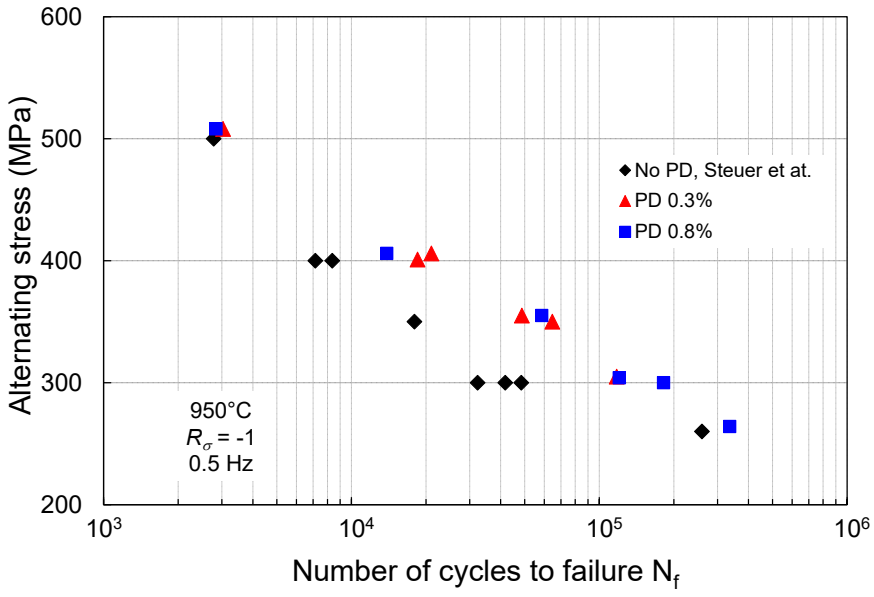

Figure 1.46. Results of high-temperature low cycle fatigue tests at 950 °C on the AM1 specimens without and with pre-deformation. R = -1, frequency = 0.5 Hz. Reference data are taken from [141].

1. 5. Research objectives

Fundamentals of Ni-based SX superalloys for turbine blade application are introduced in this Chapter. Although it has been revealed that the microstructure evolution caused by the combination of RT pre-deformation and subsequent aging treatments drastically decreases creep life of AM1 Ni-based SX superalloy, many questions remain unanswered:

- How does the microstructure evolve during aging treatments after the introduction of pre-deformation?
- How does the evolved microstructure affect high-temperature durability of AM1 and other Ni-based SX superalloys with different chemical compositions, at different creep conditions?
- What are the causes and the origins of the recrystallization during the creep deformation?
- What is the condition in which the recrystallization occurs?
- How can other pre-deformation situation affect microstructure and mechanical properties of SX superalloys? (Pre-deformation at higher-temperatures, different stages like after full heat treatment.)

From an industrial point of view,

- Are pre-deformed materials not worthy for engine operation?
- Is there any way to re-use pre-deformed materials?

The aim of this thesis research is to obtain deeper understanding about the questions mentioned above. To achieve this goal, two Ni-based SX superalloys, AM1 and CMSX-4 Plus, are used in the experiments. These alloys have many different features related to their chemical composition. Therefore, comparison of these two materials not only help understanding the scientific questions, but also gives a suggestion for the real-life application. Different preparation procedures are applied for AM1 to consider variety of possible situations that pre-deformation can be introduced to the material. Comprehensive study on the effect of production issue related deformation have never been performed elsewhere. Furthermore, concept of rejuvenation treatment is applied to the pre-deformed materials for demonstrating possibility of having pre-deformed materials back into production/operation. Re-solution treatment of SX superalloys with tensile plastic deformation is also a novel topic.

References

[1] H. Harada, High temperature materials for gas turbines: the present and future, in: Proc. Int. Gas Turbine Congr. 2003 Tokyo, Tokyo, 2003: pp. 1–6.

[2] T.M. Pollock, S. Tin, Nickel-Based Superalloys for Advanced Turbine Engines: Chemistry, Microstructure and Properties, J. Propuls. Power. 22 (2006) 361–374. doi:10.2514/1.18239.

[3] R.C. Reed, The Superalloys: Fundamentals and Applications, Cambridge University Press, Cambridge, 2006. doi:10.1017/CBO9780511541285.

[4] H. Long, S. Mao, Y. Liu, Z. Zhang, X. Han, Microstructural and compositional design of Ni-based single crystalline superalloys — A review, J. Alloys Compd. 743 (2018) 203–220. doi:10.1016/j.jallcom.2018.01.224.

[5] T. Murakumo, T. Kobayashi, Y. Koizumi, H. Harada, Creep behaviour of Ni-base single-crystal superalloys with various γ′ volume fraction, Acta Mater. 52 (2004) 3737–3744. doi:10.1016/j.actamat.2004.04.028.

[6] C. Panwisawas, H. Mathur, J.-C. Gebelin, D.C. Putman, P. Withey, N. Warnken, C.M.F. Rae, R.C. Reed, Prediction of Plastic Strain for Recrystallisation during Investment Casting of Single Crystal Superalloys, in: Superalloys 2012, John Wiley & Sons, Inc., Hoboken, NJ, USA, 2012: pp. 547–556. doi:10.1002/9781118516430.ch60.

[7] C. Panwisawas, J.-C. Gebelin, R.C. Reed, Analysis of the mechanical deformation arising from investment casting of directionally solidified nickel-based superalloys, Mater. Sci. Technol. 29 (2013) 843–853. doi:10.1179/1743284712Y.0000000197.

[8] S. Pierret, T. Etter, A. Evans, H. Van Swygenhoven, Origin of localized rafting in Ni-based single crystal turbine blades before service and its influence on the mechanical properties, Acta Mater. 61 (2013) 1478–1488. doi:10.1016/j.actamat.2012.11.024.

[9] M. Sakaguchi, M. Ike, M. Okazaki, Microstructural changes in a single crystal Ni-base superalloy induced by plastic straining, Mater. Sci. Eng. A. 534 (2012) 253–259. doi:10.1016/J.MSEA.2011.11.066.

[10] M. Sakaguchi, M. Okazaki, Distinctive role of plastic and creep strain in directional coarsening of a Ni-base single crystal superalloy, Mater. Sci. Eng. A. 710 (2018) 121–128. doi:10.1016/j.msea.2017.10.085.

[11] C.P. Liu, X.N. Zhang, L. Ge, C.Y. Wang, T. Yu, Z. Zhang, The effect of pre-deformation on the microstructure evolution of NiAl model single crystal superalloy during thermal exposure at 1000 °C, Mater. Sci. Eng. A. 754 (2019) 556–561. doi:10.1016/j.msea.2019.03.099.

[12] B.G. Choi, C.Y. Jo, H.U. Hong, I.S. Kim, S.M. Seo, H.M. Kim, Effect of pre-strain on microstructural evolution during thermal exposure of single crystal superalloy CMSX-4, Trans. Nonferrous Met. Soc. China. 21 (2011) 1291–1296. doi:10.1016/S1003-6326(11)60855-8.

[13] C. Sims, N. Stoloff, W. Hagel, Superalloys II: High-Temperature Materials for Aerospace and Industrial Power, John Wiley and Sons, 1987.

[14] L.S. Langston, Fahrenheit 3,600, Mech. Eng. 129 (2007) 34–37. doi:10.1115/1.2007-APR-3.

[15] Q. Ding, S. Li, L.-Q. Chen, X. Han, Z. Zhang, Q. Yu, J. Li, Re segregation at interfacial dislocation network in a nickel-based superalloy, Acta Mater. 154 (2018) 137–146. doi:10.1016/j.actamat.2018.05.025.

[16] S. Utada, H. Harada, K. Kawagishi, S. Suzuki, Evolution of superalloy for turbine airfoil and development of recycling technology, J. Gas Turbine Soc. Japan. 45 (2017) 445–451.

[17] H.J. Dai, J.-C. Gebelin, R.C. Reed, N. D'Souza, P.D. Prown, H.B. Dong, Grain selection during solidification in spiral grain selector, in: R.C. Reed, K.A. Green, P. Caron, T.P. Gabb, M.G. Fahrmann, E.S. Huron, S.A. Woodard (Eds.), Superalloys 2008, 2008: pp. 367–374. doi:10.7449/2008/Superalloys_2008_367_374.

[18] M. Gell, D.N. Duhl, A.F. Giamei, The development of single crystal superalloy turbine blades, in: Superalloys 1980, ASM, Champion, PA, 1980: pp. 205–214. doi:10.7449/1980/Superalloys_1980_205_214.

[19] A.D. Cetel, D.N. Duhl, Second-Generation Nickel-Base Single Crystal Superalloy, in: Superalloys 1988, 1988: pp. 235–244.

[20] K. Harris, G.L. Erickson, W.D. Brentnall, J.M. Aurrecoechea, S.L. Sikkenga, K.G. Kubarych, Development of the Rhenium Containing Superalloys CMSX-4 & CM 186 LC for Single Crystal Blade and Directionally Solidified Vane Applications in Advanced Turbine Engines, in: S.D. Antolovich, R.W. Stusrud, R.A. MacKay, D.L. Anton, T. Khan, R.D. Kissinger, D.L. Klarstrom (Eds.), Superalloys 1992, 1992: pp. 297–306. doi:10.7449/1992/Superalloys_1992_297_306.

[21] W.S. Walston, K.S. O'hara, E.W. Ross, T.M. Pollock, W.H. Murphy, Rene' N6: Third Generation

Single Crystal Superalloy, in: Superalloys 1996, 1996: pp. 27–34. doi:10.7449/1996/Superalloys_1996_27_34.

[22] G.L. Erickson, The Development and Application of CMSX®-10, in: Superalloys 1996, 1996: pp. 35–44. doi:10.7449/1996/Superalloys_1996_35_44.pdf.

[23] C.M.F. Rae, R.C. Reed, The precipitation of topologically close-packed phases in rhenium-containing superalloys, Acta Mater. 49 (2001) 4113–4125.

[24] C. Rae, M. Karunaratne, C. Small, R. Broomfield, C. Jones, R. Reed, Topologically Close Packed Phases in an Experimental Rhenium-Containing Single Crystal Superalloy, in: Superalloys 2000, 2000: pp. 767–776. doi:10.7449/2000/Superalloys_2000_767_776.

[25] R. Darolia, D.F. Lahrman, R.D. Field, R. Sisson, Formation of Topologically Closed Packed Phases in Nickle Base Single Crystal Superalloys, Superalloys 1988. (1988) 255–264.

[26] A.C. Yeh, S. Tin, Effects of Ru on the high-temperature phase stability of Ni-base single-crystal superalloys, Metall. Mater. Trans. A. 37 (2006) 2621–2631. doi:10.1007/BF02586097.

[27] A. Sato, H. Harada, A.-C. Yeh, K. Kawagishi, T. Kobayashi, Y. Koizumi, T. Yokokawa, J.X. Zhang, A 5th generation SC superalloy with balanced high temperature properties and processability, in: Superalloys 2008, 2008: pp. 131–138. doi:10.7449/2008/Superalloys_2008_131_138.

[28] K. Kawagishi, A. Yeh, T. Yokokawa, T. Kobayashi, Y. Koizumi, H. Harada, Development of an Oxidation-resistant High-Strength Sixth-Generation Single-Crystal Superalloy TMS-238, in: Superalloys 2012, 2012: pp. 189–195. doi:10.1002/9781118516430.ch21.

[29] Y. Mori, T. Yokokawa, T. Kobayashi, H. Harada, S. Suzuki, Phase Stability of Nickel-Base Single Crystal Superalloys Containing Iridium Substituting for Ruthenium, Mater. Trans. 57 (2016) 1845–1848. doi:10.2320/matertrans.MAW201606.

[30] T. Yokokawa, H. Harada, Y. Mori, K. Kawagishi, Y. Koizumi, T. Kobayashi, M. Yuyama, S. Suzuki, Design of Next Generation Ni-base Single Crystal Superalloys Containing Ir: Towards 1150°C Temperature Capability, in: Superalloys 2016, 2016: pp. 123–130. doi:10.1002/9781119075646.ch14.

[31] J.S. Van Sluytman, C.J. Moceri, T.M. Pollock, A Pt-modified Ni-base superalloy with high temperature precipitate stability, Mater. Sci. Eng. A. 639 (2015) 747–754. doi:10.1016/j.msea.2015.05.023.

[32] J. Rame, S. Utada, L.M. Bortoluci Ormastroni, L. Mataveli Suave, E. Menou, L. Després, P. Kontis, J. Cormier, Platinum containing new generation nickel-based superalloy for single crystalline application, in: S. Tin, M. Hardy, J. Clews, J. Cormier, Q. Feng, J. Marcin, C. O'Brien, A. Suzuki (Eds.), Superalloys 2020, Springer International Publishing, 2020: pp. 71–81. doi:10.1007/978-3-030-51834-9_7.

[33] P.J. Fink, J.L. Miller, D.G. Konitzer, Rhenium reduction—alloy design using an economically strategic element, JOM. 62 (2010) 55–57. doi:10.1007/s11837-010-0012-z.

[34] K. Kawagishi, T. Yokokawa, T. Kobayashi, Y. Koizumi, M. Sakamoto, M. Yuyama, H. Harada, I. Okada, M. Taneike, H. Oguma, Development of low or zero-rhenium high-performance Ni-base single crystal superalloys for jet engine and power generation applications, in: Superalloys 2016, 2016: pp. 115–122. doi:10.1002/9781119075646.ch13.

[35] J.B. Wahl, K. Harris, CMSX-4 Plus Single Crystal Alloy Development, Characterization and Application Development, in: Superalloys 2016, John Wiley & Sons, Inc., 2016: pp. 25–33. doi:10.1002/9781119075646.ch3.

[36] H.J. Dai, N. D'Souza, H.B. Dong, Grain Selection in Spiral Selectors During Investment Casting of Single-Crystal Turbine Blades: Part I. Experimental Investigation, Metall. Mater. Trans. A. 42 (2011) 3430–3438. doi:10.1007/s11661-011-0760-6.

[37] A.J. Elliott, T.M. Pollock, S. Tin, W.T. King, S.-C. Huang, M.F.X. Gigliotti, Directional solidification of large superalloy castings with radiation and liquid-metal cooling: A comparative assessment, Metall. Mater. Trans. A. 35 (2004) 3221–3231. doi:10.1007/s11661-004-0066-z.

[38] P. Caron, P.J. Henderson, T. Khan, M. McLean, On the effects of heat treatments on the creep behaviour of a single crystal superalloy, Scr. Metall. 20 (1986) 875–880. doi:10.1016/0036-9748(86)90458-8.

[39] P. Caron, T. Khan, Improvement of Creep strength in a nickel-base single-crystal superalloy by heat treatment, Mater. Sci. Eng. 61 (1983) 173–184. doi:10.1016/0025-5416(83)90199-4.

[40] J.J. Jackson, M.J. Donachie, M. Gell, R.J. Henricks, The effect of volume percent of fine γ' on creep in DS Mar-M200+Hf, Metall. Trans. A. 8 (1977) 1615–1620. doi:10.1007/BF02644867.

[41] Y. Ro, Y. Koizumi, H. Harada, High temperature tensile properties of a series of nickel-base superalloys on a γ/γ′ tie line, Mater. Sci. Eng. A. 223 (1997) 59–63. doi:10.1016/S0921-5093(96)10504-9.

[42] H. Harada, M. Yamazaki, Y. Koizumi, N. Sakuma, N. Furuya, H. Kamiya, Alloy Design for Nickel-Base Superalloys BT - High Temperature Alloys for Gas Turbines 1982, in: R. Brunetaud, D. Coutsouradis, T.B. Gibbons, Y. Lindblom, D.B. Meadowcroft, R. Stickler (Eds.), Springer Netherlands, Dordrecht, 1982: pp. 721–735.

[43] A. Heckl, R. Rettig, R.F. Singer, Solidification Characteristics and Segregation Behavior of Nickel-Base Superalloys in Dependence on Different Rhenium and Ruthenium Contents, Metall. Mater. Trans. A. 41 (2009) 202. doi:10.1007/s11661-009-0076-y.

[44] M. V Nathal, Effect of initial gamma prime size on the elevated temperature creep properties of single crystal nickel base superalloys, Metall. Trans. A. 18 (1987) 1961–1970. doi:10.1007/BF02647026.

[45] T. Grosdidier, A. Hazotte, A. Simon, Precipitation and dissolution processes in γ/γ′ single crystal nickel-based superalloys, Mater. Sci. Eng. A. 256 (1998) 183–196. doi:10.1016/S0921-5093(98)00795-3.

[46] S. Steuer, Z. Hervier, S. Thabart, C. Castaing, T.M. Pollock, J. Cormier, Creep behavior under isothermal and non-isothermal conditions of AM3 single crystal superalloy for different solutioning cooling rates, Mater. Sci. Eng. A. 601 (2014) 145–152. doi:10.1016/j.msea.2014.02.046.

[47] M. V Nathal, R.A. MacKay, R. V Miner, Influence of precipitate morphology on intermediate temperature creep properties of a nickel-base superalloy single crystal, Metall. Trans. A. 20 (1989) 133–141. doi:10.1007/BF02647500.

[48] A. Sengupta, S.K. Putatunda, L. Bartosiewicz, J. Hangas, P.J. Nailos, M. Peputapeck, F.E. Alberts, Tensile behavior of a new single-crystal nickel-based superalloy (CMSX-4) at room and elevated temperatures, J. Mater. Eng. Perform. 3 (1994) 73–81. doi:10.1007/BF02654502.

[49] D.M. Shah, D.N. Duhl, The effect of orientation, temperature and gamma prime size on the yield strength of a single crystal nickel base superalloy, Superalloys 1984. (1984) 105–114.

[50] D.L. Anton, A.F. Giamei, Porosity distribution and growth during homogenization in single crystals of a nickel-base superalloy, Mater. Sci. Eng. 76 (1985) 173–180. doi:10.1016/0025-5416(85)90091-6.

[51] T. Link, S. Zabler, A. Epishin, A. Haibel, M. Bansal, X. Thibault, Synchrotron tomography of porosity in single-crystal nickel-base superalloys, Mater. Sci. Eng. A. 425 (2006) 47–54. doi:10.1016/j.msea.2006.03.005.

[52] E. Plancher, P. Gravier, E. Chauvet, J.-J. Blandin, E. Boller, G. Martin, L. Salvo, P. Lhuissier, Tracking pores during solidification of a Ni-based superalloy using 4D synchrotron microtomography, Acta Mater. 181 (2019) 1–9. doi:10.1016/j.actamat.2019.09.040.

[53] L. Mujica Roncery, I. Lopez-Galilea, B. Ruttert, S. Huth, W. Theisen, Influence of temperature, pressure, and cooling rate during hot isostatic pressing on the microstructure of an SX Ni-base superalloy, Mater. Des. 97 (2016) 544–552. doi:10.1016/j.matdes.2016.02.051.

[54] L. Mujica Roncery, I. Lopez-Galilea, B. Ruttert, D. Bürger, P. Wollgramm, G. Eggeler, W. Theisen, On the Effect of Hot Isostatic Pressing on the Creep Life of a Single Crystal Superalloys, Adv. Eng. Mater. 18 (2016) 1381–1387. doi:10.1002/adem.201600071.

[55] A. Cervellon, J. Cormier, F. Mauget, Z. Hervier, Y. Nadot, Very High Cycle Fatigue of Ni-Based Single-Crystal Superalloys at High Temperature, Metall. Mater. Trans. A. 49 (2018) 3938–3950. doi:10.1007/s11661-018-4672-6.

[56] A.I. Epishin, T. Link, B. Fedelich, I.L. Svetlov, E.R. Golubovskiy, Hot isostatic pressing of single-crystal nickel-base superalloys: Mechanism of pore closure and effect on Mechanical properties, MATEC Web Conf. 14 (2014). doi:10.1051/matecconf/20141408003.

[57] A. Epishin, T. Link, I.L. Svetlov, G. Nolze, R.S. Neumann, H. Lucas, Mechanism of porosity growth during homogenisation in single crystal nickel-based superalloys, Int. J. Mater. Res. 104 (2013) 776–782. doi:10.3139/146.110924.

[58] A.I. Epishin, I.L. Svetlov, Evolution of pore morphology in single-crystals of nickel-base superalloys, Inorg. Mater. Appl. Res. 7 (2016) 45–52. doi:10.1134/S2075113316010056.

[59] H. Kawazoe, T. Takasugi, O. Izumi, Morphological and crystallographic features of γ-γ′ Ni-Al and Ni-Al-Ti two-phase bicrystals, J. Mater. Sci. 17 (1982) 1303–1310. doi:10.1007/BF00752239.

[60] D.J. Bacon, U.F. Kocks, R.O. Scattergood, The effect of dislocation self-interaction on the orowan stress, Philos. Mag. A J. Theor. Exp. Appl. Phys. 28 (1973) 1241–1263. doi:10.1080/14786437308227997.

[61] B. Reppich, P. Schepp, G. Wehner, Some new aspects concerning particle hardening mechanisms in γ' precipitating nickel-base alloys—II. Experiments, Acta Metall. 30 (1982) 95–104. doi:10.1016/0001-6160(82)90049-9.

[62] R.W. Kozar, A. Suzuki, W.W. Milligan, J.J. Schirra, M.F. Savage, T.M. Pollock, Strengthening Mechanisms in Polycrystalline Multimodal Nickel-Base Superalloys, Metall. Mater. Trans. A. 40 (2009) 1588–1603. doi:10.1007/s11661-009-9858-5.

[63] W.W. Milligan, S.D. Antolovich, Yielding and deformation behavior of the single crystal superalloy PWA 1480, Metall. Trans. A. 18 (1987) 85–95. doi:10.1007/BF02646225.

[64] P.H. Thornton, R.G. Davies, T.L. Johnston, The temperature dependence of the flow stress of the γ′ phase based upon Ni3Al, Metall. Trans. 1 (1970) 207–218. doi:10.1007/BF02819263.

[65] P. Beardmore, R.G. Davies, T.L. Johnston, Temperature Dependence of the Flow Stress of Nickel-Base Alloys, Trans. Metall. Soc. AlME. 245 (1969) 1537–1545.

[66] M. Feller-Kniepmeier, T. Link, I. Poschmann, G. Scheunemann-Frerker, C. Schulze, Temperature dependence of deformation mechanisms in a single crystal nickel-base alloy with high volume fraction of γ′ phase, Acta Mater. 44 (1996) 2397–2407. doi:10.1016/1359-6454(95)00354-1.

[67] B.H. Kear, H.G.F. Wilsdorf, Dislocation configurations in plastically deformed polycrystalline Cu3Au alloys, Trans. Metall. Soc. AIME. 224 (1962) 382–386.

[68] D.D. Pearson, F.D. Lemkey, B.H. Kear, Stress Coarsening of gamma prime and its Influence on Creep Properties of a Single Crystal Superalloy, in: Superalloys 1980, 1980: pp. 513–520.

[69] L. Agudo Jácome, P. Nörtershäuser, J.-K. Heyer, A. Lahni, J. Frenzel, A. Dlouhy, C. Somsen, G. Eggeler, High-temperature and low-stress creep anisotropy of single-crystal superalloys, Acta Mater. 61 (2013) 2926–2943. doi:10.1016/j.actamat.2013.01.052.

[70] L. Agudo Jácome, P. Nörtershäuser, C. Somsen, A. Dlouhý, G. Eggeler, On the nature of γ′ phase cutting and its effect on high temperature and low stress creep anisotropy of Ni-base single crystal superalloys, Acta Mater. 69 (2014) 246–264. doi:10.1016/j.actamat.2014.01.021.

[71] J.-B. le Graverend, J. Adrien, J. Cormier, Ex-situ X-ray tomography characterization of porosity during high-temperature creep in a Ni-based single-crystal superalloy: Toward understanding what is damage, Mater. Sci. Eng. A. 695 (2017) 367–378. doi:10.1016/j.msea.2017.03.083.

[72] H. Buck, P. Wollgramm, A.B. Parsa, G. Eggeler, A quantitative metallographic assessment of the evolution of porosity during processing and creep in single crystal Ni-base super alloys, Materwiss. Werksttech. 46 (2015) 577–590. doi:10.1002/mawe.201500379.

[73] S.H. Ai, V. Lupinc, M. Maldini, Creep fracture mechanisms in single crystal superalloys, Scr. Metall. Mater. 26 (1992) 579–584. doi:10.1016/0956-716X(92)90287-O.

[74] R.C. Reed, D.C. Cox, C.M.F. Rae, Damage accumulation during creep deformation of a single crystal superalloy at 1150 °C, Mater. Sci. Eng. A. 448 (2007) 88–96. doi:10.1016/J.MSEA.2006.11.101.

[75] A. Epishin, T. Link, Mechanisms of high-temperature creep of nickel-based superalloys under low applied stresses, Philos. Mag. 84 (2004) 1979–2000. doi:10.1080/14786430410001663240.

[76] R.N. Ghosh, R. V Curtis, M. McLean, Creep deformation of single crystal superalloys—modelling the crystallographic anisotropy, Acta Metall. Mater. 38 (1990) 1977–1992. doi:10.1016/0956-7151(90)90309-5.

[77] A. Epishin, T. Link, P.D. Portella, U. Brückner, Evolution of the γ/γ′ microstructure during high-temperature creep of a nickel-base superalloy, Acta Mater. 48 (2000) 4169–4177. doi:10.1016/S1359-6454(00)00197-X.

[78] A. Epishin, T. Link, U. Brückner, P.D. Portella, Kinetics of the topological inversion of the γ/γ′-microstructure during creep of a nickel-based superalloy, Acta Mater. 49 (2001) 4017–4023. doi:10.1016/S1359-6454(01)00290-7.

[79] S. Antonov, Y. Zheng, J.M. Sosa, H.L. Fraser, J. Cormier, P. Kontis, B. Gault, Plasticity assisted redistribution of solutes leading to topological inversion during creep of superalloys, Scr. Mater. 186 (2020) 287–292. doi:10.1016/j.scriptamat.2020.05.004.

[80] J. Zhang, J. Wang, H. Harada, Y. Koizumi, The effect of lattice misfit on the dislocation motion in superalloys during high-temperature low-stress creep, Acta Mater. 53 (2005) 4623–4633. doi:10.1016/j.actamat.2005.06.013.

[81] M. Kamaraj, C. Mayr, M. Kolbe, G. Eggeler, On the influence of stress state on rafting in the single crystal superalloy CMSX-6 under conditions of high temperature and low stress creep, Scr. Mater. 38 (1998) 589–594. doi:10.1016/S1359-6462(97)00520-4.

[82] J.X. Zhang, T. Murakumo, H. Harada, Y. Koizumi, Dependence of creep strength on the interfacial dislocations in a fourth generation SC superalloy TMS-138, Scr. Mater. 48 (2003) 287–293. doi:10.1016/S1359-6462(02)00379-2.

[83] R.A. MacKay, R.D. Maier, The influence of orientation on the stress rupture properties of nickel-base superalloy single crystals, Metall. Trans. A. 13 (1982) 1747–1754. doi:10.1007/BF02647830.

[84] C.M.F. Rae, M.A. Rist, D.C. Cox, R.C. Reed, N. Matan, On the primary creep of CMSX-4 superalloy single crystals, Metall. Mater. Trans. A. 31 (2000) 2219–2228. doi:10.1007/s11661-000-0139-6.

[85] C.M.F. Rae, R.C. Reed, Primary creep in single crystal superalloys: Origins, mechanisms and effects, Acta Mater. 55 (2007) 1067–1081. doi:10.1016/j.actamat.2006.09.026.

[86] P. Caron, Y. Ohta, Y.G. Nakagawa, T. Khan, Creep Deformation Anisotropy in Single Crystal Superalloys, in: S. Reichman, D.N. Duhl, G. Maurer, S.D. Antolovich, C. Lund (Eds.), Superalloys 1988, TMS, 1988: pp. 215–224. doi:10.7449/1988/Superalloys_1988_215_224.

[87] Y. Yuan, K. Kawagishi, Y. Koizumi, T. Kobayashi, T. Yokokawa, H. Harada, Creep deformation of a sixth generation Ni-base single crystal superalloy at 800°C, Mater. Sci. Eng. A. 608 (2014) 95–100. doi:10.1016/j.msea.2014.04.069.

[88] F. Diologent, P. Caron, On the creep behavior at 1033K of new generation single-crystal superalloys, Mater. Sci. Eng. A. 385 (2004) 245–257. doi:10.1016/j.msea.2004.07.016.

[89] A. Cervellon, J. Cormier, F. Mauget, Z. Hervier, VHCF life evolution after microstructure degradation of a Ni-based single crystal superalloy, Int. J. Fatigue. 104 (2017) 251–262. doi:10.1016/j.ijfatigue.2017.07.021.

[90] L.M. Bortoluci Ormastroni, L. Mataveli Suave, A. Cervellon, P. Villechaise, J. Cormier, LCF, HCF and VHCF life sensitivity to solution heat treatment of a third-generation Ni-based single crystal superalloy, Int. J. Fatigue. 130 (2020) 105247. doi:10.1016/j.ijfatigue.2019.105247.

[91] A. Cervellon, S. Hémery, P. Kürnsteiner, B. Gault, P. Kontis, J. Cormier, Crack initiation mechanisms during very high cycle fatigue of Ni-based single crystal superalloys at high temperature, Acta Mater. 188 (2020) 131–144. doi:10.1016/j.actamat.2020.02.012.

[92] L.M. Bortoluci Ormastroni, S. Utada, J. Rame, L. Mataveli Suave, K. Kawagishi, H. Harada, P. Villechaise, J. Cormier, Tensile, low cycle fatigue and very high cycle fatigue characterizations of advanced single crystal nickel-based superalloys, in: S. Tin, M. Hardy, J. Clews, J. Cormier, Q. Feng, J. Marcin, C. O'Brien, A. Suzuki (Eds.), Superalloys 2020, Springer International Publishing, 2020: pp. 341–351. doi:10.1007/978-3-030-51834-9_33.

[93] P. Kontis, Z. Li, D.M. Collins, J. Cormier, D. Raabe, B. Gault, The effect of chromium and cobalt segregation at dislocations on nickel-based superalloys, Scr. Mater. 145 (2018) 76–80. doi:10.1016/j.scriptamat.2017.10.005.

[94] R. Bürgel, P.D. Portella, J. Preuhs, Recrystallization in single crystals of nickel base superalloys, in: Superalloys 2000, 2000: pp. 229–238. doi:10.7449/2000/Superalloys_2000_229_238.

[95] D.C. Cox, B. Roebuck, C.M.F. Rae, R.C. Reed, Recrystallisation of single crystal superalloy CMSX-4, Mater. Sci. Technol. 19 (2003) 440–446. doi:10.1179/026708303225010731.

[96] Z. Li, X. Fan, Q. Xu, B. Liu, Influence of deformation temperature on recrystallization in a Ni-based single crystal superalloy, Mater. Lett. 160 (2015) 318–322. doi:10.1016/j.matlet.2015.07.120.

[97] Z. Li, Q. Xu, B. Liu, Experimental investigation on recrystallization mechanism of a Ni-base single crystal superalloy, J. Alloys Compd. 672 (2016) 457–469. doi:10.1016/j.jallcom.2016.02.149.

[98] H.N. Mathur, C. Panwisawas, C.N. Jones, R.C. Reed, C.M.F. Rae, Nucleation of recrystallisation in castings of single crystal Ni-based superalloys, Acta Mater. 129 (2017) 112–123. doi:10.1016/j.actamat.2017.02.058.

[99] L. Tian, C. Xu, C. Ma, Recrystallization of a single crystal Ni-base superalloy in ⟨011⟩ and ⟨111⟩ orientations, Mater. Charact. 127 (2017) 116–120. doi:10.1016/j.matchar.2017.01.020.

[100] L. Zhonglin, Z. Dandan, S. Xianglin, X. Qingyan, L. Baicheng, Role of as-cast dendritic microstructure in recrystallization of a Ni-based single crystal superalloy, J. Alloys Compd. 660 (2016) 115–124. doi:10.1016/j.jallcom.2015.11.072.

[101] P. Strunz, G. Schumacher, H. Klingelhöffer, A. Wiedenmann, J. Šaroun, U. Keiderling, In situ observation of morphological changes of γ′ precipitates in a pre-deformed single-crystal Ni-base superalloy, J. Appl. Crystallogr. 44 (2011) 935–944. doi:10.1107/S0021889811028147.

[102] M. Véron, Y. Bréchet, F. Louchet, Strain induced directional coarsening in Ni based superalloys, Scr. Mater. 34 (1996) 1883–1886. doi:10.1016/1359-6462(96)00062-0.

[103] J.J. Moverare, S. Johansson, R.C. Reed, Deformation and damage mechanisms during thermal–mechanical fatigue of a single-crystal superalloy, Acta Mater. 57 (2009) 2266–2276. doi:10.1016/J.ACTAMAT.2009.01.027.

[104] M. Segersäll, J.J. Moverare, K. Simonsson, S. Johansson, Deformation and Damage Mechanisms during Thermomechanical Fatigue of a Single-Crystal Superalloy in the <001> and <011> Directions, Superalloys 2012. (2012) 215–223. doi:doi:10.1002/9781118516430.ch24.

[105] M. Segersäll, P. Kontis, S. Pedrazzini, P.A.J. Bagot, M.P. Moody, J.J. Moverare, R.C. Reed, Thermal–mechanical fatigue behaviour of a new single crystal superalloy: Effects of Si and Re alloying, Acta Mater. 95 (2015) 456–467. doi:10.1016/J.ACTAMAT.2015.03.060.

[106] M. Véron, P. Bastie, Strain induced directional coarsening in nickel based superalloys: Investigation on kinetics using the small angle neutron scattering (SANS) technique, Acta Mater. 45 (1997) 3277–3282. doi:10.1016/S1359-6454(97)00035-9.

[107] R. Giraud, J. Cormier, Z. Hervier, D. Bertheau, K. Harris, J. Wahl, X. Milhet, J. Mendez, A. Organista, Effect of the Prior Microstructure Degradation on the High Temperature/Low Stress Non-Isothermal Creep Behavior of CMSX-4® Ni-Based Single Crystal Superalloy, Superalloys 2012. (2012) 265–274. doi:10.1002/9781118516430.ch29.

[108] S. Utada, Y. Joh, M. Osawa, T. Yokokawa, T. Sugiyama, T. Kobayashi, K. Kawagishi, S. Suzuki, H. Harada, Creep Property and Phase Stability of Sulfur-Doped Ni-Base Single-Crystal Superalloys and Effectiveness of CaO Desulfurization, Metall. Mater. Trans. A Phys. Metall. Mater. Sci. (2018). doi:10.1007/s11661-018-4710-4.

[109] B.F. Dyson, D.E. Henn, The effect of room temperature pre-strain on grain boundary cavitation in Nimonic 80A, J. Microsc. 97 (1973) 165–170. doi:10.1111/j.1365-2818.1973.tb03771.x.

[110] M.S. Loveday, B.F. Dyson, Prestrain-induced particle microcracking and creep cavitation in IN597, Acta Metall. 31 (1983) 397–405. doi:10.1016/0001-6160(83)90217-1.

[111] K. Shiozawa, J.R. Weertman, Studies of nucleation mechanisms and the role of residual stresses in the grain boundary cavitation of a superalloy, Acta Metall. 31 (1983) 993–1004. doi:10.1016/0001-6160(83)90194-3.

[112] Y.H. Zhang, D.M. Knowles, Prestraining effect on creep behaviour of nickel base C263 superalloy, Mater. Sci. Technol. 18 (2002) 917–923. doi:10.1179/026708302225004838.

[113] C. Stöcker, M. Zimmermann, H.-J. Christ, Effect of precipitation condition, prestrain and temperature on the fatigue behaviour of wrought nickel-based superalloys in the VHCF range, Acta Mater. 59 (2011) 5288–5304. doi:10.1016/j.actamat.2011.05.005.

[114] M.C. Pandey, A.K. Mukherjee, D.M.R. Taplin, Prior deformation effects on creep and fracture in inconel alloy X-750, Metall. Trans. A. 15 (1984) 1437–1441. doi:10.1007/BF02648573.

[115] M. Ott, H. Mughrabi, Dependence of the high-temperature low-cycle fatigue behaviour of the monocrystalline nickel-base superalloys CMSX-4 and CMSX-6 on the γ/γ′-morphology, Mater. Sci. Eng. A. 272 (1999) 24–30. doi:10.1016/S0921-5093(99)00453-0.

[116] G.L. Drew, R.C. Reed, K. Kakehi, C.M.F. Rae, Single Crystal Superalloys: The transition from Primary to Secondary Creep, in: Superalloys 2004, 2004: pp. 127–136. doi:10.7449/2004/Superalloys_2004_127_136.

[117] A. Epishin, T. Link, H. Klingelhöffer, B. Fedelich, P. Portella, Creep damage of single-crystal nickel base superalloys: mechanisms and effect on low cycle fatigue, Mater. High Temp. 27 (2010) 53–59. doi:10.3184/096034009X12603595726283.

[118] Y. Su, S. Tian, H. Yu, L. Yu, Effect of pre-compressive treatment on creep behavior of a ⟨011⟩-oriented single-crystal Ni-based superalloy, Scr. Mater. 93 (2014) 24–27. doi:10.1016/j.scriptamat.2014.08.021.

[119] H. Long, S. Mao, Y. Liu, H. Wei, Q. Deng, Y. Chen, Z. Zhang, X. Han, Effect of pre-straining treatment on high temperature creep behavior of Ni-based single crystal superalloys, Mater. Des. (2019) 107633. doi:10.1016/j.matdes.2019.107633.

[120] U. Tetzlaff, H. Mughrabi, Enhanccement of the high-temperature tensile creep strength of monocrystalline nickel-base superalloys by pre-rafting in compression, in: Superalloys 2000, 2000: pp. 273–282. doi:10.7449/2000/Superalloys_2000_273_282.

[121] H. Mughrabi, M. Ott, U. Tetzlaff, New microstructural concepts to optimize the high-temperature strength of γ′-hardened monocrystalline nickel-based superalloys, Mater. Sci. Eng. A. 234–236 (1997) 434–437. doi:10.1016/S0921-5093(97)00268-2.

[122] G. VanDrunen, J. Liburdi, Rejuvenation of Used Turbine Blades by Hot Isostatic Pressing, in: Proc. Sixth Turbomach. Symp., 1977: pp. 55–60.

[123] J. Liburdi, J. Wilson, Guidelines for Reliable Extension of Turbine Blade Life, in: P.E. Jenkins (Ed.), Proc. Twelfth Turbomach. Symp., College Station, Texas, 1983: pp. 21–30.

[124] J.P. Dennison, I.C. Elliott, B. Wilshire, An assessment of hot isostatic pressing and reheat treatment for the regeneration of creep properties of superalloys, in: Superalloys 1980, 1980: pp. 671–677.

[125] A. James, Review of rejuvenation process for nickel base superalloys, Mater. Sci. Technol. 17 (2001) 481–486. doi:10.1179/026708301101510168.

[126] L.H. Rettberg, M. Tsunekane, T.M. Pollock, Rejuvenation of nickel-based superalloys GTD444(DS) and René N5(SX), in: Superalloys 2012, 2012: pp. 341–349. doi:10.1002/9781118516430.ch37.

[127] L. Rettberg, Rejuvenation of Ni-base Superalloys GTD444 and René N5, University of California, Santa Barbara, PhD Thesis, 2016.

[128] Z. Yao, C.C. Degnan, M.A.E. Jepson, R.C. Thomson, Effect of rejuvenation heat treatments on gamma prime distributions in a Ni based superalloy for power plant applications, Mater. Sci. Technol. 29 (2013) 775–780. doi:10.1179/1743284712Y.0000000199.

[129] Z.-X. Shi, S.-Z. Liu, J.-R. Li, Rejuvenation Heat Treatment of the Second-Generation Single-Crystal Superalloy DD6, Acta Metall. Sin. (English Lett. 28 (2015) 1278–1285. doi:10.1007/s40195-015-0323-8.

[130] B. Ruttert, D. Bürger, L.M. Roncery, A.B. Parsa, P. Wollgramm, G. Eggeler, W. Theisen, Rejuvenation of creep resistance of a Ni-base single-crystal superalloy by hot isostatic pressing, Mater. Des. 134 (2017) 418–425. doi:10.1016/j.matdes.2017.08.059.

[131] B. Ruttert, O. Horst, I. Lopez-galilea, D. Langenkämper, A. Kostka, C. Somsen, J. V Goerler, M.A. Ali, O. Shchyglo, I. Steinbach, G. Eggeler, W. Theisen, Rejuvenation of Single-Crystal Ni-Base Superalloy Turbine Blades: Unlimited Service Life?, Metall. Mater. Trans. A. 49 (2018) 4262–4273. doi:10.1007/s11661-018-4745-6.

[132] O.M. Horst, B. Ruttert, D. Bürger, L. Heep, H. Wang, A. Dlouhý, W. Theisen, G. Eggeler, On the rejuvenation of crept Ni-Base single crystal superalloys (SX) by hot isostatic pressing (HIP), Mater. Sci. Eng. A. 758 (2019) 202–214. doi:10.1016/j.msea.2019.04.078.

[133] J. Pal, D. Srinivasan, E. Cheng, Effect of Rejuvenation Heat Treatment and Aging on the Microstructural Evolution in Rene N5 Single Crystal Ni Base Superalloy Blades, in: Superalloys 2016, John Wiley & Sons, Inc., 2016: pp. 285–291. doi:doi:10.1002/9781119075646.ch31.

[134] J. Komenda, P.J. Henderson, Growth of pores during the creep of a single crystal nickel-base superalloy, Scr. Mater. 37 (1997) 1821–1826. doi:10.1016/S1359-6462(97)00341-2.

[135] M. Simonetti, P. Caron, Role and behaviour of μ phase during deformation of a nickel-based single crystal superalloy, Mater. Sci. Eng. A. 254 (1998) 1–12. doi:10.1016/S0921-5093(98)00766-7.

[136] L.R. Liu, T. Jin, N.R. Zhao, X.F. Sun, H.R. Guan, Z.Q. Hu, Formation of carbides and their effects on stress rupture of a Ni-base single crystal superalloy, Mater. Sci. Eng. A. 361 (2003) 191–197. doi:10.1016/S0921-5093(03)00517-3.

[137] B. Von Grossmann, H. Biermann, H. Mughrabi, Measurement of service-induced internal elastic strains in a single-crystal nickel-based turbine blade with convergent-beam electron diffraction, Philos. Mag. A. 80 (2000) 1743–1757. doi:10.1080/01418610008219081.

[138] Z. Yao, M.A.E. Jepson, R.C. Thomson, C.C. Degnan, Microstructural evolution in a nickel based superalloy for power plant applications as a consequence of high temperature degradation and rejuvenation heat treatments, in: D. Gandy, J. Shingledecker (Eds.), Adv. Mater. Technol. Foss. Power Plants Proc. from Seventh Int. Conf. (EPRI 2013), ASM International, Waikoloa, Hawaii, USA, 2013: pp. 424–435.

[139] M. Lamm, R.F. Singer, The Effect of Casting Conditions on the High-Cycle Fatigue Properties of the Single-Crystal Nickel-Base Superalloy PWA 1483, Metall. Mater. Trans. A. 38 (2007) 1177–1183. doi:10.1007/s11661-007-9188-4.

[140] S.J. Moss, G.A. Webster, E. Fleury, Creep deformation and crack growth behavior of a single-crystal nickel-base superalloy, Metall. Mater. Trans. A. 27 (1996) 829–837. doi:10.1007/BF02649750.

[141] S. Steuer, P. Villechaise, T.M. Pollock, J. Cormier, Benefits of high gradient solidification for creep and low cycle fatigue of AM1 single crystal superalloy, Mater. Sci. Eng. A. 645 (2015) 109–115. doi:10.1016/j.msea.2015.07.045.

CHAPTER 2
EXPERIMENTAL PROCEDURES

Table of contents

Résumé : Les procédures expérimentales 51

2. 1. Materials 52

2. 2. Specimen preparation 52

2. 3. Tensile plastic deformation (pre-deformation) 53

2. 4. Heat treatment 54

2. 5. Creep tests 56

2. 6. Very high cycle fatigue tests 58

2. 7. Microstructure characterizations 59

References 59

RÉSUMÉ : LES PROCÉDURES EXPÉRIMENTALES

Deux superalliages monocristallins à base de Ni sont utilisés dans cette étude : le superalliage monocristallin de première génération AM1 [1,2] et le superalliage monocristallin de troisième génération CMSX-4 Plus [3]. Les barreaux monocristallins (désorientation de <001> moins de 10°) ont subi une mise en solution chez Safran Aircraft Engines.

Les barreaux monocristallins ont été usinés pour obtenir des éprouvettes d'une longueur de 14 mm et un diamètre de 4,0 mm [4], géométrie employée pour les pré-déformations et pour les essais de fluage. Avant la pré-déformation, la section utile de ces éprouvettes a été polie mécaniquement pour éliminer les contraintes résiduelles et les rayures héritées de l'usinage, et pour éviter la recristallisation de la surface lors des traitements thermiques ultérieurs. La pré-déformation a été introduite via une déformation en traction sous une vitesse de déformation de 5.0×10^{-4} /s à l'ambiante et à 750 °C et 950 °C. Les mêmes procédures ont été utilisées pour la pré-déformation à température ambiante du CMSX-4 Plus. Les éprouvettes pré-déformées ont été traitées thermiquement dans un four résistif dans l'air.

Des essais de fluage traction et des essais de fluage interrompus ont été réalisés sur l'AM1 et le CMSX-4 Plus sans et avec pré-déformation. Avant les essais de fluage, la surface de la section utile de l'éprouvette a été polie à nouveau et un thermocouple de type S a été soudé au milieu de la section utile. Ce thermocouple a été utilisé pour contrôler la température de l'essai de fluage. Un four à chauffage radiatif a été utilisé pour les essais de fluage. Des essais de fluage cyclés thermiquement ont aussi été réalisés en utilisant le même banc d'essai.

Des essais de fatigue gigacylique (VHCF) ont été effectués sur l'AM1, à l'air, à 1000 °C sur une machine à fatigue ultrasonore fonctionnant à 20 kHz [5]. Pour l'éprouvette de l'essai VHCF, une pré-déformation en traction a d'abord été appliquée sur une éprouvette lisse avec une conception spécifique, puis l'éprouvette a été usinée à nouveau pour obtenir une éprouvette de type diabolo. Les essais ont été effectués dans des conditions alternées (R = - 1) et avec charge moyenne appliquée (R = 0,5) avec diverses amplitudes de contraintes appliquées.

Après les traitements thermiques et les essais mécaniques, les microstructures des éprouvettes ont été observées au microscope électronique à balayage avec canon à effet de champ. L'orientation des échantillons a été analysée par diffraction des électrons rétrodiffusés (EBSD).

2. 1. Materials

In this study, two kinds of Ni-based superalloys were studied: the AM1 first generation single crystal (SX) superalloy [1,2] and the CMSX-4Plus third generation SX superalloy [3]. Their nominal compositions are given in Table 4.1. SX bars with a 14 mm diameter were casted by the Bridgman method in the foundry at Safran Aircraft Engines, Gennvilliers. Single crystals were in form of bars when received. They were solution treated at Safran Aircraft Engines using industrial furnaces.

Table 2.1 Chemical composition of alloys used in this research (wt.%, Ni bal.)

	Cr	Co	W	Mo	Ta	Al	Ti	Hf	Re	Disorientation from <001>
AM1	7.6	6.7	5.6	2.0	8.0	5.2	1.2	0.05		0-10°
CMSX-4Plus	3.5	10	6.0	0.6	8.0	5.7	0.85	0.1	4.8	6-10°

2. 2. Specimen preparation

Specimens used for pre-deformation and creep tests were machined from these SX bars (crystal disorientation from <001> within 10°) and SX plate by electron discharge machining followed by turning. Specimens have 14 mm gauge length and 4.0 mm diameter, which are similar to specimens used in previous studies at Institut Pprime (Figure 2.1) [4].

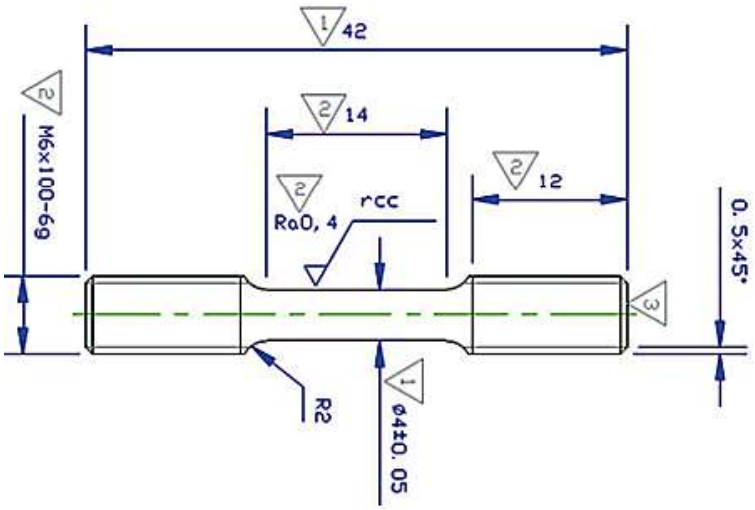

Figure 2.1. Tensile loading testing specimen

A tensile specimen was newly designed to apply pre-deformation for VHCF testing specimen. Designed geometry is shown in Figure 2.2(a) and the VHCF specimen used in other studies at Institut Pprime [5] is presented in Figure 2.2(b). Because the VHCF specimen does not have parallel gauge length, tensile testing specimen that covers all geometry must be machined first to be able to introduce a controlled plastic deformation using an extensometer. After a plastic strain is introduced in the middle of the gauge section, this tensile testing specimen was machined to have geometry suitable for VHCF test.

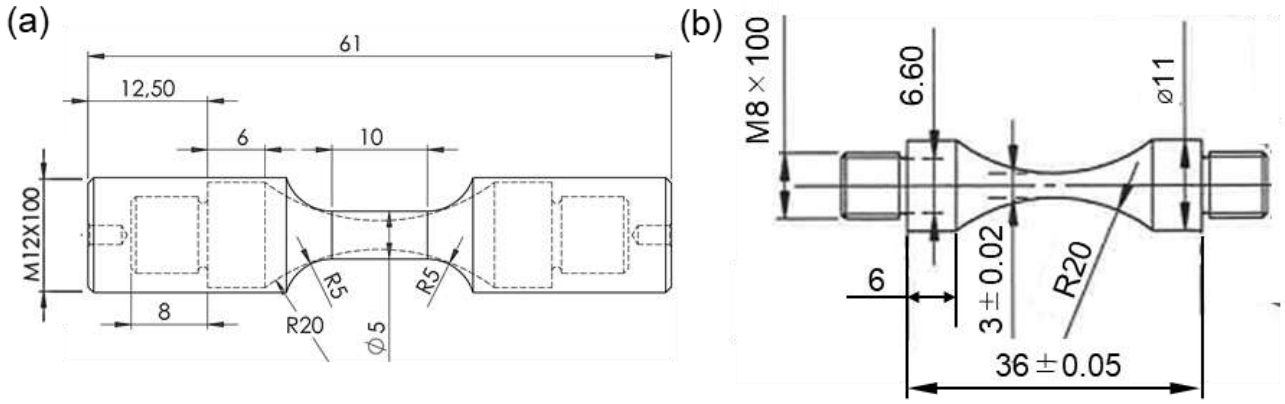

Figure 2.2. Geometries of cylindrical gauge specimen for tensile pre-deformation (a) and hourglass-shaped specimen for VHCF tests (b). Dotted lines in (a) are showing geometry of VHCF specimen in (b).

2. 3. Tensile plastic deformation (pre-deformation)

A plastic strain was introduced in the specimens by tensile plastic deformation at room-temperature to mimic the possible PD during processing of turbine components. Before tensile pre-deformation, surface of specimens' gauge section was mechanically polished using SiC abrasive paper grades from P320 to P4000 (grid size 42.5 µm to 5 µm in the Federation of European Producers of Abrasives (FEPA) standards) along longitudinal direction to remove residual stresses and scratches inherited from previous machining operations. Total depth of removed surface layer was between 0.1 to 0.05 mm after P4000 grade. This surface layer extraction is to avoid effect of residual stresses during pre-defamation and to avoid surface recrystallization during heat treatments. Plastic strain was introduced into a specimen with strain rate of 5.0×10^{-4} /s using electromechanical testing machine Instron 8562 (Figure 2.3). Strain was measured by extensometer positioned onto the specimen surface after applying initial tensile load of 100 N. Pre-deformation at 750 °C and 950 °C was performed using resistive heating furnace installed on the same testing machine. Temperature controllers were connected to thermocouples at the top and the bottom sides of the specimen grips. The furnace was stabilized for at least 30 min with an initial load of 100 N before attaching extensometer. Tensile deformation was paused as the specimen reached their plastic regime and then the tensile test was resumed until determined displacement to reach its target plastic strain. PD of AM1 at 950 °C was also conducted continuously from beginning to the target strain to avoid stress relaxation during pausing period. After specimen reaches target strain, load was decreased to zero immediately by manual control for avoiding stress relaxation.

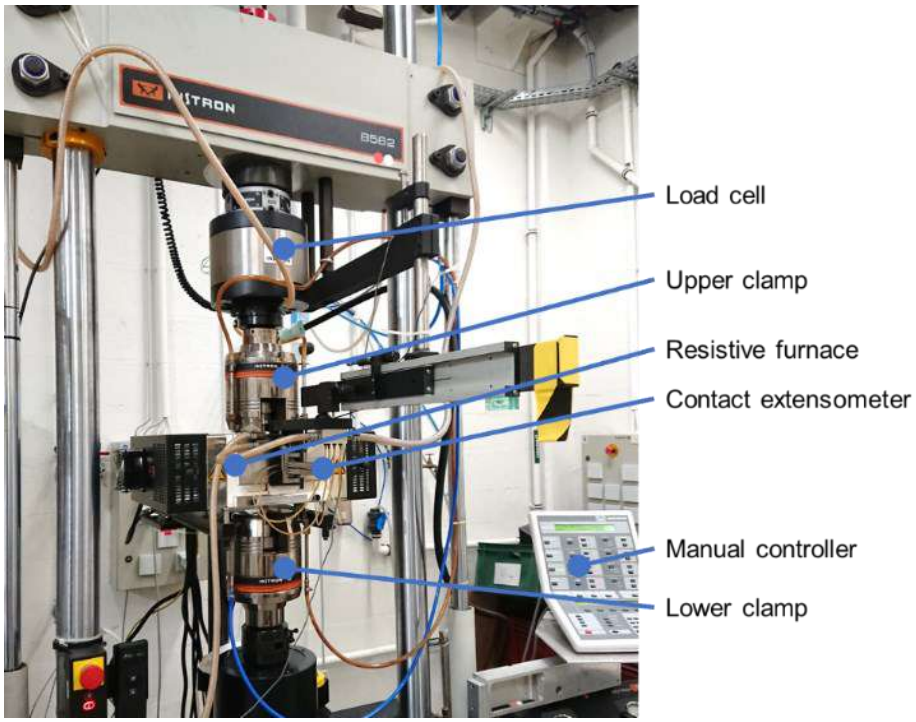

Figure 2.3. The electromechanical testing machine Instron 8562.

2. 4. Heat treatment

After the pre-deformation, gauge section of specimens was cut into pieces for microstructure analysis after different aging conditions. At least one cut surface of the pieces is along either (100) or (110) plane so that γ′ length on <001> direction can always be measured. The piece was placed in alumina crucible (Figure 2.4) when it was inserted into resistive furnace for heat treatments. The specimen for creep test or fatigue test was directly inserted into the furnace. Figure 2.5 shows resistive furnaces used in this study for heat treatments. Temperature was controlled by equipped controller and actual temperature inside the furnace was monitored by calibrated thermocouple placed in the center of the furnace, about 30mm from the bottom. Heat treatment conditions for all studied materials are listed on Table 2.2. Finally, naming list of specimens used in this study is listed on Table 2.3. Examples of specimens' thermal history are shown in Figure 2.6.

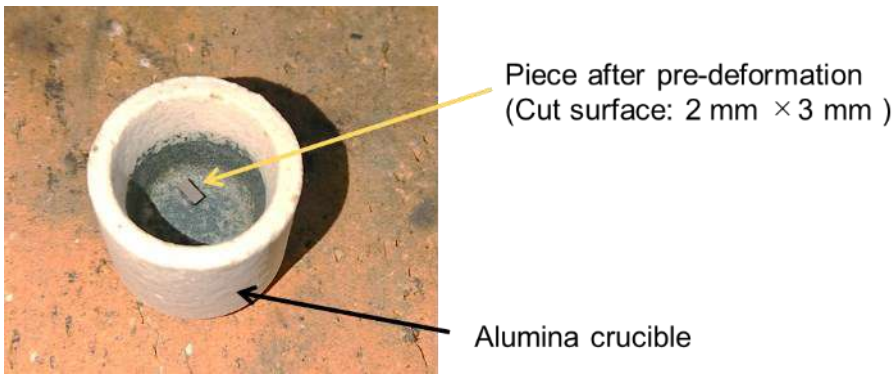

Figure 2.4. Piece after pre-deformation placed inside the alumina crucible.

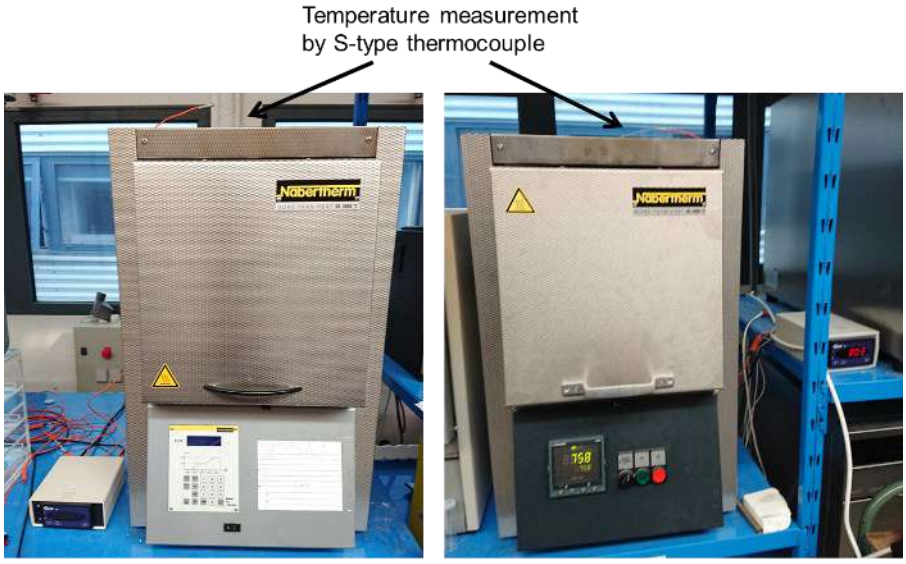

Figure 2.5. Resistive heat treatment furnaces used for heat treatments in air.

Table 2.2. Heat treatment conditions applied to the studied materials (AQ: air quench)

Solution treatment for AM1	1300 °C / 3 h (cooling rate greater than 300 °C/min)
Solution treatment for CMSX-4 Plus	1313 °C / 2 h → 1318 °C / 2 h → 1324 °C / 6 h → 1335 °C / 6 h / AQ
Aging treatments Type-1 (HT1)	1100 °C / 5 h / AQ + 870 °C / 16 h / AQ
Aging treatments Type-2 (HT2)	1165 °C / 6 h / AQ + 870 °C / 20 h / AQ

Table 2.3. Naming list of main specimens used in the experiments

Alloy	Specimen name	Preparation procedures
AM1	AM1-HT1	Solution treatment → Aging treatments Type-1
	AM1-RTPD-HT1	Solution treatment → PD at RT → Aging treatments Type-1
	AM1-HT1-RTPD	Solution treatment → Aging treatments Type-1 → PD at RT
	AM1-PD950-HT1	Solution treatment → PD at 950 °C → Aging treatments Type-1
	AM1-RTPD-Rejuv-HT1	Solution treatment → PD at RT → Rejuvenation treatment → Aging treatments Type-1
CMSX-4 Plus	C4P-HT1	Solution treatment → Aging treatments Type-1
	C4P-RTPD-HT1	Solution treatment → PD at RT → Aging treatments Type-1
	C4P-HT2	Solution treatment → Aging treatments Type-2
	C4P-RTPD-HT2	Solution treatment → PD at RT → Aging treatments Type-2
	C4P-RTPD-Rejuv-HT2	Solution treatment → PD at RT → Rejuvenation treatment → Aging treatments Type-2

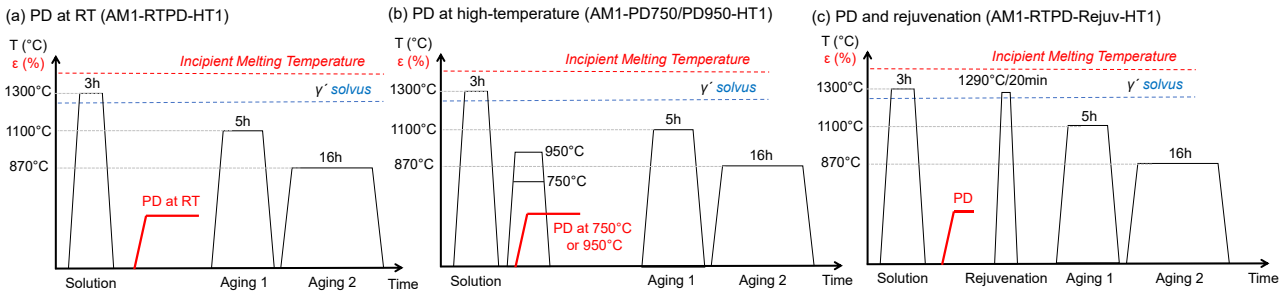

Figure 2.6. Examples of thermal history of specimens used in this study. (a) AM1-RTPD-HT1, (b) AM1-PD750/PD950-HT1, and (c) AM1-RTPD-Rejuv-HT1.

2. 5. Creep tests

Tensile creep rupture tests and creep interrupting tests were performed on AM1 and CMSX-4 Plus. Prior to the creep tests, surface of gauge section was polished again up to #4000 SiC abrasive paper along longitudinal direction to remove oxidized and γ′-depleted layers which could affect the specimen's creep behavior. Total depth of removed surface layer was between 0.1 to 0.05 mm. S-type thermocouple (wire diameter 0.35 mm) were spot-welded in the middle of the gauge section in accordance with TMF Code of Practice (Figure 2.7) [6]. It was connected to a Eurotherm 2408 temperature controller of a radiant furnace equipped on a Setra SF 2400 (serial no. 35) creep testing frame (Figure 2.8). Creep testing frame has a Keyence LS7070T contactless optical extensometer that detects distance between markers attached to each end of a specimen for strain measurement. Heating rate of 100 °C/min was used from 600 °C to a target temperature and at least 15 min as a soak time was used before applying the mechanical load. Creep tests with higher applied loads were performed using a Setra SF 2400 (serial no. 39) creep testing frame. This testing frame has a contact linear variable differential transformer (LVDT) sensor for a strain measurement. Other features such as temperature controlling method, radiant heating furnace, and heating procedures are same as the other testing frame. The list of creep tests performed in this study is on Table 2.4.

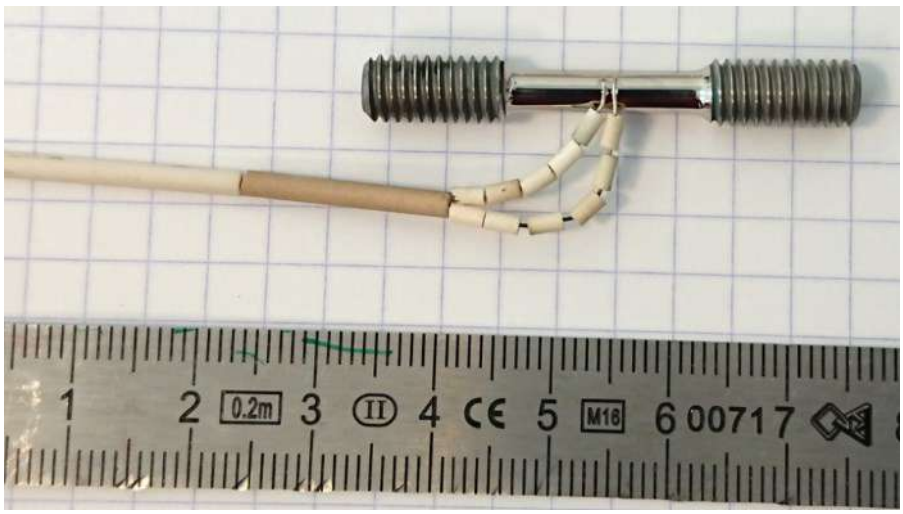

Figure 2.7. Creep testing specimen with S-type thermocouple welded in accordance with TMF Code of Practice [6].

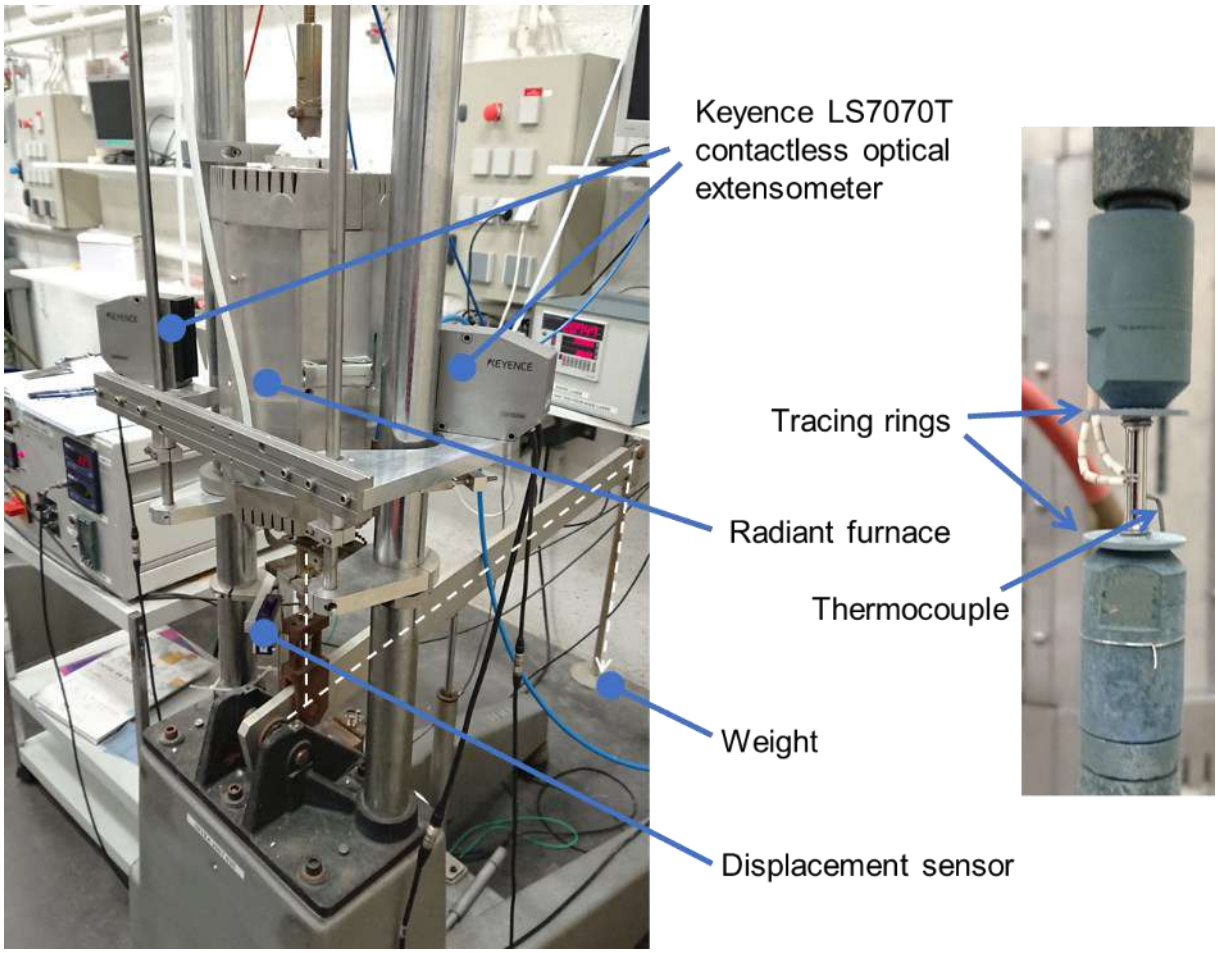

Figure 2.8. Setra SF 2400 (serial no. 35) creep testing frame equipped with Keyence LS7070T contactless optical extensometer.

Table 2.4. List of isothermal creep tests performed in this study

Alloys	Creep test conditions	Testing frame
AM1	1200 °C / 80 MPa	Setra SF 2400 (serial no. 35)
	1050 °C / 140 MPa	
	1050 °C / 200 MPa	
	950 °C / 300 MPa	
	850 °C / 500 MPa	Setra SF 2400 (serial no. 39)
CMSX-4 Plus	1250 °C / 60 MPa	Setra SF 2400 (serial no. 35)
	1150 °C / 110 MPa	
	1050 °C / 200 MPa	
	950 °C / 390 MPa	
	850 °C / 650 MPa	Setra SF 2400 (serial no. 39)

Non-isothermal creep tests were performed on AM1 and CMSX-4 Plus using same Setra SF 2400 (serial no. 35) creep testing frame. Creep loading was kept constant to have initial applied stress of 120 MPa for all testing period. Thermal cycling condition is presented in Figure 2.9.

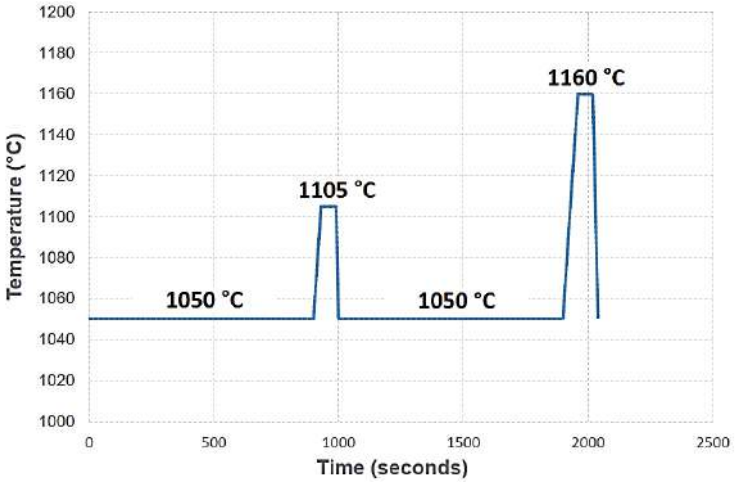

Figure 2.9. Temperature history diagram of a single cycle in the TC creep tests with applied stress of 120 MPa.

2. 6. Very high cycle fatigue tests

VHCF tests were performed on AM1 in air at 1000 °C using an ultrasonic fatigue machine working in the 20 ± 0.5 kHz frequency range. Specimen surface was mechanically polished prior to VHCF tests up to a mirror finish using 1 μm diamond suspension to remove residual stresses and to avoid any surface scratches that may lead to geometry-induced failure. During the experiment, specimen was induction heated and the temperature of the specimen center was controlled by a dual-wavelength infrared pyrometer. The specimen was held at 1000 °C for at least 35 min before starting the test in an aim to stabilize the emissivity from surface oxide. Tests were performed in fully reversed ($R = -1$) and positive ($R = 0.5$) ratio conditions with various applied stresses. Detail of the apparatus design and specific methods are explained in the reference [5,7].

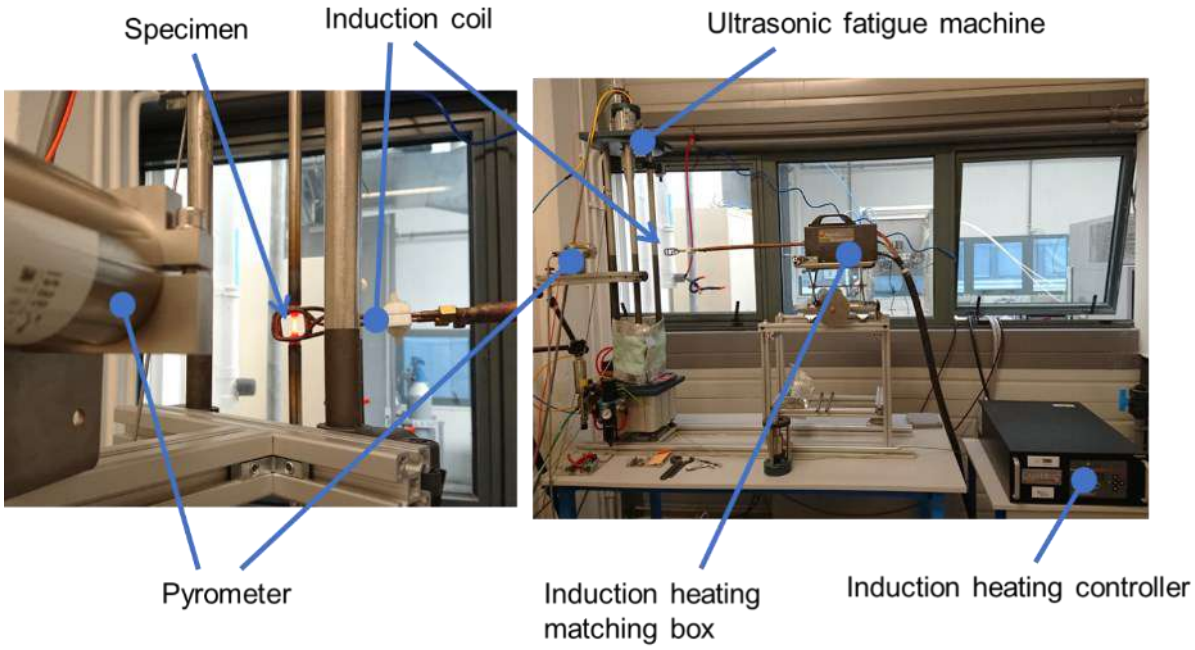

Figure 2.10. VHCF ultrasonic testing machine

2. 7. Microstructure characterizations

JEOL JSM-7000F field emission gun scanning electron microscope (FEG-SEM) equipped with backscatter electron detector were mainly used for characterization of specimens in this study. The appearance of the specimens was observed using the optical microscope. The FEG-SEM was operated at 25kV with work distance of 10-25 mm for microstructural observations. Heat-treated pieces were mounted into conductive resin and creep specimens were cut in plane of longitudinal direction. These specimens were mechanically polished down to 1-µm diamond powder spray and then the polished surface was chemically etched using aqua regia for 8-10 s at around 4 °C to reveal its γ/γ′ microstructure by selectively removing γ′ phase.

Electron backscatter diffraction (EBSD) scans were performed on creep ruptured and interrupted specimens using JEOL JSM-6100 SEM equipped with EDAX forward scatter detector controlled by TSL OIM software. Specimens for the EBSD analysis were prepared by mechanical polishing down to 1-µm diamond powder spray followed by electrochemical polishing using Struers LectroPol-5 system operated at 45 V for 6 s with a solution of perchloric acid, 2-butoxyethanol, and methanol (Struers electrolyte A3) kept at room temperature and flow level of 14 (Figure 2.11).

Figure 2.11. Struers LectroPol-5 system with electrochemical polishing parameters shown in on the screen.

References

[1] J.H. Davidson, A. Fredholm, T. Khan, J.-M.C.F. Theret, Single-crystal alloy has a nickel base matrix, FR 2557598 / US 589 4693280, 1986. https://patents.google.com/patent/FR2557598B1/en.

[2] F. Hanriot, G. Cailletaud, L. Remy, Mechanical behavior of a nickel-base superalloy single crystal, in: Winter Annu. Meet. Am. Soc. Mech. Eng., ASME, Atlanta, GA, USA, 1991: pp. 139–150.

[3] J.B. Wahl, K. Harris, CMSX-4 Plus Single Crystal Alloy Development, Characterization and Application Development, in: Superalloys 2016, John Wiley & Sons, Inc., 2016: pp. 25–33. doi:10.1002/9781119075646.ch3.

[4] J. Cormier, M. Jouiad, F. Hamon, P. Villechaise, X. Milhet, Very high temperature creep behavior of a single crystal Ni-based superalloy under complex thermal cycling conditions, Philos. Mag. Lett. 90 (2010) 611–620. doi:10.1080/09500839.2010.489887.

[5] A. Cervellon, J. Cormier, F. Mauget, Z. Hervier, VHCF life evolution after microstructure degradation of a Ni-based single crystal superalloy, Int. J. Fatigue. 104 (2017) 251–262. doi:10.1016/j.ijfatigue.2017.07.021.

[6] P. Hähner, E. Affeldt, T. Beck, H. Klingelhöffer, M. Loveday, C. Rinaldi, Final version of the Validated Code-of-Practice for Strain-Controlled Thermo-Mechanical Fatigue Testing, Luxembourg: Office for Official Publications of the European Communities, 2006.

[7] A. Cervellon, Propriétés en fatigue à grand et très grand nombre de cycles et à haute température des superalliages base nickel monogranulaires, ISAE-ENSMA Ecole Nationale Supérieure de Mécanique et d'Aérotechique, PhD Thesis, 2018.

CHAPTER 3
MICROSTRUCTURE EVOLUTION AFTER PRE-DEFORMATION, AND REJUVENATION TREATMENT

Table of contents

Résumé : Évolution de la microstructure après la pré-déformation, et traitement thermique de restauration 63

3. 1. Introduction 65

3. 2. Tensile pre-deformation of experimental materials 65

3. 3. Microstructure evolution during aging treatments of AM1 after pre-deformation at room-temperature 67

3. 3. 1. Standard aging treatments 67

3. 3. 2. Aging treatments at different temperatures 71

3. 3. 3. Effect of inheriting internal strain from room-temperature pre-deformation on the microstructural behavior during high-temperature exposure 75

3. 4. Microstructures of AM1 after higher-temperature pre-deformation 80

3. 5. Effect of chemical compositions on the microstructure evolution behavior 87

3. 6. Rejuvenation treatment on the pre-deformed materials 92

3. 6. 1. Determination of rejuvenation treatment conditions 92

3. 6. 2. Effects of deformation methods on the rejuvenation capability 98

3. 7. Summary 99

References 100

RÉSUMÉ : ÉVOLUTION DE LA MICROSTRUCTURE APRÈS LA PRÉ-DÉFORMATION, ET TRAITEMENT THERMIQUE DE RESTAURATION

Ce chapitre se concentre sur l'évolution de la microstructure des matériaux pré-déformés lors des traitements thermiques de revenu suivants.

Une déformation plastique a été appliquée aux superalliages monocristallins base-Ni AM1 à différentes températures (ambiante, 750 °C et 950 °C). La limite d'élasticité de l'AM1 après traitement de mise en solution était la plus élevée à 750 °C et la plus faible à 950 °C. À 750 °C, le glissement dévié des dislocations est actif, ce qui augmente la limite d'élasticité. À 950 °C, la baisse progressive de la limite d'élasticité est le résultat de la déformation provoquée par le contournement des dislocations aux interfaces γ/γ'. Ce sont les mécanismes de déformation par traction typiques des superalliages base-Ni à forte fraction volumique γ′ [1,2].

La déformation plastique par traction selon l'orientation ⟨001⟩ à des températures inférieures à 750 °C introduit des bandes de glissement le long des plans cristallins {111} dans un superalliage monocristallin. Au cours du traitement thermique de revenu à 1100 °C, les précipités γ′ évoluent plus rapidement à proximité des bandes de glissement que dans les zones éloignées de la bande. L'évolution de la microstructure a été influencée par la déformation élastique locale autour des bandes de glissement [3]. Elle a montré une morphologie similaire à la mise en radeaux γ′ dans les superalliages base-Ni, dans des directions parallèle et transversale à l'axe de chargement. Dans la bande à microstructure grossière, des dislocations interfaciales γ/γ′ sont observées. L'image de contraste de diffraction dans l'axe du faisceau [101] a montré que la majorité des dislocations sont distribuées dans la matrice γ et que ce sont des dislocations de type 1/2⟨101⟩{111}.

Un léger grossissement directionnel a été observé après une pré-déformation à 950 °C et les traitements thermiques de revenu suivants. La relaxation des déformations de cohérence a été provoquée par des dislocations interfaciales introduites pendant la pré-déformation par le mécanisme de contournement [4,5]. Comme la déformation plastique était distribuée uniformément, l'évolution de la microstructure a été observée dans toute la section de l'éprouvette. L'amplitude de la coalescence orientée a diminué et a été perturbée par l'augmentation de la déformation plastique. La réduction de la taille des radeaux avec l'augmentation de la déformation plastique dans le matériau pré-déformé à 950 °C est probablement due à la plus grande densité de dislocations stockée dans la matrice γ pendant la déformation plastique. Les dislocations interfaciales ont ralenti le grossissement des précipitations au cours des traitements de revenu.

Le superalliage monocristallin CMSX-4 Plus a également été pré-déformé à température ambiante et les traitements thermiques de revenu ont été appliqués pour comparer son comportement microstructural avec celui de l'AM1. En effet, après les traitements de revenu, les précipités γ′ dans les bandes à microstructure grossière de CMSX-4 Plus étaient plus grossiers que les précipités loin de ces bandes de glissement. Des dislocations interfaciales ont également été observées dans le CMSX-4 Plus après le premier revenu. La densité de dislocations visibles sur les images MEB a diminué dans l'AM1 après le deuxième revenu, alors qu'elles

étaient encore observables dans CMSX-4 Plus. Les précipités dans la bande de CMSX-4 Plus étaient moins anisotropes que ceux dans les bandes de pré-déformation pour l'AM1. Globalement, l'effet de pré-déformation sur la microstructure du matériau était mineur pour le CMSX-4 Plus Ce phénomène est dû aux caractéristiques de déformation des matériaux au cours de la pré-déformation. Comme l'AM1 a une plus grande résistance au cisaillement des précipités γ′ à température ambiante, on en déduit qu'une contrainte interne plus élevée est stockée sur chaque bande de glissement. En outre, le CMSX-4 Plus présente une plus grande densité de bandes de glissement après une déformation en traction à température ambiante pour la même amplitude de pré-déformation que l'AM1. En d'autres termes, l'AM1 transporte un glissement plus élevé sur chaque bande de glissement comparativement au CMSX-4 Plus. Par conséquent, l'énergie de déformation élastique et plastique stockée dans une bande de glissement étant plus faible pour le CMSX-4 Plus, cela réduit l'effet de la pré-déformation sur sa microstructure.

Le traitement thermique de restauration a été appliqué à l'AM1 pré-déformé à différentes températures (ambiante, 750 °C et 950 °C) pour démontrer son efficacité sur la microstructure. Il a également été testé pour le CMSX-4 Plus pré-déformé à température ambiante. En outre, le traitement de restauration contribue à comprendre comment les différentes structures de dislocations affectent la microstructure à des températures proches de la température de solvus et en conditions supersolvus

Le traitement thermique de restauration a permis de régénérer la microstructure de l'AM1 après une déformation plastique à température ambiante inférieure à 1,86 % ou une déformation plastique à 950 °C inférieure à 0,87 %. Il a également fonctionné avec succès pour CMSX-4 Plus avec une déformation plastique de 0,79 %. Les conditions de restauration appropriées sont de 20 min à 1290 °C pour l'AM1 et de 1 h à 1330 °C pour le CMSX-4 Plus. Ces deux conditions sont légèrement inférieures aux (dernières) températures de traitement de mise en solution car les matériaux ont déjà été homogénéisés et la solvus globale est plus basse.

L'échantillon AM1 pré-déformé à 950 °C avec une déformation plastique plus grande (2,17 %) a présenté une recristallisation après le traitement de restauration à une température sub-solvus (à 1280 °C). La recristallisation a commencé à la surface de l'échantillon (assistée par l'oxydation) et le cristal originel est resté intact dans les espaces interdendritiques. Cette recristallisation est provoquée par la dissolution des précipités γ′ assistée par les dislocations stockées. Si la déformation macroscopique est de même amplitude, la densité des dislocations stockées augmente à mesure que la température de déformation augmente [6]. Par conséquent, le risque de recristallisation au cours de la restauration est plus faible si la pré-déformation a été appliquée à une température plus basse.

3. 1. Introduction

This chapter focuses on the microstructure evolution that was observed in the pre-deformed material from the precedent results. PD was introduced to various Ni-based SX superalloys at RT and higher-temperatures to understand the effect of different pre-straining procedures. From an industrial point of view, rejuvenation treatment for microstructure restoration was tested to the pre-deformed materials at different conditions.

3. 2. Tensile pre-deformation of experimental materials

Typical tensile curves of pre-deformation (plastic strain ~0.8 %) are shown in Figure 3.1. The highest tensile strength at 750 °C and decreased tensile strength at 950 °C of as-solutioned AM1 compared to RT are common characteristics that can be explained by γ/γ′ misfit and deformation processes in a Ni-based superalloy consisting of the FCC disordered matrix and ordered $L1_2$ structure [1,2,7]. Tensile curve of AM1 at 950 °C is showing mild transition from elastic regime to plastic regime meaning that plastic deformation had occurred by typical dislocation by-passing mechanism of Ni-based superalloys. Two separated curves shown in Figure 3.1 are PD at 950 °C paused at yield point for about 1 min and resumed until the target plastic strain (curve labeled as AM1-PD950(B)). Dotted line shows stress relaxation and creep deformation occurring during the pause. In the as-solutioned state, AM1 has higher yield strength compared to CMSX-4 Plus at RT which is consistent with the tensile properties after full heat-treatment [8]. The highest yield stress of AM1 after aging treatments (AM1-HT1-RTPD) is a result of optimized size, shape, and volume fraction of γ′ precipitates [8–10]. Young's modulus and yield strength at 0.05% plastic strain are shown in Table 3.1. Specimens with higher or lower plastic strain were obtained by simply interrupting tensile deformation later or earlier.

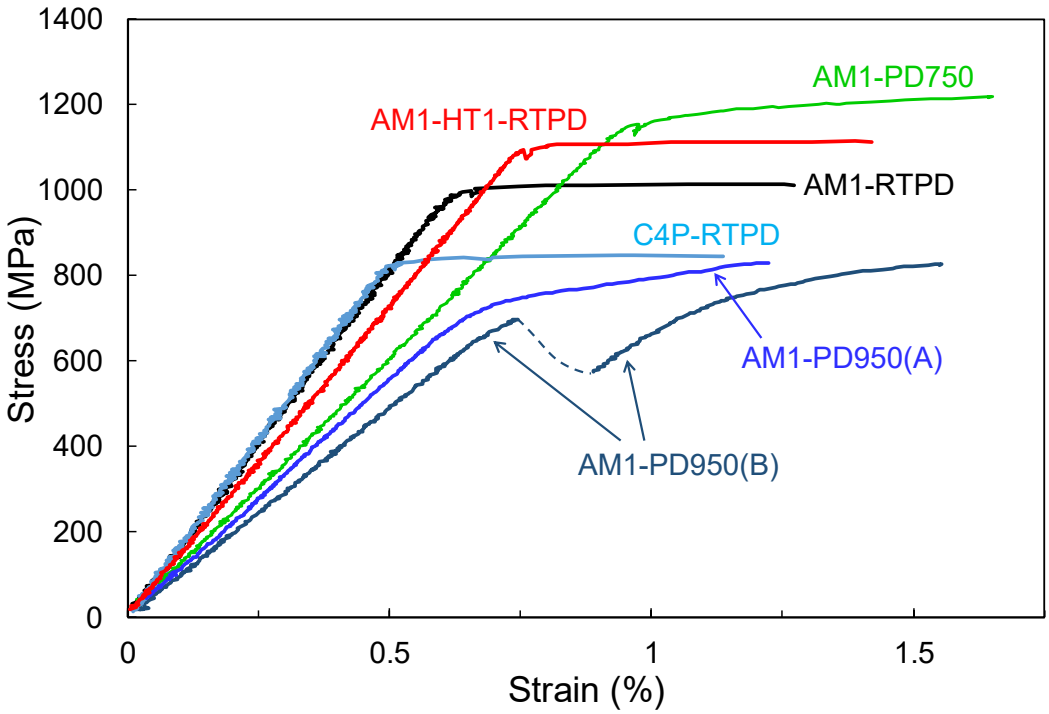

Figure 3.1. Tensile curves of pre-deformation applied to as-solutioned AM1 at RT (AM1-RTPD), at 750 °C (AM1-PD750), at 950 °C (AM1-PD950), and at RT after aging treatments Type-1 (AM1-HT1-RTPD), and applied to as-solutioned CMSX-4 Plus at RT (C4P-RTPD). Stress relaxation and creep during pause of tensile deformation are expressed as dashed line for AM1 pre-deformed at 950 °C (AM1-PD950(B)).

Table 3.1. Tensile properties of pre-deformation applied to AM1 and CMSX-4 Plus specimens

Alloy	Specimen	Young's modulus (GPa)	Yield stress /0.05% (MPa)
AM1	AM1-RTPD	155	997
	AM1-PD750	122	1155
	AM1-PD950	114	735
	AM1-HT1-RTPD	146	1094
CMSX-4 Plus	C4P-RTPD	167	833

Appearances of cylindrical specimens after pre-deformation are shown in Figure 3.2 with the density of observable slip bands in the determined section labeled. These images were obtained by an optical microscope. Although C4P-RTPD has the lowest plastic strain, it has the highest density of observable slip bands of all. This analysis presents a trend of increasing yield strength with decreasing density of observable slip bands in the cylindrical surface. Higher yield strength means that the resistance to the precipitation shearing is higher, which suggests that more energy is required for the activation of a slip system and to form a slip band. Because slip bands are strongly marked in AM1-HT1-RTPD compared to others, that the local slip on each single band is suggested to be higher. In other words, when the materials are deformed at RT (i.e. within the γ′-shearing regime) and have equivalent macro strain, material with lower yield strength has a greater number of slip bands introduced but slip on each band is less. This is confirmed by microstructures shown in Figure 3.3. In AM1-RTPD, slip band is visible only in surface layer where deformation is more pronounced by free surface intersection. On the other hand, deformation band was observed in the cylindrical center of AM1-HT1-RTPD.

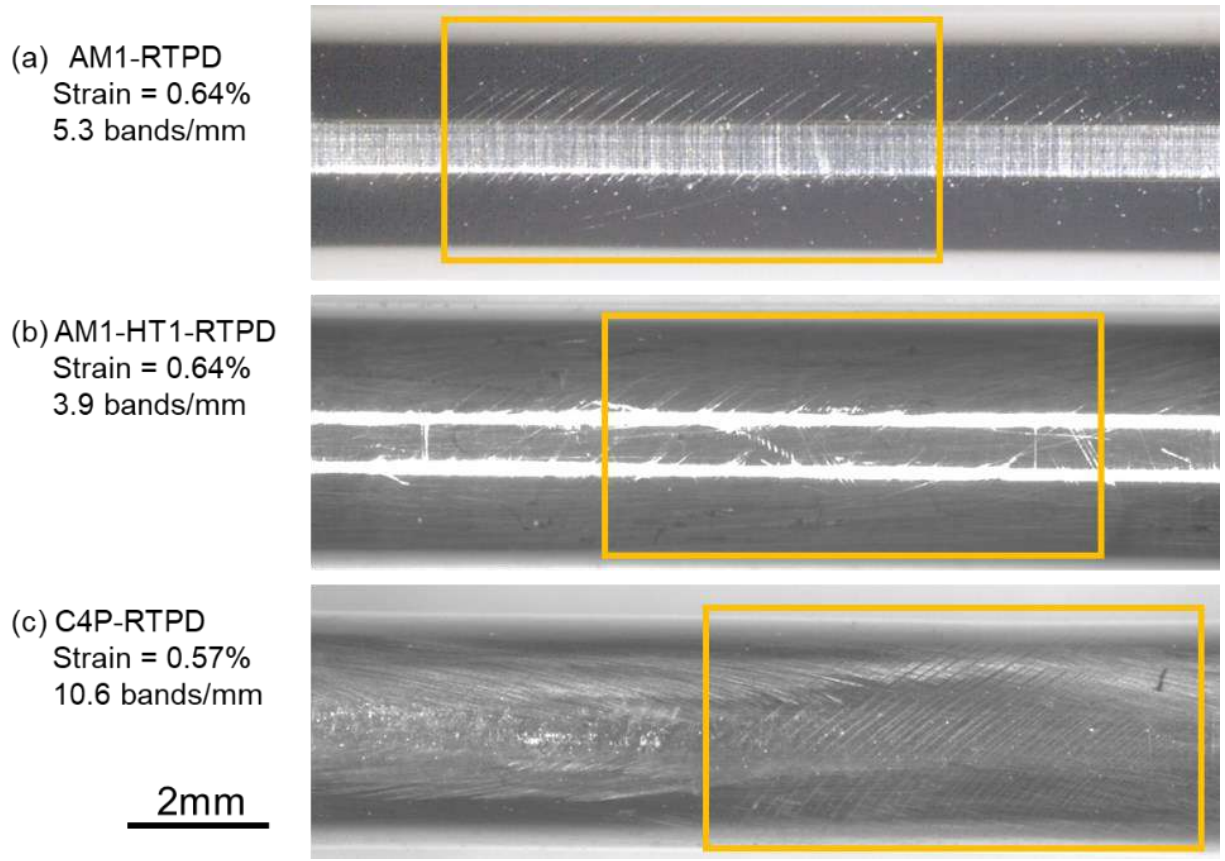

Figure 3.2. Appearance of cylindrical specimens after pre-defamation. Applied plastic strain and density of visible slip bands within the length shown by a box are labeled.

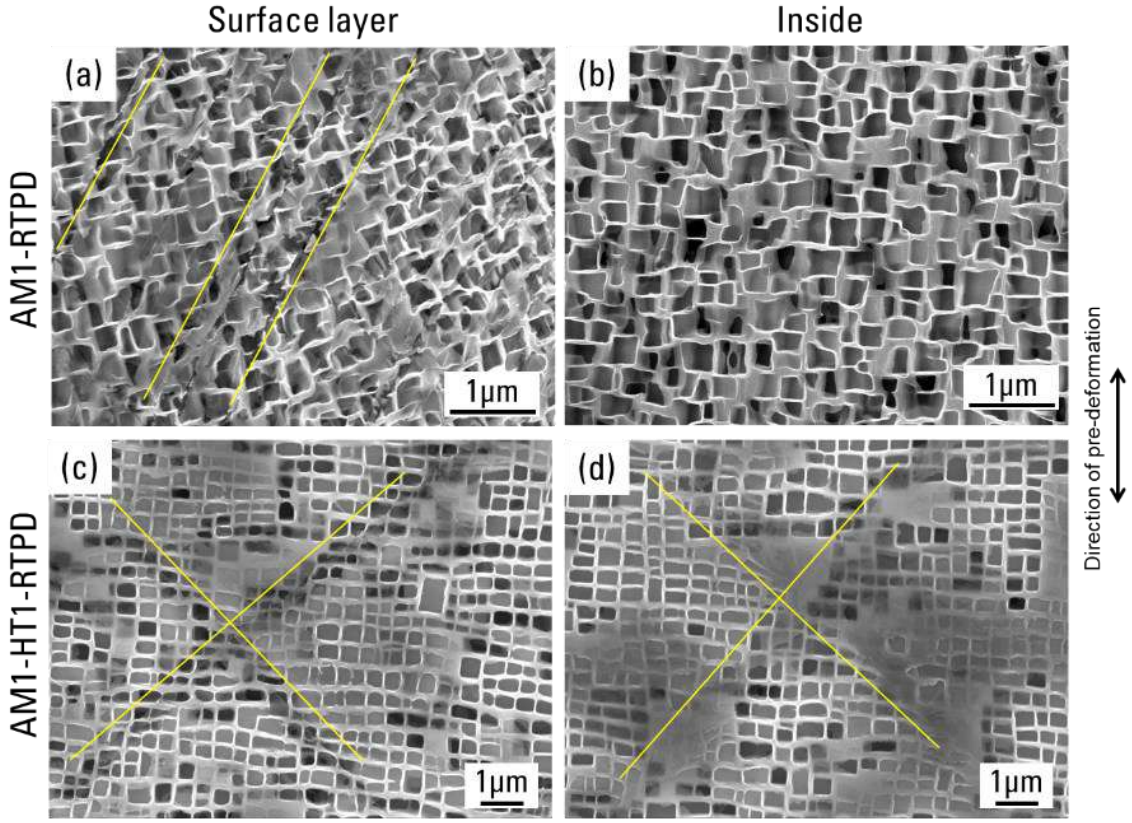

Figure 3.3. Microstructure of AM1 specimens after pre-deformation at RT, without any subsequent aging treatments.

3. 3. Microstructure evolution during aging treatments of AM1 after pre-deformation at room-temperature

3. 3. 1. Standard aging treatments

In order to understand the processes of microstructural evolution, special attention was paid to the mechanism of γ′ precipitation coarsening during heat treatments. Microstructures of AM1 pre-deformed after solution treatment followed by first stage of aging treatment with various aging time were observed in (110) plane and are shown in Figures 3.4 and 3.5. The bands are hardly visible after aging treatment less than 1 h at 1100 °C (Figures 3.4 (a-c)). After annealing from 1 h until 5 h at 1100 °C, the bands become thicker and γ′ precipitations in the band have coarsened directionally in either parallel or perpendicular to the direction of pre-deformation with increasing duration of aging time (Figures 3.5 (d-f)). Sakaguchi et al. have reported similar microstructure coarsening around former slip plane in CMSX-4 pre-strained at RT and aged at 1080 °C [3,11]. Outside the band, precipitates are forming typical cuboidal structure.

Microstructures of the same specimens with additional second stage aging at 870 °C for 16 h are shown in Figures 3.6 and 3.7. Similar to the microstructures after first stage aging, the bands appeared clearly after 1 h in first stage treatment. Size of γ′ precipitation in an area out of the band (i.e. without effect of the PD) after second stage treatment is nearly the same to that of after first stage. Width of the affected bands had not changed significantly in between first and second stage. By recalling to EBSD-IPF maps shown in Figure 1.39, the microstructure coarsened band after two aging treatments has neither measurable lattice rotation, nor recrystallization.

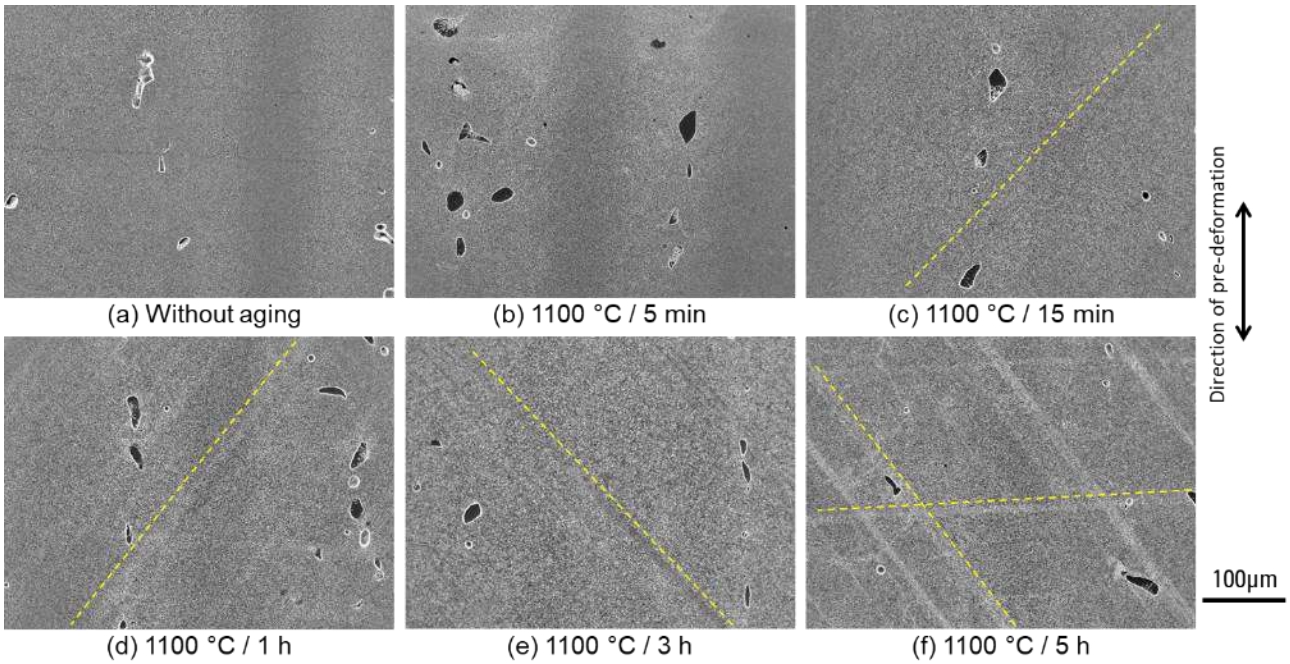

Figure 3.4. Microstructures of pre-deformed specimen after solution treatment, in (110) plane without aging and after 5 min to 5 h of the first stage aging treatment at 1100 °C.

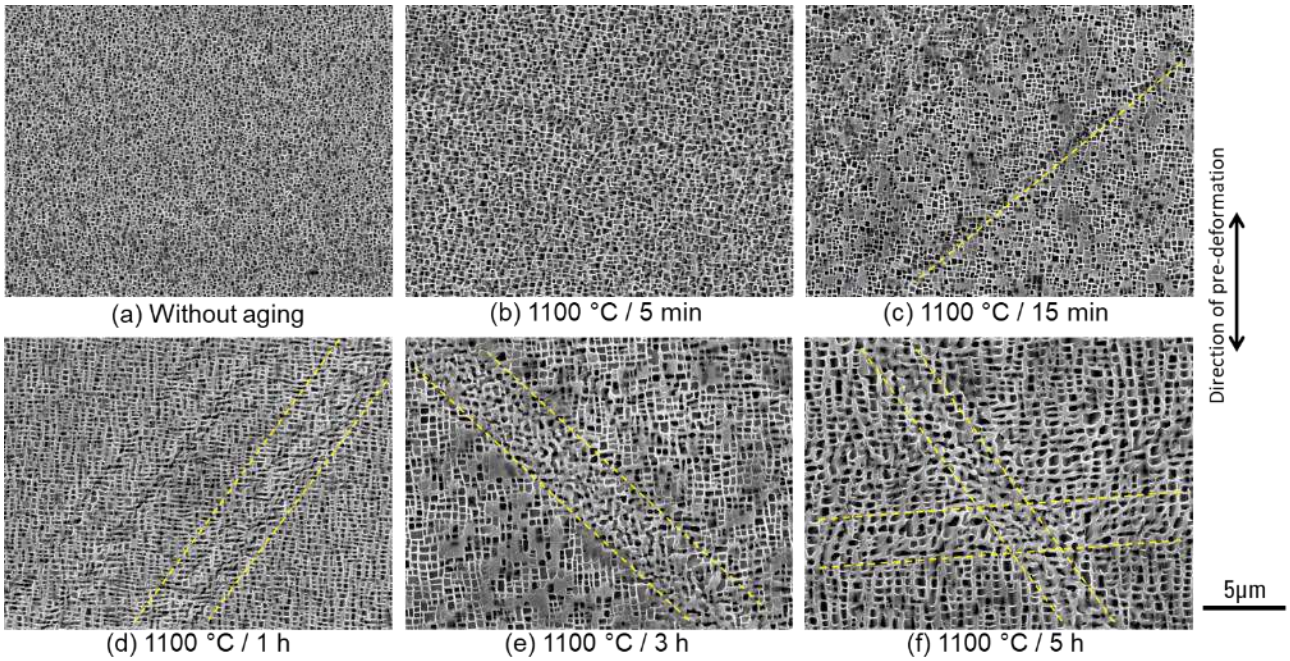

Figure 3.5. Microstructures of pre-deformed specimen after solution treatment, in (110) plane without aging and after 5 min to 5 h of the first stage aging treatment at 1100 °C, in higher magnification.

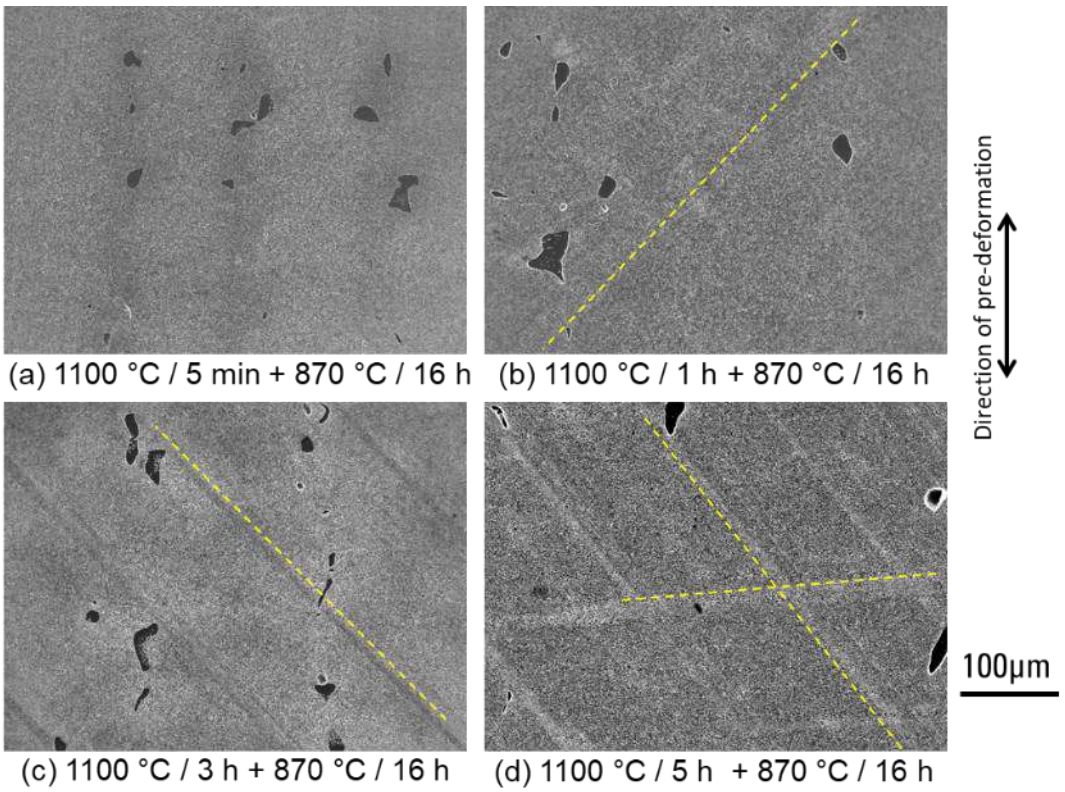

Figure 3.6. Microstructures of pre-deformed specimen after solution treatment, in (110) plane after 5 min to 5h of the first stage aging treatment at 1100 °C followed by the second stage aging treatment at 870 °C for 16 h.

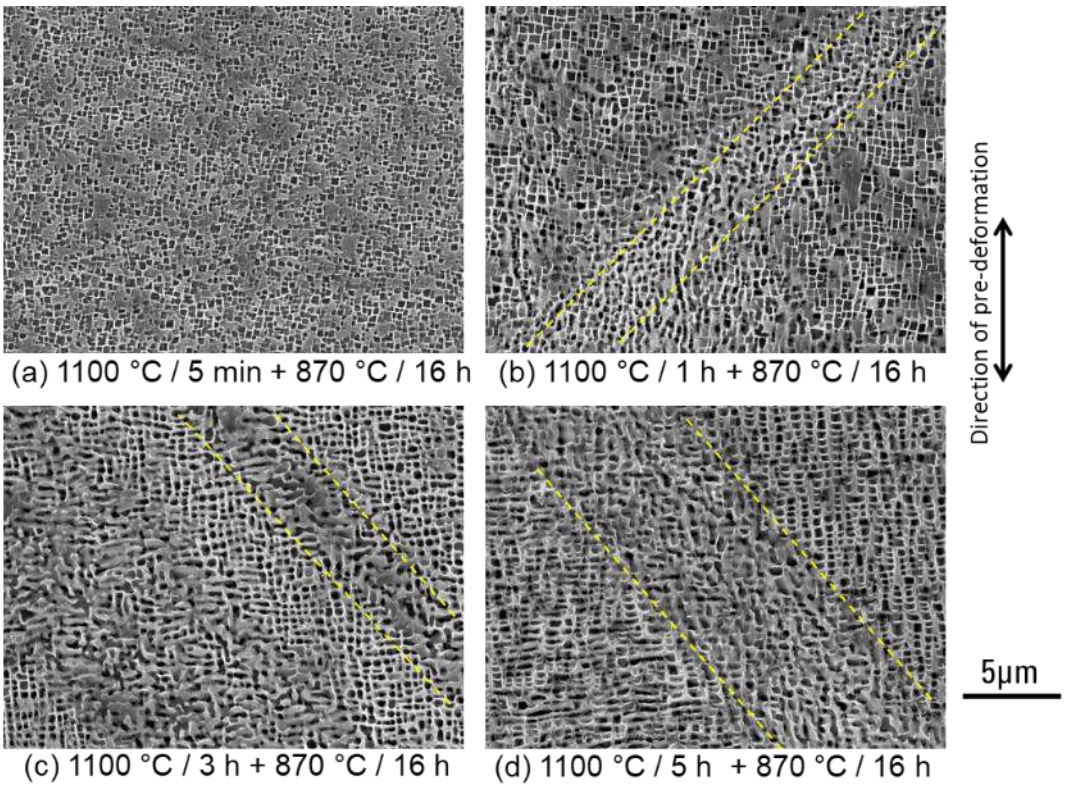

Figure 3.7. Microstructures of pre-deformed specimen after solution treatment, in (110) plane after 5 min to 5 h of the first stage aging treatment at 1100 °C followed by the second stage aging treatment at 870 °C for 16 h, in higher magnification.

Precipitate width along the ⟨001⟩ direction (direction of PD) was measured for the typical cuboidal structure (outside of the bands) and for the affected area (inside of the bands) to have quantitative explanation. At least 100 precipitates were measured for the quantification. Results after first stage aging (up to 5 h at 1100 °C) and varying first stage plus second aging (870 °C for 16 h) are shown in Figures 3.8(a) and (b), respectively. This analysis shows that the γ′ precipitate inside the bands has faster coarsening rate than that of outside after 1 hour of first stage aging. The coarsening rate is not dependent on the magnitude of introduced strain, which confirms that the magnitude of the strain changes the number of slip bands introduced in the specimen's gauge section, but probably magnitude of slip on each band is weakly affected. Coarsening direction of precipitate was similar to previous study on the effect of RT plastic deformation and subsequent aging (1080 °C for 20 h) introduced after all heat treatment procedures [1]. The effect of second aging treatment has less impact on the evolution of γ′ precipitate. Since volume fraction of γ′ phase is higher at 870 °C, width of γ phase matrix channel has become thinner making overall γ′ size bigger (Figure 3.8(b)). The volume fractions of γ′ phase in AM1 are ~50% at 1100 °C and 60-70% at 870 °C (Figure 3.9(a)) [12–14].

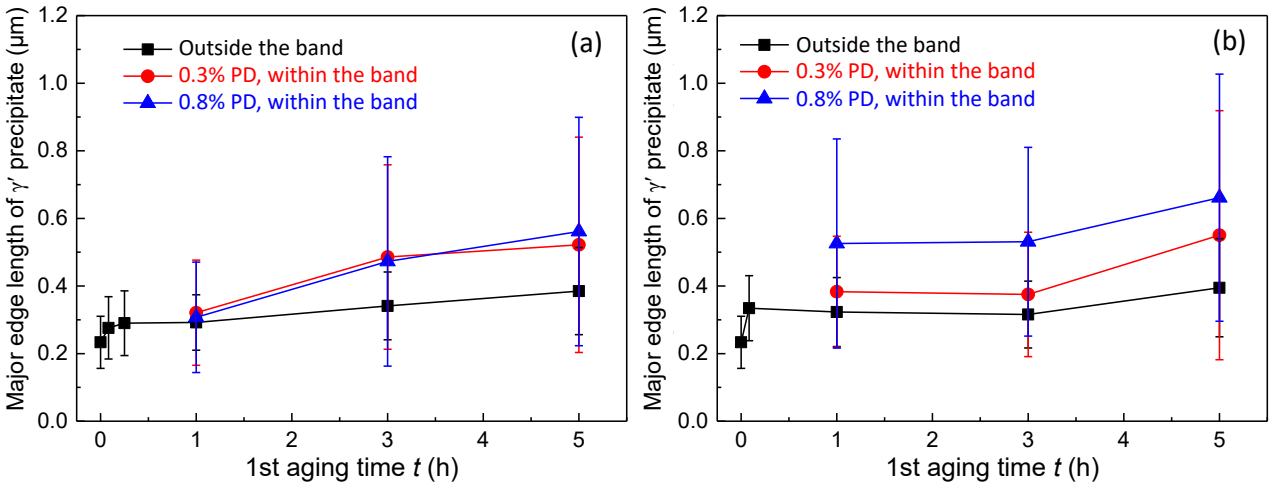

Figure 3.8. Evolution of γ′ precipitate maximum edge length as a function of aging time at 1100 °C without (a) and with (b) second aging at 870 °C for 16 h.

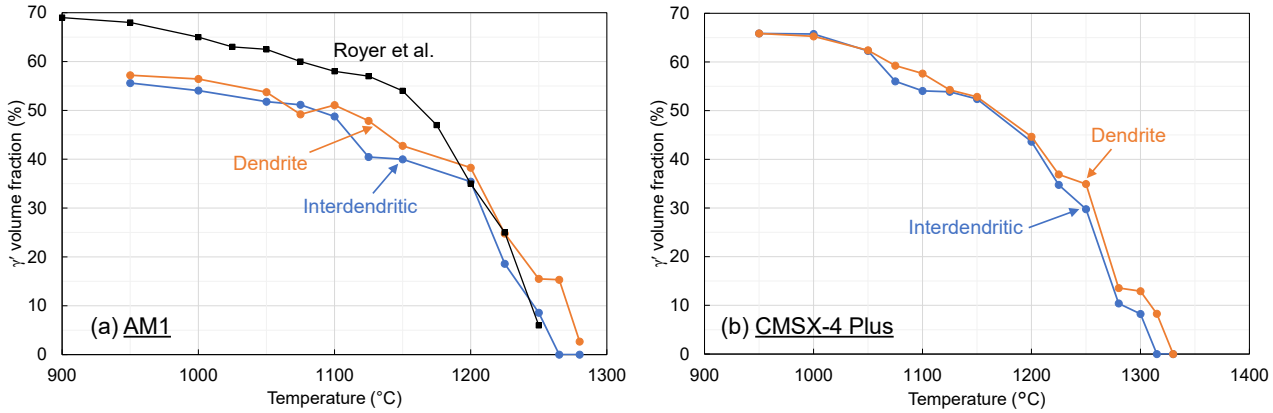

Figure 3.9. Volume fraction of γ′ phase as a function of temperature for AM1 (a) and CMSX-4 Plus (b). Data plotted for dendrite and interdendritic area of both materials were provided by J. Cormier and L. Despres (internal characterizations at Institut Pprime). Data from the work by Royer et al. [12] are plotted in (a).

3. 3. 2. Aging treatments at different temperatures

Different aging treatments (at 950°C for 5 h, standard condition for AM1 at 1100°C for 5 h, and standard condition for CMSX-4 Plus at 1165°C for 6 h) were applied to AM1 with pre-deformation (~0.8%) and microstructures are shown in Figure 3.10. In a higher magnification image, dislocation networks are observed at γ/γ′ interfaces after standard first stage aging (white arrows in Figure 3.10(h)). This indicates that plastic activity in the matrix around slip band had occurred during this first stage at 1100 °C to relax local stress, thus, precipitate size was mostly determined at this stage (Figure 3.8). The octagonal dislocation network seen in this interface is similar to that developed during high temperature/low stress creep of SX superalloy [15].

After aging at 950 °C for 5 h, the band traces become apparent in the higher magnification, but the precipitate size is not clearly different from others outside the band. Still, the band is distinguishable from others because some precipitates are coalesced as indicated by ovals in Figure 3.10(g) and less refection of electrons in this area appears as darker image contrast. Dislocation grooves have not yet appeared after aging at 950°C for 5h.

The microstructure coarsened area was difficult to distinguish in AM1 with aging condition of CMSX-4 Plus. For this generation of alloy with low content of refractory elements, plasticity is very active and effect of PD can spread to larger area. Also, the lower γ′ volume fraction at higher temperature facilitates recovery of dislocations by climb activity. These made it difficult to locate the band after aging at 1165 °C for 6 h. Precipitate scale image after aging at 1165 °C for 6 h in Figure 3.10(f) shows thick and connected γ phase, some coalesced and elongated γ′ precipitates, and tertiary γ′ in the matrix. Dislocation grooves are found in the interface of γ matrix and secondary γ′ precipitates (white arrows in Figure 3.10(i)). Thick γ matrix is a result of very low volume fraction of γ′ phase at 1165°C (~35%) [12,14].

Microstructures of AM1 after PD at RT with full aging treatments in two conditions (AM1 type and CMSX-4 Plus type) are shown in Figure 3.11. Traces of interfacial dislocations were still observed in the band after both conditions (Figure 3.11(g, h)), but their quantity had decreased from the microstructures after first stage aging treatment (Figure 3.11 (h, i)). After HT2 (CMSX-4 Plus type treatment), almost all area presented directional coarsening like structure as shown in Figure 3.11(c). The bands were distinguishable because of very large γ′ precipitates in Figure 3.11(f) that formed by eliminating thinner channels during large volume fraction increase from 1165 °C to 870 °C. Figure 3.11(e) is area with less effect of PD, but this area has large γ′ precipitates and thick γ matrix with secondary γ′ precipitated during cooling from very high temperature aging at 1165 °C.

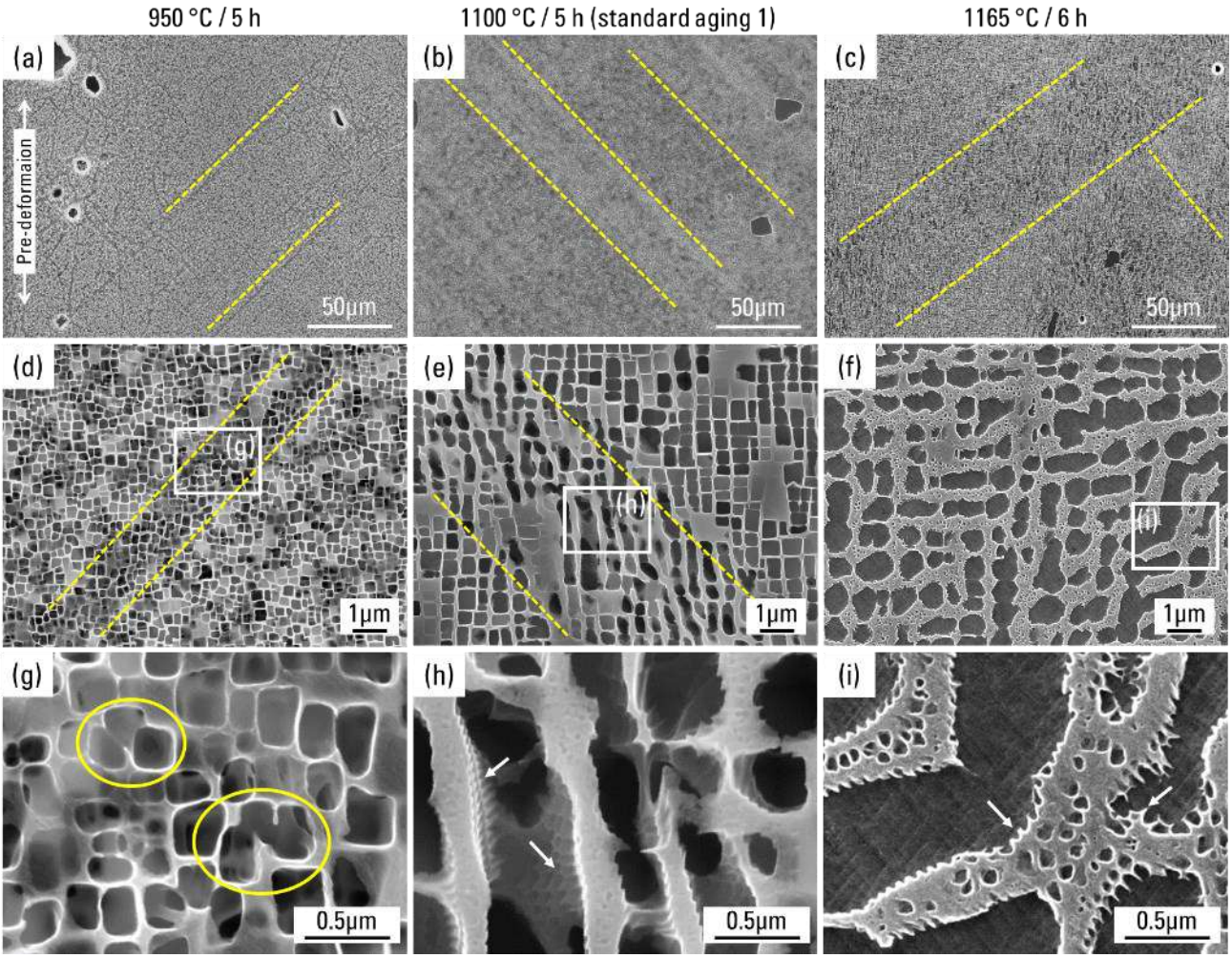

Figure 3.10. Microstructure of AM1 with PD at RT (~0.8%) followed by different aging treatments. Aging conditions are at 950 °C for 5 h (a, d, g), standard for AM1 at 1100 °C for 5 h (b, e, h), and standard for CMSX-4 Plus at 1165 °C for 6h (c, f, i). Dotted lines are indicating microstructure coarsened band. (g-f) are magnified image of rectangles in (d-i), respectively. Ovals in (g) are showing coalesced precipitates. White arrows in (h, i) are pointing at dislocation traces at the γ/γ′ interfaces.

Precipitate size in different directions are measured for the images in Figures 3.10 and 3.11 by the rotational intercept method (RIM) using in-house RIM-X software developed by Caccuri et al. [16,17]. Results of RIM analyses in Figure 3.12 give the values different from Figure 3.8, especially for specimens with PD. RIM method measures through all width within the image and this also counts thin edge length of irregular γ′ precipitates observed after PD and aging treatments. Therefore, error bars are a better representation for the distribution of the precipitate size. Figures 3.13 and 3.14 are showing average size for all the angles intercepted in this measurement that represents both precipitate size and shape. If the precipitate is cuboidal, rose diagram presents near square shape with 45° rotation (Figure 3.13(a)). When a rose diagram has one preferential direction (90°/270° in Figure 3.13(b) and 0°/180° in Figure 3.14(c)), it means the precipitates in the analyzed image have tendency of either N-type or P-type directional coarsening. Figures 3.13(c) and 3.14(b) are showing oval with 45° rotation, which means precipitates are elongated in both horizontal and vertical (⟨100⟩ and ⟨001⟩) directions equally.

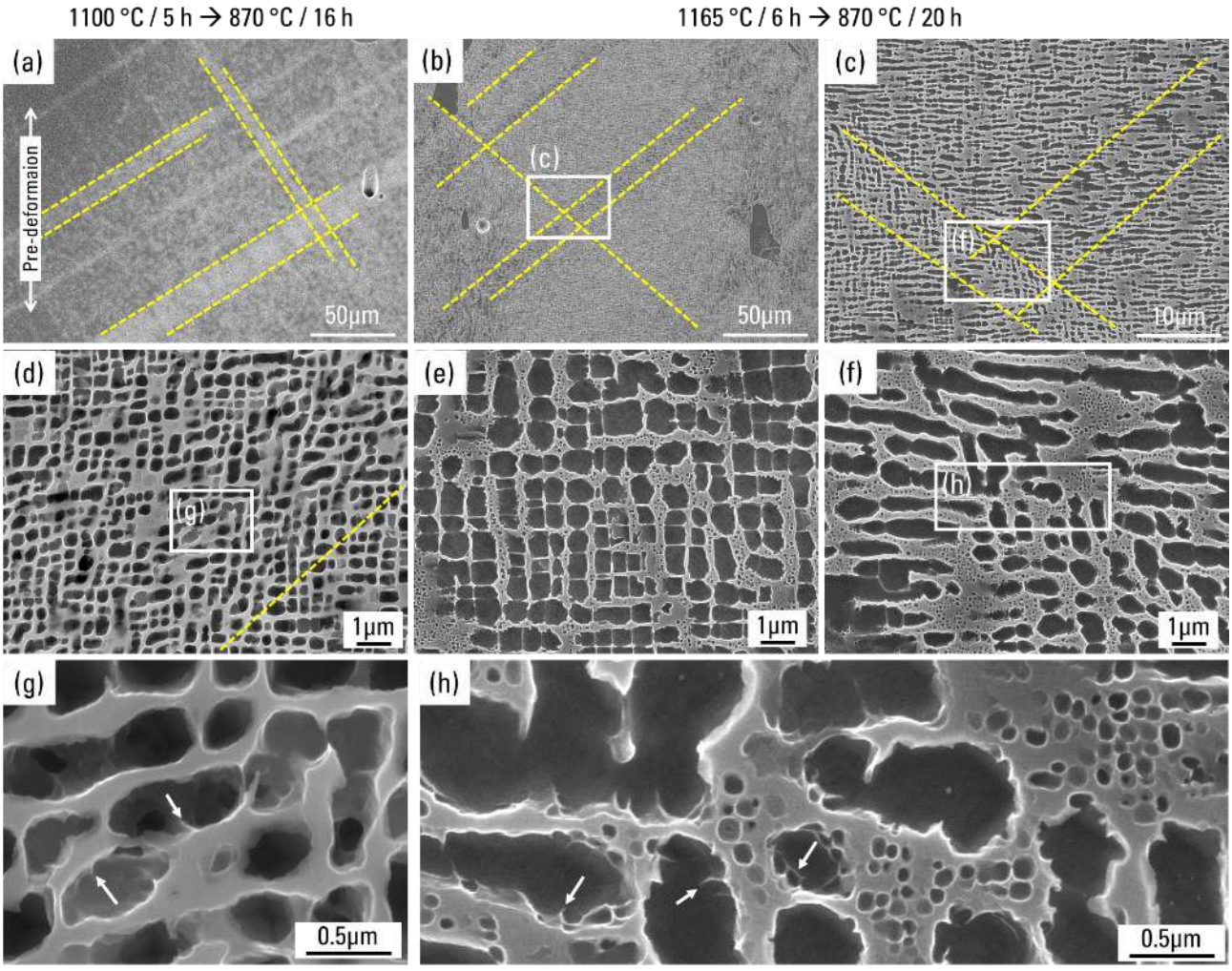

Figure 3.11. Microstructure of AM1 with PD at RT (~0.8%) followed by different aging treatments. Aging conditions are standard for AM1 at 1100 °C for 5 h + 870 °C for 16 h (a, d, g), and standard for CMSX-4 Plus at 1165 °C for 6 h + 870 °C for 20 h (b, c, e, f, h). Dotted lines are indicating microstructure coarsened band. (c, f, g, h) are magnified image of rectangles in (b, c, d, f), respectively. White arrows are pointing at dislocation traces at the γ/γ′ interfaces.

The secondary aging treatment in both HT1 and HT2 are adjusting volume fraction of the γ′ precipitates and they do not contribute so much to the precipitation coarsening. Different shapes (horizontal/vertical preferential direction and tilted oval) are presented to show that two types of microstructure coarsened bands were observed at the former slip plane during aging treatments. When either N-type or P-type directional coarsening dominantly appears, major precipitate length (90° of RTPD + Aging 1 in Figure 3.12) is much longer than other directions and has a large deviation of their size expressed as error bar.

Standard HT1 was applied to AM1 with PD at RT after 5 h at 950 °C and observed microstructures are presented in Figure 3.15. This treatment was intended to see effect of lower temperature aging on the dislocation movement during subsequent standard aging treatments. Dislocation traces appeared after aging at 1100 °C for 5 h (Figure 3.15(c)) and their quantity decreased after aging at 870 °C for 16 h (Figure 3.15(d)) similarly to the standard HT1 without additional treatment at 950 °C. This suggests that additional aging has almost no effect in microstructural behavior nor dislocation structure. Remaining elastic strain around former slip band was similarly released during aging at 1100 °C.

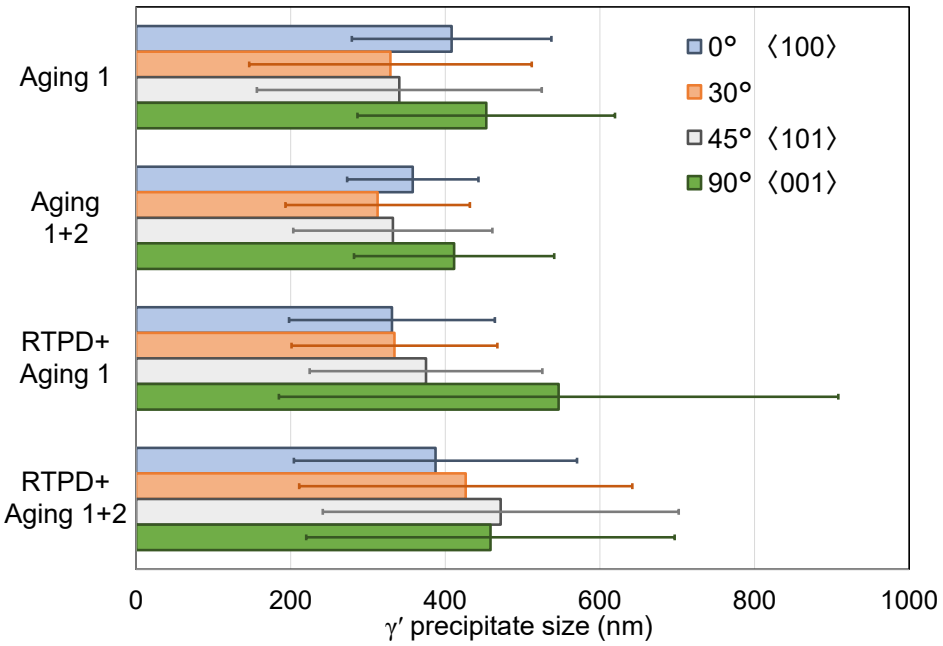

Figure 3.12. Result of RIM analysis using RIM-X software on AM1 with PD at RT. Average size of γ′ precipitate is shown as solid bars and error bars are standard deviation.

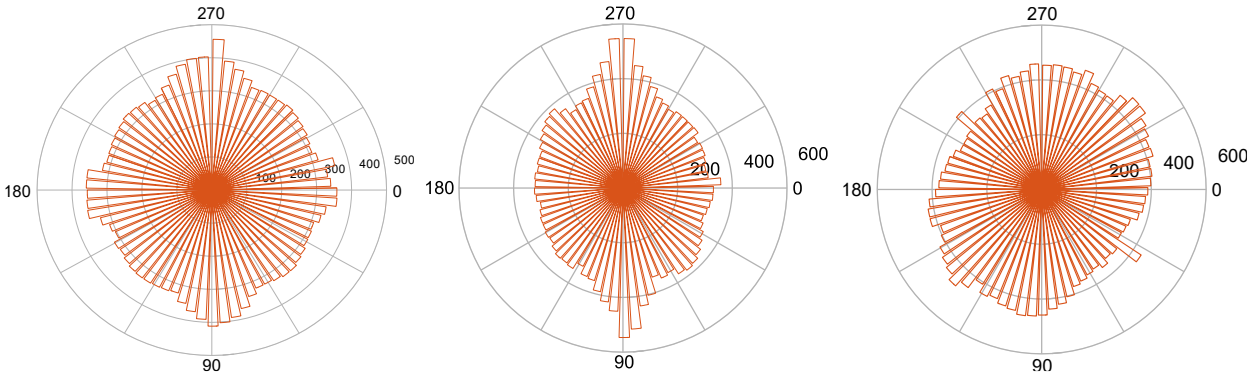

Figure 3.13. Rose diagram of γ′ precipitate size obtained by RIM-X analyses on AM1 with PD at RT followed by aging treatments of standard AM1 condition (HT1). At 1100 °C for 5 h for aging 1 and at 870 °C for 16 h for aging 2. Concentric scale in nm.

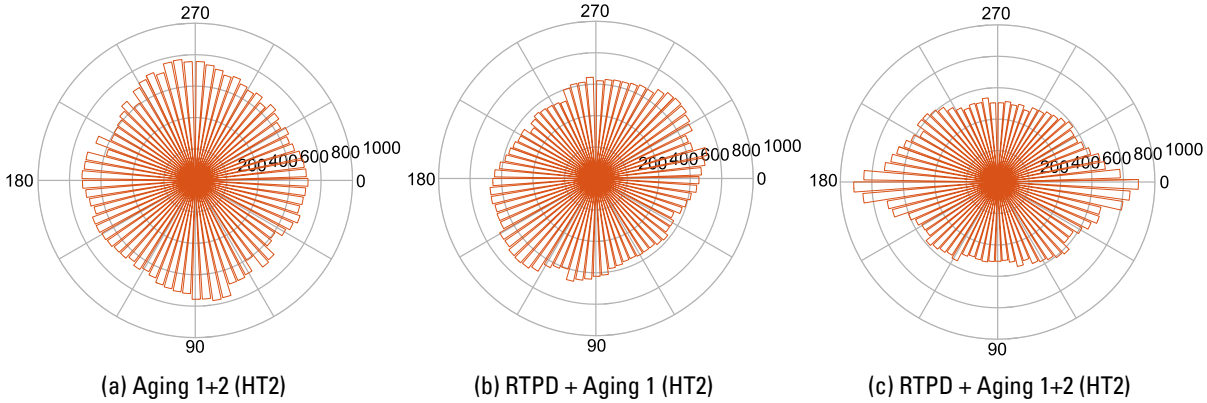

Figure 3.14. Rose diagram of γ′ precipitate size obtained by RIM-X analyses on AM1 with PD at RT followed by aging treatments of standard CMSX-4 Plus condition (HT2). At 1165 °C for 6 h for aging 1 and at 870 °C for 20 h for aging 2. Concentric scale in nm.

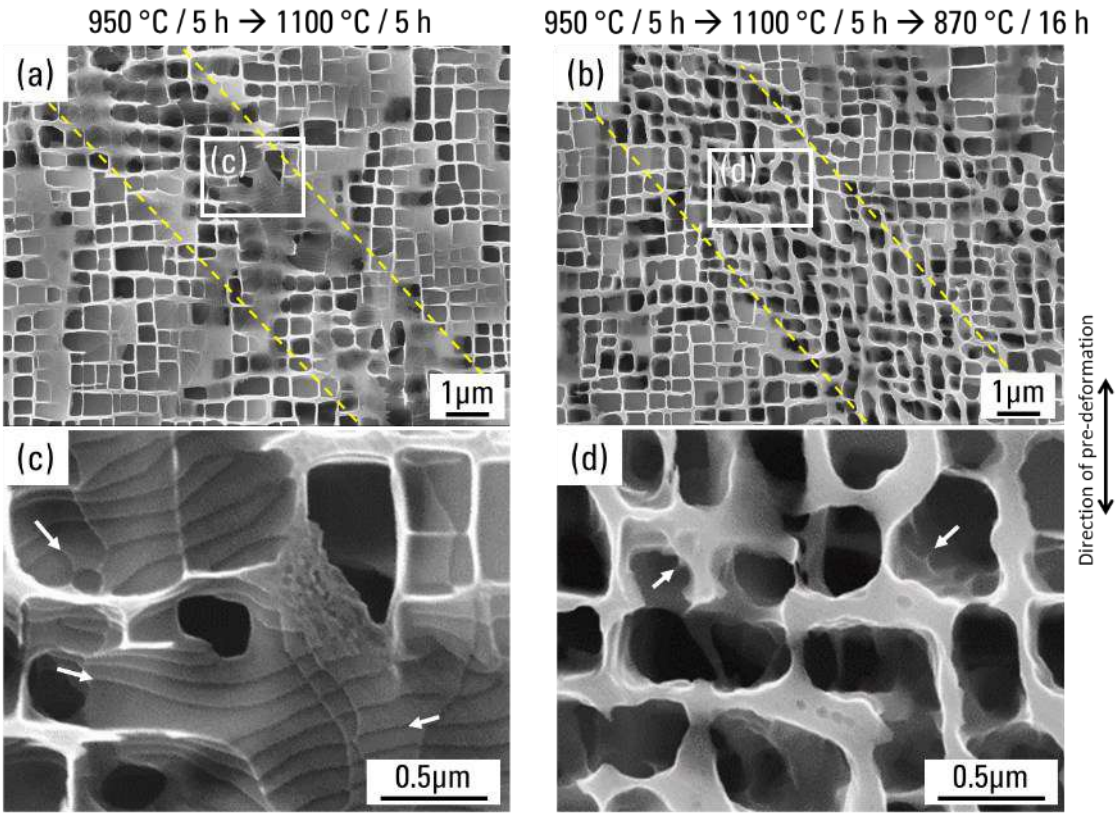

Figure 3.15. Microstructure of AM1 with PD at RT (~0.8%) followed by 5 h / 950 °C + standard first (a, c) and second (b, d) aging treatments. Dotted lines are indicating microstructure coarsened band. (c, d) are magnified image of rectangles in (a, b), respectively. White arrows are pointing at dislocation traces at the γ/γ′ interface.

3. 3. 3. Effect of inheriting internal strain from room-temperature pre-deformation on the microstructural behavior during high-temperature exposure

Dislocation structures are discussed in this section for understanding how the pre-deformation affected the precipitate's evolution behaviors during aging treatments.

Deeply-etched microstructure of AM1 in the microstructure coarsening band is presented in Figure 3.16. This image was obtained by observation from ~(100) plane, but slightly tilted so that (001) plane of the precipitates can be observed. Interfacial dislocation traces parallel to ⟨010⟩ direction in the (001) face of the precipitates are probably the misfit dislocations that decreases elastic strain between two phases (Figure 3.16 A). Dislocation traces appearing as 45° tilt are 60° mixed [101] dislocations that are in the process of gliding into [010] edge dislocation or climbing to form dislocation network (Figure 3.16 B) [18]. Examples of octagonal and square dislocation networks are indicated as C and D in Figure 3.16, respectively. These dislocation structures are similar to that reported by Gao et al. in the second-generation Ni-based SX superalloy DD5 after aging at 1100 °C for 20 h [19].

Diffraction contrast images of the area consists of the microstructure coarsened band in AM1-PD-HT1 obtained by scanning transmission electron microscopy (STEM) with different beam conditions are shown in Figure 3.17. Majority of the dislocations decreases their contrast in the image obtained by two-beam condition shown in Figure 3.17(b). These dislocations are determined to be on {111} system that are in γ matrix and are mobile by glide and climb (also indicated as B in Figure 3.16). Ram et al. reported [101] and [010] dislocations

developed by dislocation emission from low-angle boundaries of SX superalloy under high-temperature exposure with very small or no stress, and the dislocations migrate within the distance of 5 μm from the low-angle boundaries [20]. The source of dislocations in Figure 3.17 can be such emission from slip band created by APB shearing of 1/2⟨110⟩ pair dislocations during tensile pre-deformation. However, the microstructure coarsened band appearing as dislocation band in the STEM image has homogeneous density within its width. Dislocation source is not clearly identified like in the case of emission from low-angle boundaries [20]. This implies that formation of dislocations in the microstructure coarsened band is driven by the internal elastic strain that locally exists in the vicinity of the slip band. It also means that precipitate coarsening proceeds by the mechanism similar to other Ni-based superalloys with very high γ/γ′ interfacial misfit strain, under non-loading thermal exposure [18,19].

By comparing the SEM images of pre-deformed AM1 after first (Figure 3.9) and second (Figure 3.10) aging treatments, number of dislocation grooves decreased after secondary stage. The number of dislocation grooves intersecting a line drawn toward [001] direction was counted for both conditions, after the first and the secondary aging treatments, and the dislocation spacings are 100 nm and 132 nm, respectively. Dislocation spacing of 96 nm was similarly obtained by counting intersection of dislocation line and [001] intercepting line in Figure 3.17(a), which is comparable to the value obtained from SEM image after PD and first stage aging. Most of dislocations in Figure 3.17 are in the matrix and overall density is assumed to be higher. Therefore, it is unrealistic to think that dislocations had just disappeared after secondary aging. It is more reasonable to assume that the dislocation structure was mostly constructed during the first stage aging treatment and it had not changed drastically during secondary stage, which is in accordance with the fact that precipitate shapes were maintained and only their size increased due to the increasing volume fraction of γ′ phase. If dislocation had more mobility, directional coarsening and construction of dislocation network should have proceeded further [18].

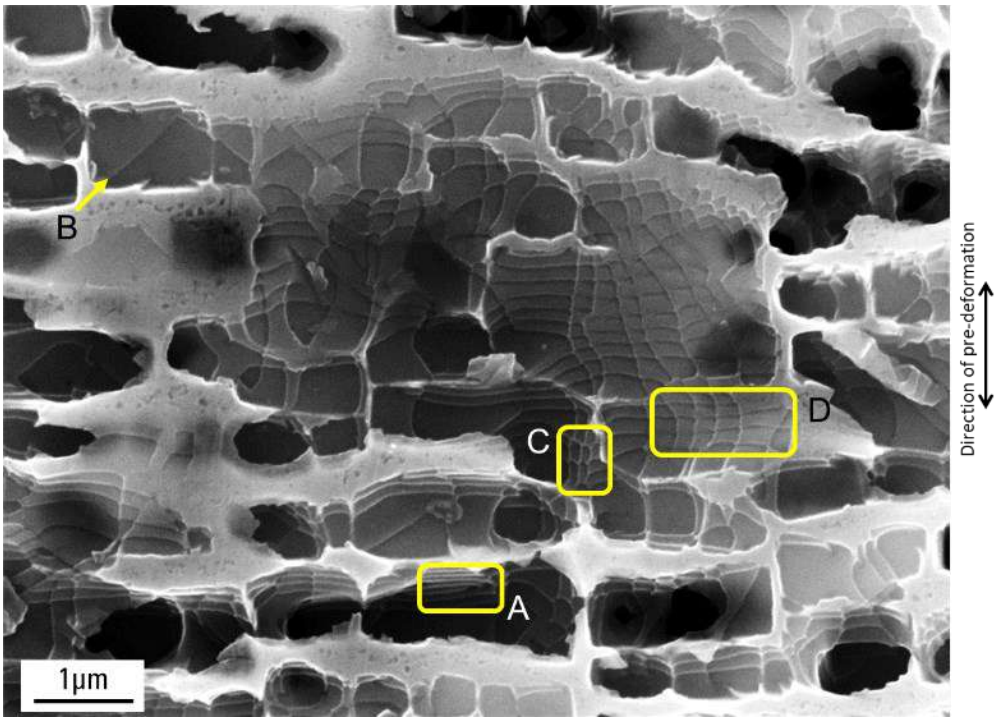

Figure 3.16. Dislocation structure in deep-etched microstructure of AM1 after PD at RT followed by aging treatment at 1100 °C for 5 h.

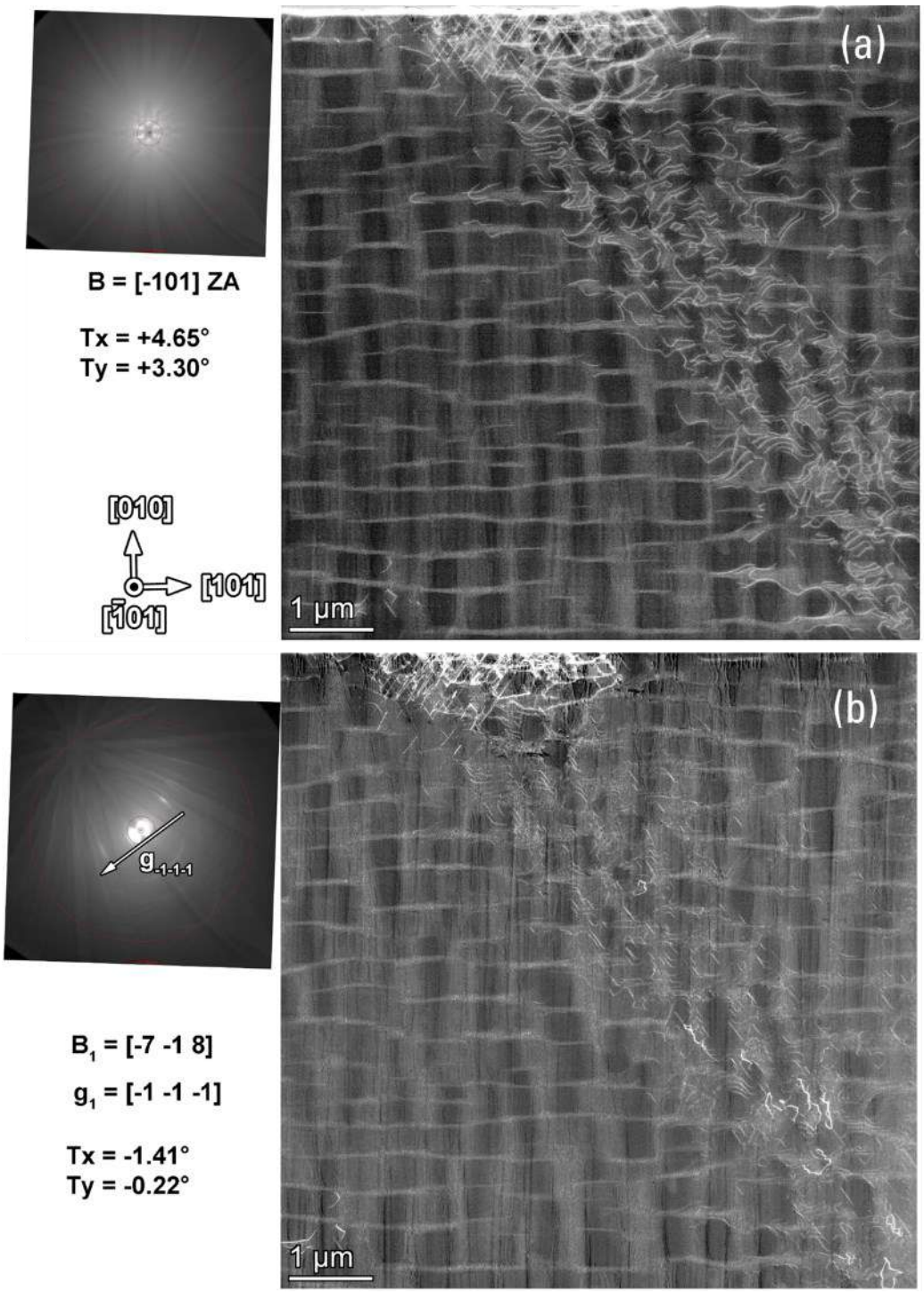

Figure 3.17. Diffraction contrast images of AM1-RTPD-HT1 (PD at RT + 5 h / 1100 °C + 16 h / 870 °C), obtained by low-angle annular dark-field scanning transmission electron microscopy (LAADF-STEM). Images are provided by M. Heczko and A. Egan of Center for Electron Microscopy and Analysis (CEMAS), The Ohio State University.

Dislocation grooves appears in the γ′ deeply-etched specimen because of enriching γ-element (specifically Cr and Co) along the dislocation lines [21–24]. Moreover, drastic increase in γ′ volume fraction during cooling process is necessary for swelling of γ′ between dislocation lines and to project the solute-segregated dislocations [24,25]. Therefore, aging temperatures should be above 1000 °C to have sufficient transition of volume fraction change during cooling in air. These are the mechanisms by which dislocation traces were observed in this experiment after first aging treatment at 1100 °C and Figures 3.18(a, b) are schematic explanation of the mechanism.

There are two possible reasons for a smaller number of dislocation grooves observed by SEM after secondary aging: 1) Increase in precipitate size during secondary aging means γ/γ′ interface moves toward γ matrix side. If the interfacial dislocations are kept at the same position, those dislocations formally at the interface will be pushed inside the γ′ precipitates as the interface moves to the matrix side (Figure 3.18(c1)). Isolated dislocations within the precipitates could not be observed in this experimental method, the combination of deep γ′-etching and SEM. However, STEM image shows that dislocations are not found in the γ′ precipitates (Figure 3.17) and this case is unlikely to occur. 2) Since misfit dislocations are reducing interfacial misfit strain, they are more stable at the interface. While the specimen is aged at 870 °C, the γ/γ′ interface slowly moves at the speed that interfacial dislocations can follow (Figure 3.18(c2)). As seen from irregular interface in Figure 3.10(d), coarsened precipitates had decreased their coherency with the matrix, which suggests the possible existence of dislocations at the interface [26,27]. During cooling from secondary aging at 870 °C, volume fraction does not drastically change. Swelling mechanism in the interfacial dislocation does not take place like in the case for the first stage at 1100 °C [25], consequently, number of dislocation grooves had decreased after secondary aging treatment.

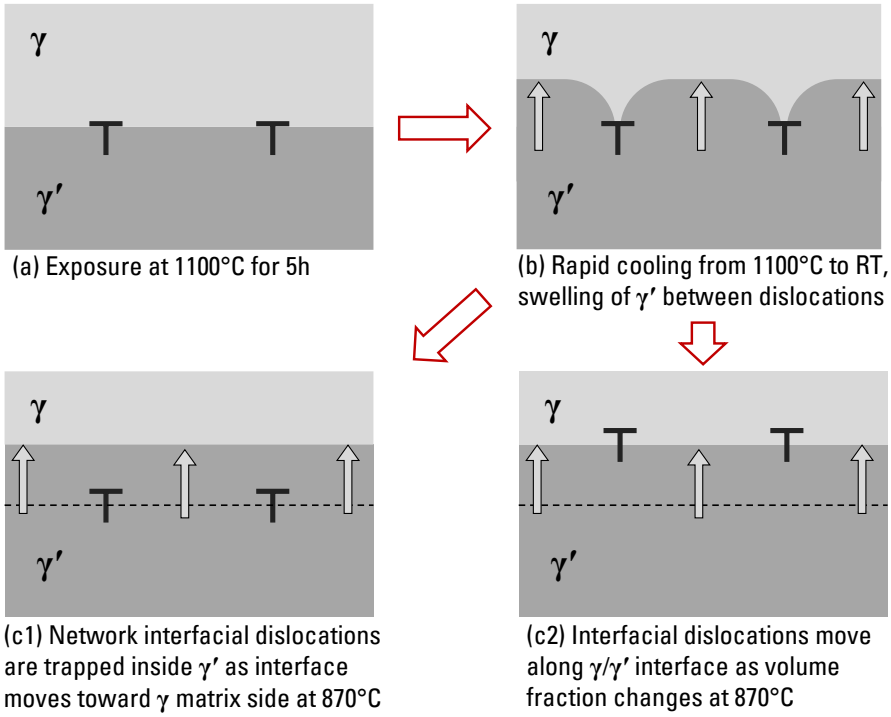

Figure 3.18. Schematic illustration of the mechanism that exposes dislocation traces during SEM observation of deeply etched AM1 specimens.

This AM1 alloy naturally has a lattice misfit close to zero at temperatures below 900°C [12,28]. Coarser precipitate with longer edge length decreases the absolute misfit. For example, in the rafted structure of AM1, misfit in (200) reflected direction is zero [12,28]. If so, small amount of interfacial dislocations is required for misfit strain relaxation. Therefore, it is still possible that interfacial dislocations actually disappear during secondary aging treatment and only dislocations in the matrix were observed in STEM analysis.

In Figure 3.11, dislocation grooves are mainly observed at the former cubic corners that had become rounded. To have the lowest interfacial strain energy, cubic precipitates' ideal shape is tetrakaidecahedron having {111} facet on the cubic corners when complete dislocation network is formed [15,29]. It is well known that Ni-Al

superalloy with higher misfit forms cubic precipitates with sharp edges and misfit strain is highest at the corners [12,30]. During long term annealing or very short creep at higher temperature and lower stress, dislocation networks first form at these corners [19,22,26,31]. This type of dislocation grooves was visible after full heat treatment because dislocation assisted dissolution was more prominent at the corners [31].

According to the comparison between microstructures of pre-deformed AM1 (in this study) and previous studies, it can be said that irregular microstructure evolution observed in pre-deformed AM1 after aging treatments are similar to that observed in long term aged Ni-based superalloys. The difference is such microstructure and dislocation evolution in the vicinity of the former slip band occurred in a very short period of time compared to the other studies. Again, microstructure evolution is just accelerated by internal elastic strain inherited from the prior PD. In addition, precipitate morphology is similar to the K465 with prolonged aging [26] when there are preferential coalescence direction shown in Figure 3.10(e) and length distribution of "RTPD + Aging 1" in Figure 3.12. This suggests that the microstructure coarsened band showing Figure 3.13(b) type size distribution should have lower local elastic strain compared to the other type shown in Figure 3.13(c). Figure 3.13(b) type bands have relatively smaller width (< 5μm) and longer maximum precipitate length compared to the other type. Faster formation of more dense dislocation network is predicted in the thicker band (> 5μm) which originally has higher local elastic strain before aging treatment, which resulted in shorter maximum precipitate length [26].

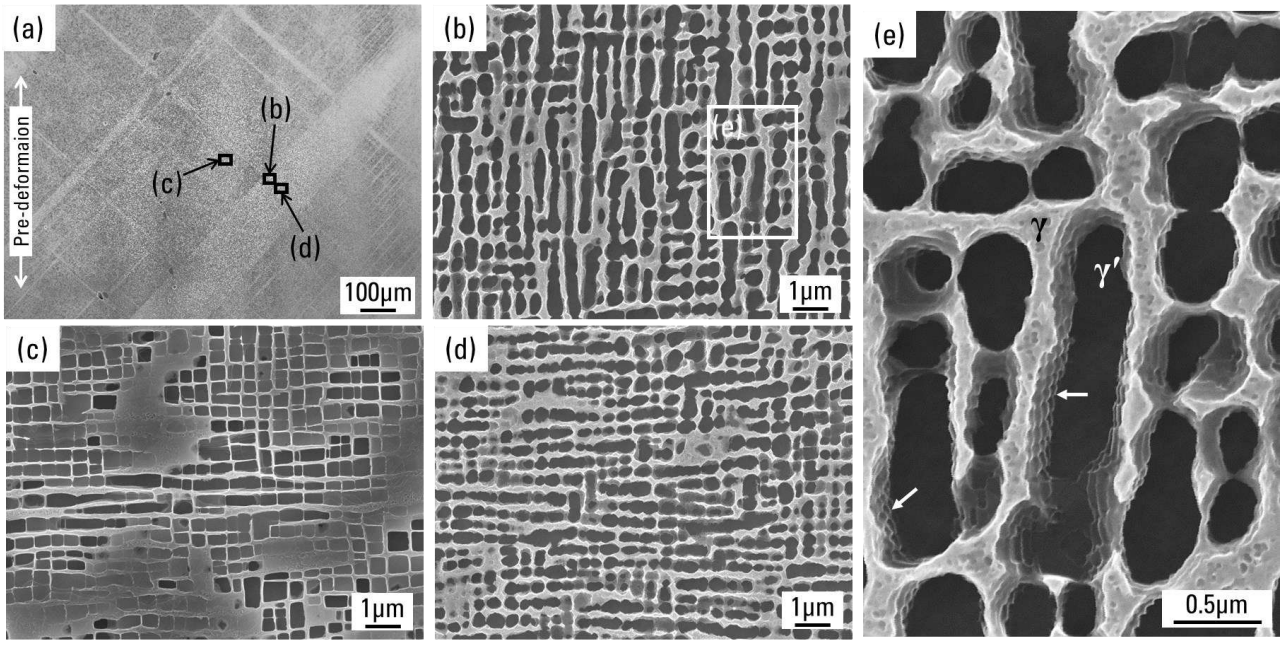

Figure 3.19. Microstructure of AM1-HT1-RTPD followed by additional aging at 1100 °C for 5 h. White arrows are indicating γ/γ′ interfacial dislocation networks.

If PD was applied to the full aged specimen and then first stage at 1100 °C for 5 h is applied again, much thicker microstructure coarsened band was observed (Figure 3.19). In the thicker band, directional coarsening of γ′ precipitates was much more pronounced compared to the PD applied to solutioned specimen. Regardless of the band thickness, dislocation network structures were similar. This experimental procedure and coarsening behaviors were similar to the research of Sakaguchi et al. using CMSX-4 [3]. As explained previously, specimen after HT1 has higher yield strength and strongly marked slip bands that create strong elastic field in

their vicinity. The very thick microstructure coarsened band is created by relaxation of very large elastic field introduced during PD. However, it should be noted that scale of precipitation coarsening is different for pre-deformation applied in as-solutioned state and in fully heat-treated state. Although coarsening occurred in fully heat-treated specimen with pre-deformation and another aging at 1100 °C, shorter edge length (width of elongated precipitate) has not changed drastically (Figure 3.19(e), ~0.4 μm). While microstructure evolution of as-solutioned specimen with pre-deformation starts from ~0.2 μm (Figure 3.5(a)) to have shorter edge length ~0.4 μm.

3. 4. Microstructures of AM1 after higher-temperature pre-deformation

In the tensile deformation of Ni-based SX superalloys, the material deforms by shearing of γ′ precipitate at low temperature (< 800 °C) and by the dislocation by-passing in the γ/γ′ interface at higher temperatures [1,7]. The microstructure evolution during heat-treatments is driven by the dislocations and local elastic strain energy introduced by the pre-deformation [3,32,33]. Therefore, existence of any kind of influence due to different deformation temperatures can easily be predicted but has never been compared. For the sake of clarification, specimens with different deformation temperatures (750 °C and 950 °C) were prepared as presented in earlier section of this chapter, and aging treatments were applied to these specimens.

Microstructures of AM1 specimens after PD (plastic strain ~0.8 %) at high temperatures are shown in Figure 3.20. In the specimen's bulk, all conditions showed similar morphology to the AM1 with PD at RT. Precipitates in Figures 3.20(d-f) seem to be different in morphology. This is due to the deepness of the chemical etching applied to the samples. Since exposure at deformation temperatures was 3 h at maximum, heating, dwell at maximum temperature, and cooling sequences during pre-deformation at 950 °C did not assist microstructure evolution.

Microstructures after standard first stage aging treatment and standard full aging treatments are shown in Figures 3.21 and 3.22, respectively. AM1-PD750 showed similar precipitation coarsening seen in AM1-RTPD, in both parallel and perpendicular to the tensile direction with development of the γ/γ′ interfacial dislocation structures (Figure 3.21(g)). Precipitates outside the emphasized band in Figure 3.21(a) also showed the γ/γ′ interfacial dislocation structures and cubic shaped precipitates had decreased compared to the specimen with the same aging history after PD at RT. After the secondary aging treatment, the density of dislocation traces decreased (Figure 3.22(g)).

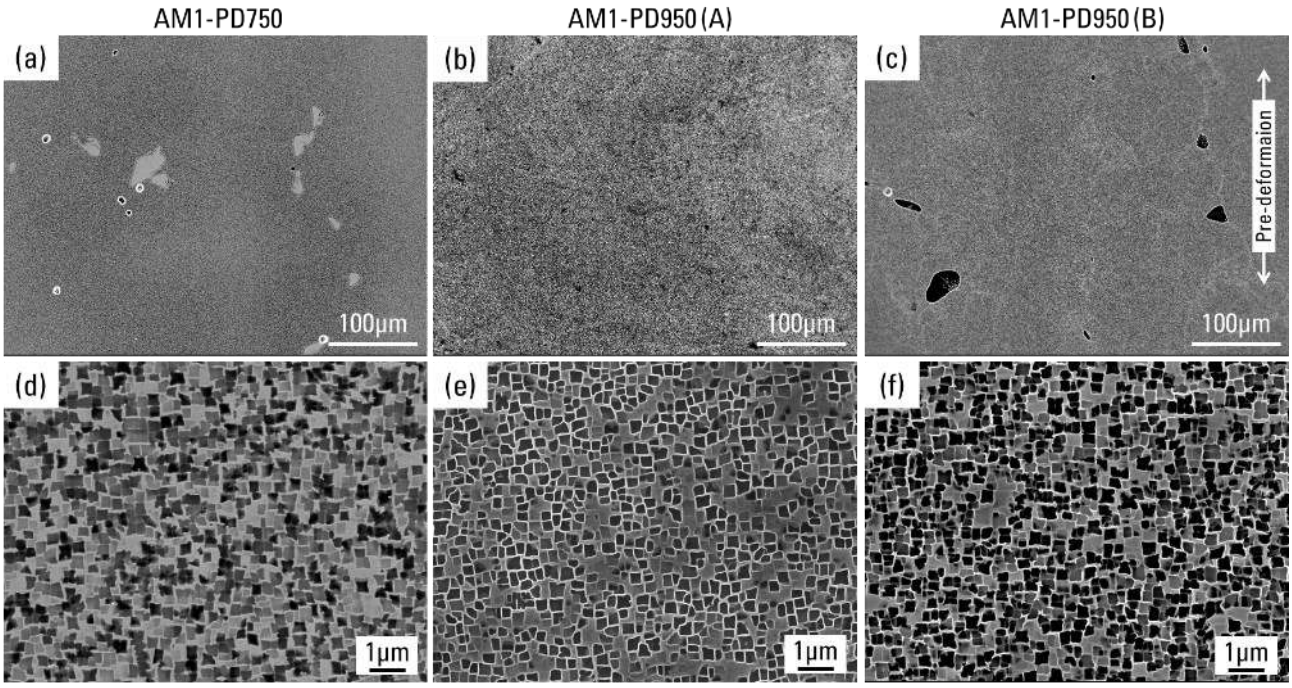

Figure 3.20. Microstructures of AM1 after PD at 750 °C (a, d), 950 °C with continuous deformation (b, e), and 950 °C with paused deformation (c, f).

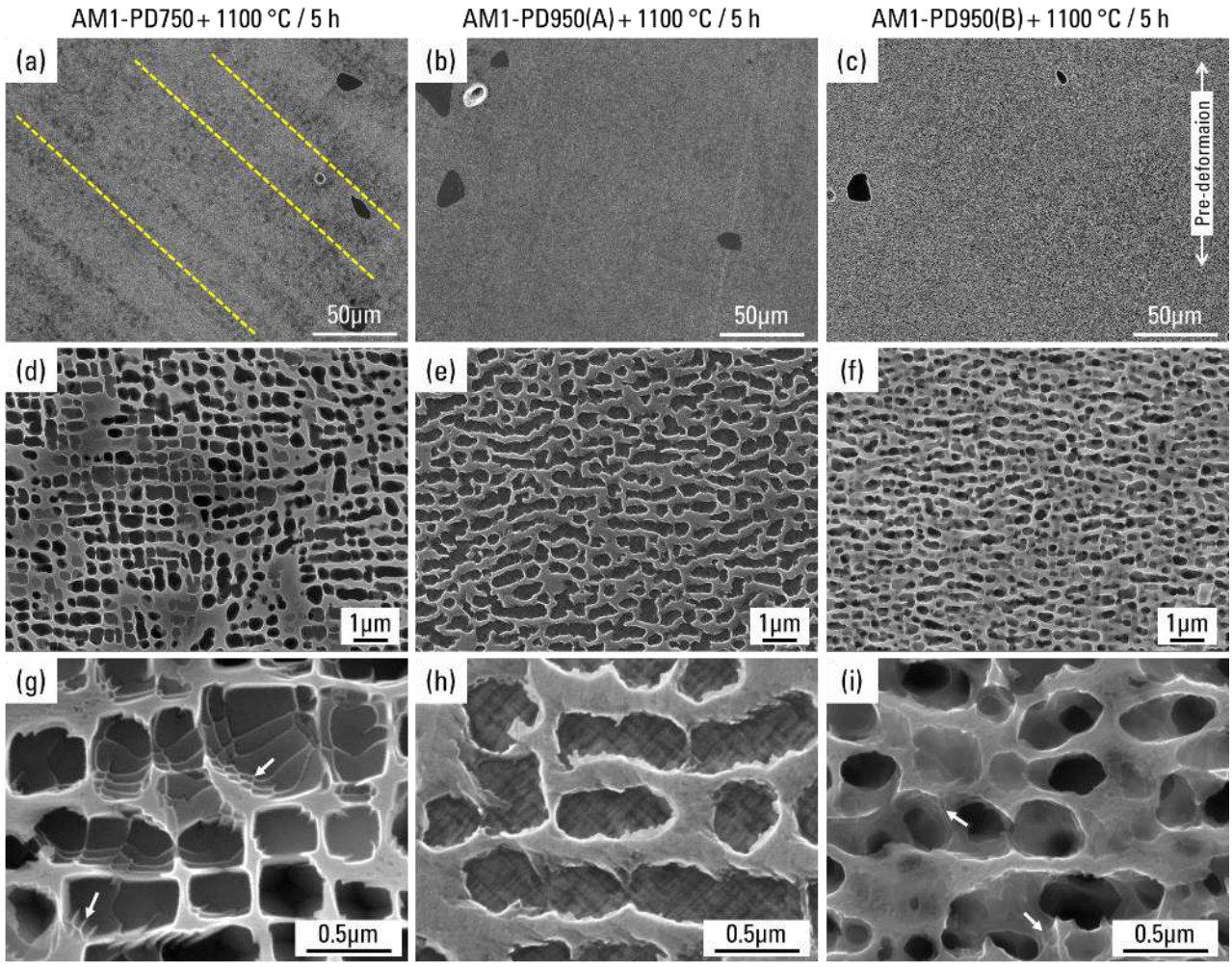

Figure 3.21. Microstructures of AM1 after PD at 750 °C (a, d, g), 950 °C with continuous deformation (b, e, h), and 950 °C with paused deformation (c, f, i), followed by the first stage aging treatment (1100 °C / 5 h). White arrows are indicating traces of γ/γ′ interfacial dislocations.

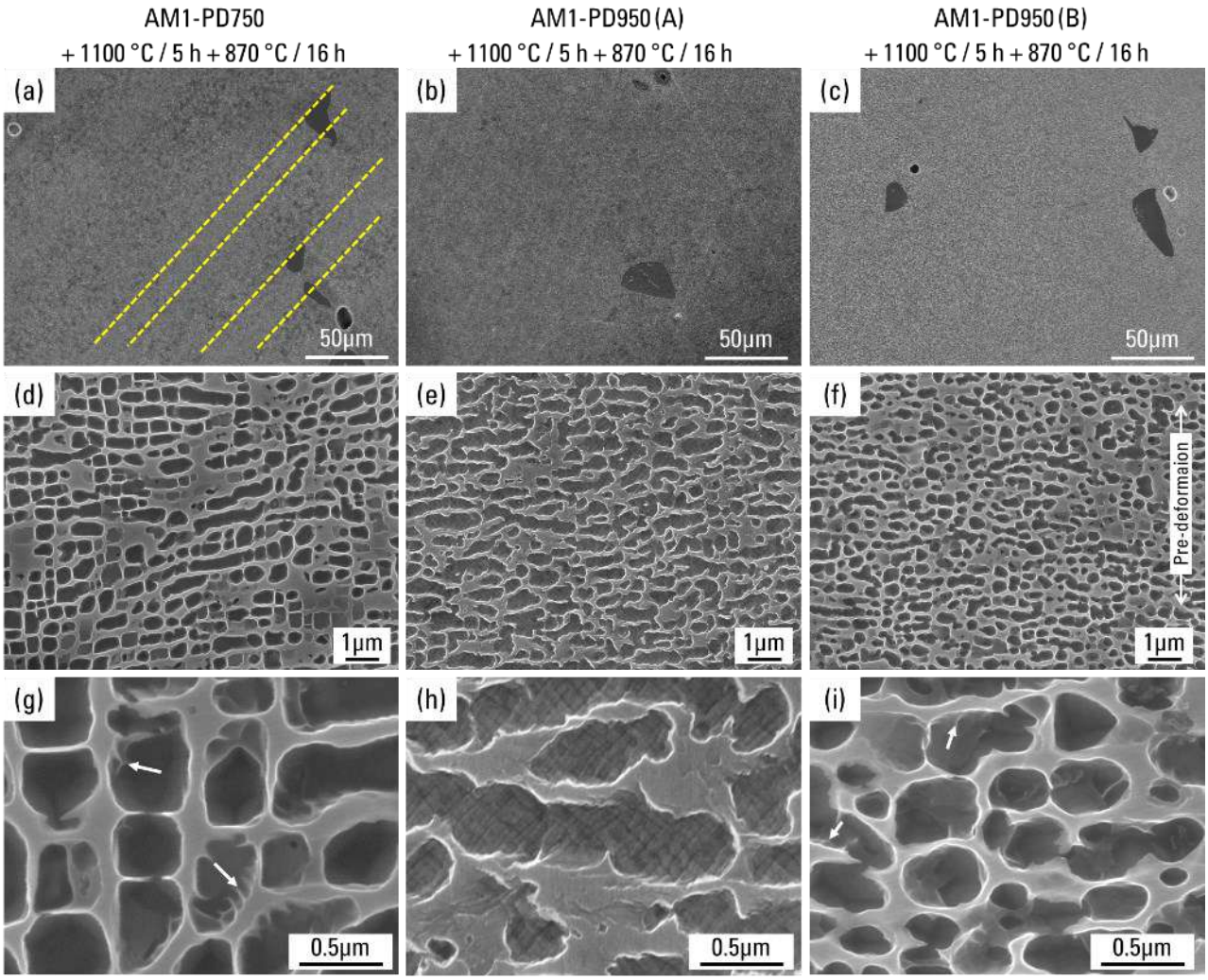

Figure 3.22. Microstructures of AM1 after PD at 750 °C (a, d, g), 950 °C with continuous deformation (b, e, h), and 950 °C with paused deformation (c, f, i), by the standard aging treatments (1100 °C / 5 h + 870 °C / 16 h). Dotted lines are showing microstructure coarsened band and white arrows are indicating traces of γ/γ′ interfacial dislocations.

AM1-PD750 presented higher yielding stress compared to AM1-HT1-RTPD, however, AM1-PD750 did not show clear slip band before aging treatments like in AM1-HT1-RTPD. This is contradicting to the statement mentioned earlier that higher energy is stored in one slip band when yield strength is higher. The effect of precipitate size must be discussed to explain this difference. At around 750 °C, Kear-Wilsdorf lock is formed by cross-slip of APB from {111} to {100} plane, creating yield stress anomaly in the high γ′ volume fraction Ni-based superalloys [34]. On the other hand, AM1-HT1-RTPD improved yield strength by increasing precipitate size that creates strong coupling of APB which leads to higher resistant to the precipitate sharing [35]. Pure resistance of precipitate shearing was lower in AM1-PD750 because of smaller precipitate size, but overall yield strength and hardening degree were higher than AM1-HT1-RTPD because of the cross-slip activation in cubic plane [35,36]. Since higher energy is required for the introduction of a slip band, AM1-HT1-RTPD accumulated more strain in a slip band which enabled to observe the band before subsequent aging treatments. Because of lower APB energy at higher temperature, dislocation should be widely distributed in AM1-PD750 and thus, γ′ precipitates away from the emphasized band also affected by internal strain that formed dislocation network during aging treatments [37]. Going back to the tensile curve of full heat treated AM1 at 750 °C in Figure 1.44(a), yield strength of AM1 after HT1 is similar to (or slightly lower than) the as-

solutioned state shown in Figure 3.1. This also supports the fact that precipitate size is not an essential factor for determining yield stress at 750 °C. Moreover, PD at 950 °C after HT1 (Figure 1.44(b)) and PD at 950 °C after solution (Figure 3.1) have almost the same deformation behavior near yielding, which means that precipitation size is not important for tensile behavior at 950 °C as well. Temperature sensitivity of tensile strength on the precipitate morphologies were studied by Pessah-Simonetti et al. and it appears strongest at the room temperature [38].

After PD at 950 °C and following aging treatments, precipitates are no longer cuboidal and they showed no sign of the band like affected ones like for the other two pre-deformation temperatures (Figure 3.22(b, c)). The γ′ precipitates after PD at 950 °C and aging treatments tend to coarsen in the transverse direction to the pre-deformation direction (Figures 3.22(e, f)), which can be called "pre-rafted" structure. The pre-rafting is attributed to the deformation mechanism that proceeds by dislocations introduced on the γ matrix side of γ/γ′ interface and its inhomogeneous distribution between horizontal and vertical channels [2]. Relaxation of γ/γ′ misfit strain by rearrangement of introduced dislocations during aging treatments is the main driving force of the pre-rafting. Such coarsening mechanism is similar to the γ′-rafting of Ni-based superalloys during creep deformation [4,5].

Directional coarsening during aging treatment at above 1000 °C in the specimens with pre-deformation at elevated temperatures is in accordance with studies by Véron and Bastie [39] and Sakaguchi and Okazaki [11]. Moreover, this pre-rafted microstructure is very similar to the rafted microstructure observed in the core of the service-ready SX turbine blade for power-generation gas turbines [40]. The microstructure of this turbine blade was successfully solution treated but exhibited rafted structure after aging treatments without any external load. In the study by Pierret et al., plastic strain introduced during cooling from solution treatment (due to the thermal contraction mismatch between the surface and the bulk of the components) was suspected as the origin of γ′-rafts in the turbine blade [40].

AM1 specimens with different plastic strains, 0.36% and 2.17%, were prepared and their microstructures are presented in Figures 3.23 and 3.24, respectively. Microstructure of four different specimens were analyzed using RIM-X and their average precipitate lengths are presented in Figures 3.25 and 3.26. It can be observed from microstructure and quantitative measurements shown as rose diagrams in Figures 3.26(a, b) that pre-rafts became shorter and disturbed as plastic strain increases from 0.36% to 0.87%. Precipitates in the specimens with 0.87% and 2.17% strain presented similar size profile for all directions (Figures 3.25 and 3.26(b, c)). Comparing RIM analyses of two deformation types (AM1-PD950(A) and (B)), continuous tensile deformation (A) results in longer precipitates whereas the paused one (B) results in round edged smaller precipitates, and shorter error bars in the Figure 3.25 represents homogeneous size distribution than others.

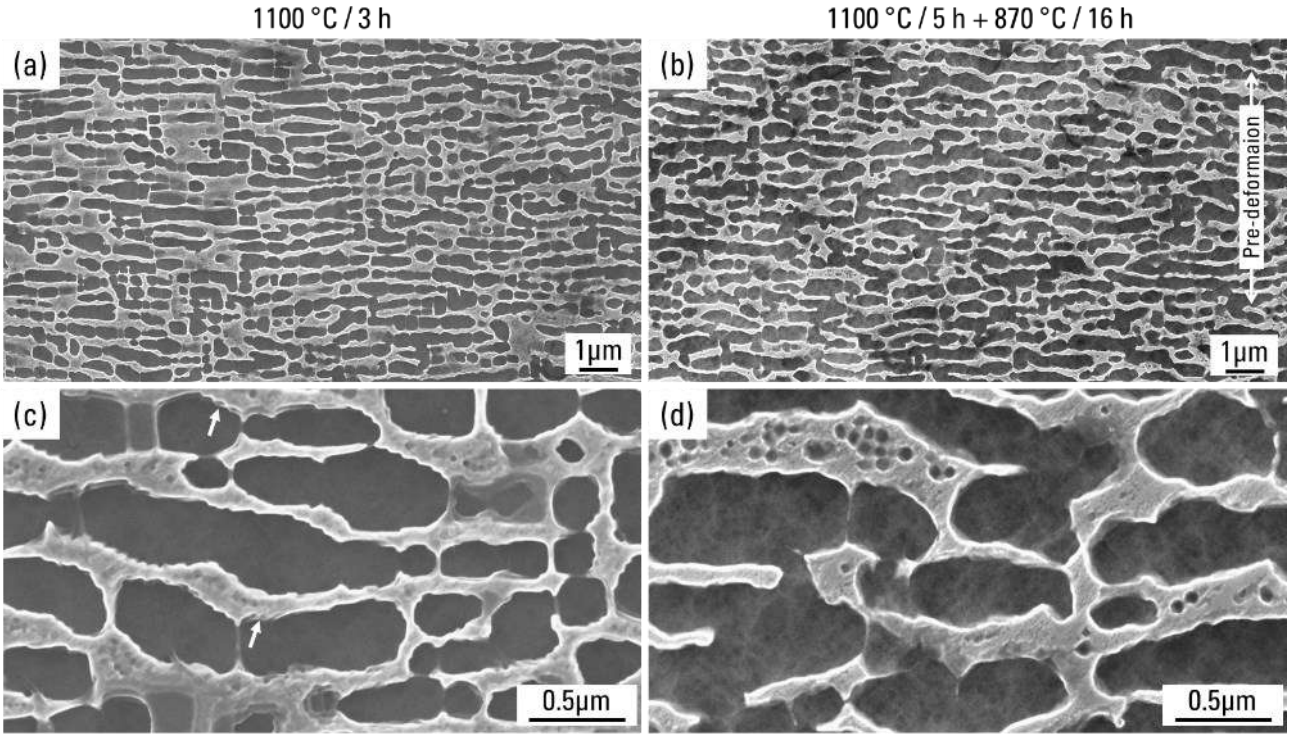

Figure 3.23. Microstructures of AM1 with PD at 950 °C (plastic strain = 0.36%) followed by aging treatments labeled on the top. Area fraction of γ′ phase in (a) and (b) are 51.2% and 58.5%, respectively. White arrows are indicating traces of γ/γ′ interfacial dislocations.

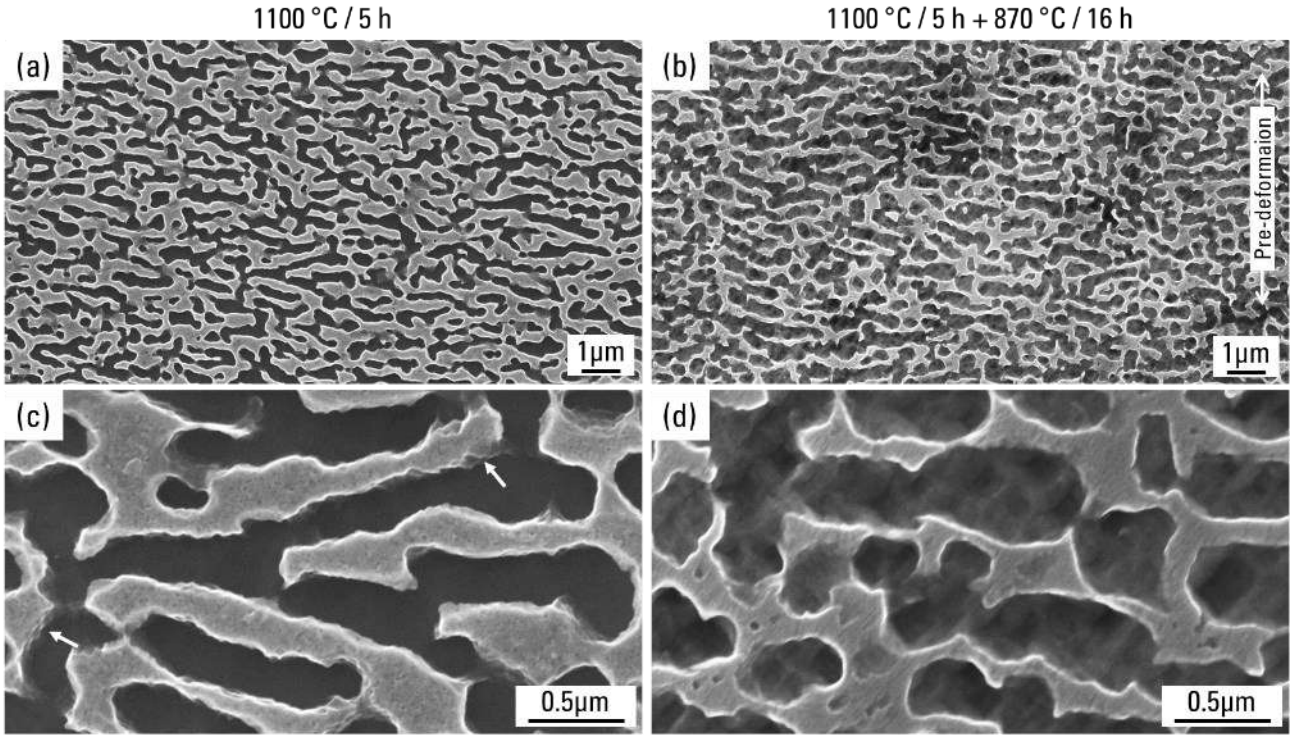

Figure 3.24. Microstructures of AM1 with PD at 950 °C (plastic strain = 2.17%) followed by aging treatments labeled on the top. Area fraction of γ′ phase in (a) and (b) are 45.0% and 58.7%, respectively. White arrows are indicating traces of γ/γ′ interfacial dislocations.

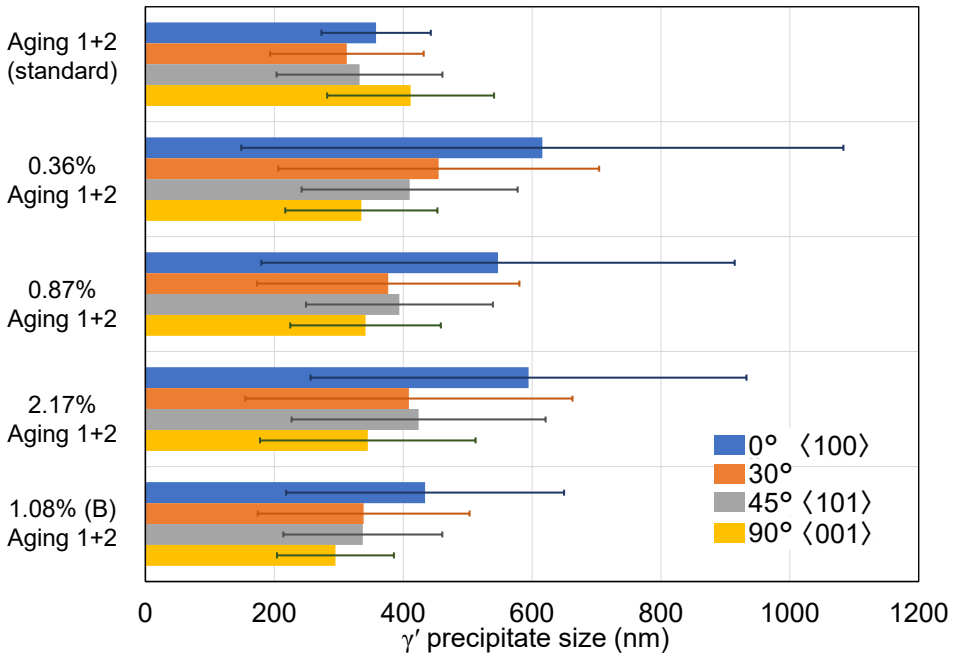

Figure 3.25. Result of RIM analysis using RIM-X software on AM1 specimens pre-deformed at 950 °C. Average size of γ′ precipitate is shown as solid bars and error bars are standard deviation.

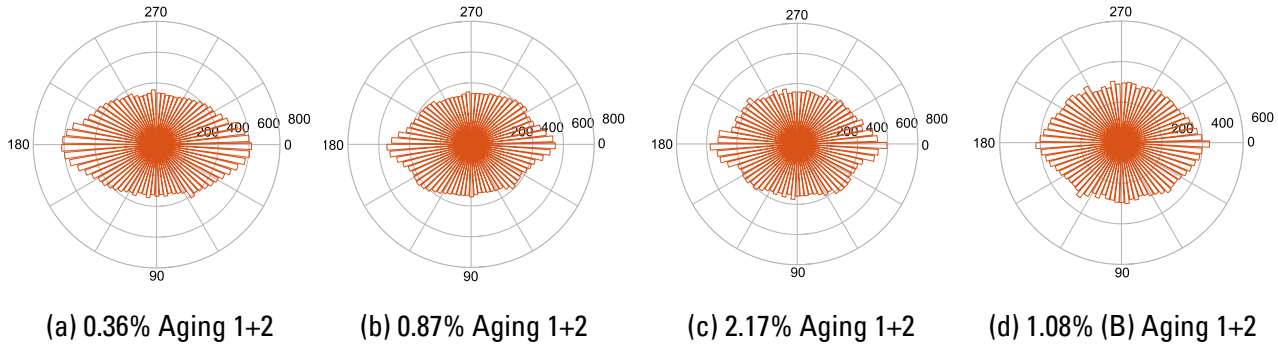

Figure 3.26. Rose diagrams of γ′ precipitate size obtained by RIM-X analyses on AM1 with PD at 950°C followed by aging treatments of standard AM1 condition (HT1, 1100 °C / 5 h + 870 °C / 16 h). (a-c) were deformed continuously and (d) was paused at yielding point as shown in Figure 3.1. Concentric scale in nm.

In the specimen with PD at 950 °C, precipitate size (specifically in horizontal ⟨100⟩ direction) decreased when plastic strain increased from 0.36% to 0.87%. Since tensile PD at 950 °C is driven by dislocation by-passing and piling-up at the matrix side of γ/γ′ interface, plastic strain is homogeneously distributed [41]. Difference from PD at RT is that higher dislocation density should be accumulated at the γ side of the γ/γ′ interface during deformation at 950 °C resulting in a microstructure homogeneously disturbed after aging treatments [1,6,37]. And amount of stored dislocations should increase as magnitude of plastic strain increases.

Misfit dislocations were observed after 3 h at 1100 °C on the specimen with 0.36% plastic strain (Figure 3.23(c)), and they were similar to the ones observed on the specimen after PD at RT. This is an evidence that precipitation coarsening in γ′-rafting style and construction of dislocation networks are proceeding by the same mechanism to those reported in many studies. Interfacial dislocations after 5 h at 1100 °C on the specimen with 2.17% plastic strain (Figure 3.24(c)) were in form of networks but not clear compared to that in the specimen with 0.36% strain. Disturbed precipitate shape and decreased amount of pronounced interfacial

dislocation traces in 2.17% strain specimen are obviously caused by higher dislocation density. Increased dislocation density filling-up the γ-matrix, especially at the γ/γ′ interfaces, is a possible reason of suppressing precipitation coarsening and observed shorter horizontal length in 2.17% specimen. Trend of increasing plastic strain with more disturbed microstructure is indirectly indicating that dislocation migration is anisotropic at the beginning (preferably in the vertical channels) and then it migrates in both horizontal and vertical matrix channels as plastic strain increases [2].

Although the macro plastic strain is just around 1%, the pre-deformation paused at yield point (AM1-PD950(B)) may store much higher dislocation density during stress relaxation and creep at holding time. Lower flow stress of AM1-PD950(B) in Figure 3.1 also supports that dislocations introduced during the holding decreased resistance to the tensile pre-deformation. Microstructure after aging treatment showed dislocation network similar to (A) type with 2.17% plastic strain, meaning that the basic mechanism is the same. Round and homogeneous precipitate size distribution in Figures 3.25 and 3.26(d) compared to type (A) with 2.17% strain is an indication that (B) type pre-deformation introduced higher dislocation density than (A) type.

The decreased mobility of γ/γ′ interfaces by an increased interfacial dislocation density is also suggested in the study by Yang et al. that presented decreasing precipitation coarsening rate with formation of interfacial dislocation walls [26]. Similar coarsening suppression was also demonstrated in the elastic domain aging of Ni-Al binary system with very small misfit [42]. In CMSX-4 pre-deformed at 900 °C, precipitate size after aging at 1080 °C / 20 h increased as applied plastic strain increase from 0.05 to 0.2% [11]. However, precipitate sizes are comparable for specimens with plastic strain between 0.2 and 1.5% [11]. Once the misfit is relaxed by a given dislocation density (by creep strain or plastic strain), γ′-rafting can then proceed without application of external stress [43]. This is a reasonable explanation for comparable precipitate size after pre-deformation of CMSX-4 at 900 °C with plastic strain between 0.2 and 1.5% [11]. The results on pre-deformed CMSX-4 were not deeply discussed in the article [11], but there is still a possibility that interfacial dislocations prevented the precipitation coarsening once they reached sufficient amount. Another study demonstrated that overheating at the primary creep stage of non-isothermal creep condition can improve the creep life by increasing effective γ/γ′ lattice mismatch [44]. In this case, early formation of the finer γ/γ′ interfacial dislocation network (by higher absolute lattice mismatch) possibly suppressed microstructure evolution during following creep loading.

Strain induced microstructure evolution is discussed in many forged alloys; however, the objectives are mainly on precipitation of new grain, grain size, and recrystallization morphologies [45]. In other case, grain boundary is responsible for strain induced γ′ precipitation of solutioned Udimet 720, which occurred during high-temperature deformation above 1100 °C followed by stress relaxation annealing [46]. With lower volume fraction of γ′ phase and lower γ/γ′ misfit, these results cannot be adopted for the discussion of the present research. Mrozowski et al. investigated precipitate size of AD730^{TM} in dwell fatigue condition and dwelling of 300 s during maximum stress presented smaller precipitate size compared to the fatigue without dwelling time [47]. This case can be explained by the γ/γ′ interfacial misfit strain. Fatigue tests were performed in elastic regime at 750 °C and therefore, there is a possibility that interfacial dislocation development during dwelling and prevented precipitation growth. Another study on the γ′ dissolution kinetics of CMSX-4 after creep pre-straining showed that the dissolution kinetics increases as accumulated plastic strain increases [48]. However,

heat treatment temperature for this dissolution is different from the aging temperature in the present study and the mechanism cannot be applied. Overall, plastic strain dependence on γ′ size has not been discussed deeply in very small strain (~1%) and the case without recrystallization.

3. 5. Effect of chemical compositions on the microstructure evolution behavior

To understand the effect of chemical composition, plastic strain of about 0.8% was applied to CMSX-4 Plus, high-misfit Re-containing alloy, by tensile deformation and then the heat treatments were performed similarly to AM1.

Figure 3.27 shows the typical microstructures of CMSX-4 Plus outside the microstructure coarsened band, in the dendrite cores. Because the first aging stage was at higher temperature and for longer duration, γ′ precipitate size of CMSX-4 Plus after standard treatments (HT2) is much larger than AM1-type heat treatment (HT1). The precipitate sizes either after HT1 (Figure 3.27(f)) or HT2 (Figure 3.27(c)) are smaller compared to that of AM1 after the same conditions (Figures 3.13(a) and 3.14(a)). Lower internal diffusivity of CMSX-4 Plus linked to its alloy chemistry is a reason for this difference. RIM-X results in Figures 3.27(c, f) are showing precipitates in both conditions have cubic shape with equivalent length in both horizontal and vertical directions if they are not affected by the pre-deformation.

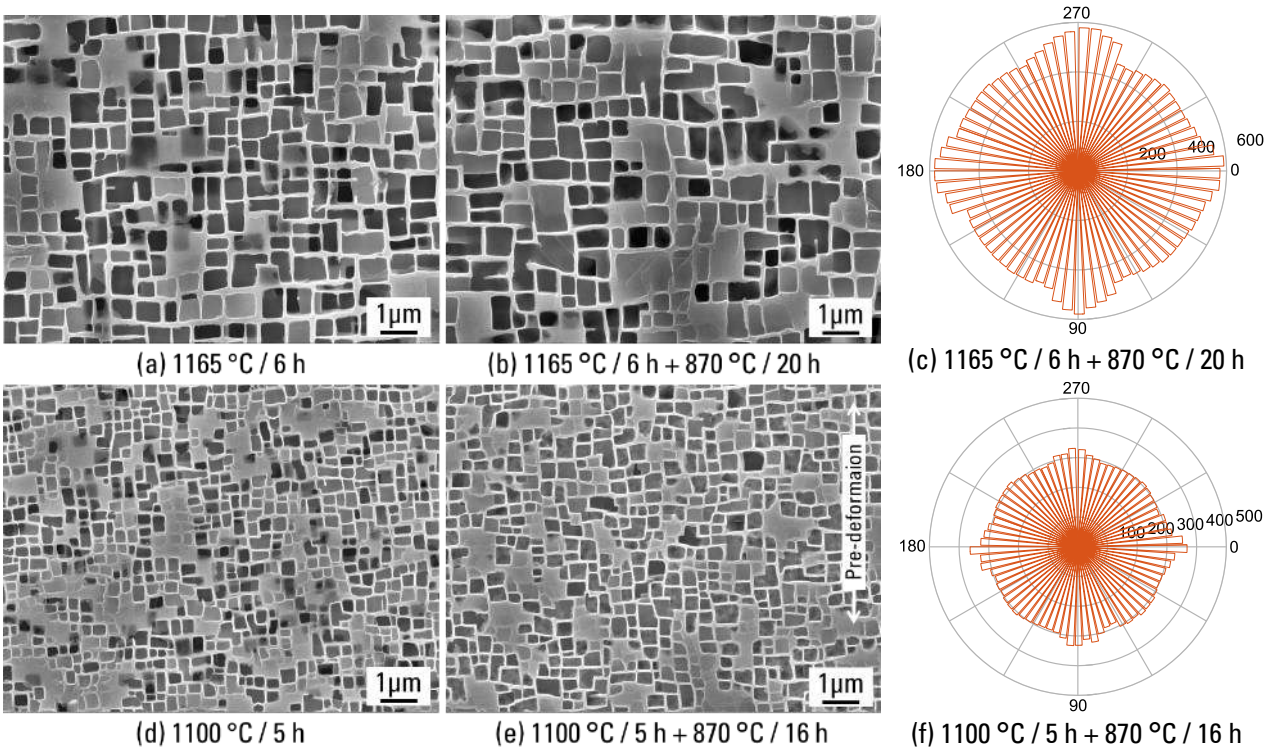

Figure 3.27. Typical microstructure of CMSX-4 Plus in the primary dendrite arms after aging treatments labeled to each image (a, b, d, e). (c) and (f) are rose diagrams of average γ′ precipitate size obtained by RIM-X analyses on images (b) and (e). Concentric scale of the rose diagrams is in nm.

Figures 3.28 and 3.29 are microstructures of CMSX-4 Plus after pre-deformation and two different kinds of aging treatments (HT2 and HT1). Similarly to AM1, slip bands were only observed at the surface regions in the specimen just after pre-deformation. After aging treatments, bands were pronounced by microstructure evolution. Compared to AM1, more and thinner microstructure coarsened bands were observed in former {111} slip planes of CMSX-4 Plus (lower magnification images are presented in the following section). Indeed, precipitates inside the microstructure coarsened band are bigger than that of AM1 for HT2 conditions. Dislocation traces at the γ/γ′ interfaces were observed both after the first stage (Figure 3.28(h)) and after full heat treatments (Figure 3.28(i)). In the specimens after HT1 condition, microstructure evolution was not so drastic like HT2, but disturbed precipitates with interfacial dislocation traces were observed (Figure 3.29). RIM-X results on the precipitate size in the microstructure coarsened band are presented in Figure 3.30. Although the precipitates are heavily coarsened after first stage at 1165 °C (Figure 3.30(a)), precipitates tend to maintain rectangular shape in the observed plane, and secondary stage was just to increase volume fraction of γ′ phase. Precipitate shape after HT1 also showed rectangular shape and not a directional coarsening feature.

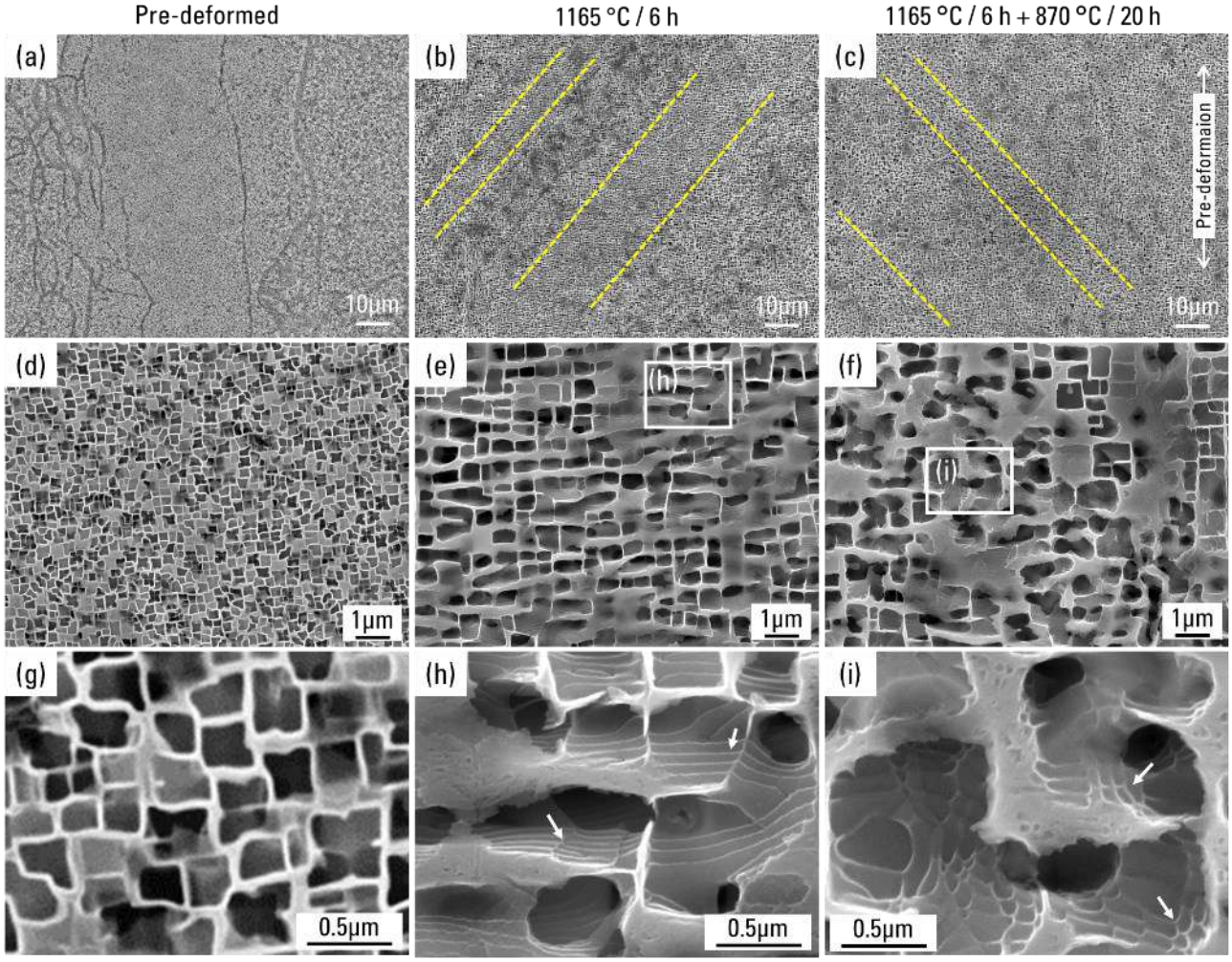

Figure 3.28. Microstructure of CMSX-4 Plus with PD at RT (~0.8%) (a, d, g) followed by first (b, e, h) and second (c, f, i) aging treatments for standard CMSX-4 Plus conditions (HT2). Dotted lines are indicating microstructure coarsened band and white arrows in (h, i) are pointing at dislocation traces at the γ/γ′ interfaces.

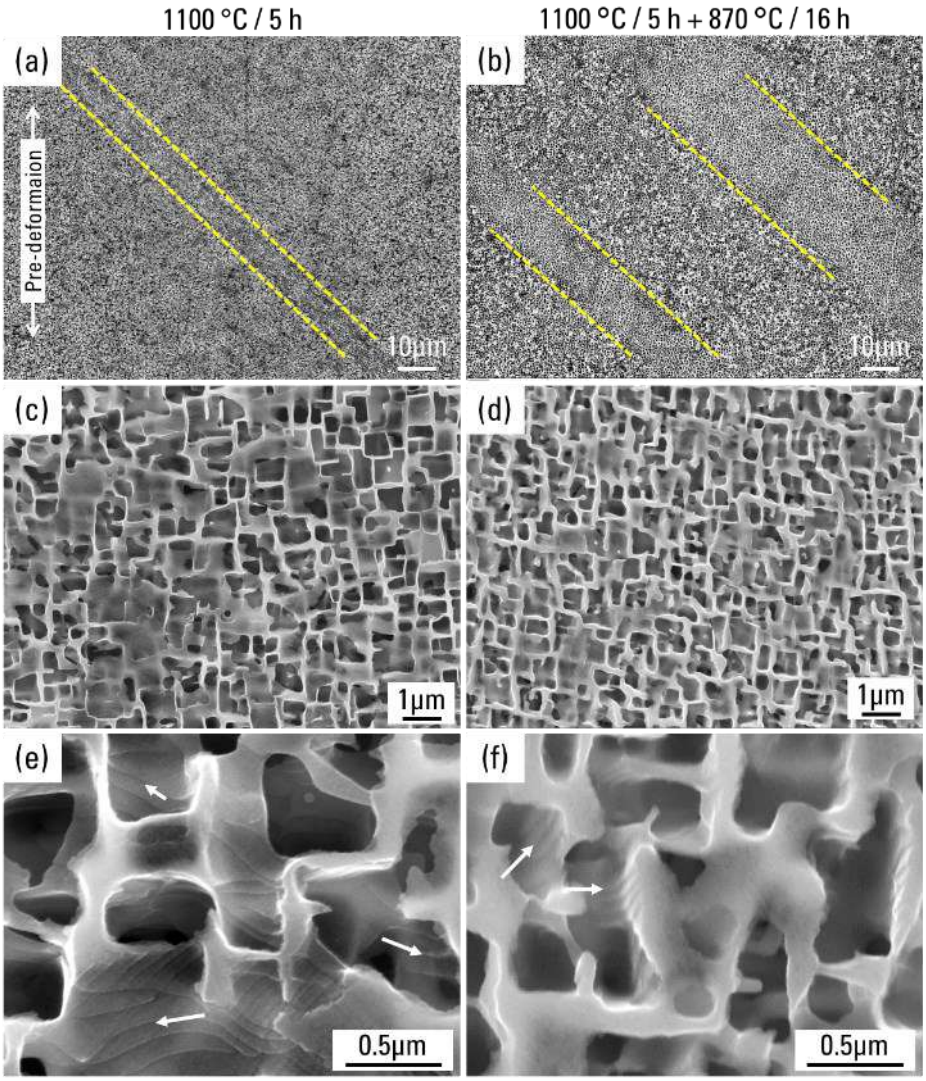

Figure 3.29. Microstructure of CMSX-4 Plus with PD at RT (~0.8%) followed by first (a, c, e) and second (b, d, f) aging treatments for standard AM1 conditions (HT1). Dotted lines are indicating microstructure coarsened band and white arrows in (h, i) are pointing at dislocation traces at the γ/γ′ interface.

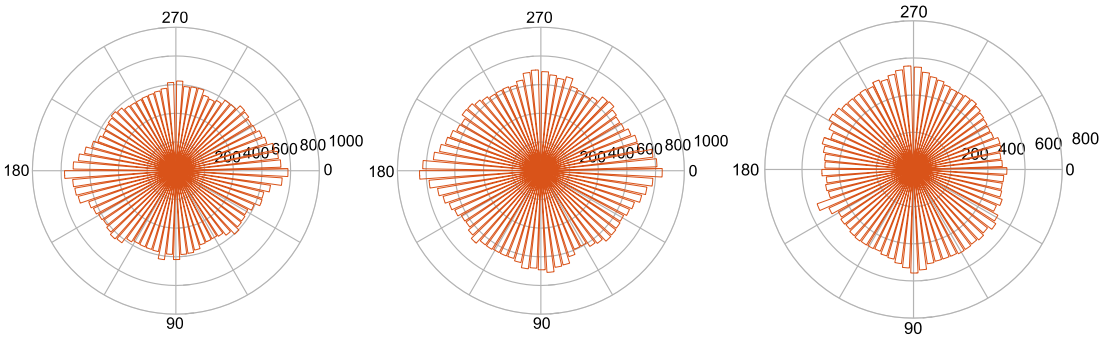

Figure 3.30. Rose diagrams of average γ′ precipitate size obtained by RIM-X analyses on CMSX-4 Plus with PD at RT followed by different aging treatments. Concentric scale of the rose diagrams is in nm.

There are two major differences in microstructure evolution behavior between AM1 and CMSX-4 Plus, precipitate size/shape and interfacial dislocation structures. Regardless of aging conditions, γ′ precipitates in AM1 showed anisotropic coarsening during first stage aging treatment that seems to be driven by the mechanism similar to the γ′-rafting. Formation of [010] edge misfit dislocations and dislocation networks were both observed after first aging stage. In CMSX-4 Plus, coarsening anisotropy was not so pronounced, and coalescence of nearby precipitates seemed to be more prominent. Dislocations after HT2 of CMSX-4 Plus in Figure 3.28(i) has finer network structure whereas a majority of dislocations after first aging treatment in the Figure 3.28(h) is parallel to neighboring ones. The parallel dislocations are possibly [010] edge dislocations which was similarly observed in AM1. On the other hand, [011] type and those gliding into edge dislocations were mainly observed for CMSX-4 Plus after 1100 °C / 5 h (first stage HT1). Indeed, these analyses are only done by SEM observations on deeply-etched specimens and TEM observations are necessary to define exact types.

Chemical composition of CMSX-4 Plus suggests that this alloy has lower APB energy of γ′ precipitates; thus, the resistance to shearing is lower than for AM1 [8]. Main alloying elements contributing the APB energy of the precipitates are Ti and Ta which substitutes to Al in the $L1_2$ ordered structure [49,50]. Also, this type of alloy with higher Re content is known to have lower yield strength at lower temperatures [8,49,51,52]. Like the relationship between as-solutioned AM1 and fully heat treated AM1, after ~0.8% pre-deformation, CMSX-4 Plus with lower shearing resistance has higher number of slip bands compared to AM1. Higher number of the microstructure coarsened bands observed in CMSX-4 Plus after HT2 is in accordance with Figure 3.2 showing CMSX-4 Plus with higher density of observable slip bands.

The precipitate coarsening in the band of CMSX-4 Plus proceeds by coalescence of nearby precipitates, instead of the γ′-rafting-like anisotropic growth [19]. Similar precipitation coarsening that starts from vanishment of γ channels during over-aging of Re-containing alloys were reported [53,54]. However, the interfacial dislocation density is much higher after shorter aging in this study with pre-deformation. Indeed, the enhanced precipitation coarsening and interfacial dislocation development in pre-deformed CMSX-4 Plus were triggered by elastic strain introduced during pre-deformation. It is suggested that, because elastic strain introduced in one single band was very small, microstructure evolution did not proceed with strong anisotropic behavior.

In comparison with AM1, there are several possible reasons of CMSX-4 Plus having clear interfacial dislocations in deeply-etched samples even after secondary aging treatment. First, dislocation traces appeared after first stage both at 1100 °C and 1165 °C can be explained like for AM1 at 1100 °C. Rapid cooling creates dislocation grooves by swelling of γ′ phase. From Figure 3.9, volume fraction of γ′ phase in CMSX-4 Plus at 1165 °C and that in AM1 at 1100 °C are similar, and so as at 870 °C. Thus, change in volume fraction from first stage to second stage can be assumed as (almost) the same. If dislocations are trapped inside the γ′ phase during second aging treatment, interfacial dislocation traces should not be observed for CMSX-4 Plus specimen as well. If interfacial dislocations moved along γ/γ′ interfaces, considering lower internal diffusivity of CMSX-4 Plus, swelling is difficult to occur during cooling from 870 °C and interfacial dislocations should look similar to the case of AM1. One of the remaining possibilities is that the interfacial dislocations moved with γ/γ′ interfaces, but it was slower that dislocations were kept in γ′ side of the interface. Another possibility is that coherency misfit is still present after secondary stage, at least partly, in the microstructure coarsened

band of pre-deformed CMSX-4 Plus. This may be attributed to the significantly higher misfit of CMSX-4 Plus compared to AM1 at the first aging temperature which can be predicted from their compositions [18,55,56].

The discussions made above are describing characteristics of typical type of the microstructure coarsened bands. When a slip band has relatively higher strain, the microstructure affected region appears as thicker band as compared in Figure 3.31. Two images in Figure 3.31 were obtained after the same procedures, PD at RT and then aging at 1165°C for 6h. Figure 3.31(a) shows large area affected by the pre-deformation, whereas Figure 3.31(b) has clear contrast between the band and area not affected. Precipitate scale microstructures from the same tensile specimen as Figure 3.31(b) are shown in Figure 3.32. Precipitates in Figure 3.32 have anisotropic growth compared to the those observed in Figure 3.28. Besides the precipitate shape, interfacial dislocations were still observed both after first (parallel type dislocation lines) and secondary (network type dislocations) aging stages.

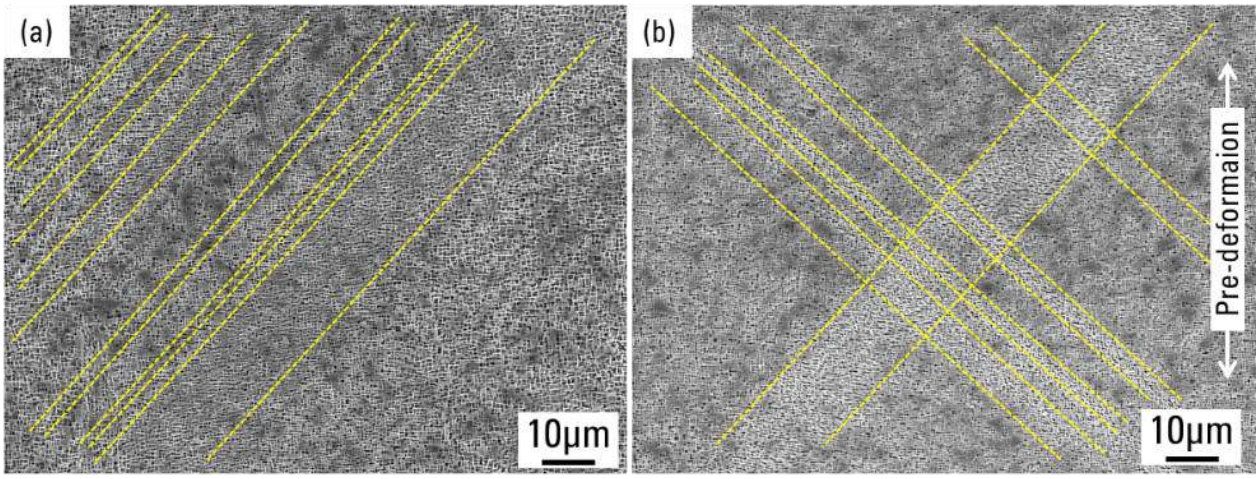

Figure 3.31. Microstructure of CMSX-4 Plus with PD at RT (~0.8%) followed by first aging at 1165 °C for 6 h. Two images are taken from different tensile specimens. Plastic strains are 0.79% (a) and 0.71% (b).

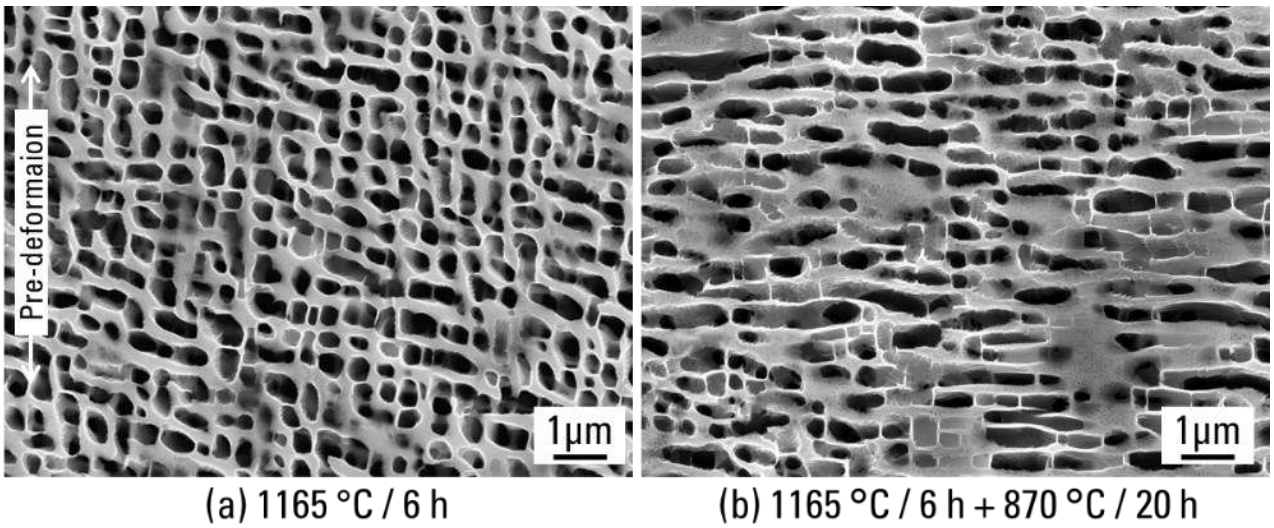

Figure 3.32. Microstructure of CMSX-4 Plus with PD at RT (~0.8%) followed by first (a) and second (b) aging treatments for standard CMSX-4 Plus conditions (HT2). Images are taken from specimen with 0.71% plastic strain (same tensile specimen with Figure 3.31(b)).

3. 6. Rejuvenation treatment on the pre-deformed materials

In the previous experimental results, pre-deformation applied between solution and aging treatment was found to have huge impact on the creep properties of AM1 SX superalloy. This is clearly due to the microstructure evolution caused by pre-deformation. The concept of rejuvenation heat treatment that dissolves γ′ precipitates and restores microstructure can be effective to erase detrimental effect of pre-deformation and/or prior creep-induced microstructure degradation [57–66]. From a scientific point of view, damage quantity and type that prevent component from successful microstructure evolution are not clearly discussed for SX superalloys. Rejuvenation treatment on AM1 specimens with different deformation procedures can help understanding the limit of the rejuvenation. From an industrial point of view, this is a very important study for improving yield rate of the turbine blade foundry.

3. 6. 1. Determination of rejuvenation treatment conditions

Temperature history diagram is shown in Figure 3.33. Rejuvenation treatment was inserted between pre-deformation and the aging treatment. Rejuvenation temperatures for AM1 were at 1270 °C, 1275 °C, 1280 °C, and 1290 °C for 20 min and for CMSX-4 Plus were at 1310 °C, 1320 °C, 1325 °C, 1330 °C, and 1335 °C for 20 min and 1 h.

Microstructures of AM1 with PD at RT after rejuvenation treatment and aging treatments are shown in Figures 3.34 and 3.35. Low magnification images with rejuvenation temperatures below 1280°C (Figures 3.34(a, c) and 3.35(d-f)) showed line traces that correspond to the former slip plane which clearly appears when aging treatments are directly applied (Figures 3.35(a-c)). When the rejuvenation temperature is far below from solvus temperature, severe precipitation coarsening occurs which can be described as very high temperature aging (Figure 3.34(b)). Slip plane traces are still present after rejuvenation at 1280 °C when the specimen has been submitted to higher plastic strain (Figure 3.35(e)) or PD was applied after HT1 (Figure 3.35(f)). These remaining slip line traces are also an indication of incomplete solutioning, which disappeared when rejuvenation was performed at 1290 °C. Interdendritic area is always not displaying ideal γ′ cuboidal structure (Figure 3.34(g, i)). This is because of initial sub-grain boundaries inherited from casting process, and this kind of sub-boundaries are observed typically in the interdendritic area of Ni-based SX superalloys. Pre-deformation introducing higher local strain in the interdendritic area is another possibility of incomplete microstructure restoration [67]. RIM-X analyses on the rejuvenated microstructures are shown in Figure 3.36 and precipitate sizes after the rejuvenation at 1290 °C are equivalent to the ones obtained for the original material. Considering all the results, rejuvenation treatment should be applied to AM1 at 1290 °C for 20 min to restore the optimal microstructure. In addition, microstructure was successfully restored in AM1 with PD at 750 °C by the same rejuvenation condition.

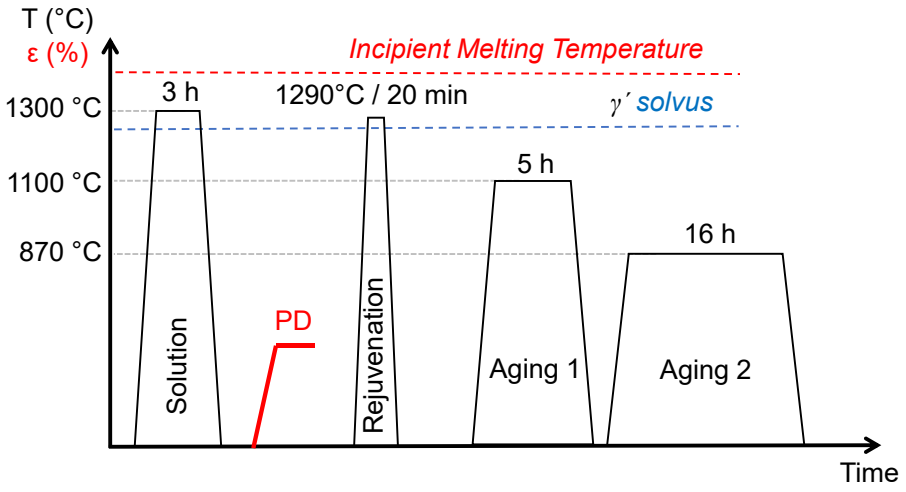

Figure 3.33. Temperature history diagram for AM1 with rejuvenation treatment after pre-deformation.

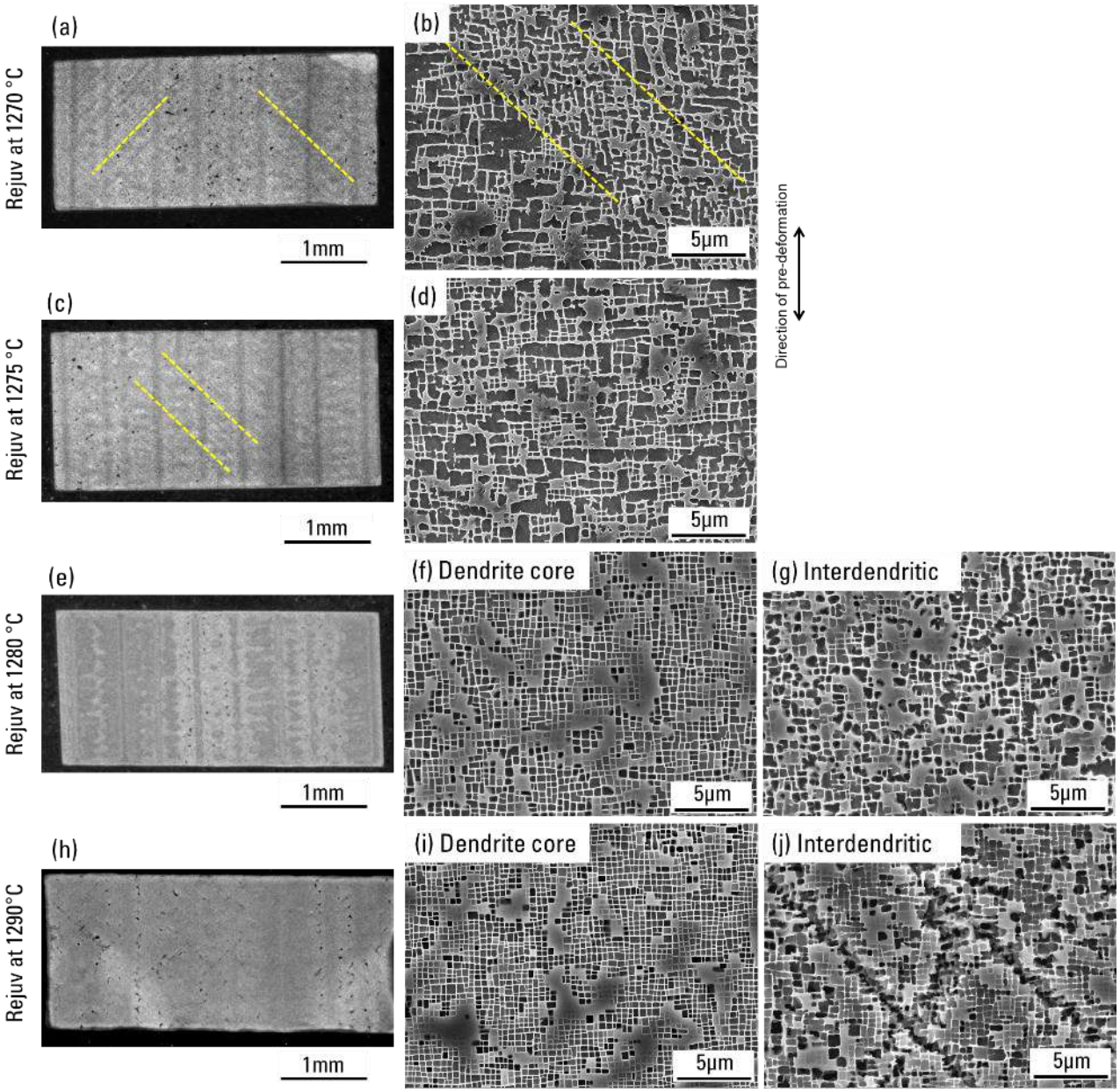

Figure 3.34. Microstructures of AM1 with PD at RT (strain = 0.87%) followed by rejuvenation treatment and standard aging treatments (HT1). Rejuvenation temperatures are labeled on the left and duration was 20 min.

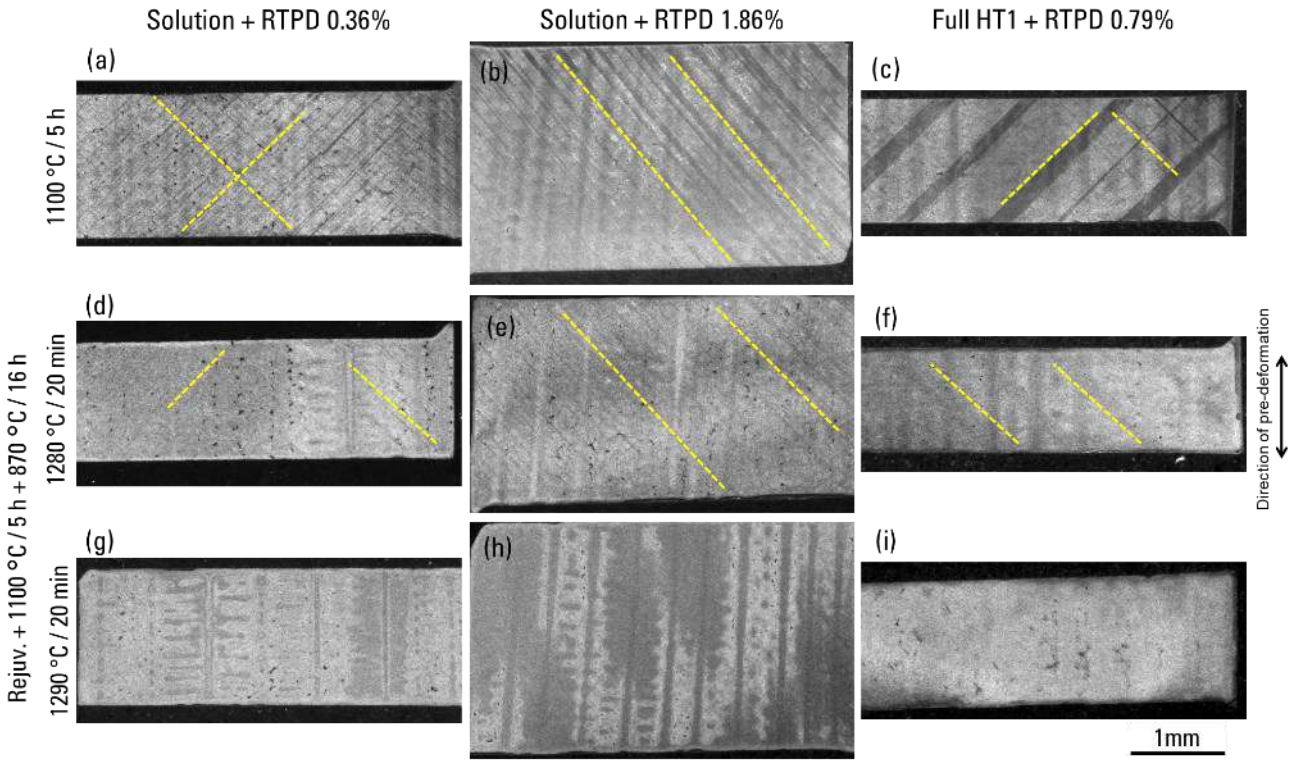

Figure 3.35. Low magnification images of AM1 with different pre-deformation at RT and subsequent rejuvenation and/or aging treatment. Conditions are labeled on the left. Plastic deformation was applied after aging treatments for (c, f, i).

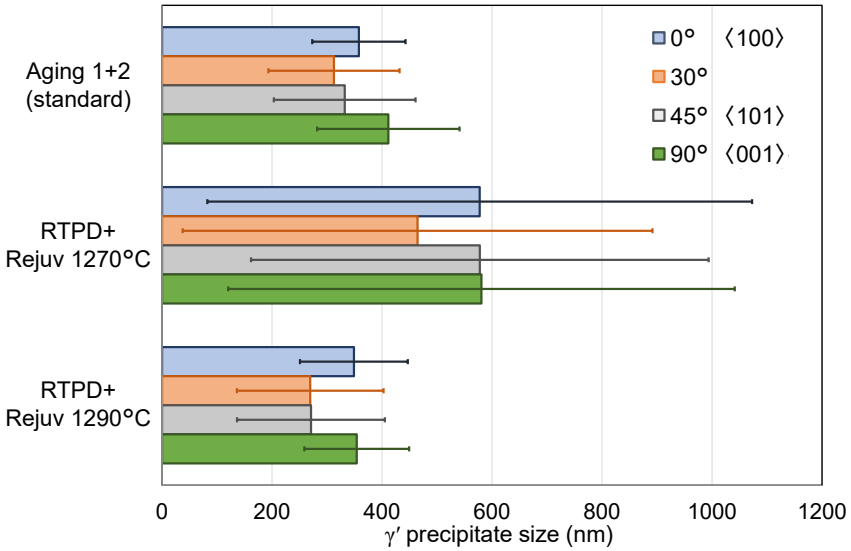

Figure 3.36. Result of RIM analysis using RIM-X software on AM1 with PD at RT followed by different rejuvenation temperatures. Standard aging treatments (1100 °C / 5 h + 870 °C / 16 h) were applied subsequently. Average size of γ′ precipitate is shown as solid bars and error bars are standard deviation.

Rejuvenation treatment at 1290 °C for 20 min on the AM1 with PD at 950 °C was also succeeded when the applied plastic strain was below 1% (Figure 3.37). On the other hand, recrystallization was observed in the specimens with higher plastic strain (= 2.17%) introduced at 950 °C, after rejuvenation at lower temperature of 1280 °C (Figure 3.37(c)). Recrystallization is confirmed to occur in the primary dendrite arms because grains in that region have cuboidal γ′ precipitates that sharing a different orientation with respect to the original (010) cutting surface of the specimen (Figure 3.38). Recrystallized grains are connected to the specimen

surface which was similarly seen in another study about the impact of PD on the recrystallization sensitivity during solution treatment [68]. Specimen that was paused after reaching the yield stress (Figure 3.1(B)) had its microstructure fully recrystallized during the rejuvenation at 1290 °C, including the interdendritic area (Figure 3.39(b)).

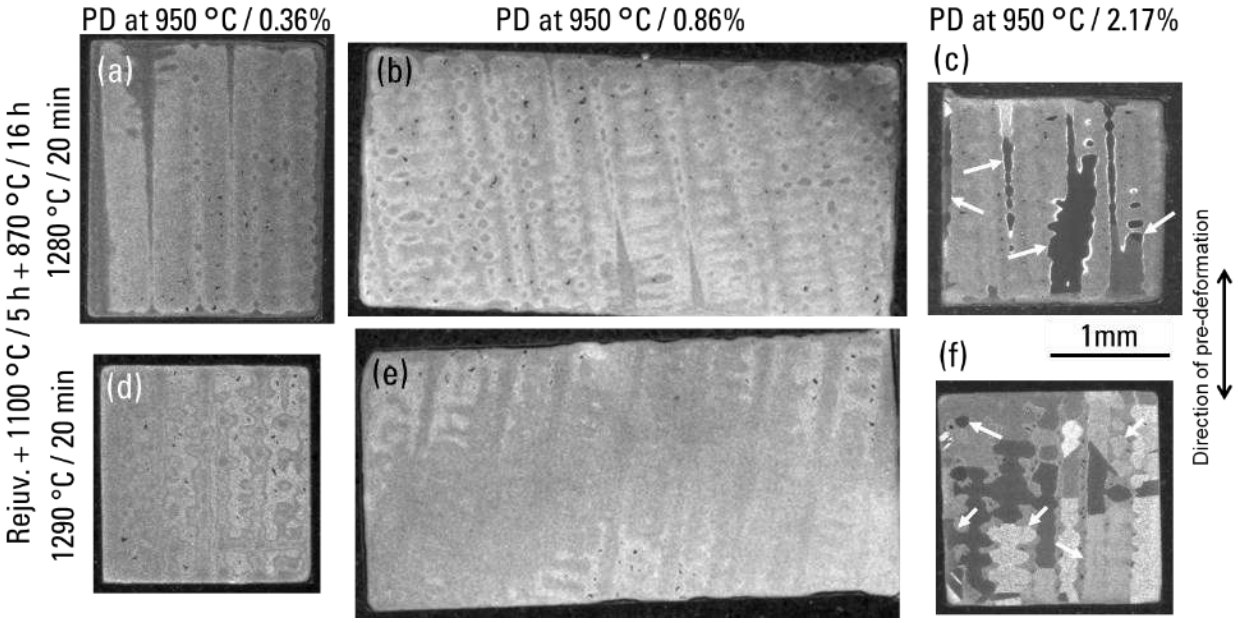

Figure 3.37. Low magnification images of AM1 with PD at 950°C followed by rejuvenation and aging treatments. Arrows in (c, f) are pointing at recrystallized grains.

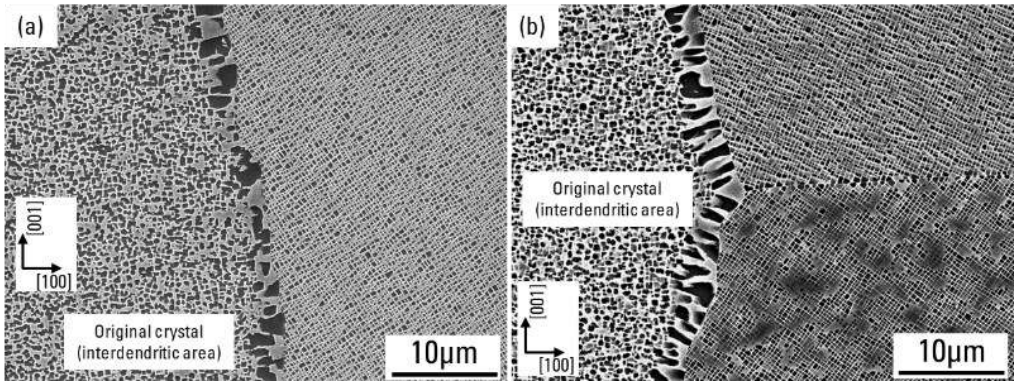

Figure 3.38. Grain boundaries between original crystal and recrystallized grain in AM1 specimens with PD at 950 °C, after rejuvenation at 1280 °C (a) and 1290 °C (b) for 20 min, followed by aging treatments (HT1).

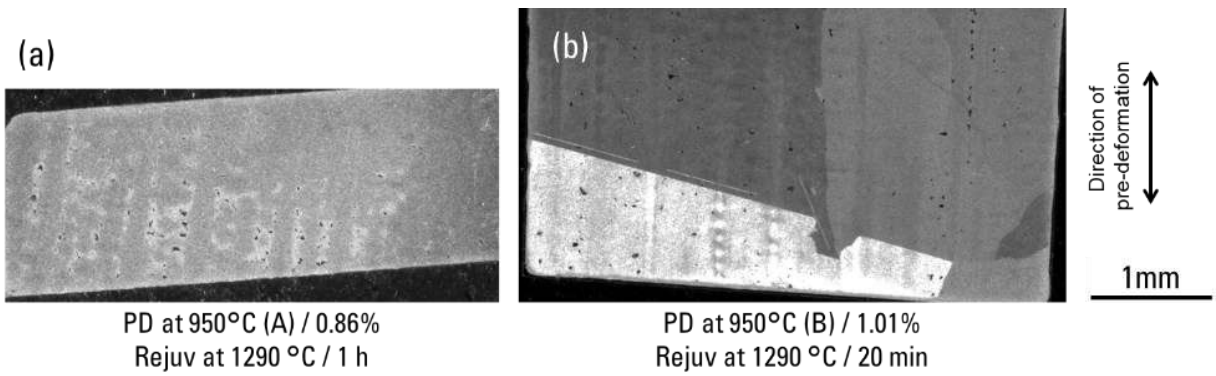

Figure 3.39. Low magnification images of AM1 with pre-deformation at 950 °C, deformed by continuous (a) and paused (b) procedure. Followed by rejuvenation at 1290 °C for 1 h in (a) and 20 min in (b) and aging treatments (HT1).

Dendritic structure is observed in low-mag images of the specimens without recrystallization and the contrast is strongly emphasized. The contrast difference remains in wider area when the rejuvenation temperature is lower (at 1280°C, Figure 3.34(e)), the plastic strain applied at RT is higher (Figure 3.35(h)), or if the specimens are pre-deformed at 950 °C (Figure 3.37(a, b)). The brighter area corresponds to interdendritic area with non-cubic precipitates and the darker area has ideal cubic precipitates. Such contrast is created because the higher surface fraction of matrix lies on (010) observation plane and decreases reflection from edges, leads to darker contrast. Those listed above contain large areas that had not been restored completely. Figure 3.40 is an example of the contrast border after rejuvenation and subsequent aging on the specimen with PD at 950 °C. The unrestored area had decreased when the rejuvenation treatment was extended to 1 h (Figure 3.39(a)). Stepwise heating-up to solution temperature with longer heating time can reduce internal strain gradually and can be an option for specimens with larger plastic strain.

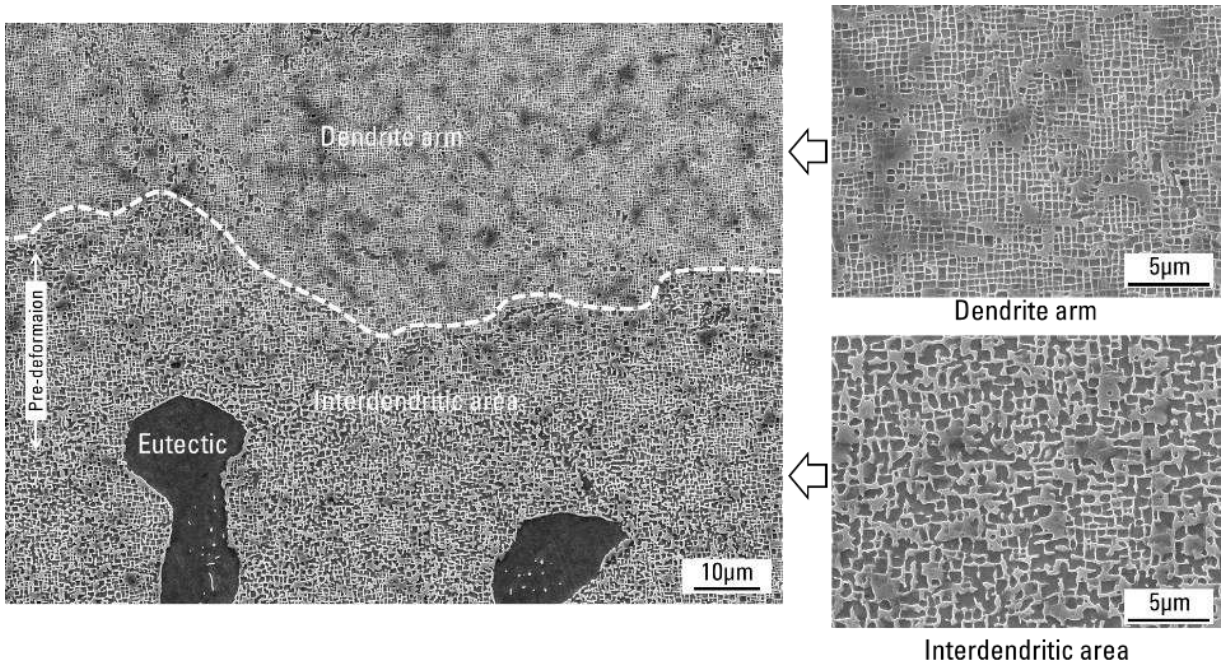

Figure 3.40. Microstructure of AM1 after PD at 950 °C with plastic strain of 0.87% followed by rejuvenation at 1290 °C for 20 min and two aging treatments. Dotted line indicates border between full-resorted dendrite arm and interdendritic area.

Results of rejuvenation tests on CMSX-4 Plus pre-deformed at RT are shown in Figures 3.41 and 3.42. Similarly to AM1, rejuvenation temperature below γ′ solvus at 1310 °C did not help but instead, degraded the microstructure with severe precipitate coarsening (Figure 3.41(b)). Slip plane traces were not visible after rejuvenation at 1325 °C. However, precipitates in the interdendritic areas are still coarse which indicates that the rejuvenation temperature is not yet optimal (Figures 3.41(c, d)). Microstructure is restored both in primary dendrite arms and in the interdendritic areas after rejuvenation at 1330 °C (Figures 3.42(b, c)), and the homogeneity improved after rejuvenation at 1335 °C (Figures 3.42(d-f)). In these specimens with successful restoration of internal microstructures, surface recrystallization was observed for both specimens rejuvenated at 1330 °C and 1335 °C (arrows in Figure 3.42). Oxidation can help the recrystallization by dissolution of γ′ precipitates at the γ′-depleted layer. However, the recrystallization only occurred at the former cylindrical surface side (see arrows in Figure 3.42). Plastic strain is locally higher at the specimen surface since it acts as free surface during PD and locally higher stored energy probably activated recrystallization when the

temperature exceeded the γ′ solvus. From the results above, suitable rejuvenation condition for CMSX-4 Plus with PD at RT is determined as at 1330 °C for 1 h.

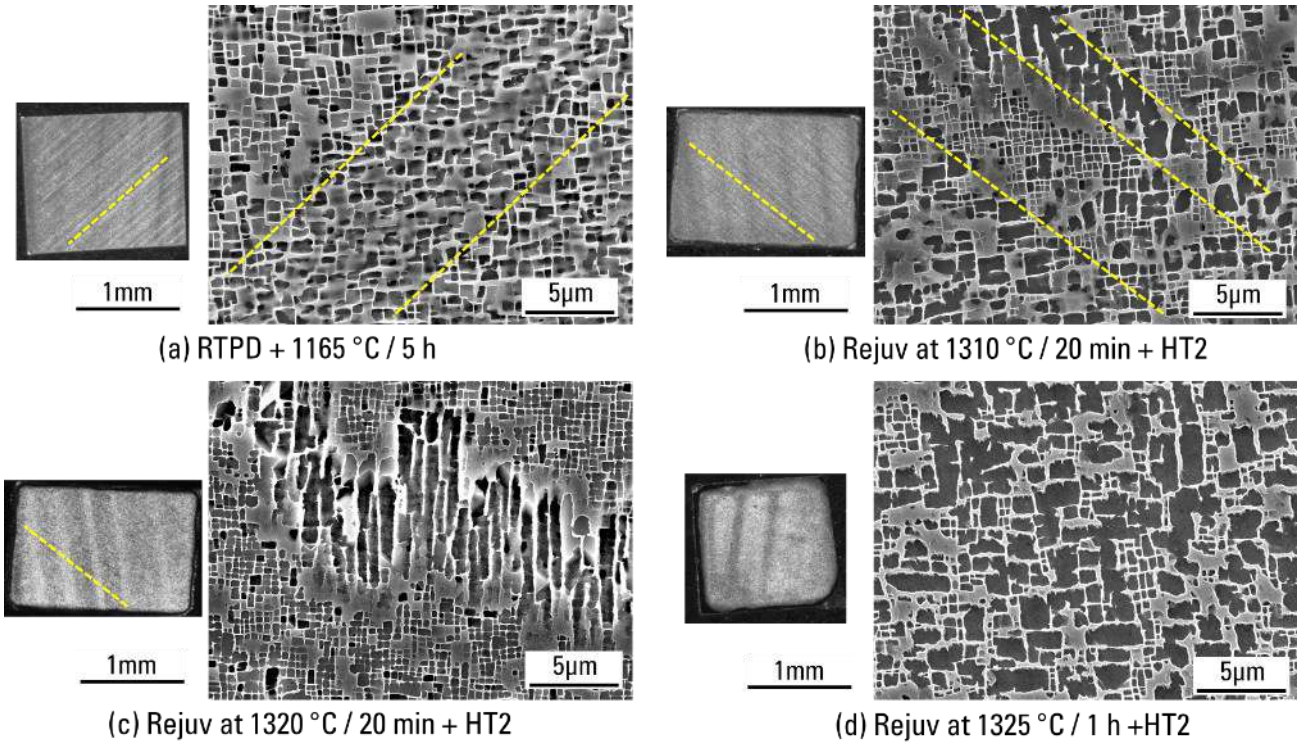

Figure 3.41. Microstructure of CMSX-4 Plus after PD at RT. (a) is for comparison with other images, only first aging treatment of HT2 applied. (b-c) are with rejuvenation treatment and subsequent HT2 aging treatments.

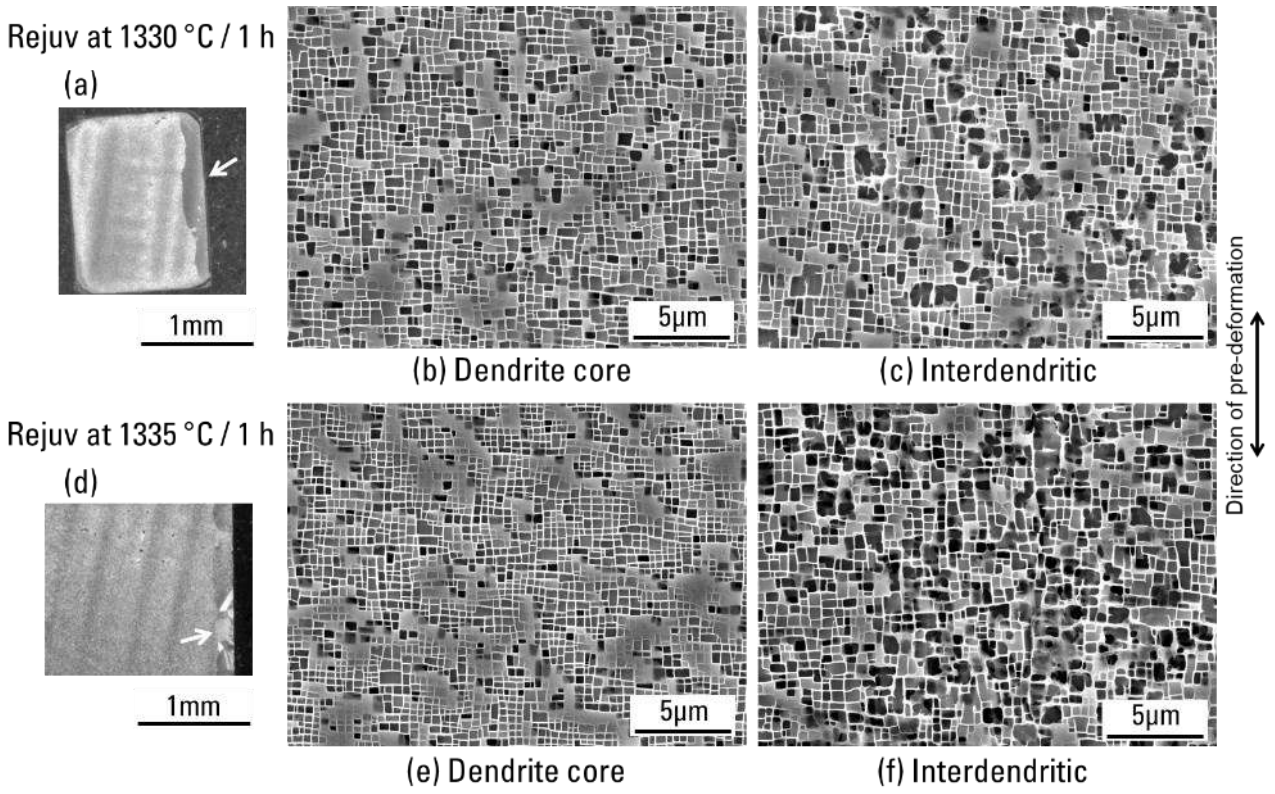

Figure 3.42. Microstructure of CMSX-4 Plus after PD at RT with rejuvenation treatment and subsequent HT2 aging treatments. Arrows are indicating surface recrystallization at the cylindrical surface.

3. 6. 2. Effects of deformation methods on the rejuvenation capability

Microstructures and creep properties (creep test results are presented in following chapter) were restored by rejuvenation treatment without HIP. Rejuvenation treatment is known to effectively restore creep damaged Ni-based SX superalloys [59–63], however, this study is the first one to show the possibility of rejuvenating SX superalloys with tensile PD at low temperature (i.e. highly localized plasticity). Although recrystallization is always a risk for rejuvenation, research on the condition which may cause recrystallization is not available. To discuss rejuvenation capability, some rejuvenation results on crept Ni-based SX superalloys are taken from other studies [59,61,63] and they are plotted in Figure 3.43 with the results in this study.

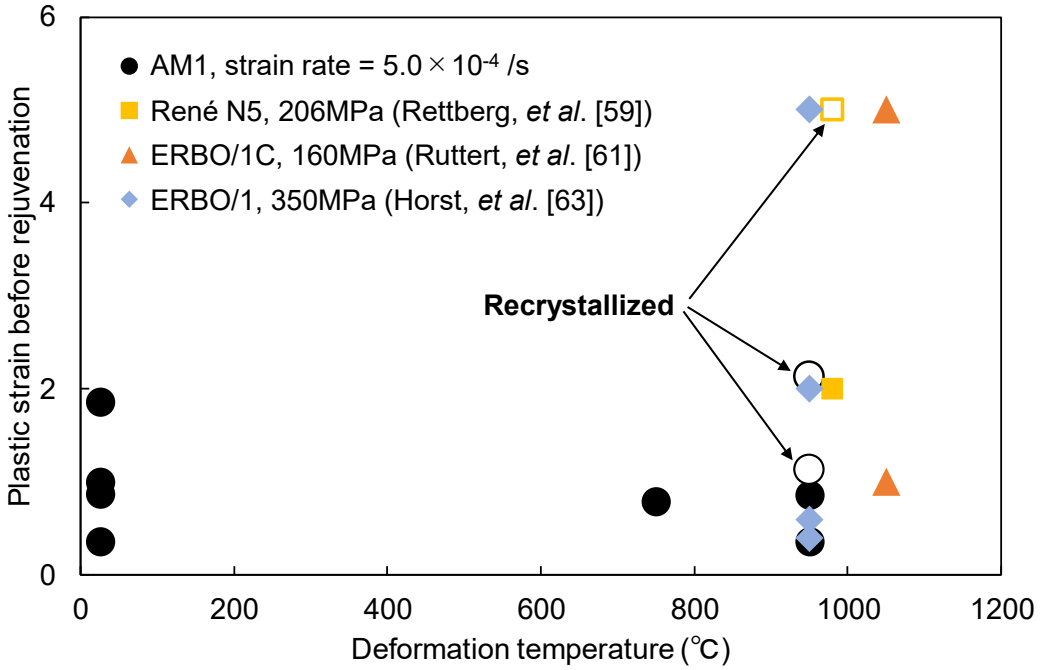

Figure 3.43. Relationship between deformation temperature and plastic strain before rejuvenation treatment for different alloys. Filled plots are showing successful rejuvenation. Plastic strain values adopted from other studies [59,61,63] are introduced by creep.

According to the result from this study, PD at high temperature (at 950 °C) can cause recrystallization during rejuvenation treatment. Similar relationship of recrystallization sensitivity after high-temperature PD (especially at PD temperature between 900-1000 °C) with subsequent annealing above 1280 °C on a SX superalloy has been reported in the study for understanding recrystallization during solution treatment [6,69,70]. Since deformation at 950 °C is driven by dislocation by-passing at γ/γ′ interface [1], plastic strain is macroscopically homogeneous. However, a higher dislocation density than PD at RT should be accumulated at the γ side of the γ/γ′ interfaces that enhances microstructure evolution in all areas during aging. Dislocation filling up in the matrix and the γ/γ′ interface is probably the source of recrystallization occurring during rejuvenation treatment.

In other studies about rejuvenation after creep deformation at 950 °C, microstructure was restored without recrystallization even with much higher plastic strain (up to 5%, Figure 3.43) [62,63]. In these studies, typical directionally coarsened microstructures were observed before rejuvenation treatment and the precipitate size is obviously larger compared to the ones observed in the present study. Meanwhile, compressive plastic

deformation at 980 °C is reported to introduce stacking faults into γ′ precipitates during deformation and it may facilitate recrystallization during solution treatment [62,63]. However, such sub-structure is unlikely to appear neither during creep deformation with lower applied stress nor during tensile deformation with lower strain rates. In Rene N5 after creep at 950 °C, recrystallization was reported in the vicinity of carbides which may have different morphology compared to carbon-free superalloys [59,60]. These are the indications that dislocation types, distribution, and quantity determined by the active deformation mechanisms have different reordering and annihilating behavior during dissolution of γ′ phase, and the magnitude of plastic strain cannot be a simple indicator for boundary condition. Further experiments on the rejuvenation treatment and microstructure analyses are necessary to clearly identify the precise condition that activates recrystallization.

3. 7. Summary

Plastic deformation was introduced to AM1 and CMSX-4 Plus Ni-based single crystal superalloys and subsequent aging treatments were applied to mimic the industrial process that causes creep life debit shown in the Chapter 1. Microstructural behaviors with different pre-deformation and heat treatment combinations were analyzed in this chapter to understand how precipitate morphologies evolved during the processes.

The followings main are results have been obtained from microstructure analyses after pre-deformation at room-temperature:

- From the quantitative analysis on the γ′ precipitate size evolution during aging treatments, precipitate evolution is shown to mainly occur during aging treatment at higher temperature (above 1100 °C), in both AM1 and CMSX-4 Plus. It was also the same regardless of the temperature at which pre-deformation was applied. Precipitate size evolution after the secondary aging is due to the adjustment of precipitate size for equilibrated γ′ volume fraction at 870 °C.

- Because AM1 has higher resistance to γ′ shearing at room temperature, higher internal strain is assumed to be stored in a single band compared to CMSX-4 Plus that showed higher density of slip bands after room temperature tensile deformation for the same pre-strain magnitude. Microstructure evolution in AM1 in the vicinity of the slip band was more anisotropic and showed similar characteristic to the directional coarsening, or γ′-rafting. Lower stored energy of a slip band in CMSX-4 Plus showed less anisotropy and evolved precipitates in the vicinity of the band were closer to cuboidal.

- STEM analysis after full heat treatment of pre-deformed AM1 showed that dislocations in the microstructure coarsened band are mainly of 1/2⟨101⟩{111} type, which favors climb and glide when exposed at high temperature like 1100 °C. This is similar microstructure evolution mechanism that occurs during prolonged high temperature exposure or creep loading at high temperature (≥ 1000 °C) and low stress (≤ 150 MPa) conditions.

Pre-deformation at higher temperatures (at 750 °C and 950 °C) was introduced to AM1 between solution and aging treatments and obtained microstructures were compared with the same alloy pre-deformed at room-temperature.

- Microstructure evolved differently during aging treatments after a plastic deformation introduced either in precipitate shearing regime (≤ 750 °C) or in the γ/γ′ interface dislocation by-passing regime (950 °C). Mild directional coarsening (pre-rafting) was observed after pre-deformation at 950 °C with subsequent aging treatments. The magnitude of directional coarsening decreased and become sluggish as plastic strain introduced at 950 °C increases.

- Decreased size of pre-rafts with increasing plastic strain in pre-deformation at 950 °C is probably due to the higher dislocation density stored in the γ matrix during plastic deformation. The interfacial dislocations suppressed precipitation coarsening during aging treatments.

Rejuvenation treatment has been introduced after pre-deformation at different temperatures for demonstrating microstructure restoration, and also to understand how different dislocation structures affect the microstructure at close-to-solvus and supersolvus temperatures.

- Rejuvenation treatment successfully restored microstructure of AM1 after room-temperature plastic deformation with plastic strain below 1.86% or plastic deformation at 950 °C with plastic strain below 0.87%. It was also successful for CMSX-4 Plus with plastic strain of 0.79%. Suitable rejuvenation conditions are at 1290 °C for 20 min for AM1 and at 1330 °C for 1 h for CMSX-4 Plus.

- Recrystallization occurred in the specimen with higher strain (2.17%) during rejuvenation treatment at sub-solvus temperature (1280 °C). It is triggered by dissolution of γ′ through densely stored dislocations. The risk for recrystallization during rejuvenation is smaller if pre-deformation was applied at lower temperature.

References

[1] W.W. Milligan, S.D. Antolovich, Yielding and deformation behavior of the single crystal superalloy PWA 1480, Metall. Trans. A. 18 (1987) 85–95. doi:10.1007/BF02646225.

[2] H. Mughrabi, Microstructural aspects of high temperature deformation of monocrystalline nickel base superalloys: some open problems, Mater. Sci. Technol. 25 (2009) 191–204. doi:10.1179/174328408X361436.

[3] M. Sakaguchi, M. Ike, M. Okazaki, Microstructural changes in a single crystal Ni-base superalloy induced by plastic straining, Mater. Sci. Eng. A. 534 (2012) 253–259. doi:10.1016/J.MSEA.2011.11.066.

[4] T.M. Pollock, A.S. Argon, Directional coarsening in nickel-base single crystals with high volume fractions of coherent precipitates, Acta Metall. Mater. 42 (1994) 1859–1874. doi:10.1016/0956-7151(94)90011-6.

[5] T. Ichitsubo, D. Koumoto, M. Hirao, K. Tanaka, M. Osawa, T. Yokokawa, H. Harada, Rafting mechanism for Ni-base superalloy under external stress: elastic or elastic–plastic phenomena?, Acta Mater. 51 (2003) 4033–4044. doi:10.1016/S1359-6454(03)00224-6.

[6] D.C. Cox, B. Roebuck, C.M.F. Rae, R.C. Reed, Recrystallisation of single crystal superalloy CMSX-4, Mater. Sci. Technol. 19 (2003) 440–446. doi:10.1179/026708303225010731.

[7] P.H. Thornton, R.G. Davies, T.L. Johnston, The temperature dependence of the flow stress of the γ′ phase based upon Ni_3Al, Metall. Trans. 1 (1970) 207–218. doi:10.1007/BF02819263.

[8] L.M. Bortoluci Ormastroni, S. Utada, J. Rame, L. Mataveli Suave, K. Kawagishi, H. Harada, P. Villechaise, J. Cormier, Tensile, low cycle fatigue and very high cycle fatigue characterizations of

advanced single crystal nickel-based superalloys, in: S. Tin, M. Hardy, J. Clews, J. Cormier, Q. Feng, J. Marcin, C. O'Brien, A. Suzuki (Eds.), Superalloys 2020, Springer International Publishing, 2020: pp. 341–351. doi:10.1007/978-3-030-51834-9_33.

[9] P. Beardmore, R.G. Davies, T.L. Johnston, Temperature Dependence of the Flow Stress of Nickel-Base Alloys, Trans. Metall. Soc. AlME. 245 (1969) 1537–1545.

[10] A. Sengupta, S.K. Putatunda, L. Bartosiewicz, J. Hangas, P.J. Nailos, M. Peputapeck, F.E. Alberts, Tensile behavior of a new single-crystal nickel-based superalloy (CMSX-4) at room and elevated temperatures, J. Mater. Eng. Perform. 3 (1994) 73–81. doi:10.1007/BF02654502.

[11] M. Sakaguchi, M. Okazaki, Distinctive role of plastic and creep strain in directional coarsening of a Ni-base single crystal superalloy, Mater. Sci. Eng. A. 710 (2018) 121–128. doi:10.1016/j.msea.2017.10.085.

[12] A. Royer, P. Bastie, M. Veron, In situ determination of γ′ phase volume fraction and of relations between lattice parameters and precipitate morphology in Ni-based single crystal superalloy, Acta Mater. 46 (1998) 5357–5368. doi:https://doi.org/10.1016/S1359-6454(98)00206-7.

[13] P. Caron, C. Ramusat, F. Diologent, Influence of the γ′ fraction on the γ/γ′ topological inversion during high temperature creep of single crystal superalloys, in: Superalloys 2008, TMS Warrendale, PA, 2008: pp. 159–167.

[14] J. Cormier, Thermal Cycling Creep Resistance of Ni-Based Single Crystal Superalloys, in: Superalloys 2016, John Wiley & Sons, Inc., 2016: pp. 383–394. doi:doi:10.1002/9781119075646.ch42.

[15] A. Lasalmonie, J.L. Strudel, Interfacial dislocation networks around γ′ precipitates in nickel-base alloys, Philos. Mag. A J. Theor. Exp. Appl. Phys. 32 (1975) 937–949. doi:10.1080/14786437508221665.

[16] V. Caccuri, R. Desmorat, J. Cormier, Tensorial nature of γ′-rafting evolution in nickel-based single crystal superalloys, Acta Mater. 158 (2018) 138–154. doi:https://doi.org/10.1016/j.actamat.2018.07.033.

[17] V. Caccuri, J. Cormier, R. Desmorat, γ′-Rafting mechanisms under complex mechanical stress state in Ni-based single crystalline superalloys, Mater. Des. 131 (2017) 487–497. doi:10.1016/j.matdes.2017.06.018.

[18] H. Long, H. Wei, Y. Liu, S. Mao, J. Zhang, S. Xiang, Y. Chen, W. Gui, Q. Li, Z. Zhang, X. Han, Effect of lattice misfit on the evolution of the dislocation structure in Ni-based single crystal superalloys during thermal exposure, Acta Mater. 120 (2016) 95–107. doi:10.1016/j.actamat.2016.08.035.

[19] Q. Gao, L. Liu, X. Tang, Z. Peng, M. Zhang, S. Tian, Evolution of interfacial dislocation networks during long term thermal aging in Ni-based single crystal superalloy DD5, China Foundry. 16 (2019) 14–22. doi:10.1007/s41230-019-8113-y.

[20] F. Ram, Z. Li, S. Zaefferer, S.M. Hafez Haghighat, Z. Zhu, D. Raabe, R.C. Reed, On the origin of creep dislocations in a Ni-base, single-crystal superalloy: an ECCI, EBSD, and dislocation dynamics-based study, Acta Mater. 109 (2016) 151–161. doi:https://doi.org/10.1016/j.actamat.2016.02.038.

[21] A. Epishin, T. Link, G. Nolze, SEM investigation of interfacial dislocations in nickel-base superalloys, J. Microsc. 228 (2007) 110–117. doi:10.1111/j.1365-2818.2007.01831.x.

[22] P. Kontis, Z. Li, D.M. Collins, J. Cormier, D. Raabe, B. Gault, The effect of chromium and cobalt segregation at dislocations on nickel-based superalloys, Scr. Mater. 145 (2018) 76–80. doi:10.1016/j.scriptamat.2017.10.005.

[23] J.R. Mianroodi, P. Shanthraj, P. Kontis, J. Cormier, B. Gault, B. Svendsen, D. Raabe, Atomistic phase field chemomechanical modeling of dislocation-solute-precipitate interaction in Ni–Al–Co, Acta Mater. 175 (2019) 250–261. doi:10.1016/j.actamat.2019.06.008.

[24] D. Qi, L. Wang, P. Zhao, L. Qi, S. He, Y. Qi, H. Ye, J. Zhang, K. Du, Facilitating effect of interfacial

grooves on the rafting of nickel-based single crystal superalloy at high temperature, Scr. Mater. 167 (2019) 71–75. doi:10.1016/j.scriptamat.2019.04.001.

[25] T. Link, A. Epishin, M. Paulisch, T. May, Topography of semicoherent γ/γ′-interfaces in superalloys: Investigation of the formation mechanism, Mater. Sci. Eng. A. 528 (2011) 6225–6234. doi:https://doi.org/10.1016/j.msea.2011.04.049.

[26] J.X. Yang, Q. Zheng, X.F. Sun, H.R. Guan, Z.Q. Hu, Morphological evolution of γ′ phase in K465 superalloy during prolonged aging, Mater. Sci. Eng. A. 457 (2007) 148–155. doi:10.1016/j.msea.2006.12.041.

[27] R.A. Ricks, A.J. Porter, R.C. Ecob, The growth of γ′ precipitates in nickel-base superalloys, Acta Metall. 31 (1983) 43–53. doi:10.1016/0001-6160(83)90062-7.

[28] A. Royer, P. Bastie, D. Bellet, J.L. Strudel, Temperature dependence of the lattice mismatch of the AM1 superalloy influence of the γ′ precipitates' morphology, Philos. Mag. A. 72 (1995) 669–689. doi:10.1080/01418619508243792.

[29] A.K. Singh, N. Louat, K. Sadananda, Dislocation network formation and coherency loss around gamma- prime precipitates in a nickel- base superalloy, Metall. Trans. A. 19 (1988) 2965–2973. doi:10.1007/BF02647723.

[30] J.S. Van Sluytman, T.M. Pollock, Optimal precipitate shapes in nickel-base γ–γ′ alloys, Acta Mater. 60 (2012) 1771–1783. doi:10.1016/j.actamat.2011.12.008.

[31] A.B. Parsa, P. Wollgramm, H. Buck, A. Kostka, C. Somsen, A. Dlouhy, G. Eggeler, Ledges and grooves at γ/γ′ interfaces of single crystal superalloys, Acta Mater. 90 (2015) 105–117. doi:10.1016/j.actamat.2015.02.005.

[32] L. Tian, C. Xu, C. Ma, Recrystallization of a single crystal Ni-base superalloy in ⟨011⟩ and ⟨111⟩ orientations, Mater. Charact. 127 (2017) 116–120. doi:10.1016/j.matchar.2017.01.020.

[33] C.P. Liu, X.N. Zhang, L. Ge, C.Y. Wang, T. Yu, Z. Zhang, The effect of pre-deformation on the microstructure evolution of NiAl model single crystal superalloy during thermal exposure at 1000 °C, Mater. Sci. Eng. A. 754 (2019) 556–561. doi:10.1016/j.msea.2019.03.099.

[34] D. Caillard, A. Couret, Chapter 50 Dislocation Cores and Yield Stress Anomalies, in: F.R.N. Nabarro, M.S.B.T.-D. in S. Duesbery (Eds.), L12 Ordered Alloy., Elsevier, 1996: pp. 69–134. doi:https://doi.org/10.1016/S1572-4859(96)80005-2.

[35] D.M. Shah, D.N. Duhl, The effect of orientation, temperature and gamma prime size on the yield strength of a single crystal nickel base superalloy, Superalloys 1984. (1984) 105–114.

[36] R.W. Kozar, A. Suzuki, W.W. Milligan, J.J. Schirra, M.F. Savage, T.M. Pollock, Strengthening Mechanisms in Polycrystalline Multimodal Nickel-Base Superalloys, Metall. Mater. Trans. A. 40 (2009) 1588–1603. doi:10.1007/s11661-009-9858-5.

[37] A. Pineau, S.D. Antolovich, High temperature fatigue of nickel-base superalloys – A review with special emphasis on deformation modes and oxidation, Eng. Fail. Anal. 16 (2009) 2668–2697. doi:10.1016/j.engfailanal.2009.01.010.

[38] M. Pessah-Simonetti, P. Caron, T. Khan, Effect of a long-term prior aging on the tensile behaviour of a high-performance single crystal superalloy, Le Journal de Physique IV Colloque. 3 (1993) C7-347.

[39] M. Véron, P. Bastie, Strain induced directional coarsening in nickel based superalloys: Investigation on kinetics using the small angle neutron scattering (SANS) technique, Acta Mater. 45 (1997) 3277–3282. doi:10.1016/S1359-6454(97)00035-9.

[40] S. Pierret, T. Etter, A. Evans, H. Van Swygenhoven, Origin of localized rafting in Ni-based single crystal turbine blades before service and its influence on the mechanical properties, Acta Mater. 61 (2013) 1478–1488. doi:10.1016/j.actamat.2012.11.024.

[41] Z.P. Luo, Z.T. Wu, D.J. Miller, The dislocation microstructure of a nickel-base single-crystal superalloy after tensile fracture, Mater. Sci. Eng. A. 354 (2003) 358–368. doi:10.1016/S0921-

5093(03)00039-X.

[42] S. V Prikhodko, A.J. Ardell, Coarsening of γ′ in Ni-Al alloys aged under uniaxial compression: III. Characterization of the morphology, Acta Mater. 51 (2003) 5021–5036. doi:10.1016/S1359-6454(03)00328-8.

[43] N. Matan, D.C. Cox, C.M.F. Rae, R.C. Reed, On the kinetics of rafting in CMSX-4 superalloy single crystals, Acta Mater. 47 (1999) 2031–2045. doi:10.1016/S1359-6454(99)00093-2.

[44] J.-B. le Graverend, J. Cormier, F. Gallerneau, S. Kruch, J. Mendez, Highly non-linear creep life induced by a short close γ′-solvus overheating and a prior microstructure degradation on a nickel-based single crystal superalloy, Mater. Des. 56 (2014) 990–997. doi:https://doi.org/10.1016/j.matdes.2013.12.025.

[45] T. Konkova, S. Rahimi, S. Mironov, T.N. Baker, Effect of strain level on the evolution of microstructure in a recently developed AD730 nickel based superalloy during hot forging, Mater. Charact. 139 (2018) 437–445. doi:10.1016/j.matchar.2018.03.027.

[46] H. Monajati, F. Zarandi, M. Jahazi, S. Yue, Strain induced γ′ precipitation in nickel base superalloy Udimet 720 using a stress relaxation based technique, Scr. Mater. 52 (2005) 771–776. doi:10.1016/j.scriptamat.2004.12.006.

[47] N. Mrozowski, G. Hénaff, F. Hamon, A.-L. Rouffié, J.-M. Franchet, J. Cormier, P. Villechaise, Aging of γ′ Precipitates at 750 °C in the Nickel-Based Superalloy AD730TM: A Thermally or Thermo-Mechanically Controlled Process?, Metals. 10 (2020). doi:10.3390/met10040426.

[48] R. Giraud, Z. Hervier, J. Cormier, G. Saint-Martin, F. Hamon, X. Milhet, J. Mendez, Strain Effect on the γ′ Dissolution at High Temperatures of a Nickel-Based Single Crystal Superalloy, Metall. Mater. Trans. A. 44 (2013) 131–146. doi:10.1007/s11661-012-1397-9.

[49] P. Caron, F. Diogolent, S. Drawin, Influence of chemistry on the tensile yield strength of nickel-based single crystal superalloys, in: Adv. Mater. Res., Trans Tech Publ, 2011: pp. 345–350.

[50] D. Raynor, J.M. Silcock, Strengthening Mechanisms in γ′ Precipitating Alloys, Met. Sci. J. 4 (1970) 121–130. doi:10.1179/msc.1970.4.1.121.

[51] H. Zhou, H. Harada, Y. Ro, I. Okada, Investigations on the thermo-mechanical fatigue of two Ni-based single-crystal superalloys, Mater. Sci. Eng. A. 394 (2005) 161–167. doi:10.1016/j.msea.2004.11.013.

[52] Y. Ro, H. Zhou, Y. Koizumi, T. Yokokawa, T. Kobayashi, H. Harada, I. Okada, Thermal-Mechanical Fatigue Property of Ni-Base Single Crystal Superalloys TMS-82+ and TMS-75, Mater. Trans. 45 (2004) 396–398. doi:10.2320/matertrans.45.396.

[53] Y.S. Huang, X.G. Wang, C.Y. Cui, J.G. Li, L.H. Ye, G.C. Hou, Y.H. Yang, J.L. Liu, J.D. Liu, Y.Z. Zhou, X.F. Sun, The effect of coarsening of γ′ precipitate on creep properties of Ni-based single crystal superalloys during long-term aging, Mater. Sci. Eng. A. 773 (2020) 138886. doi:10.1016/j.msea.2019.138886.

[54] S. Tang, L.K. Ning, T.Z. Xin, Z. Zheng, Coarsening Behavior of Gamma Prime Precipitates in a Nickel Based Single Crystal Superalloy, J. Mater. Sci. Technol. 32 (2016) 172–176. doi:10.1016/j.jmst.2015.10.005.

[55] T. Link, A. Epishin, B. Fedelich, Inhomogeneity of misfit stresses in nickel-base superalloys: Effect on propagation of matrix dislocation loops, Philos. Mag. 89 (2009) 1141–1159. doi:10.1080/14786430902877810.

[56] T. Yokokawa, H. Harada, K. Kawagishi, Y. Koizumi, T. Kobayashi, Quantitative Analysis of Creep Strengthening Factors in Ni-Base Single Crystal Superalloys, in: Superalloys 2012, 2012: pp. 285–292. doi:10.1002/9781118516430.ch31.

[57] G. VanDrunen, J. Liburdi, Rejuvenation of Used Turbine Blades by Hot Isostatic Pressing, in: Proc. Sixth Turbomach. Symp., 1977: pp. 55–60.

[58] J. Liburdi, 40 Years of Reliable Life Extension of Industrial and Aero Turbine Components, in: Turbine Forum 2017, 2017.

[59] L.H. Rettberg, M. Tsunekane, T.M. Pollock, Rejuvenation of nickel-based superalloys GTD444(DS) and René N5(SX), in: Superalloys 2012, 2012: pp. 341–349. doi:10.1002/9781118516430.ch37.

[60] L. Rettberg, Rejuvenation of Ni-base Superalloys GTD444 and René N5, University of California, Santa Barbara, PhD Thesis, 2016.

[61] B. Ruttert, D. Bürger, L.M. Roncery, A.B. Parsa, P. Wollgramm, G. Eggeler, W. Theisen, Rejuvenation of creep resistance of a Ni-base single-crystal superalloy by hot isostatic pressing, Mater. Des. 134 (2017) 418–425. doi:10.1016/j.matdes.2017.08.059.

[62] B. Ruttert, O. Horst, I. Lopez-galilea, D. Langenkämper, A. Kostka, C. Somsen, J. V Goerler, M.A. Ali, O. Shchyglo, I. Steinbach, G. Eggeler, W. Theisen, Rejuvenation of Single-Crystal Ni-Base Superalloy Turbine Blades: Unlimited Service Life?, Metall. Mater. Trans. A. 49 (2018) 4262–4273. doi:10.1007/s11661-018-4745-6.

[63] O.M. Horst, B. Ruttert, D. Bürger, L. Heep, H. Wang, A. Dlouhý, W. Theisen, G. Eggeler, On the rejuvenation of crept Ni-Base single crystal superalloys (SX) by hot isostatic pressing (HIP), Mater. Sci. Eng. A. 758 (2019) 202–214. doi:10.1016/j.msea.2019.04.078.

[64] J. Pal, D. Srinivasan, E. Cheng, Effect of Rejuvenation Heat Treatment and Aging on the Microstructural Evolution in Rene N5 Single Crystal Ni Base Superalloy Blades, in: Superalloys 2016, John Wiley & Sons, Inc., 2016: pp. 285–291. doi:10.1002/9781119075646.ch31.

[65] Z.-X. Shi, S.-Z. Liu, J.-R. Li, Rejuvenation Heat Treatment of the Second-Generation Single-Crystal Superalloy DD6, Acta Metall. Sin. (English Lett.) 28 (2015) 1278–1285. doi:10.1007/s40195-015-0323-8.

[66] L. Wang, Y. Liu, J. Liang, Effect of Rejuvenation Heat Treatment on the Creep Property and Microstructural Evolution of a Ni-Base Superalloy, Appl. Sci. 10 (2020) 1187. doi:10.3390/app10031187.

[67] L. Wang, F. Pyczak, J. Zhang, L.H. Lou, R.F. Singer, Effect of eutectics on plastic deformation and subsequent recrystallization in the single crystal nickel base superalloy CMSX-4, Mater. Sci. Eng. A. 532 (2012) 487–492. doi:10.1016/j.msea.2011.11.015.

[68] R. Bürgel, P.D. Portella, J. Preuhs, Recrystallization in single crystals of nickel base superalloys, in: Superalloys 2000, 2000: pp. 229–238. doi:10.7449/2000/Superalloys_2000_229_238.

[69] Z. Li, X. Fan, Q. Xu, B. Liu, Influence of deformation temperature on recrystallization in a Ni-based single crystal superalloy, Mater. Lett. 160 (2015) 318–322. doi:10.1016/j.matlet.2015.07.120.

[70] Z. Li, Q. Xu, B. Liu, Experimental investigation on recrystallization mechanism of a Ni-base single crystal superalloy, J. Alloys Compd. 672 (2016) 457–469. doi:10.1016/j.jallcom.2016.02.149.

CHAPTER 4
CREEP DAMAGING MECHANISMS OF PRE-DEFORMED NI-BASED SINGLE CRYSTAL SUPERALLOYS

Table of contents

Résumé : Mécanismes de dégradation par fluage des superalliages monocristallins base-Ni avec pré-déformation 107

4. 1. Introduction 110

4. 2. Creep damaging mechanisms of SX superalloys with pre-deformation at RT 110

4.2.1. Creep results on AM1-RTPD-HT1 at higher temperatures (1050 °C, 950 °C) 110

4.2.2. Microstructure characterizations on AM1 after creep tests at higher temperatures (1050 °C, 950 °C) 113

A) AM1 without PD 113

B) AM1 with PD, creep test at 1050 °C / 140 MPa 115

C) AM1 with PD at 1050 °C / 200 MPa 117

D) AM1 with PD at 950 °C / 300 MPa 118

4.2.3. Local lattice misorientation in the microstructure coarsened band 121

4.2.4. Creep results on 4P-RTPD-HT1 and 4P-RTPD-HT2 at higher temperatures (1150 °C, 1050 °C) 122

4.2.5. Microstructure characterizations of CMSX-4 Plus after creep tests at higher temperatures (1150 °C and 1050 °C) 124

A) CMSX-4 Plus at 1150 °C / 110 MPa 124

B) CMSX-4 Plus at 1050 °C / 200 MPa 129

4.2.6. Void nucleation and growth during heat treatment and creep 131

A) Stereological analyses of voids 131

B) Void nucleation and growth mechanism 134

4.2.7. Localized shearing and damage accumulation mechanisms during high temperature creep 136

A) γ′-rafting regime (volume fraction ~50%) 136

B) Topological inversion regime (volume fraction >50%) 139

4.2.8. Effect of pre-deformation at RT on creep properties at lower temperatures 141

A) AM1 at 850 °C / 500 MPa and 750 °C / 800 MPa 141

B) CMSX-4 Plus at 950 °C / 390 MPa and 850 °C / 650 MPa 145

4.2.9. Ultra-high temperature creep (≥ 1200 °C) 148

4. 3. Examination of damage localization using different material histories and test conditions 151

4.3.1. Pre-deformation at higher temperature and rejuvenation effect 151

4.3.2. Pre-deformation after aging treatment 155

4.3.3. Thermal cycling creep tests 159

4. 4. Summary 161

References 163

RÉSUMÉ : MÉCANISMES DE DÉGRADATION PAR FLUAGE DES SUPERALLIAGES MONOCRISTALLINS BASE-NI AVEC PRÉ-DÉFORMATION

L'objectif de ce chapitre est de comprendre l'effet des différents types de pré-déformation sur les propriétés de fluage des superalliages monocristallins base-Ni. Des essais de fluage ont été réalisés sur les superalliages monocristallins AM1 et CMSX-4 Plus dont les microstructures ont été présentées dans le chapitre précédent.

L'introduction d'une déformation plastique à température ambiante dans l'AM1 après le traitement thermique de mise en solution réduit les propriétés de fluage isotherme dans toutes les conditions d'essai étudiées : 1200 °C / 80 MPa, 1050 °C / 140 MPa, 1050 °C / 200 MPa, 950 °C / 300 MPa, 850 °C / 500 MPa, et 750 °C / 800 MPa. Les mêmes charactérisations ont été réalisées avec le CMSX-4 Plus et des essais de fluage ont été effectués à 1250 °C / 60 MPa, 1150 °C / 110 MPa, 1050 °C / 200 MPa, 950 °C / 390 MPa et 850 °C / 500 MPa. La pré-déformation réduit la durée de vie du CMSX-4 Plus en fluage à haute température (≥ 1150 °C), mais n'a pas d'impact significatif à basse température (≤ 1050 °C).

Au cours des traitements thermiques de revenu, la microstructure de γ/γ′ grossit plus rapidement à proximité des bandes de glissement {111} de la pré-déformation comme expliqué dans le chapitre 3. Les analyses stéréologiques ont révélé que le nombre de (très) petits pores de déformation (D-pores [1]) a augmenté dans l'AM1 pré-déformée avant l'essai de fluage. Cela indique que la nucléation et la croissance des D-pores sont renforcées à proximité des bandes de glissement au cours des traitements de revenu par le transport de lacunes. Leur transport est favorisé par la montée des dislocations.

Une évolution sous forme de radeaux γ′ inclinés est observée dans les bandes à microstructure grossie lors de la déformation par fluage à 1050 °C et 950 °C pour l'AM1 et à 1150 °C pour le CMSX-4 Plus. Le cisaillement des dislocations {111} facilité dans les précipités γ′ grossiers est une cause de l'inclinaison des radeaux γ′. En plus des pores formés lors des traitements thermiques de revenu, la nucléation et la croissance des pores de fluage ont été accélérées dans les bandes en raison de l'accumulation des dislocations et du grossissement de la microstructure rapides. La concentration de contraintes autour des pores dans ces bandes induit de la recristallisation dans les toutes dernières étapes des essais de fluage. Il en résulte une durée de vie en fluage très faible avec une surface de rupture très planaire et proche d'un plan cristallin {111}.

Dans l'AM1, la localisation du dommage de fluage est beaucoup plus marquée à 1050 °C / 140 MPa par rapport à 950 °C / 300 MPa. Comme le transport et la condensation des lacunes sont à l'origine de la localisation du dommage, une température de fluage plus élevée favorise ce processus de dommage contrôlé par diffusion. Dans le CMSX-4 Plus, le dommage par fluage à 1050 °C / 200 MPa et 950 °C / 390 MPa n'a pas présenté une telle localisation et l'impact de la pré-déformation est très peu prononcé. En raison d'une diffusivité interne plus basse pour le CMSX-4 Plus, ces processus activés thermiquement sont plus lents par rapport à ceux opérants dans l'AM1.

En résumé, si la température de l'essai de fluage diminue ou que la charge appliquée augmente, les processus d'endommagement induit par la diffusion s'en retrouvent ralentis, voire, supprimés. Par contre, le cisaillement de la microstructure par activation du glissement devient un facteur dominant dans les mécanismes de déformation du fluage. Comme indiqué dans le chapitre précédent, la microstructure de l'AM1 a été largement affectée par la pré-déformation par rapport à celle sur CMSX-4 Plus en raison de la différence d'énergie de déformation élastique accumulée sur charque bande de glissement. La cohérence entre la matrice γ et les précipités γ′ dans les bandes à microstructure grossière est éliminée par l'évolution de la microstructure au cours du traitement thermique de revenu après la pré-déformation, en particulier sur l'AM1. Cela conduit à une réduction de la résistance au cisaillement des précipités γ′ dans l'AM1. Par conséquent, les propriétés en fluage de l'AM1 à des températures inférieures à 950 °C sont plus sensibles à la pré-déformation par rapport à celle du CMSX-4 Plus.

Pour évaluer les différents cas de localisation l'endommagement, différentes méthodes de préparation/pré-déformation ont été appliquées. Les procédures ont été : 1) pré-déformation à 950 °C entre les traitements de mise en solution et de revenu, 2) pré-déformation après mise en solution suivie de traitements de restauration et de revenu, 3) pré-déformation après traitement thermique complet, 4) pré-déformation entre les deux traitements de revenu, 5) pré-déformation après traitement thermique complet suivie d'un autre traitement de revenu primaire, 6) pré-déformation après traitement thermique complet suivie d'un autre traitement thermique complet. Des essais de fluage isotherme ont été réalisés sur ces matériaux. Des essais de fluage en cycle thermique ont également été effectués pour mieux comprendre les processus de localisation de l'endommagement fluage.

En raison de la légère mise en radeaux induite par la pré-déformation à 950°C suivie des revenus, la déformation par fluage a opéré de manière homogène dans les éprouvettes (i.e. pas/peu de localisation). Les propriétés en fluage de cette éprouvette à 1050 °C / 140 MPa sont comparables à celles de la référence sans pré-déformation. Par contre, cette mise en radeaux préalable induit une très faible durée de vie en fluage à 850 °C / 500 MPa. La microstructure de l'AM1 pré-dégradée (légèrement mise en radeaux/bandes avec précipités grossis) est défavorable aux conditions de fluage avec une charge appliquée plus élevée.

L'introduction d'une pré-déformation à température ambiante pour l'AM1 à différents étapes de « préparation » a moins d'impact sur leur durée de vie en fluage à 1050 °C / 140 MPa. Par contre, si l'échantillon avec la pré-déformation introduite après un traitement thermique complet a subi un revenu supplémentaire à 1100 °C pendant 5 h, une localisation de l'endommagement de fluage est à nouveau observée avec une rupture planaire proche d'un plan {111}, mais sans que cela n'implique une chute de la durée de vie en fluage. La structure de dislocation développée au cours du revenu à haute température par la relaxation des contraintes internes est une raison possible pour ce mode de rupture spécifique. La pré-déformation entre les traitements thermiques de mise en solution et de revenus est donc la procédure de « préparation » la plus néfaste parmi toutes celles étudiées et analysées.

La pré-déformation n'a pas affecté les propriétés de fluage de l'AM1 et du CMSX-4 Plus lors d'essais de fluage cyclés thermiquement. Les transitions fréquentes et rapides de la fraction volumique de γ′ ont lieu pendant le cycle thermique (1050 °C → 1110 °C → 1050 °C → 1160 °C). Les dislocations peuvent ainsi facilement

pénétrer dans la phase γ′ pendant cette transition de température [2,3]. Ainsi, la structure initiale déformation ne contribue plus à la localisation des dommages activés thermiquement (inclinaison du mise en radeaux par exemple).

Les éprouvettes d'AM1 et CMSX-4 Plus ayant reçu un traitement thermique de restauration supplémentaire après la pré-déformation, présentent des propriétés de fluage équivalentes aux matériaux d'origine sans pré-déformation. Ceci est dû au choix de traitement de restauration appropriées qui ont été déterminées dans le chapitre précédent. Si la pré-déformation est appliquée après les traitements de revenu, elle peut diminuer la ductilité de fluage et affecter les mécanismes de rupture en fonction de l'historique thermique du matériau. Le traitement de restauration est étape efficace pour restaurer des propriétés acceptables en vue des conditions de service.

4. 1. Introduction

Creep properties of the pre-deformed materials at different temperature/stress conditions are presented in this chapter using AM1 and CMSX-4 Plus SX superalloys, without and with pre-deformation. Mechanism of creep life debit caused by pre-deformation and situations causing intense creep damage localization are discussed. A list of specimens and their history is shown in Table 4.1. The same creep testing rig was used for each testing condition to limit scatter.

Table 4.1 List of specimen history used for mechanical tests

Alloy	Specimen	history
AM1	AM1-HT1	Solution + 1100 °C / 5 h + 870 °C / 16h
	AM1-RTPD-HT1	Solution + PD at RT + 1100 °C / 5 h + 870 °C / 16h
	AM1-PD950-HT1	Solution + PD at 950 °C + 1100 °C / 5 h + 870 °C / 16h
	AM1-RTPD-Rejuv-HT1	Solution + PD at RT + 1290 °C / 20 min + 1100 °C / 5 h + 870 °C / 16h
	AM1-HT1-RTPD	Solution + 1100 °C / 5 h + 870 °C / 16h + PD at RT
	AM1-AT1-RTPD-AT2	Solution + 1100 °C / 5 h + PD at RT + 870 °C / 16h
	AM1-HT1-RTPD-A1	Solution + 1100 °C / 5 h + 870 °C / 16h + PD at RT + 1100 °C / 5 h
	AM1-HT1-RTPD-HT1	Solution + 1100 °C / 5 h + 870 °C / 16h + PD at RT + 1100 °C / 5 h + 870 °C / 16h
CMSX-4 Plus	4P-HT1	Solution + 1100 °C / 5 h + 870 °C / 16h
	4P-HT2	Solution + 1165 °C / 6 h + 870 °C / 20h
	4P-RTPD-HT1	Solution + PD at RT + 1100 °C / 5 h + 870 °C / 16h
	4P-RTPD-HT2	Solution + PD at RT + 1165 °C / 6 h + 870 °C / 20h
	4P-RTPD-Rejuv-HT2	Solution + PD at RT + 1330 °C / 1 h + 1165 °C / 6 h + 870 °C / 20h

4. 2. Creep damaging mechanisms of SX superalloys with pre-deformation at RT

After the precedent experiments, a detailed mechanism of early creep failure caused by PD during HT processes become a major remaining question. Recrystallization observed after failure was assumed to be the mechanism responsible for earlier onset of tertiary creep and shorter time to failure. This section analyzes isothermal creep test results on AM1 SX superalloy with pre-deformation introduced between solution and aging heat treatments. To understand the effect of alloy composition on the creep durability and rejuvenation capability of the pre-deformed specimen, similar tests were conducted on high-Re containing Ni-based SX superalloy CMSX-4 Plus. Step-by-step creep failure scenarios for different creep conditions and effects of alloy composition are discussed.

4.2.1. Creep results on AM1-RTPD-HT1 at higher temperatures (1050 °C, 950 °C)

Some creep test results presented in this section are reproduced from the previous results so that the same creep rig is used for the same testing conditions. Figures 4.1-4.5 are the results of creep tests performed on AM1 without and with pre-deformation (AM1-HT1 and AM1-RTPD-HT1) at 1050 °C / 140 MPa, 1050 °C / 200 MPa, and 950 °C / 300 MPa. In general, PD between solution and aging treatments (AM1-RTPD-HT1) results in a huge creep life debit, decreased ductility, and planar fracture surface parallel to {111} slip plane in most

of the creep conditions as presented in Chapter 1 (Figures 1.40 and 1.41). These creep properties of the specimen with PD are different from typical creep deformation characteristics described in the literature [4–7].

The pre-deformation most drastically affected the creep conditions within the "γ′-rafting regime" (T > 1000 °C). At 1050 °C / 140 MPa, very early onset of tertiary creep stage occurred on the specimen with a prior PD and it failed with very low ductility (Figure 4.1). The pre-deformed specimen in this condition showed the largest creep life and ductility debit of all conditions for AM1 (creep life and ductility reduced to 1/3 from the reference material). Two interrupted creep tests (Figure 4.2) were performed to characterize microstructures just after the primary creep stage (25 h, creep strain = 0.24 %) and at the beginning of the tertiary creep stage (105 h, creep strain = 1.09 %). The creep strain rate during the primary stage until the beginning of the secondary stage is similar for all specimens (Figure 4.2). Although the creep strain at the minimum creep rate is different, the primary stage can be considered as equivalent for all specimens because the specimens without PD and with PD interrupted at 0.24 % creep strain have very similar strain profile (Figure 4.5(a)). Specimens with PD show a short secondary creep stage, as suggested by their higher minimum creep rate in Figure 4.5(a).

A different stress level of 200 MPa was also applied at the same temperature of 1050 °C (Figure 4.3). Earlier onset of tertiary creep stage, decreased ductility, and planar fracture surface of a pre-deformed specimen are similar to the test at 1050 °C /140 MPa. However, the magnitude of creep life debit becomes smaller at 1050 °C / 200 MPa.

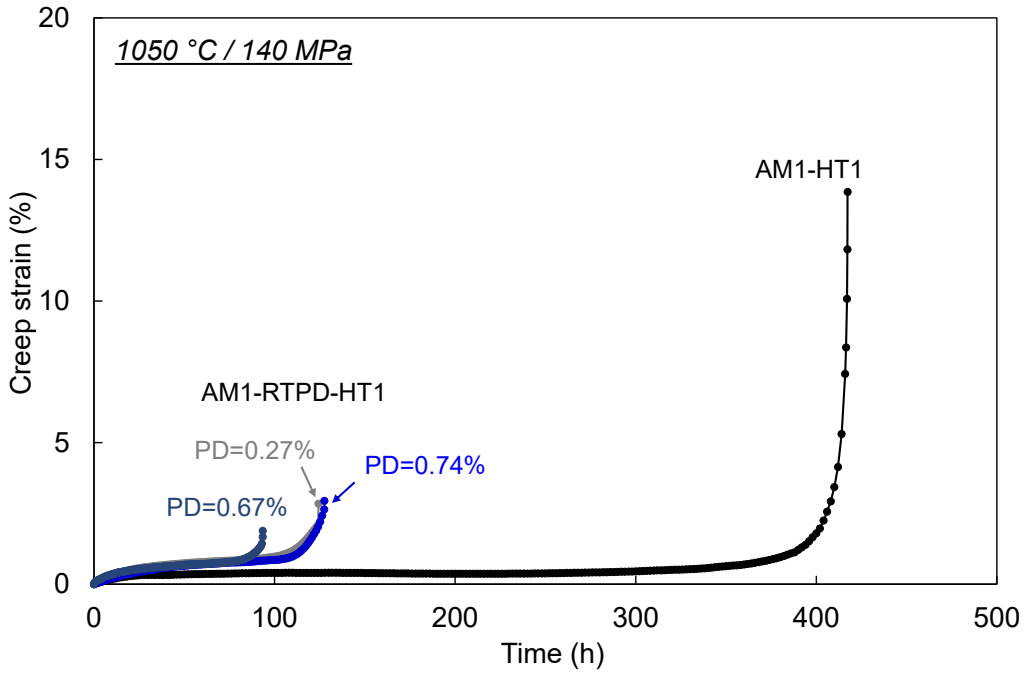

Figure 4.1. Creep curves of AM1 specimens without and with pre-deformation tested at 1050 °C / 140 MPa.

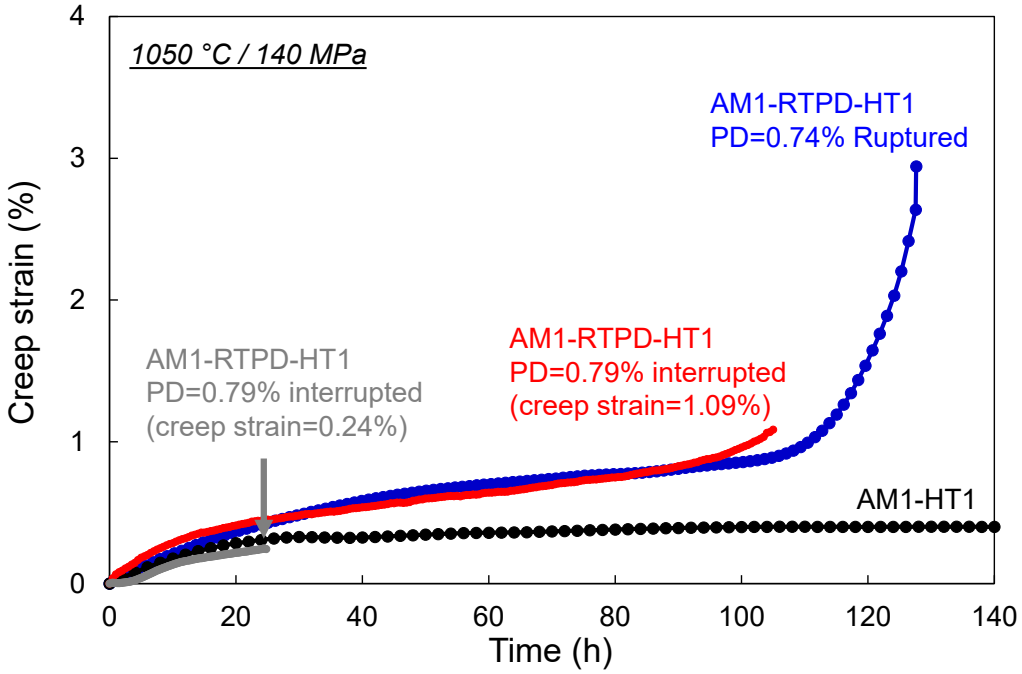

Figure 4.2. Creep curves from interrupted tests on AM1 at 1050 °C / 140 MPa.

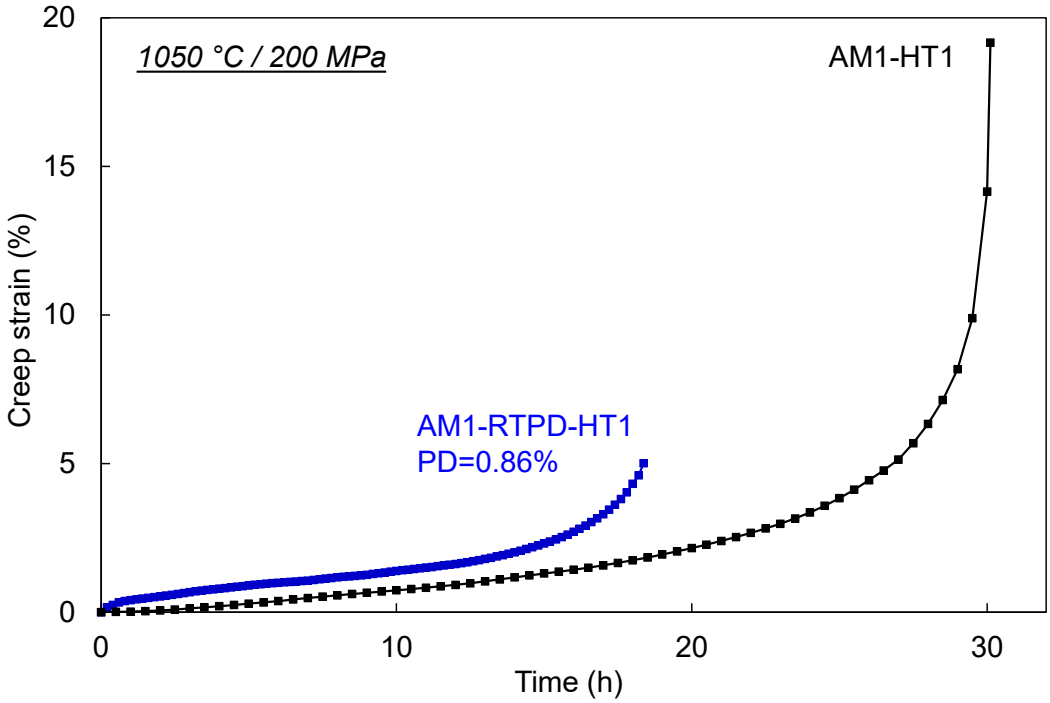

Figure 4.3. Creep curves of AM1 specimens without and with pre-deformation tested at 1050 °C / 200 MPa.

Creep curves at 950 °C / 300 MPa are showing an increasing creep rate for almost all the test duration (Figure 4.4). Such increasing creep rate, or softening, after very short primary creep is common in this intermediate creep temperature/intermediate stress as a result of the γ/γ′ topological inversion [5,8–10]. The differences after introducing PD are that a specimen with PD has a higher creep strain rate after reaching a minimum creep rate and it has failed at lower strain (Figures 4.4 and 4.5(b)). More specifically, the specimen interrupted within the accelerating stage (71 h, creep strain = 6.65 %) shows a higher creep rate for all the periods.

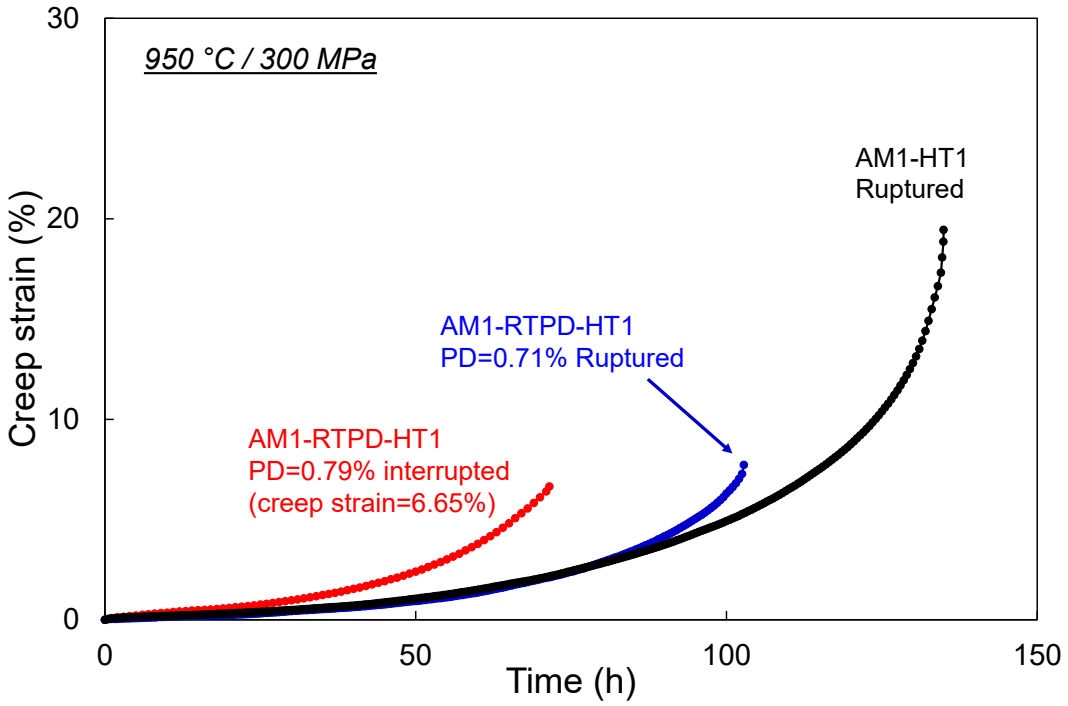

Figure 4.4. Creep curves of AM1 specimens without and with pre-deformation tested at 950 °C / 300 MPa.

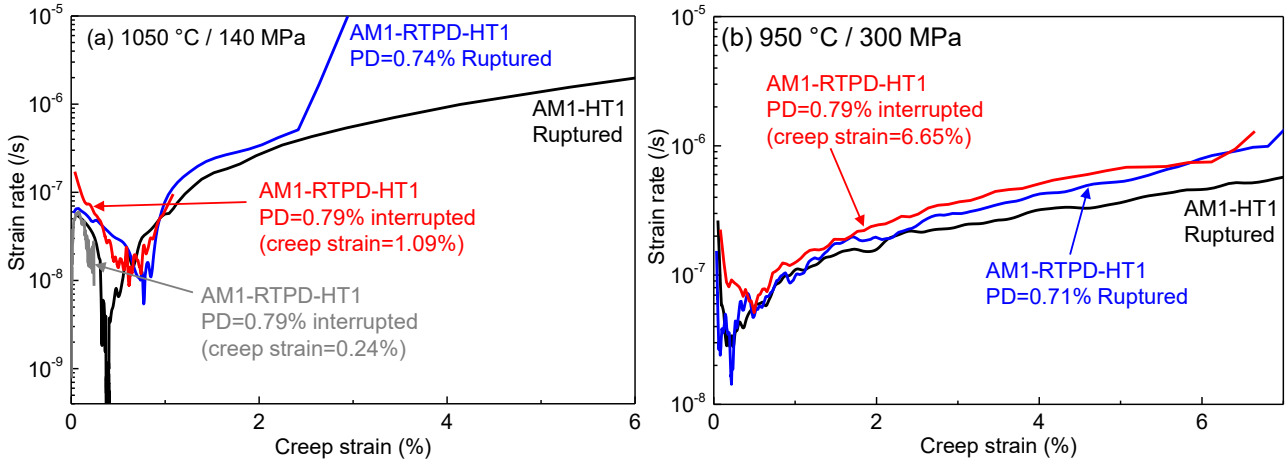

Figure 4.5. Creep strain rate vs. creep strain for creep tests on AM1 without and with pre-deformation, tested at 1050 °C / 140 MPa (a) and 950 °C / 300 MPa (b).

4.2.2. Microstructure characterizations on AM1 after creep tests at higher temperatures (1050 °C, 950 °C)

SEM and EBSD techniques were used for microstructure characterization on crept specimens. This section analyzes microstructures after isothermal creep tests at temperatures of 1050 °C and 950 °C which is considered as a higher temperature creep. Longitudinal cross-sections of crept specimens prepared for SEM observations (mechanical polishing + etching) are shown in Figure 4.6.

A) AM1 without PD

Creep ruptured specimens without pre-deformation have typical ductile failure involving a necking in the rupture area (Figures 4.6(a, c, e)) [11–14]. They also show cracks initiated from creep voids located in the interdendritic area and crack propagation along the γ/γ′ interfaces of disordered raft structure (Figure 4.7). At

1050 °C, fracture characteristics of AM-HT1 were similar for 140 MPa and 200 MPa. Coalescence of creep voids occurred in the creep test at 950 °C / 300 MPa (Figure 4.7(b)). In addition, γ/γ′ eutectics pools remaining after the heat treatment sequence were found in the interdendritic area of all specimens, including the ones with PD.

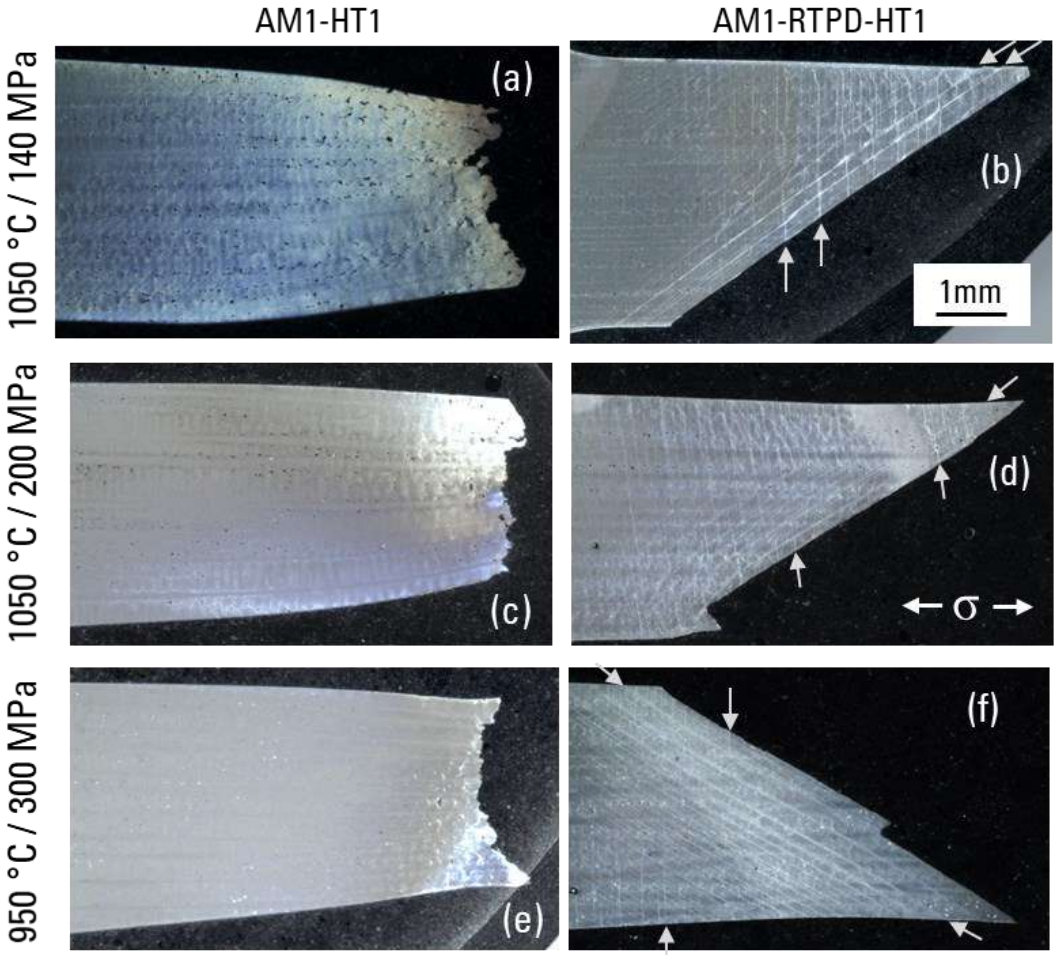

Figure 4.6. Longitudinal cross-sections of AM1-HT1 (a, c, e) and AM1-RTPD-HT1 (b, d, f) tested at 1050 °C / 140 MPa (a, b), 1050 °C / 200 MPa (c, d), and 950 °C / 300 MPa prepared for microstructure observations. Arrows are pointing at the traces of the microstructure coarsened bands.

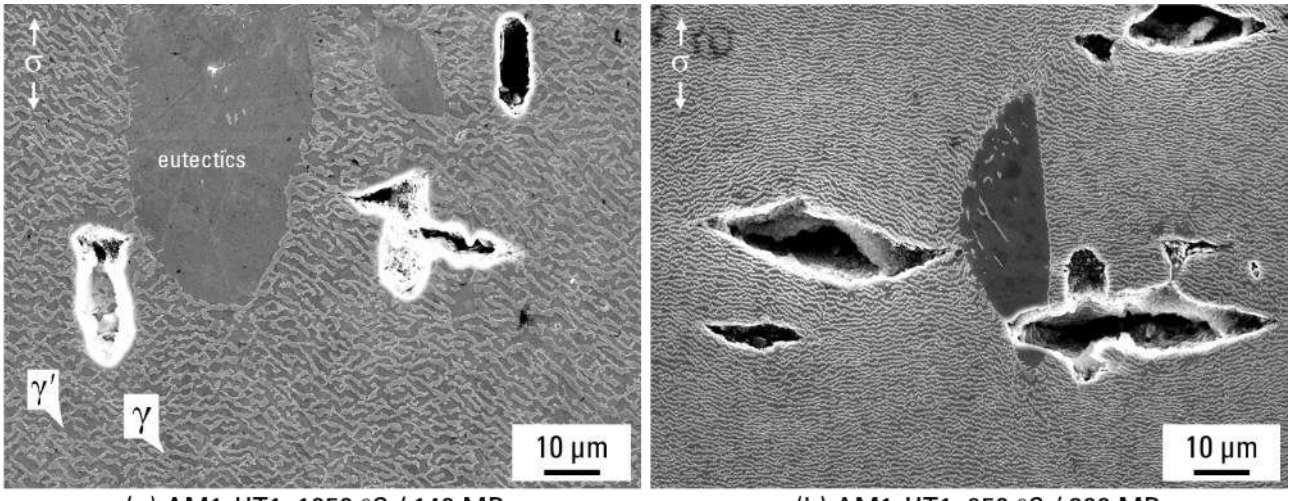

(a) AM1-HT1, 1050 °C / 140 MPa (b) AM1-HT1, 950 °C / 300 MPa

Figure 4.7. Typical creep voids and crack propagation of AM1-HT1 (without PD) after creep rupture tests at 1050 °C / 140 MPa (a) and 950 °C / 300 MPa (b).

B) AM1 with PD, creep test at 1050 °C / 140 MPa

Low-magnification images after creep rupture and interrupted tests at 1050 °C / 140 MPa are presented in Figure 4.8. Traces of the microstructure coarsened band on the former {111} slip plane are observed in both specimens and they are parallel to the fracture surface. These lines correspond to the areas with microstructure evolution that occurred during aging treatments after PD, as previously shown in Figures 3.11(a, d). The precipitation scale image in Figure 4.9 shows the intersection of two bands with recrystallized grain-boundaries. Recrystallization in the band has been already confirmed in the specimen creep ruptured at 1050 °C/140 MPa in the preceding experiments (Figure 1.42). The microstructure in the recrystallized band is no more in a pattern of the γ′-rafts which still observed in the area outside the band. Horizontal bands shown in Figure 4.8(a) and 4.9(a) are intercepted by the band parallel to the fracture surface. This indicates that the plastic strain is higher in the band and suggests the grain boundary sliding occurred here after recrystallization. Interception of the bands at their intersections were not observed in the creep interrupted specimen (105 h, Figure 4.8(b)), which means the sliding at the bands occurred at the tertiary creep stage.

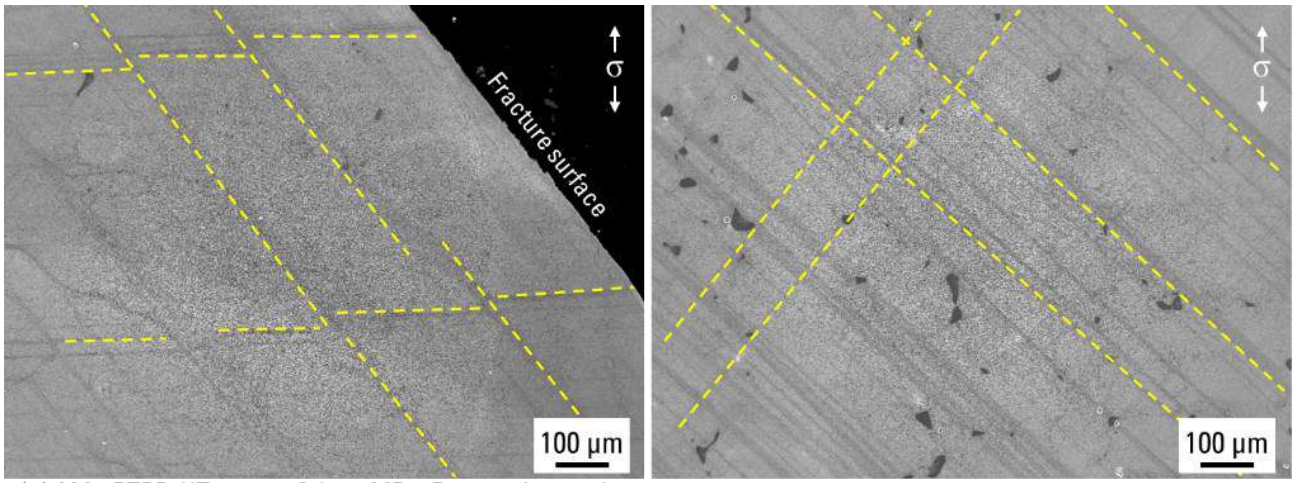

(a) AM1-RTPD-HT1, 1050 °C / 140 MPa, Ruptured at 125 h (b) AM1-RTPD-HT1, 1050 °C / 140 MPa, Interrupted at 105 h

Figure 4.8. Low-magnification images of AM1-RTPD-HT1 after creep tests at 1050 °C / 140 MPa.

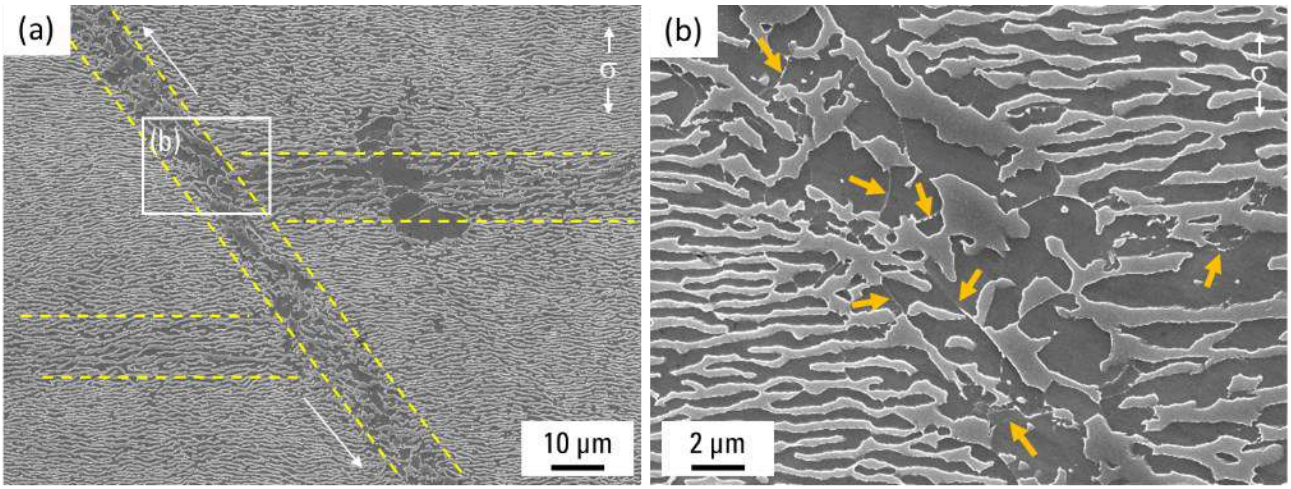

AM1-RTPD-HT1, 1050 °C / 140 MPa, Ruptured at 125 h

Figure 4.9. Precipitation scale microstructures of AM1-RTPD-HT1 after creep rupture test at 1050 °C / 140 MPa. In (a), dotted lines are showing microstructure coarsened bands and arrows are indicating direction of sliding. (b) is a magnified image of the area surrounded by the rectangle in (a). Arrows in (b) are pointing at recrystallized grain boundaries.

Precipitate scale microstructures after creep interrupted tests at 1050 °C / 140 MPa are shown in Figure 4.10. γ′-rafting is already completed after 25 h both inside and outside the microstructure coarsened bands. The inclination of the γ′-raft in the band is already proceeding at this stage (Figure 4.10(a)). Comparing images at 25 h (Figure 4.10(a)), 105 h (Figure 4.10(b)), and 125 h (ruptured specimen, Figure 4.9(b)), inclined γ′-rafts in the band are coarsening much faster than outside of the band during creep deformation. More specifically, during the tertiary creep stage after 105 h, γ/γ′ phases are connected along former {111} slip plane and they are forming very wide plates in three-dimensional shape, indicated by an arrow in Figure 4.10(b). In this microstructure coarsened band, dislocations were cutting from γ/γ′ interfaces into the γ′ phase (traces shown by arrows in Figure 4.10(d)) [15]. The strong segregation of γ-phase elements (Cr and Co more specifically for AM1 alloy in these creep conditions) along the dislocation lines selectively reveals dislocation traces after chemical etching by aqua regia [16,17]. In the same specimen after 105 h (Figure 4.10(c)), density of such traces is higher around eutectics and the morphology of this area is very similar to the recrystallized grains in Figure 4.9(b).

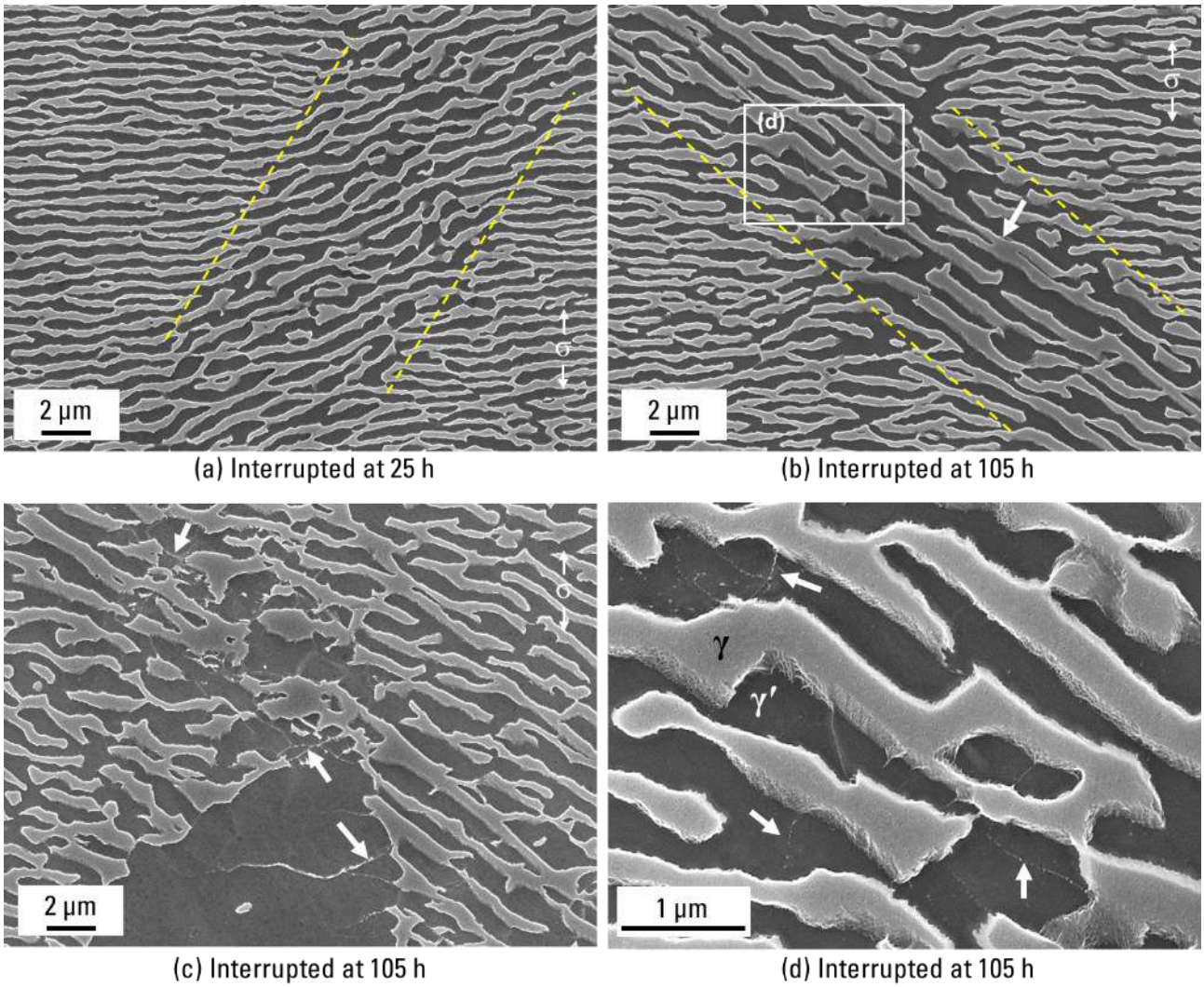

Figure 4.10. Precipitation scale microstructures of AM1-RTPD-HT1 after creep tests at 1050 °C / 140 MPa, interrupted at 25 h (a) and at 105 h (c-d). Dotted lines in (a, b) show the regions of the microstructure coarsened bands. (d) is a magnified image of the area surrounded by the rectangle in (b). Arrow in (b) indicates a very wide connected plane of the γ phase along the band. Arrows in (c) point out possible grain boundaries in the γ′ phase. Arrows in (d) are pointing at dislocation traces in the γ′ phase.

In other parts of the creep specimen interrupted at 105 h, distinctive voids growing in the microstructure coarsened bands were observed, as shown in Figure 4.11. Unlike the primary growth of typical creep voids, such voids in the band have a growth direction along the {111} former slip plane and their width is linked to the width of the bands as indicated by dotted lines in Figure 4.11(c, d).

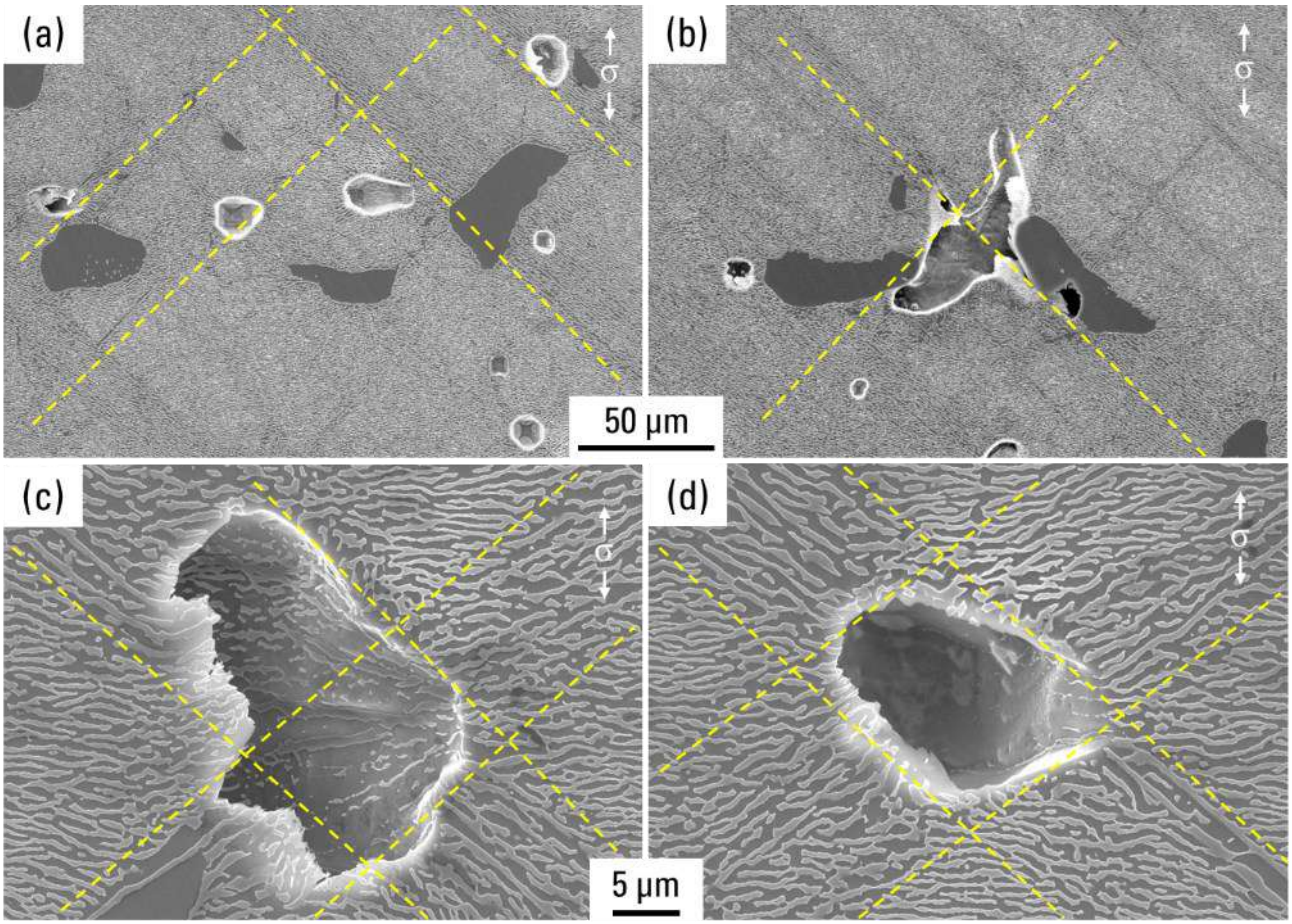

Figure 4.11. Different voids observed in AM1-RTPD-HT1 after creep test at 1050 °C/140 MPa, interrupted at 105 h, at low (a, b) and high (c, d) magnifications. Dotted lines in (a, b) indicate direction of the microstructure coarsened bands and dotted lines in (c, d) show the regions of the bands.

C) AM1 with PD at 1050 °C / 200 MPa

As observed in the low-magnification images (Figure 4.6), fracture morphologies are similar for 140 MPa and 200 MPa at 1050 °C in both AM1-HT1 and AM1-RTPD-HT1. Especially in the AM1-HT1, precipitate scale microstructure was similar in both stress conditions, which is typical γ′-rafting and creep void cracking. Microstructure of AM1-RTPD-HT1 after creep test at 1050 °C / 200 MPa is shown in Figure 4.12. All types of former {111} slip system was observed as microstructure coarsened band and two planes were intercepted by major plane which become fracture surface (Figure 4.12(a)). Recrystallized grains were observed in these bands. In non-recrystallized bands, very long shear trace was observed along the major sliding plane (Figure 4.12(c)).

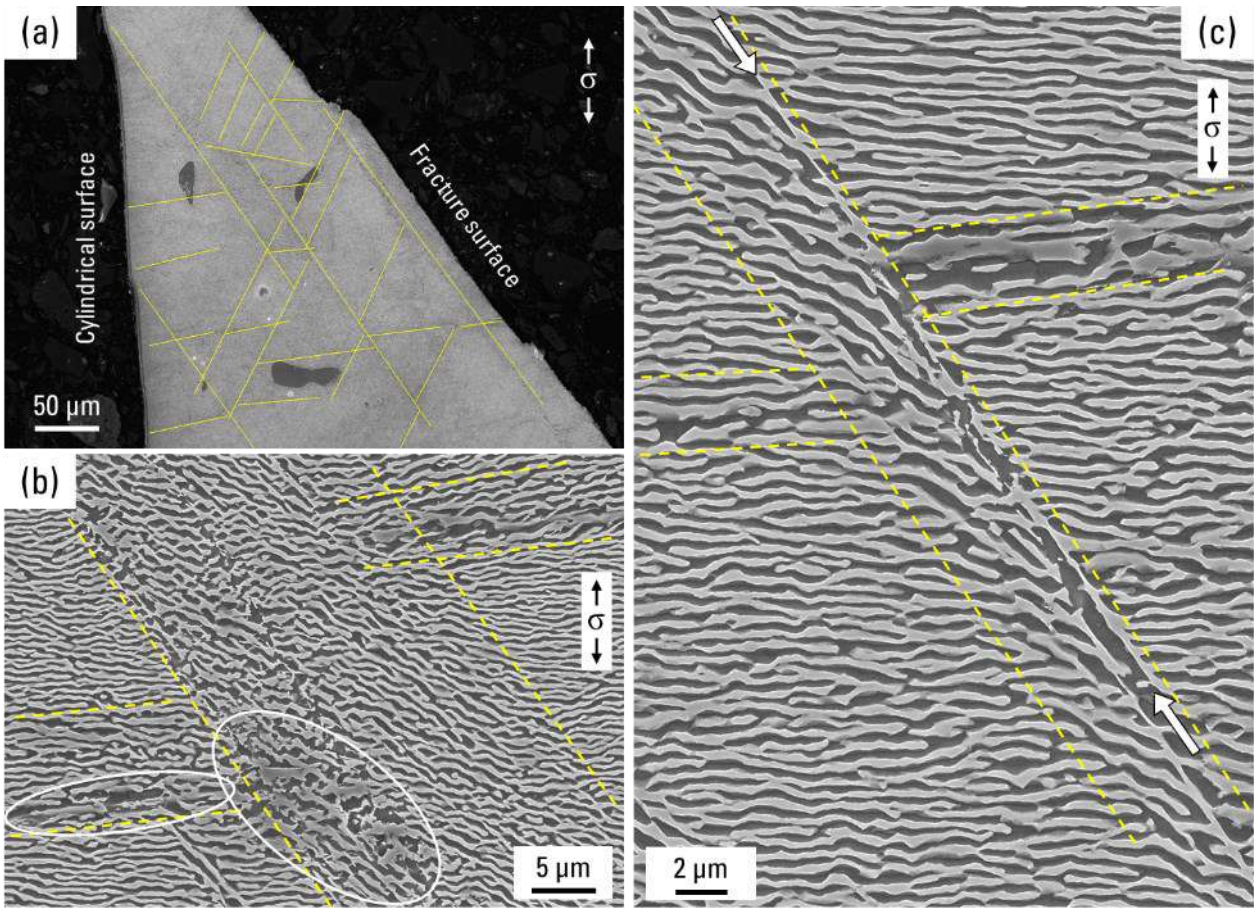

Figure 4.12. Microstructures of AM1-RTPD-HT1 after creep rupture test at 1050 °C / 200 MPa. Lines in (a) and dotted lines in (b, c) are showing microstructure coarsened bands. Ovals in (b) are areas with recrystallized grains. Arrows in (c) are indicating shearing plane in the microstructure coarsened band.

D) AM1 with PD at 950 °C / 300 MPa

Fracture in this creep condition also showed {111} former slip plane with inclined γ′-rafts inside the band (Figure 4.13). Horizontal band intercepted by the major band is also similar to the tests at 1050 °C (Figure 4.13(b)). Faster microstructure coarsening in the bands of creep interrupted specimen (Figure 4.14(a, b)), and recrystallization in the bands after creep rupture (Figure 4.15) were also observed in the creep test at 950 °C / 300 MPa. Size and growth direction of larger voids in the interrupted specimen (Figure 4.14(c, d)) were affected by the bands, which is another common feature of the creep conditions at 950 °C / 300 MPa and 1050 °C / 140 MPa. Moreover, shear traces in Figure 4.13(c) is similarly observed after the test at 1050 °C / 200 MPa (Figure 4.12(c)), but not observed at 1050 °C / 140 MPa. However, some microstructural details are different. In the band near fracture surface, typical crack propagation from creep voids was observed (Figure 4.13(a)). Instead of having very long connected rafts, coarsened and distorted microstructures with higher fraction of γ′ phase were observed inside the bands of the sample tested at 950 °C. This suggests that γ/γ′ topological inversion [8–10] occurs faster in the bands (Figures 4.14(a, b)). In these particular bands with the topological inversion, deformation-induced creep voids that nucleated from the γ/γ′ interface (D-pores [1]) are confirmed (white arrows in Figure 4.14(b)). In the same Figure 4.14(b), dislocation traces entering from the γ/γ′ interface into γ′ phase are indicated by black arrows. D-pores nucleating from the γ/γ′ interface were also observed in the area surrounding the large void shown in Figures 4.14(d, e).

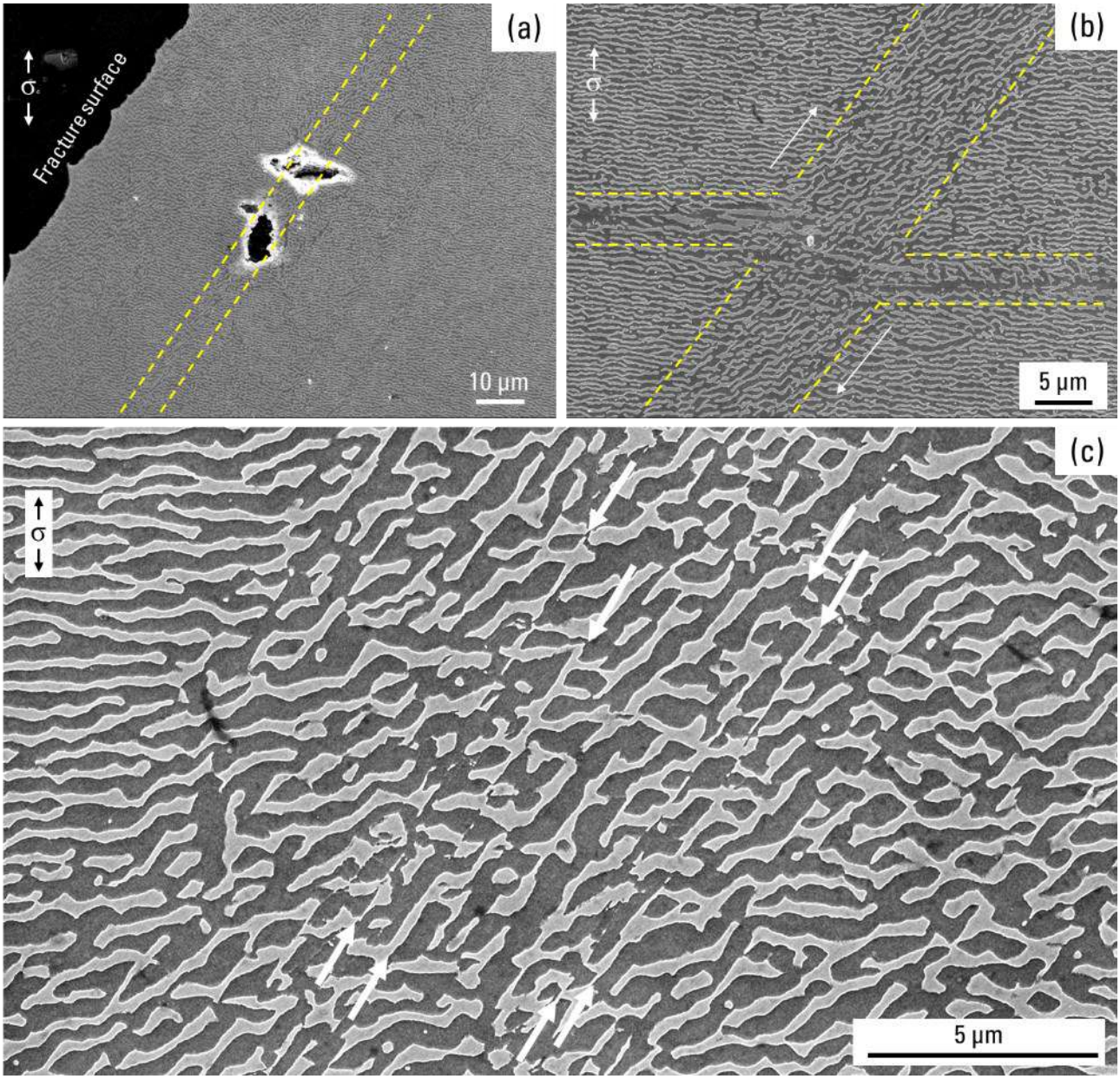

Figure 4.13. Microstructures of AM1-RTPD-HT1 after creep rupture test at 950 °C / 300 MPa (creep life 103 h). Dotted lines show the regions of the microstructure coarsened band. Arrows in (b) are indicating direction of sliding. Arrows in (c) are indicating shearing plane in the microstructure coarsened band.

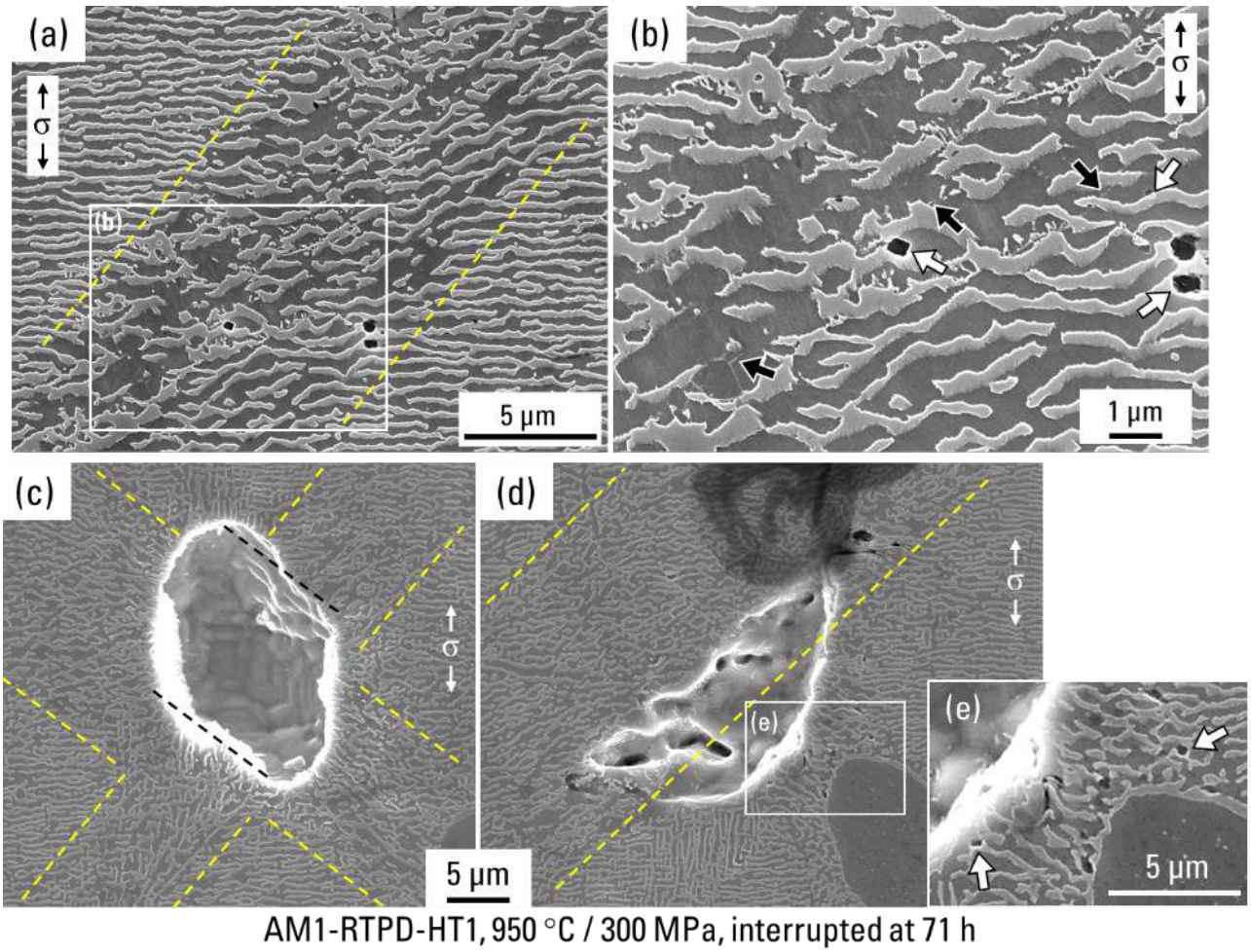

Figure 4.14. Microstructures of AM1-RTPD-HT1 after creep test at 950 °C / 300 MPa, interrupted at 71 h. (b) and (e) are magnified images of the area surrounded by the rectangle in (a) and (d), respectively. Dotted lines show the regions of the microstructure coarsened band. Black arrows are indicating dislocation traces in γ′ phase and white arrows are pointing at voids nucleating from γ/γ′ interface.

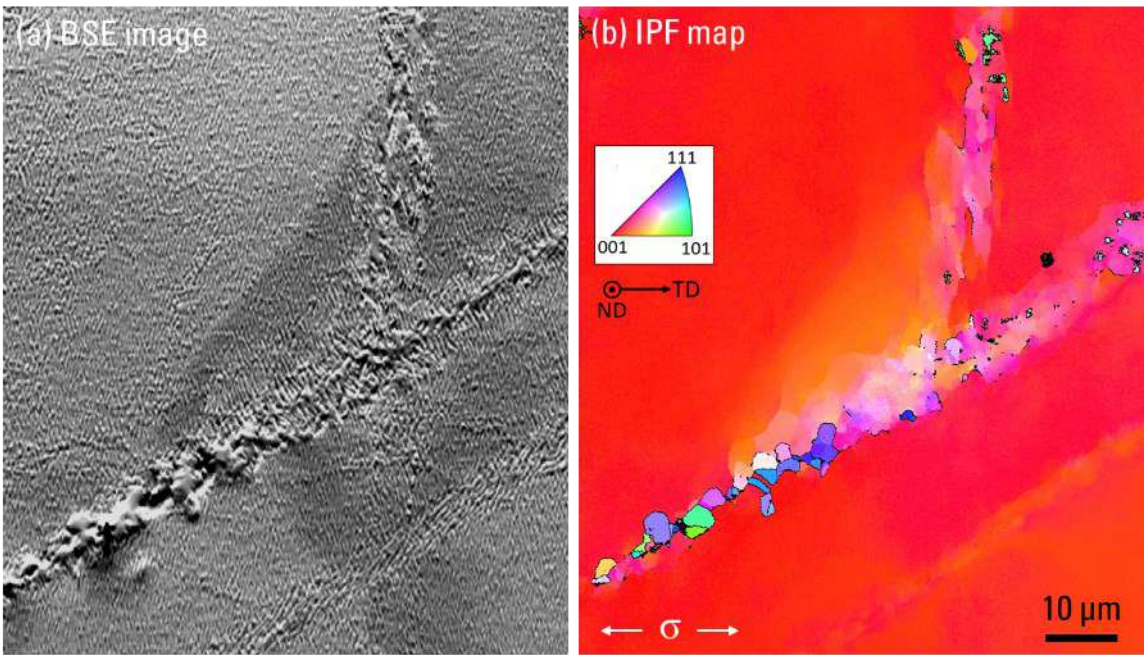

Figure 4.15. BSE image (a) and IPF color-coded orientation maps referring to the tensile direction (b) after creep rupture test on AM1-RTPD-HT1 at 950 °C / 300 MPa.

4.2.3. Local lattice misorientation in the microstructure coarsened band

From the microstructure characterizations (Figures 1.42 and 4.15), recrystallization along the major band system parallel to the fracture surface was observed. In order to discuss the mechanism that activates the recrystallization, creep interrupted specimens were also analyzed using EBSD.

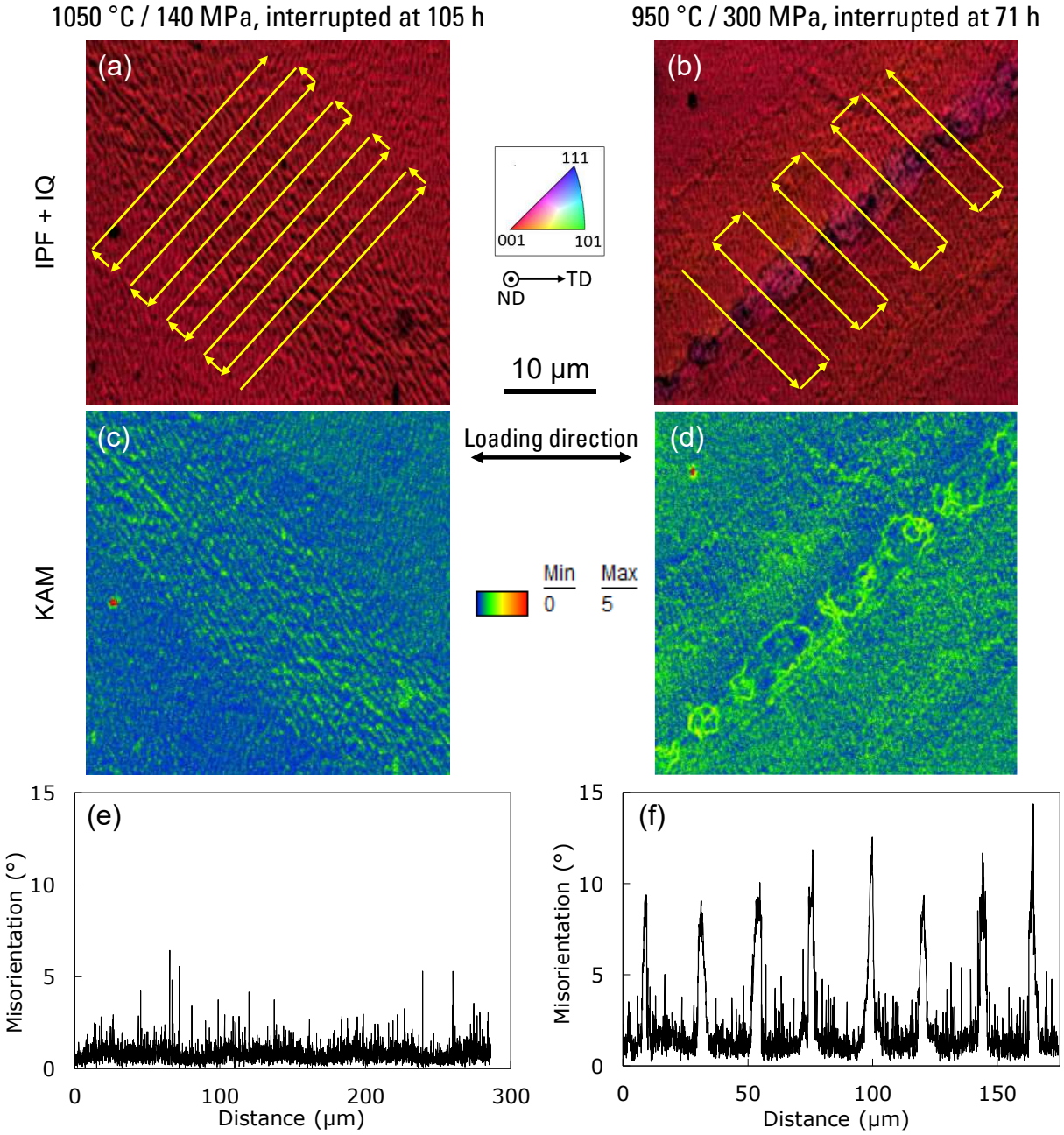

Figure 4.16. PF color-coded orientation maps referring to the tensile direction with image quality (IQ) map after creep interrupted tests (a, b). KAM map in the same scanning areas (c, d). Misorientation profile from [001] direction following arrows of (a) and (b) are shown in (e) and (f), respectively. Creep tests on AM1-RTPD-HT1 were at 1050 °C/ 140 MPa and interrupted at 105 h with creep strain = 1.09% (a, c, e), and 950 °C / 300 MPa and interrupted at 71 h with creep strain = 6.79% (b, d, f).

IPF maps, kernel average orientation (KAM) maps, and misorientation profiles of the creep interrupted specimens tested at 950 °C / 300 MPa and 1050 °C / 140 MPa were obtained by EBSD analyses and are shown in Figure 4.16. In both creep conditions, recrystallization was not observed, even at the beginning of the tertiary creep stage (i.e. increasing creep rate). This supports the fact that the traces observed in Figures 4.10(c, d) and

4.14(b) are not grain boundaries formed through a recrystallization process. They are likely to be γ′-shearing events. More importantly, the absence of recrystallization during the creep acceleration stage means that the recrystallization observed after creep rupture occurred just before the failure. It is indeed worth recalling here that the creep frame is designed to stop heating almost immediately after creep failure (in less than 20 seconds) with a very fast cooling rate (at ~ 10 °C/s down to 800 °C [18]), hence preventing recrystallization to occur after failure. The misorientation profile in Figure 4.16(e) shows almost no local lattice rotation within the observed microstructure coarsened band after the creep test at 1050 °C / 140 MPa interrupted at 105 h. On the contrary, 4-10° local lattice misorientation can be seen in Figure 4.16(f) after creep test at 950 °C / 300 MPa interrupted at 71 h. KAM map from the specimen after the creep test at 950 °C / 300 MPa shows an arc-shaped local misorientation area (Figure 4.16(d)). The highly misoriented area highlighted by the KAM map is known to quantitatively indicate the presence of geometrically necessary dislocations before the occurrence of recrystallization. Both misorientation profile and KAM map tell that a higher density of dislocations is locally stored in the band during creep at 950 °C / 300 MPa and the specimen is "ready-for-recrystallization" according to Figure 4.16(d).

Misorientation profiles along the gauge section of two interrupted test specimens were also obtained by EBSD analyses and shown in Figure 4.17. Higher bulk misorientation was observed at the center of the specimen after creep test at 1050 °C / 140 MPa for 105 h compared to the specimen after 71 h creep at 950 °C / 300 MPa. Misorientation jumps of 3-9° in Figure 4.17(b) correspond to a local lattice misorientation presented in Figure 4.14(f).

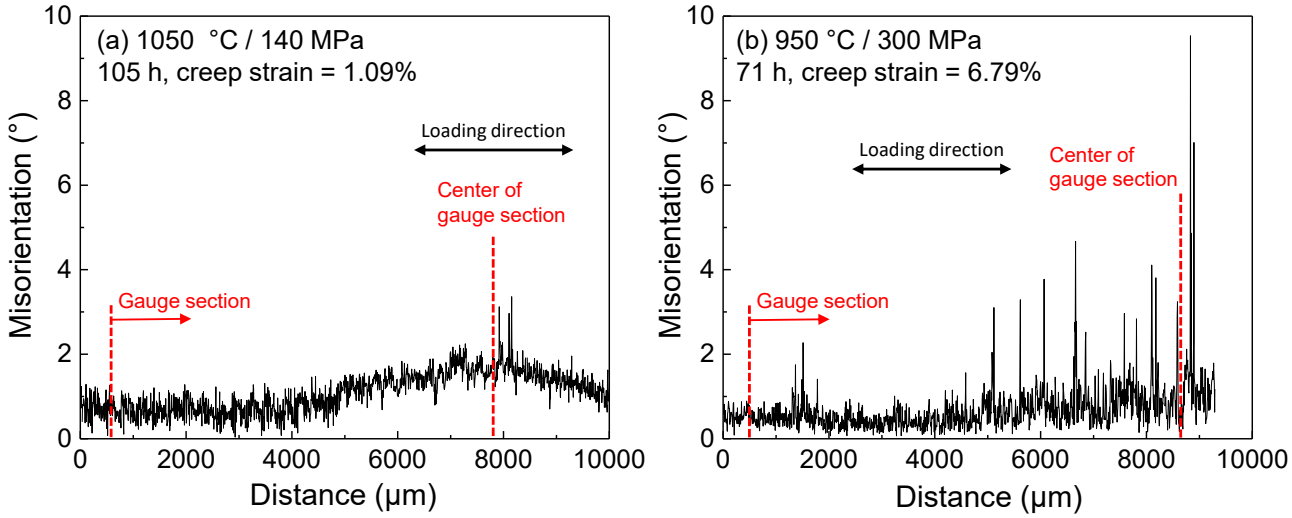

Figure 4.17. Misorientation angle profile from the [001] direction, analyzed from threaded (head) section to gauge section in the longitudinal tensile direction of creep specimens. Creep tests on AM1-RTPD-HT1 were at 1050 °C / 140 MPa and interrupted at 105 h (a), and 950 °C / 300 MPa and interrupted at 71 h (b).

4.2.4. Creep results on 4P-RTPD-HT1 and 4P-RTPD-HT2 at higher temperatures (1150 °C, 1050 °C)

CMSX-4 Plus without PD has creep deformation characteristics similar to AM1 but for different temperature range and they are generally 100 °C higher than that of AM1. This is mainly due to a high-Re content and higher γ′ volume fraction in CMSX-4 Plus compared to AM1 (Figure 3.9). Because of these general

characteristics of alloys, the impact of pre-deformation appeared differently in CMSX-4 Plus and AM1. In comparison with higher temperature creep of AM1 at 1050 °C and 950 °C, creep tests at 1150 °C and 1050 °C are categorized as higher temperature for CMSX-4 Plus. Creep curves of CMSX-4 Plus specimens tested at 1150 °C / 110 MPa and at 1050 °C / 200 MPa are presented in Figures 4.18 and 4.19, respectively.

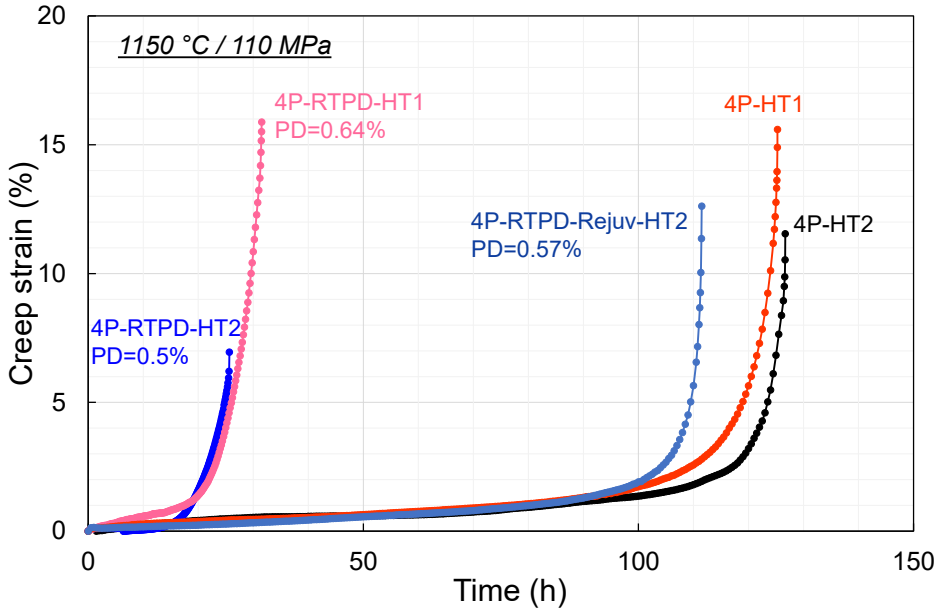

Figure 4.18. Creep curves of CMSX-4 Plus without and with PD tested at 1150 °C / 110 MPa.

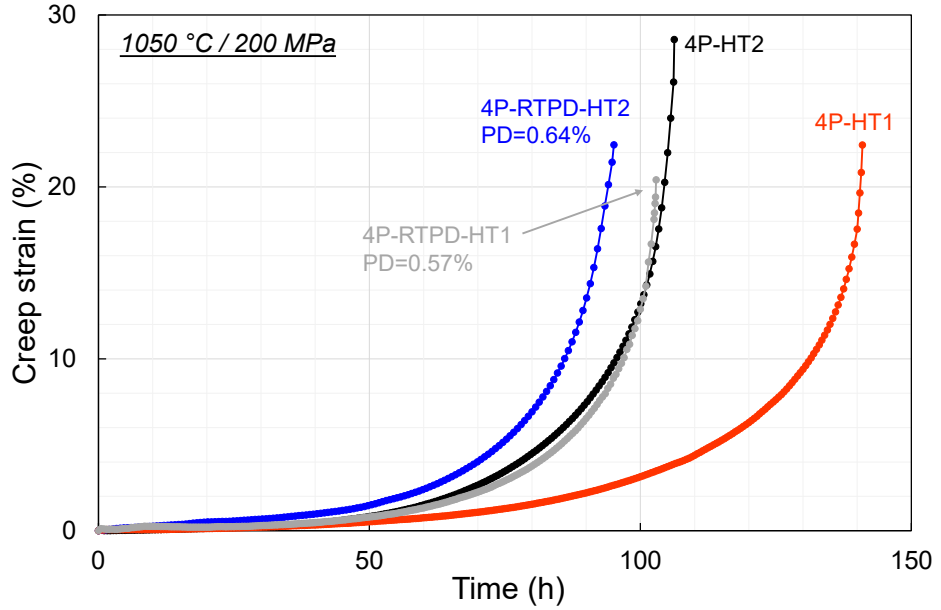

Figure 4.19. Creep curves of CMSX-4 Plus without and with PD tested at 1050 °C / 200 MPa.

Creep tests above 1150 °C showed huge life debits induced by pre-deformation at RT with either CMSX-4 Plus-type (HT2) or AM1-type (HT1) subsequent heat treatments (Figure 4.18). In these conditions, fracture surface is affected by {111} slip plane of plastic deformation as can be seen from low-magnification images in Figures 4.20(b, d). The largest debit was observed in the γ′-rafting regime condition at 1150 °C / 110 MPa with very early onset of tertiary creep stage, as similarly observed in creep at 1050 °C for AM1. Aging treatment conditions did not affect creep life at 1150 °C / 110 MPa. However, although it has planar fracture surface on {111} plane, the ductility of 4P-RTPD-HT1 was similar to non-deformed 4P-HT1, whereas 4P-

RTPD-HT2 has huge ductility loss (Figure 4.18).

Contrary to creep at 1150 °C / 110 MPa, the creep resistance (rupture life and ductility) of CMSX-4 Plus below 1050 °C is hardly affected by a pre-deformation when HT2 was applied subsequently. Fracture of 4P-RTPD-HT2 at 1050 °C / 200 MPa does not present influence of the microstructure coarsened bands (Figure 4.21(b)). Creep life at 1050 °C / 200 MPa has dropped with addition of pre-deformation when AM1-type HT1 was applied, but ductility was maintained. Creep properties of CMSX-4 Plus at 950 °C / 390 MPa and 850 °C / 650 MPa were not affected by pre-deformation, which are presented and discussed later in this chapter.

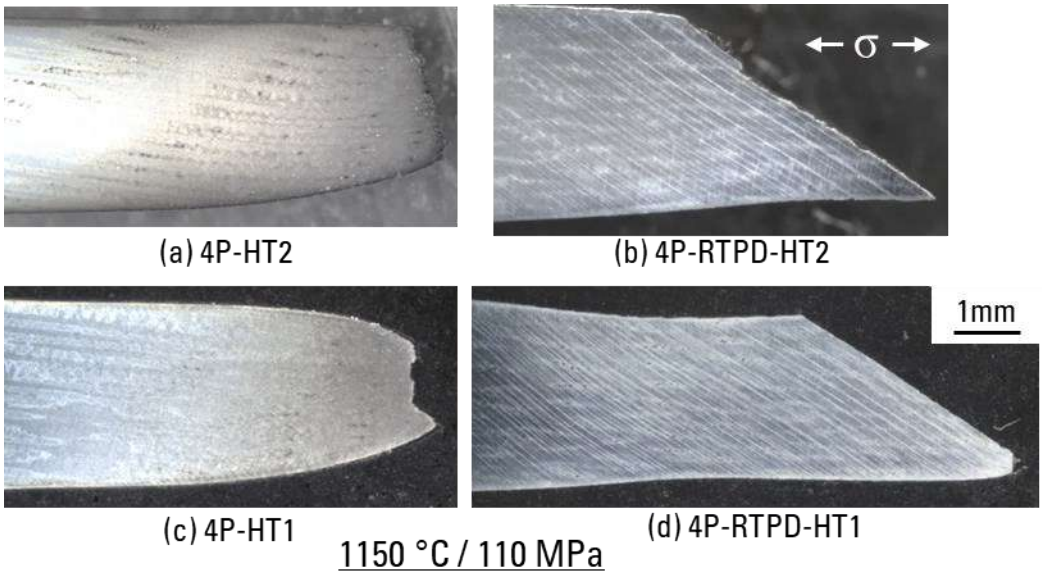

Figure 4.20. Longitudinal cross sections of CMSX-4 Plus creep specimens tested at 1150 °C / 110 MPa prepared for microstructure observations.

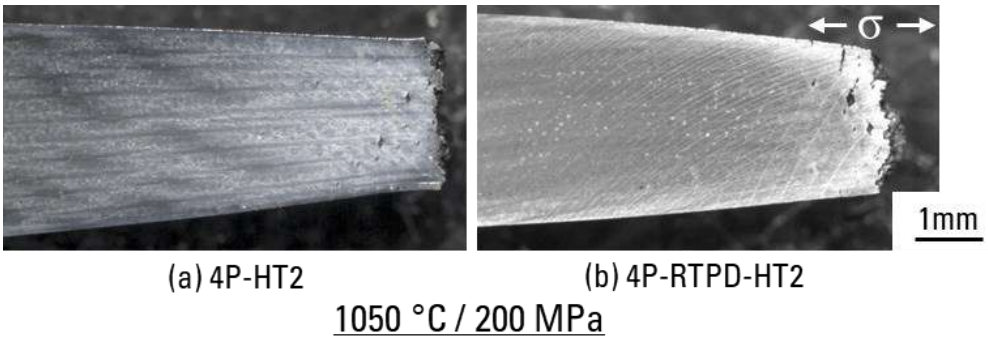

Figure 4.21. Longitudinal cross sections of CMSX-4 Plus creep specimens tested at 1050 °C / 200 MPa prepared for microstructure observations.

4.2.5. Microstructure characterizations of CMSX-4 Plus after creep tests at higher temperatures (1150 °C and 1050 °C)

A) CMSX-4 Plus at 1150 °C / 110 MPa

4P-HT2 has typical post-creep microstructure with γ′-rafting (Figure 4.22(d)), crack propagation from internal creep voids (Figure 4.22(a, c)), and heavily disturbed microstructure near fracture surface with recrystallization (Figure 4.22(b)). Plate shaped TCP precipitates on {111} plane were observed in the dendrite core of 4P-HT2, but their quantity was minor and should not have strong impact on creep failure mechanisms.

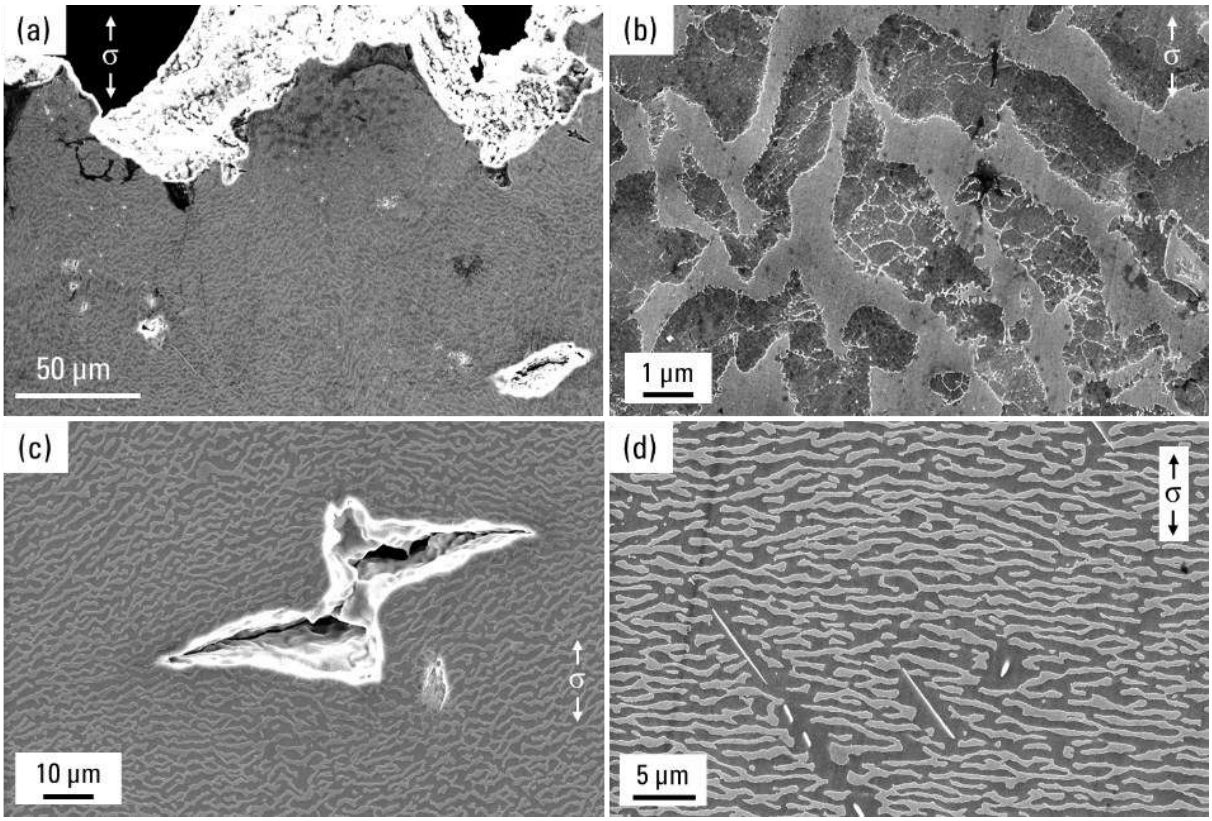

Figure 4.22. Microstructures of 4P-HT2 (without pre-deformation) after creep rupture test at 1150 °C / 110 MPa. Near fracture surface (a, b), typical creep void with crack propagation (c), and γ′-rafted structure with TCP phase (d).

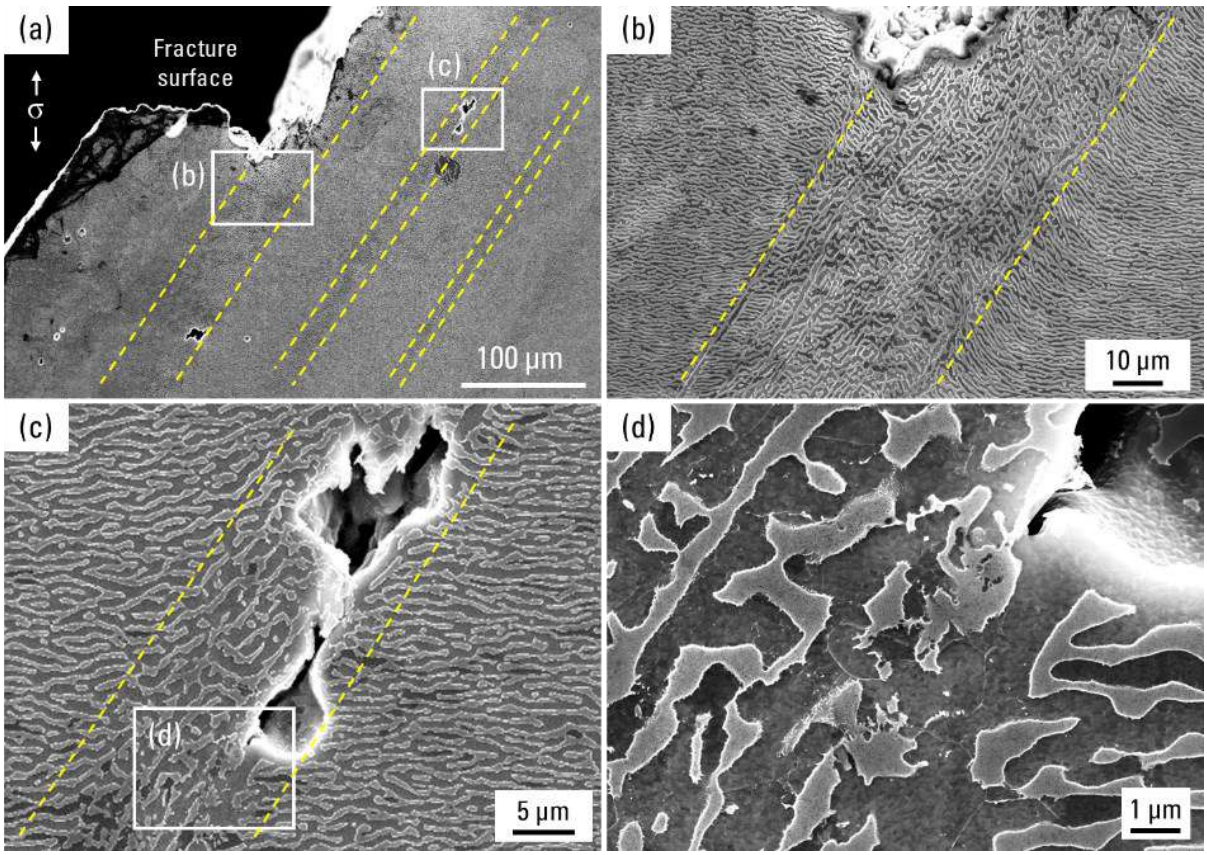

Figure 4.23. Microstructures of 4P-RTPD-HT2 after creep rupture test at 1150 °C / 110 MPa. (b), (c), and (d) are magnified images of the area surrounded by the rectangle in (a) and (c). Dotted lines are indicating microstructure coarsened bands.

Near the planar fracture surface of 4P-RTPD-HT2 after creep at 1150 °C / 110 MPa, many deformed voids were observed in the microstructure coarsened bands (Figure 4.23(a)). Observable dislocations and grain boundaries are in very high density around the deformed void (Figure 4.23(c, d)). γ′-rafting outside the band is typical one but they are heavily deformed in the vicinity of the band (Figure 4.23(b)). In another band, microstructure shearing was observed near the void (Figure 4.24). Inside the band observed 5 mm away from the fracture plane, dislocation traces entering from γ/γ′ interface into γ′ phase were observed, and they are along the {111} plane which is parallel to the inclination of the γ′-rafts (Figure 4.25). TCP phase was not observed in this specimen.

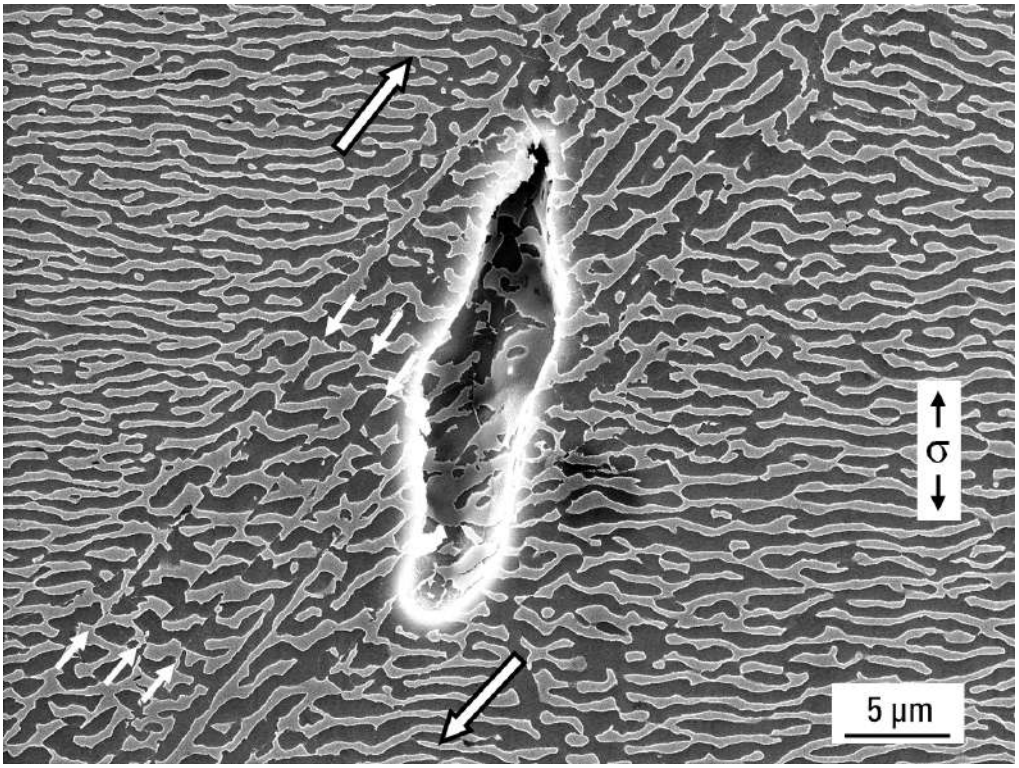

Figure 4.24. Microstructure coarsened band with void observed at 2 mm away from fracture plane in 4P-RTPD-HT2 after creep rupture test at 1150 °C / 110 MPa. Microstructure shearing are indicated by small arrows. Larger arrows are direction of sliding.

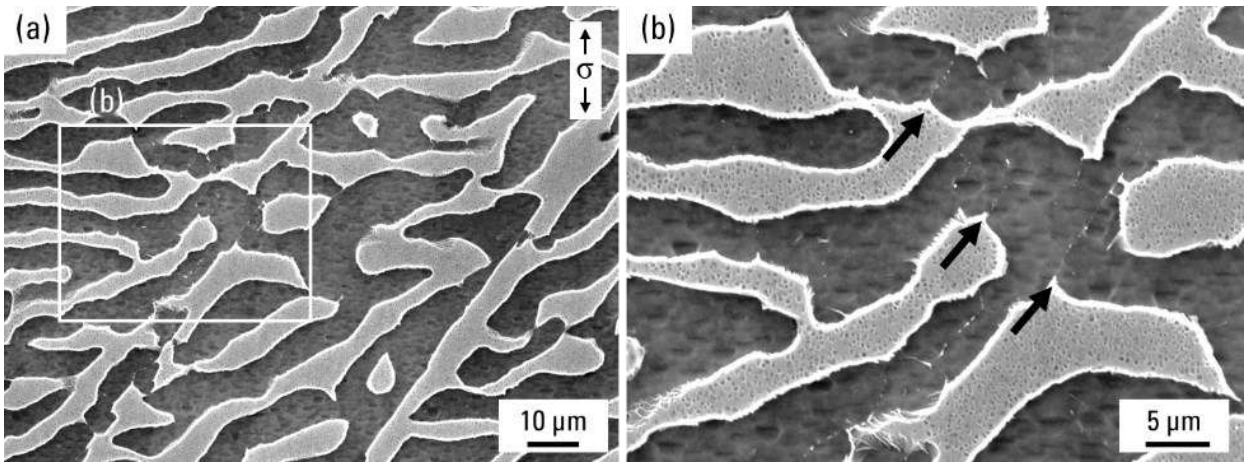

Figure 4.25. Microstructure coarsened band at 5 mm away from fracture plane in 4P-RTPD-HT2 after creep rupture test at 1150 °C / 110 MPa. Arrows in magnified image are pointing at dislocation traces entering from γ/γ′ interface into γ′ phase (b).

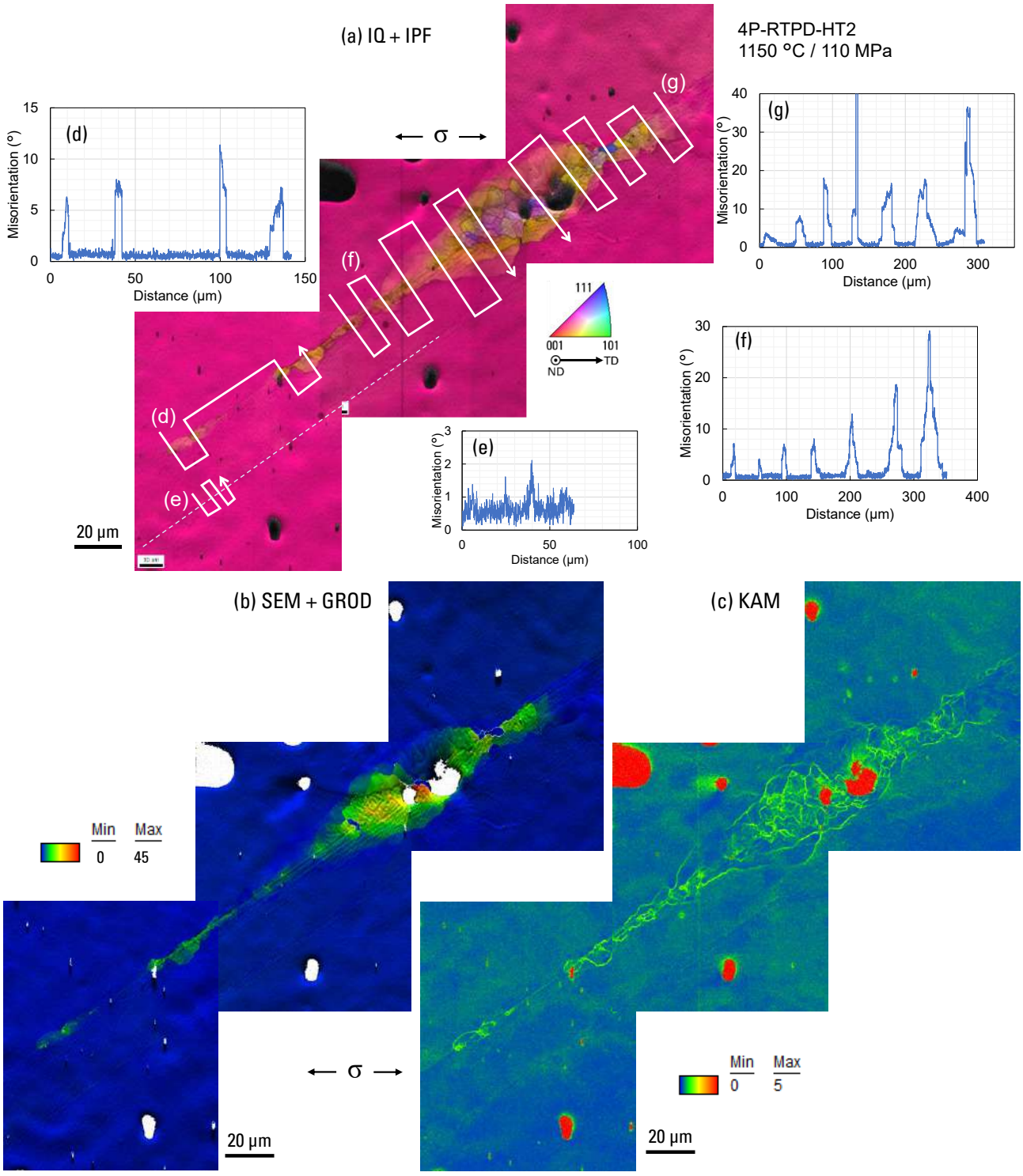

Figure 4.26. Result of EBSD analysis on 4P-RTPD-HT2 after creep test at 1150 °C / 110 MPa. (a) IQ + IPF map, (b) SEM + GROD map, and (c) KAM map. Misorientation profiles (d-g) are obtained from line analysis following arrows in (a). Dotted line in (a) is showing microstructure coarsened band with almost no misorientation.

By EBSD analysis performed on 4P-RTPD-HT2 after creep rupture test at 1150 °C / 110 MPa, recrystallization from the void on the band was confirmed (Figure 4.26(a)). GROD map (Figure 4.26(b)), KAM map (Figure 4.26(c)) and misorientation profiles (Figure 4.26(d-g)) in the same area shows almost no misorientation in the area outside the main band. When misorientation is < 10° (line profile in Figures 4.26(d, f)), KAM map has arc-shaped areas that resemble to AM1 in Figure 4.33(d) at 950 °C / 300 MPa. Recrystallization has not spread throughout the band in this observation, and the magnitude of the misorientation is increasing toward the void

in Figure 4.26(f). This is an evidence that recrystallization is starting from the void lying on the band, stress concentration is occurring at its vicinity, and spreading along the band. Damage (strain) accumulation, lattice rotation expressed by the GROD map in this case, is highly localized at the band and almost absent outside the band. Misorientation in another band indicated by dotted line in Figure 4.26(a) is less than 2°, which means this band locating next to the recrystallized band has stored almost no creep damage.

Microstructures in Figure 4.27 were obtained from CMSX-4 Plus specimens with AM1-type aging treatments (4P-HT1 and 4P-RTPD-HT1) after creep tests at 1150 °C / 110 MPa. Difference from microstructures of the same alloy with CMSX-4 Plus-type aging treatments is TCP precipitates observed at the creep voids (Figure 4.27(a)), and they were observed in the pre-deformed specimens as well (Figures 4.27(c, d)). TCP precipitates in pre-deformed specimen were always connected to the recrystallized grain boundaries as shown in Figure 4.27(d). The sliding in the bands was observed more frequently in 4P-RTPD-HT1 compared to 4P-RTPD-HT2 which is clearly related to the higher rupture strain of this specimen at the same creep condition (Figure 4.18).

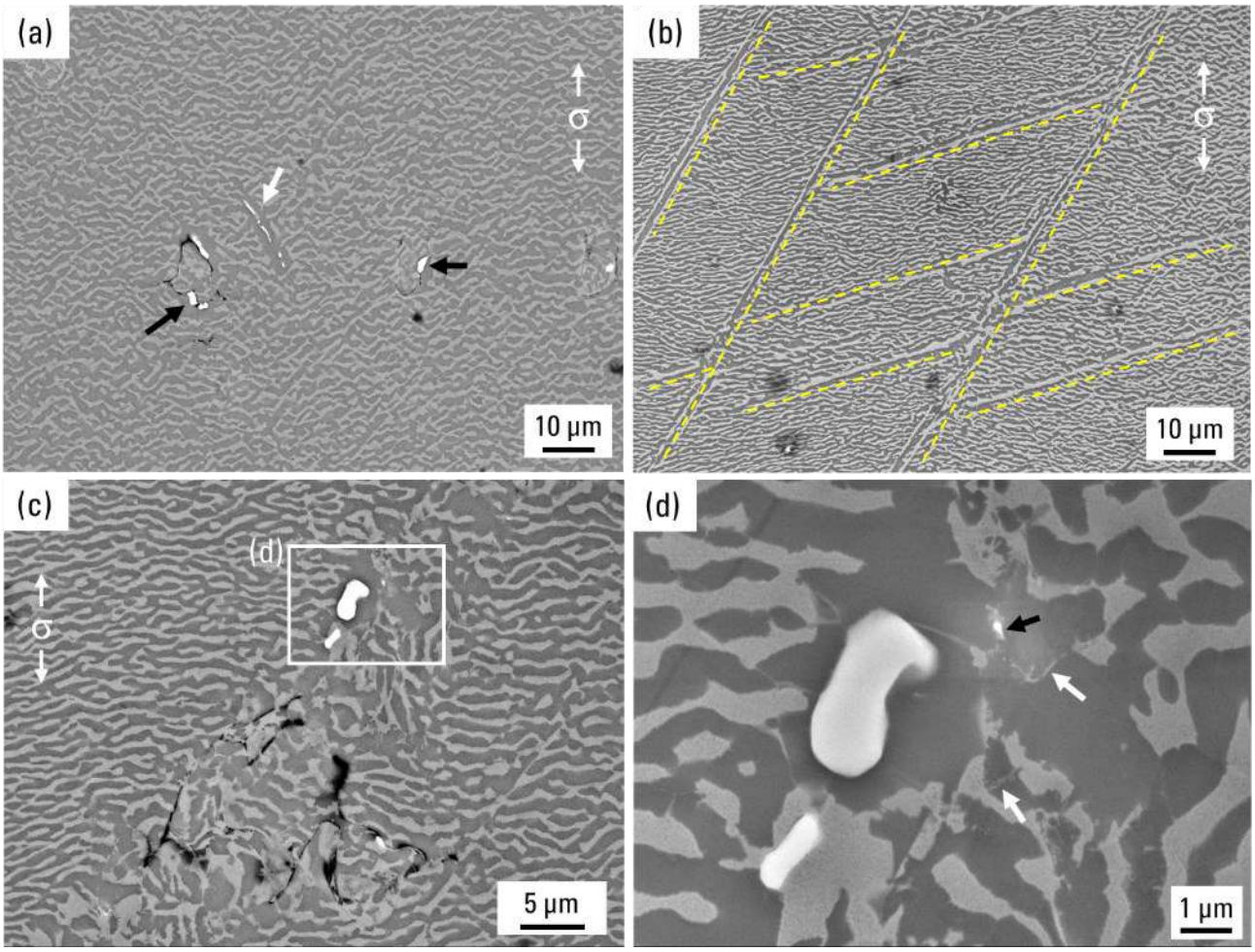

Figure 4.27. Microstructures of 4P-HT1 (a) and 4P-RTPD-HT1 (b-d) after creep rupture test at 1150 °C / 110 MPa, (a, c) are BSE and (b, d) are SEI. White arrow in (a) is TCP precipitate in {111} plane and black arrows in (a) are TCP precipitate in creep voids. Dotted lines in (b) are showing the microstructure coarsened bands. White arrows in (d) are grain boundaries and black arrow is a TCP precipitate nucleated at grain boundary.

B) CMSX-4 Plus at 1050 °C / 200 MPa

Figures 4.28 and 4.29 are microstructures after creep tests at 1050 °C / 200 MPa on 4P-HT2 and 4P-RTPD-HT2, respectively. As shown in creep curves and appearance of specimens in Figures 4.20 and 4.21, creep properties and fracture types are similar for these specimens. Typical crack propagation from interdendritic creep voids and their coalescence leading to a failure is observed in Figure 4.28. γ′-rafting structure in the interdendritic area of 4P-HT2 was disturbed with presence of dislocation traces as shown in Figure 4.28(c). In lower magnification images (Figures 4.28(a) and 4.29(a)), pre-deformed specimen has larger creep voids that connected to the microstructure coarsened bands. When the bands are intersecting at the interdendritic area, crack initiation without creep voids (or tip of crack imitated from creep void) was observed (Figure 4.29(b, c)). In the microstructure coarsened bands, γ/γ′ structure was not monotonically inclined like AM1 or CMSX-4 Plus at 1150 °C. Irregular shape was observed mainly at intersection of the bands and there were not big difference when this particularly disturbed area (Figure 4.29(c)) is compared with interdendritic area in 4P-HT2 (Figure 4.28(c)).

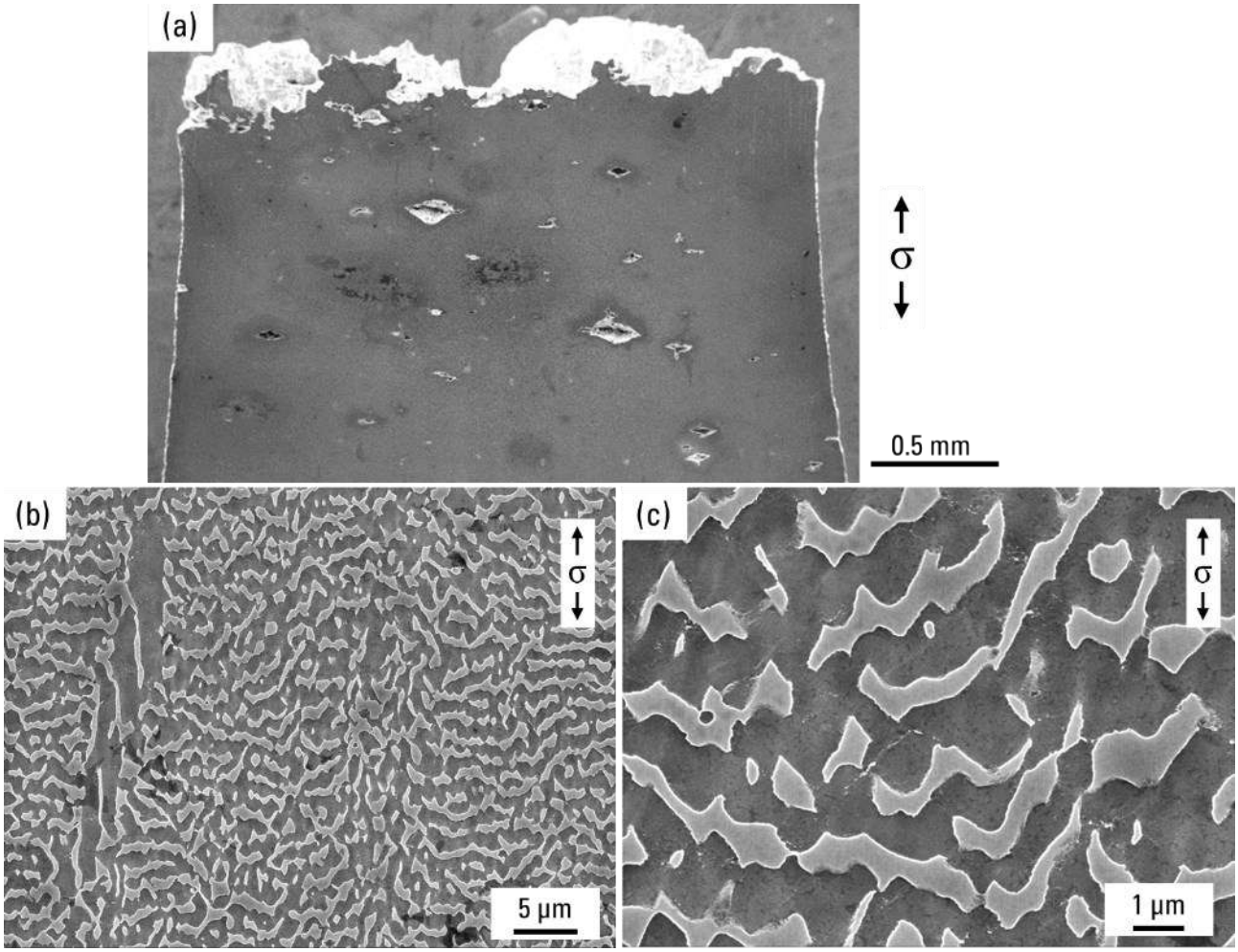

Figure 4.28. Microstructures of 4P-HT2 after creep rupture test at 1050 °C / 200 MPa. Low-magnification image showing fracture surface (a), interdendritic area 3 mm away from fracture surface (b), and the same area at higher magnification (c).

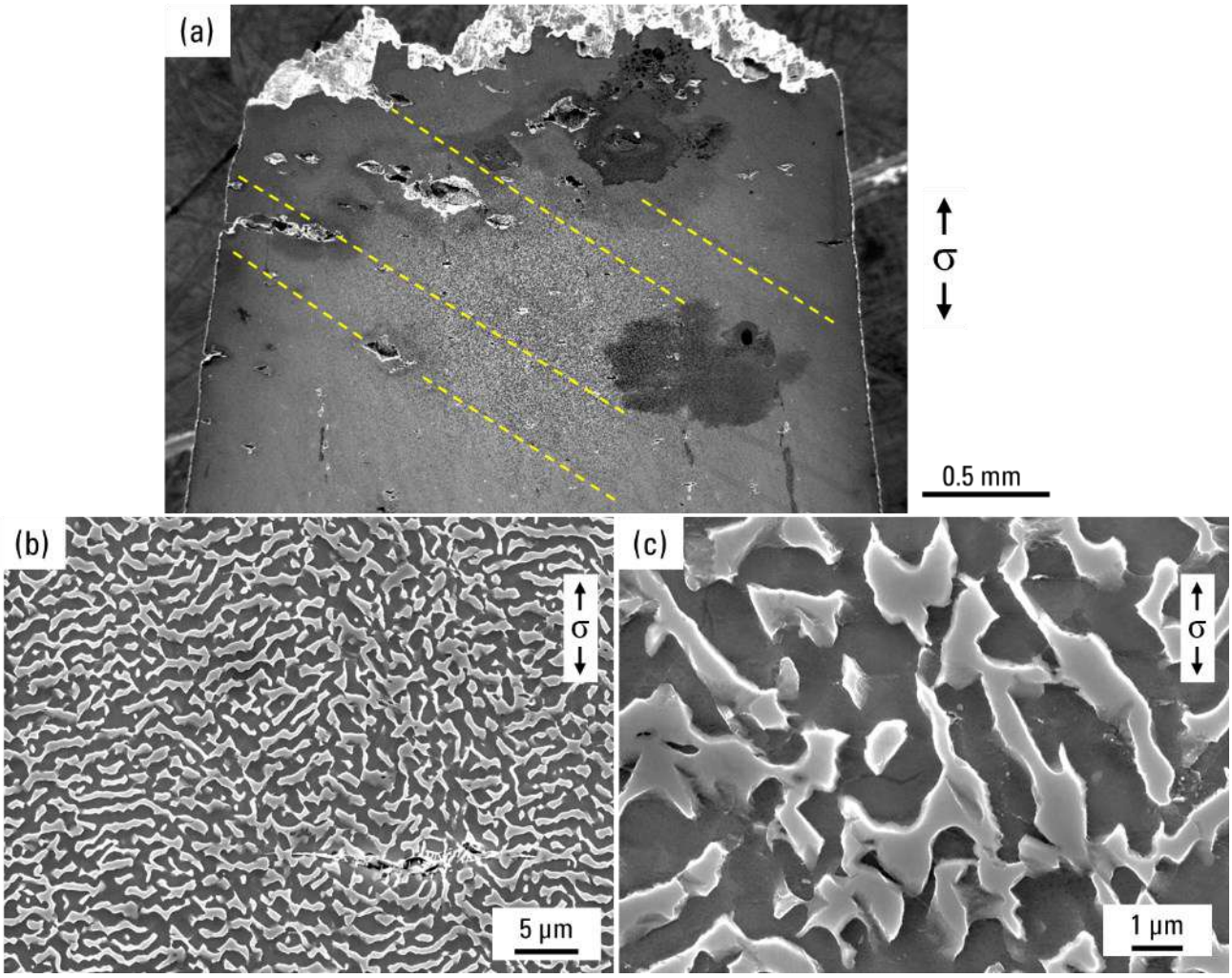

Figure 4.29. Microstructures of 4P-RTPD-HT2 after creep rupture test at 1050 °C / 200 MPa. (a) is low-magnification image showing fracture surface and the microstructure coarsened band indicated by dotted lines. (b) is interdendritic area 3 mm away from fracture surface with crack initiation. (c) is interdendritic area at the intersection of two bands.

Although the creep deformation type of CMSX-4 Plus at 1050 °C / 200 MPa can be categorized as similar to that of AM1 at 950 °C / 300 MPa, effect of pre-deformation appeared differently. This is also confirmed in the EBSD analysis presented in Figure 4.30 which was obtained at 2 mm away from the fracture surface of 4P-RTPD-HT2 tested at 1050 °C / 200 MPa. More than 8 different bands were analyzed for this specimen and none of them presented recrystallized grain, even near the cracks initiated from creep voids (Figure 4.30(b)). In GROD map shown in Figure 4.30(c), misoriented regions from average orientation are highlighted. It is certain that local strain (local lattice rotation) is higher in the microstructure coarsened bands, but it is widely spread toward area outside the band. Misorientation profiles of two bands in Figures 4.30(d, e) show that the misorientation between the band and the bulk is 10° at maximum. This is similar magnitude to the AM1 at 950 °C / 300 MPa (Figure 4.16(f)), but arc-shaped misoriented area (like Figures 4.16(d) and 4.26(c)) was not observed.

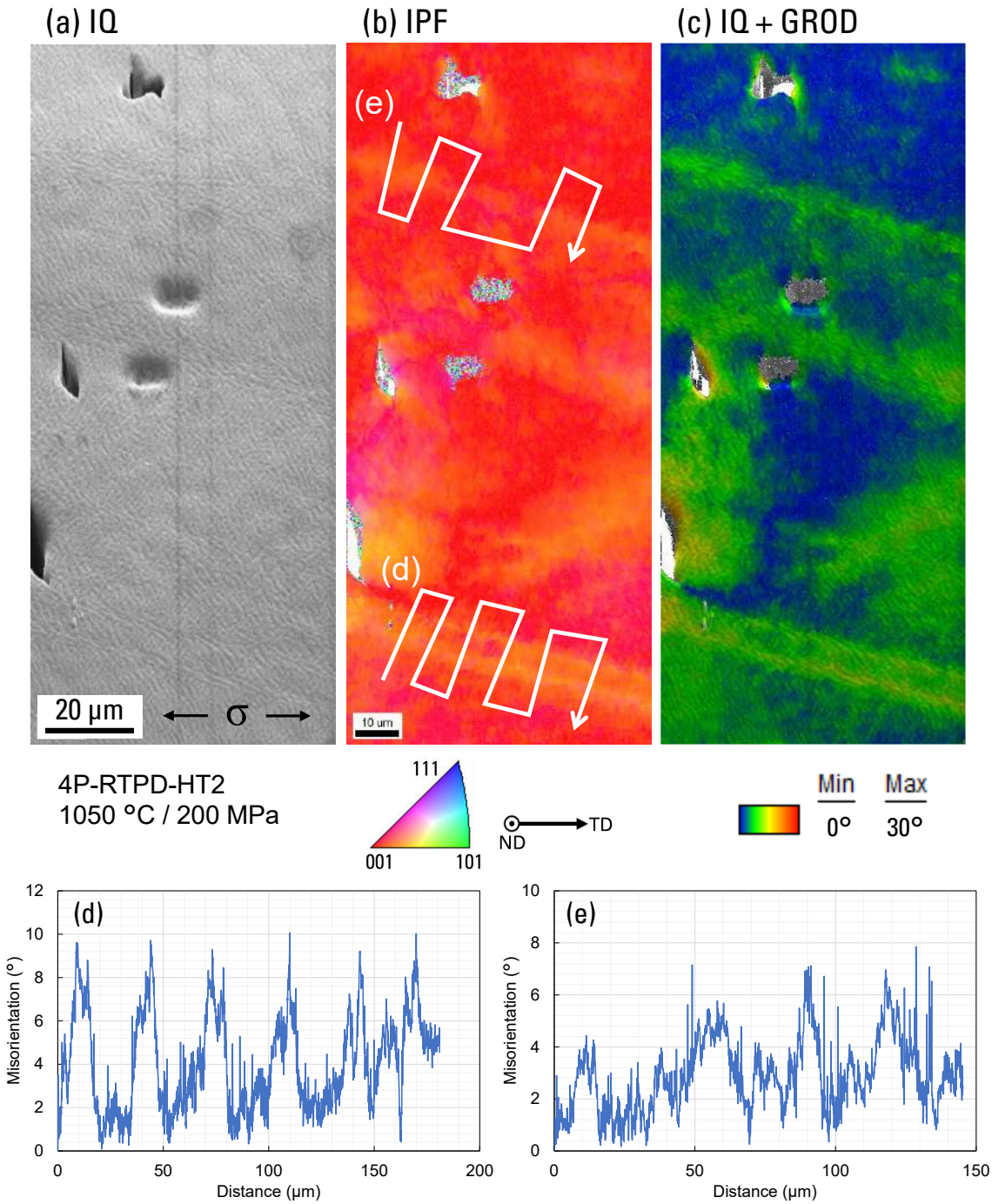

Figure 4.30. IQ map (a), IPF color-coded orientation maps referring to the tensile direction (b), and IQ + GROD map (c) on 4P-RTPD-HT2 after creep test at 1050 °C / 200 MPa obtained at 1 mm away from fracture surface. Misorientation profiles (d, e) are obtained from line analysis following arrows in (b).

4.2.6. Void nucleation and growth during heat treatment and creep

A) Stereological analyses of voids

According to the microstructure characterizations, cavitation was observed in the bands with the occurrence of recrystallized grains close to pores. Moreover, void nucleation and coarsening along the former slip plane were observed in the creep test interrupted specimens. Histograms were obtained by analyzing low-magnification images from different stages to verify the processes and origin of void nucleation, void growth, and recrystallization.

Five images with the resolution of 1280 px × 970 px (1 px corresponds to 1.07 µm, total area of 5.42 mm^2) were taken from the center of the creep specimens' gauge section by FEG-SEM operated at lower magnification (examples of analyzed images are in Figures 4.8 and 4.31(a, b)). Microstructures of the specimen after solution treatment (As-solutioned), specimen without PD after aging treatments (AM1-HT1), and pre-deformed specimen before creep test (AM1-RTPD-HT1) were also taken for this analysis. Because of resolution limitation, voids with an area smaller than 10 μm^2 were not included in the histogram of void size distribution. This resolution is enough for the analyses since fully heat-treated Ni-based SX superalloys processed by the Bridgman method generally have a mean void diameter of around 8 µm [11–13,19].

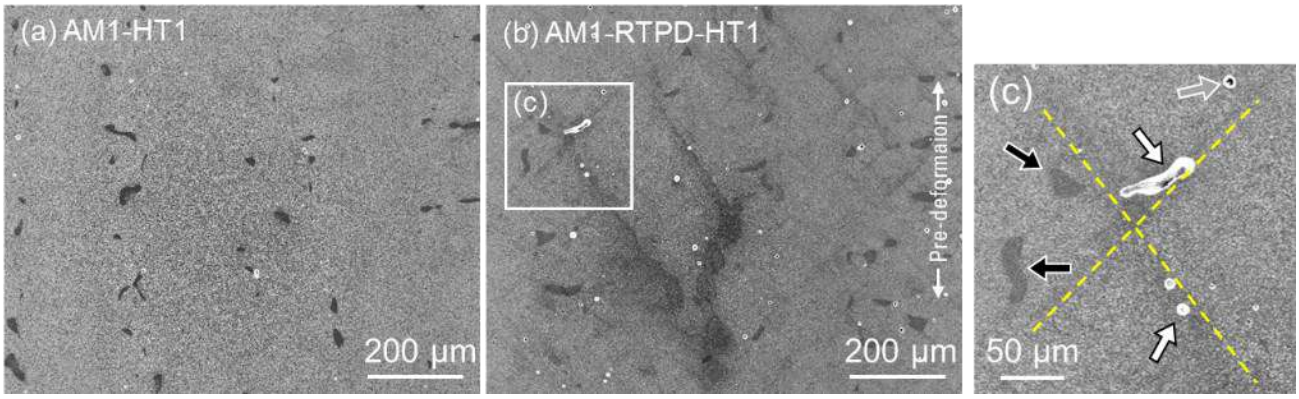

Figure 4.31. Examples of low-magnification images used in the image analyses (all before creep test). (c) is enlarged image in (b). Dotted lines are the microstructure coarsened bands. Black edge/white arrows, white edge/gray arrows, and white edge/black arrows in (c) are indicating examples of voids in the microstructure coarsened bands, voids outside the bands, and eutectics, respectively.

Histograms of all voids observed in the images are shown in Figure 4.32. Because void size in Ni-based SX superalloy normally follows a log-normal distribution [20,21], logarithmic void size is used for the horizontal axis of this histogram. The voids located within the microstructure coarsened bands and voids outside the bands are counted separately and histograms of voids in the bands are presented in Figure 4.33. A clearly higher density of voids is observed within the bands, according to the percentages of these voids among all the void population shown in Figure 4.33. In these analyses, micropores shown in Figure 4.14(b) (see white arrows) are not counted due to the limitation of image resolution in this low magnification. AM1-RTPD-HT1 is showing bimodal size distribution (see arrows in Figure 4.32(c)) and has by far more voids compared to the original AM1-HT1 (Figure 4.32(b)) meaning that PD enhances void nucleation during aging treatments. In the logarithmic scale, size distribution is following a normal distribution. Therefore, the median (comparable to mean of logarithmic values) of void size at different stages are compared in Figure 4.34 to analyze the trend of void growth. Increasing void size, or void coarsening, as a function of creep time in Figure 4.34 is in good agreement with other studies regarding void growth during creep deformation [12,13,20]. Because most of the voids in Figure 4.32 are also counted in Figure 4.33, and especially large ones (examples shown in Figures 4.11(b) and 4.13(a)) are always counted in Figure 4.33, the band is confirmed to be preferred void nucleation and growth site. The decrease in void size after creep rupture shown in Figure 4.34 is because the largest pores are separated since they are mostly located in the fracture surface and they are hence no longer counted as voids. Also, the area farther from the gauge center had to be observed for ruptured specimens in order to have the same total observation area to the interrupted specimens.

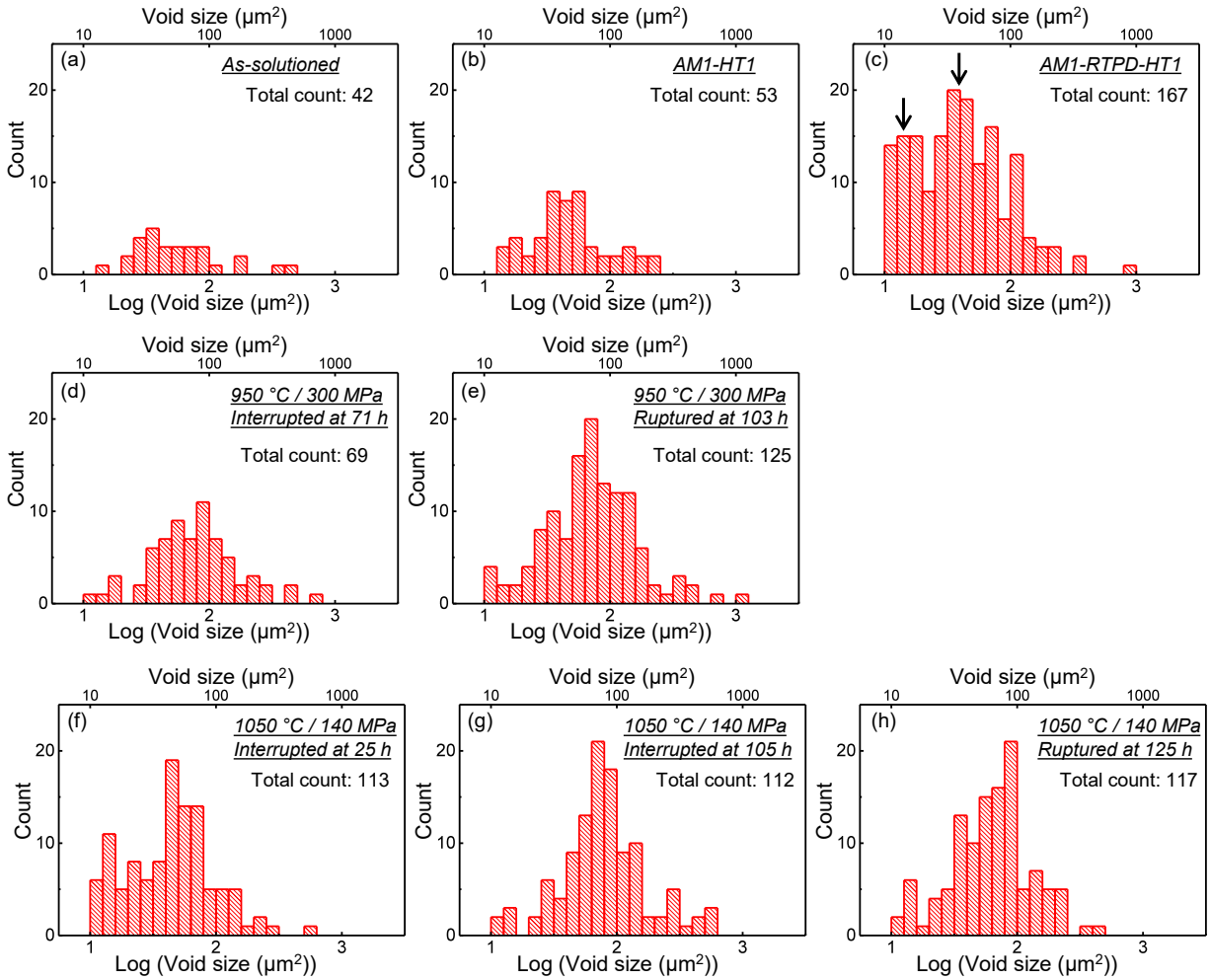

Figure 4.32. Histograms of void count vs. void size in a logarithmic scale of μm² obtained by image analyses along a longitudinal section of AM1 specimens. The total count of voids is labeled in the figures. Arrows in (c) are indicating two peaks of a bimodal distribution.

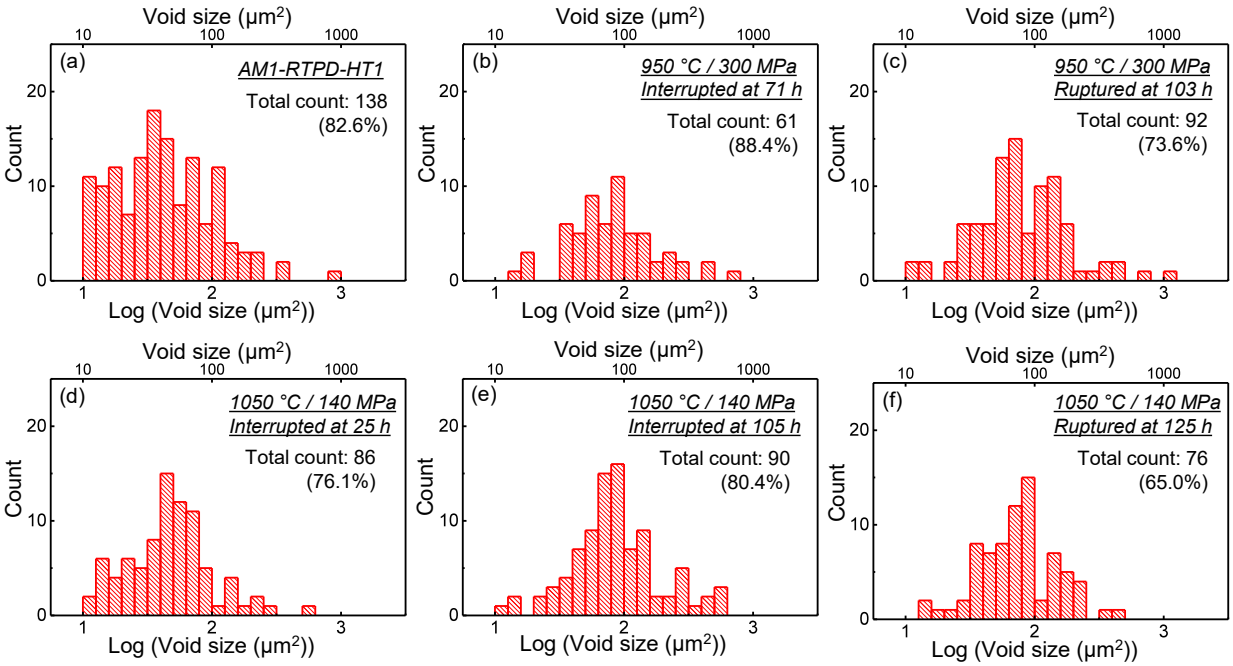

Figure 4.33. Histograms of counts of voids in the microstructure coarsened bands vs. void size in a logarithmic scale of μm² obtained by image analyses along longitudinal sections of AM1 specimen. The total void count and percentage of voids in the band are labeled in the figures.

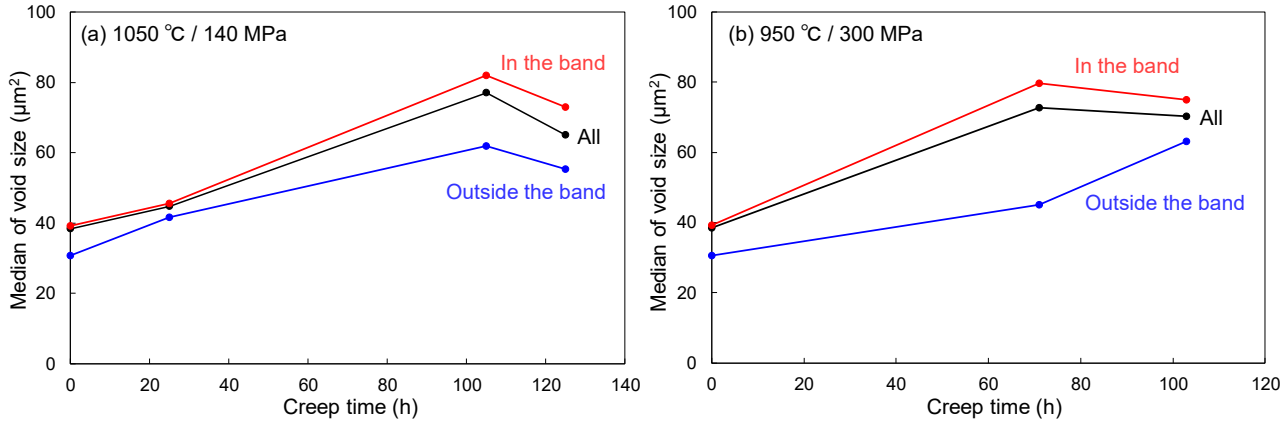

Figure 4.34. The median of void size in μm² is plotted as a function of creep time at creep conditions of 1050 °C / 140 MPa (a) and 950 °C / 300 MPa (b). Three lines are for all voids, voids in the microstructure coarsened bands, and voids found outside the bands.

B) Void nucleation and growth mechanism

Enhanced void nucleation and growth was statistically shown in the previous subsection. Using the results above, void nucleation and growth mechanism is discussed hereafter with schematic illustrations presented in Figure 4.35.

The introduction of a room-temperature PD after solution treatment is shown to deeply affect both microstructure and creep life in the γ′-rafting regime. The PD proceeds by γ/γ′ shearing with practically no dislocation introduced outside of the slip bands (Figure 4.35(a)) [22,23], which is confirmed by the typical cuboids observed in the microstructure before creep tests (Figure 1.38(c)) located outside of the microstructure coarsened bands. During the first aging heat treatment at 1100 °C, local elastic strains surrounding slip bands are relaxed by activated plasticity within the γ phase associated with the formation of dislocation structure (Figures 3.16 and 3.17). As discussed in the previous chapter, γ′ precipitates have a tendency for N/P-type directional coarsening along ⟨001⟩ directions or tilted due to the imbalanced tensile/compressive components (Figure 4.35(b)).

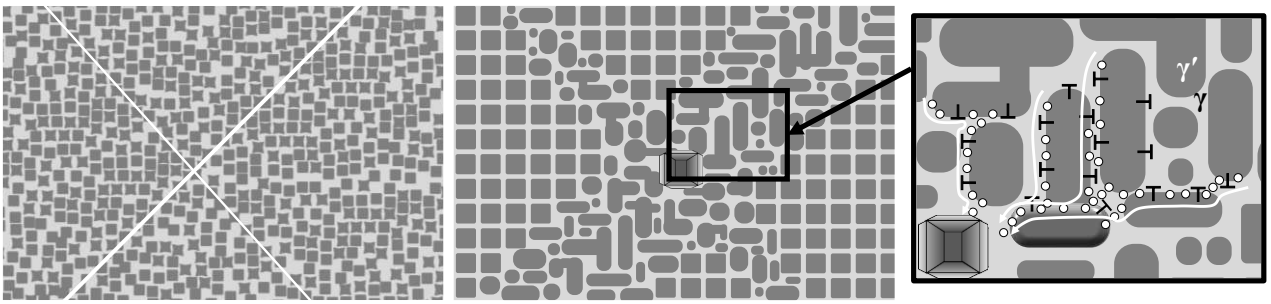

Figure 4.35. Schematic illustration of microstructures after room-temperature tensile PD (a) and after aging treatments (b). (c) is a magnification of (b) showing vacancy transportation through γ/γ′ interfacial dislocations that enhances D-pore type void growth.

As shown in the literature review, strong chemical segregation in a Ni-based SX superalloy creates S-pores and H-pores [24–26]. These S-pores and H-pores are the voids counted for the histogram in Figure 4.32(a), i.e. the microstructure before the pre-deformation. The slight increase in the number of voids counted from as-solutioned (Figure 4.32(a)) to AM1-HT1 (Figure 4.32(b)) is possibly due to a coarsening of smaller voids into

a detectable size (≥ 10 μm^2) during the aging treatments. On the other hand, the drastic increase of void counts in AM1-RTPD-HT1 (Figure 4.32(c)) and the significant difference from AM1-HT1 cannot be explained only by the mechanisms related to S/H-pores evolution.

Figure 4.36 presents various types of voids found before and after creep tests. Figures 4.36(a, b) represent an example of S-pore and H-pore, respectively. Faceted voids lying in the microstructure coarsened band in Figure 4.36(c) are very similar to the pores observed in the specimen after creep interrupted tests (Figure 4.36(d, e)). This dodecahedral crystallographic void is a typical D-pore that usually nucleates and grows in the other SX superalloys by vacancy transportation during high-temperature/low-stress creep loading or very long-term annealing [13,20,25,27]. The D-pore nucleation appears as the first peak of bimodal void size distribution at the early stage (~1 % creep strain) of high-temperature/low-stress creep [20]. Size of D-pore type void in Figure 4.36 is consistent with a very high void count under 100 μm^2 in Figure 4.32(c), more specifically the first peak (on the left) of the bimodal distribution. Therefore, the introduction of PD strongly enhances D-pore type void nucleation during aging treatment without any external loading.

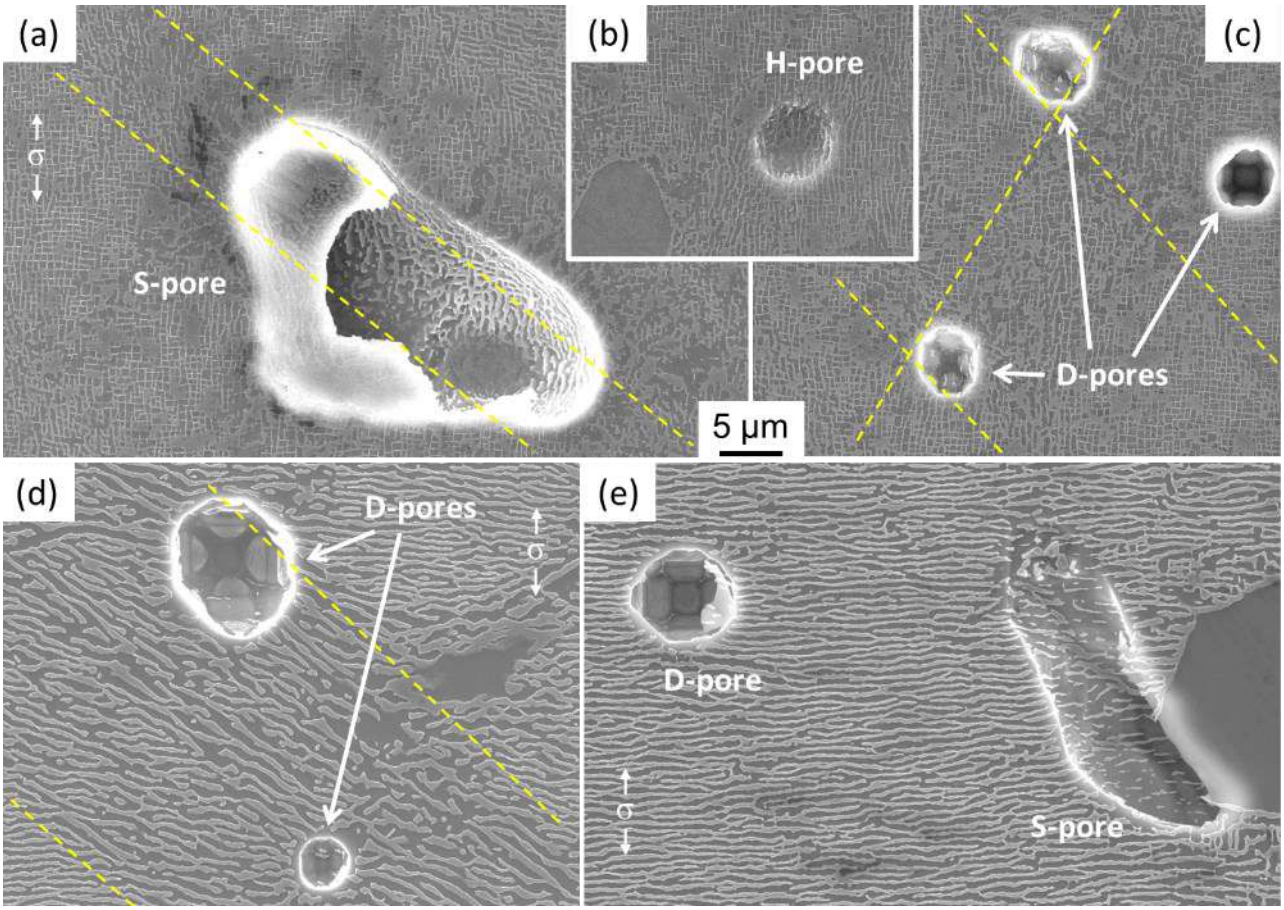

Figure 4.36. Examples of different voids found in AM1-RTPD-HT1 before creep test (a-c). AM1-RTPD-HT1 after creep test at 1050 °C / 140 MPa interrupted at 105 h, middle of gauge section (d), and 1 mm from specimen thread toward gauge section (e). Dotted lines are indicating the direction of the microstructure coarsened bands.

Strong elastic fields exist around slip bands after PD and this is the main reason for the microstructure evolution with the formation of γ/γ′ interfacial dislocations [28]. Simultaneously, dislocation climb and associated dislocation pipe diffusion of vacancies into a preferential site occur during high-temperature aging treatment. This is supported by the STEM image in Figure 3.17 that shows mobile dislocations that can facilitate vacancy

transportation by dislocation climb. High internal elastic strain can also decrease the critical radius for void nucleation since the formation of voids helps the local stress relaxation. Therefore, D-pore type voids are assumed to nucleate/grow with the same mechanism as common D-pore nucleation/growth during creep deformation which was originally proposed by Epishin and Link [1,20]. In this study, D-pore nucleation/growth were only resulting from the residual internal strain (introduced by a PD prior to the aging treatments) and not by the application of an external macroscopic stress. Figure 4.35(c) represents the void nucleation and growth mechanism in these experiments.

As presented in Figure 4.31, large voids are mainly found in the interdendritic area where a higher density of defects such as sub-grain boundaries, remaining γ/γ′ eutectic pools, and S/H-pores are already existing. Slip system activation may occur with higher frequency from those defects [29]. In the slip band introduced on the same plane of existing S/H-pores, those pores also grow rapidly in the direction of the bands for stress relaxation (Figure 4.36(a)). Interaction of slip bands and sub-grain-boundaries may also assist void nucleation and growth.

4.2.7. Localized shearing and damage accumulation mechanisms during high temperature creep

Considering all microstructural analyses performed on AM1 and CMSX-4 Plus, creep rupture mechanisms of Ni-based SX superalloys with pre-deformation between solution and aging treatments are discussed in this section with schematic illustrations. Creep mechanisms are separated into two regimes, rafting and topological inversion. These cannot be strictly divided, but separated for convenience in this discussion. Rafting regime represents creep temperature at which the volume fraction of γ′ phase is close to 50% and creep stages consists of primary stage, secondary stable stage, and tertiary stage (1050 °C for AM1 and 1150 °C for CMSX-4 Plus). Topological inversion regime is representing creep deformation at 950 °C for AM1 and 1050 °C for CMSX-4 Plus (γ′ volume fraction >50%) that has no primary stage and continuously increasing creep rate.

A) γ′-rafting regime (volume fraction ~50%)

In the first step of creep deformation at 1050 °C / 140 MPa, γ′-rafts are slightly tilted toward former slip plane in the microstructure coarsened bands (schematically shown in Figure 4.37(a)) which is due to the inhomogeneous precipitate shape that caused misoriented interfacial strain between the precipitates and the matrix. The inclined γ′-rafts have a faster coarsening rate during the secondary creep stage as presented in Figure 4.10(b). Native dislocations that formed during aging treatments are contributing to the faster coarsening and further inclination of γ′-rafts until being almost parallel to the former slip plane (Figure 4.37(b1)). Certain amount of {111} system dislocations have been already stored in the matrix (Figure 3.17) and this can enhance local γ′ shearing during early stages of the creep deformation (Figure 4.25). If this kind of dislocations cutting into γ′ phase is facilitated, γ element transportation in the {111} plane is assisted by PARIS (Plasticity Assisted Redistribution of Interacting Solutes) mechanism [16,30–32] (Figure 5.37(b2)) and it extends γ phase in the same {111} plane like in Figures 4.10 and 4.23. This is also evidenced by EDS analyses on the non-recrystallized band with thick and continuous γ′-raft sandwiched by γ phase (being boundary of the band). This γ phase in the non-recrystallized band has very strong segregation of Al, Cr, and Co and very high density of dislocations confirmed by ECCI.

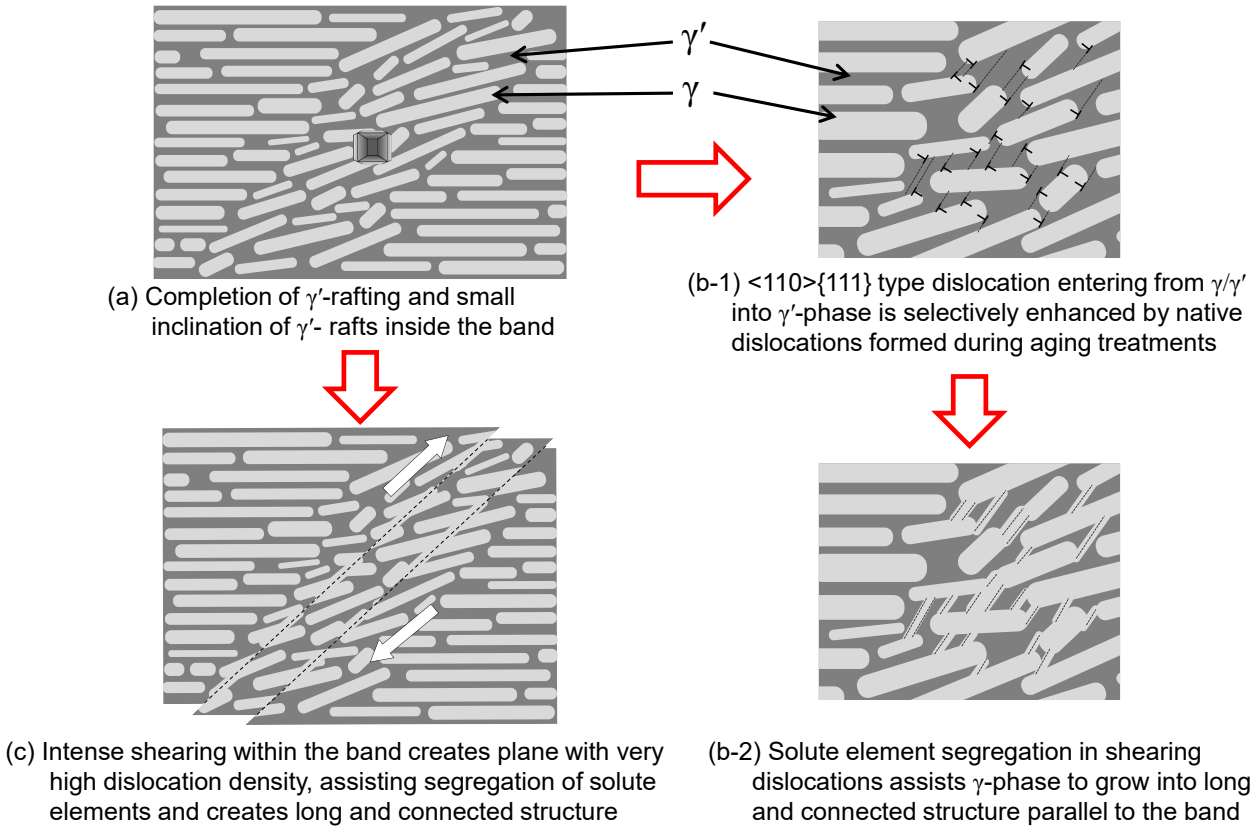

Figure 4.37. Schematic illustration of γ′-raft inclination mechanism in the microstructure coarsened band during higher temperature creep (AM1-RTPD-HT1 at 950-1050 °C or 4P-RTPD-HT2 at 1150 °C / 110 MPa in the present case).

Another case is when slip band is created by local sliding as shown in Figures 4.13 and 4.24). This slip plane has higher dislocation density and assists diffusion, which also creates long and connected γ phase by the same PARIS effect (Figure 4.37(c)). Slip band type was not observed in the AM1 specimen tested at 1050 °C / 140 MPa, but present in AM1 at 1050 °C / 200 MPa and CMSX-4 Plus at 1150 °C / 110 MPa that have shorter creep life. Two different types in Figures 4.37(b, c) are representing difference in contribution of stress and temperature on activation of dislocation motion. During creep of AM1 at 1050 °C / 140 MPa, secondary creep stage is extremely flat (almost no strain increment for more than 200 h) that thermally activated dislocation motion and accumulation are necessary to trigger tertiary stage (i.e. mainly time dependent process). Instead, creep tests on AM1 at 1050 °C / 200 MPa and CMSX-4 Plus at 1150 °C / 110 MPa have secondary stage with slow but progressive strain accumulation. The contribution of stress on the dislocation motion is higher in these conditions that can trigger local slip in existence of initial dislocation structure (inside the microstructure coarsened band) created by pre-deformation.

The dislocation traces entering γ′ phase (Figures 4.10 and 4.25) and higher dislocation density suggested by KAM map (Figure 4.16(c)) are evidences that microstructural damage accumulation is faster in the inclined γ′-rafts than outside the bands. Such thick and connected γ′-rafts help vacancy transportation toward existing voids for growth or nucleation of new D-pore type voids (Figures 4.11, 4.36(d) and 4.38(a)). Once void (including S/H/D-pores) in the microstructure coarsened band have grown and reached a size close to the width of the bands, voids have preferential growth direction toward the plane of the bands. Figure 4.11(d) is the example of a void size determined by the width of the band. Former S-pore type voids shown in Figures 4.11(b,

c) also have their growth direction affected by the bands. Void in Figure 4.36(c) is also showing growth in {111} plane (note that observation is in ~(101) plane). Anisotropic void growth suggests that vacancies are supplied from the band of inclined and coarsened rafts. This anisotropic growth direction is lying on the {111} plane which is schematically shown in Figure 4.38(b).

Subsequently, during the very last stages of creep deformation, the enlarged voids are inducing stress concentration in their vicinity, leading to an increase of the local dislocation density. The energy barrier for recrystallization is reduced by the faster diffusion along dislocation lines and stored energy surrounding voids. This triggers γ′ dissolution and dynamic recrystallization along the band in the very last stages of creep deformation just prior to failure (Figure 4.38(c)) [60]. In the creep deformation with higher stress assisted damage contribution (4P-RTPD-HT2 at 1150 °C / 110 MPa), recrystallization starting from void is similarly shown with increasing misorientation of the band toward void (Figure 4.26). Finally, generated grain boundaries will slide (Figure 4.9(a) and 4.27(b)) and become crack propagation route, resulting in macroscopically (apparent) planar creep failure with very low overall ductility (Figure 4.38(d)).

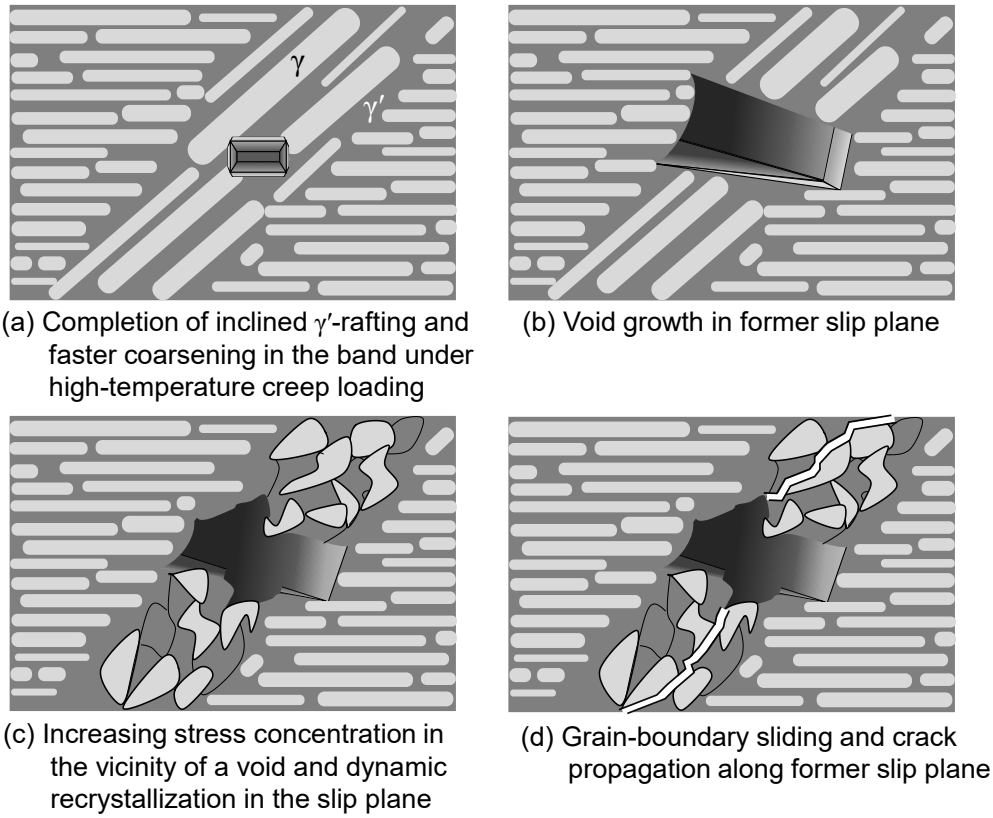

(a) Completion of inclined γ′-rafting and faster coarsening in the band under high-temperature creep loading

(b) Void growth in former slip plane

(c) Increasing stress concentration in the vicinity of a void and dynamic recrystallization in the slip plane

(d) Grain-boundary sliding and crack propagation along former slip plane

Figure 4.38. Schematic illustration of creep damage acceleration and failure mechanism on SX superalloy with PD at high temperature/low applied stress (AM1-RTPD-HT1 at 1050 °C or 4P-RTPD-HT2 at 1150 °C / 110 MPa in the present case).

During creep at the same condition on CMSX-4 Plus but having different heat treatments (4P-HT1 and 4P-RTPD-HT1), the most striking difference is that the pre-deformed specimen has very short creep life (equivalent to 4P-RTPD-HT2) but ductility had not decreased (Figure 4.18). The observed differences in specimens with different heat treatments are initial precipitate size and unexpected TCP precipitation during short test that lasted only about 32 h in 4P-RTPD-HT1. However, the reason for different creep properties cannot be clearly stated from the results.

B) Topological inversion regime (volume fraction >50%)

Some damage contributing factors are different between creep of AM1-RTPD-HT1 at 1050 °C / 140 MPa and 950 °C / 300 MPa, and they are more apparent for CMSX-4 Plus at 1150 °C / 110 MPa and 1050 °C / 200 MPa.

The inclined γ′-raft structure also forms in the bands (Figure 4.39(a)) after a certain period of creep loading at 950 °C / 300 MPa with possibly the same mechanism presented in Figure 4.37. Instead of very fast coarsening and formation of connected γ′-rafts as observed at 1050 °C / 140 MPa, topological inversion in the bands is the main event that proceeds during creep deformation at 950 °C / 300 MPa. Micropore nucleating from the γ/γ′ interfaces shown in Figure 4.14(b) is a direct indication that creep damages and creep deformation is driven by the same mechanism as for SX superalloys without PD. Large creep voids near the fracture surface in Figure 4.13(a) are showing crack propagation similar to Figure 4.7(b) which also supports the fact that creep damage mechanisms of AM1-RTPD-HT1 proceeding in this condition are similar to that operating in the original material AM1-HT1. The pore shown in Figure 4.14(d) is an example of multiple voids coalescence and growth. At the same time, dodecahedral D-pore type void growth assisted by the bands is observed as presented in Figure 4.14(c). Because precipitate coarsening is sluggish as compared to creep at 1050 °C / 140 MPa, the diffusion path for vacancies' concentration is not completely connected to the voids existing before creep tests. Therefore, multiple void nucleation/growth/coalescence mechanisms play a role in the creep deformation at 950 °C / 300 MPa. The very last stage of failure should be grain-boundary sliding and crack propagation throughout recrystallized grains generated by stress concentration near enlarged voids (Figure 4.39(d)), as for creep tests at 1050 °C.

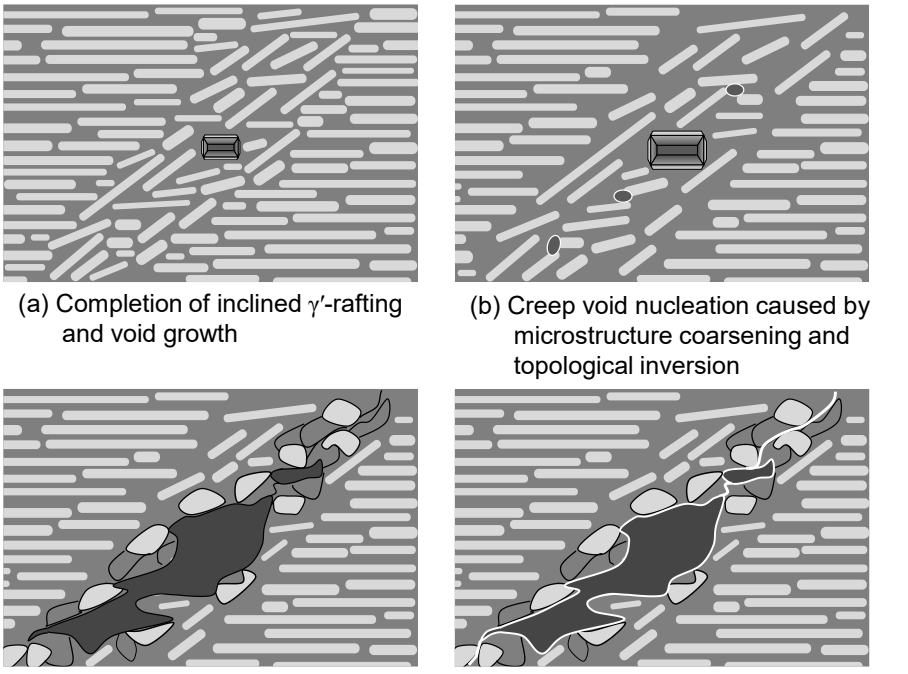

Figure 4.39. Schematic illustration of creep damage acceleration and failure mechanism on SX superalloy with PD at intermediate temperature/medium applied stress (AM1-RTPD-HT1 at 950 °C / 300 MPa in the present case).

The main differences in the creep deformation and damage mechanisms between both creep temperatures can be explained from EBSD analyses as well. As presented in Figure 4.16, the microstructure coarsened band after creep at 950 °C / 300 MPa has crystal lattice misorientation, which did not occur at 1050 °C/140 MPa. The KAM map and the misorientation profile suggest that the band has higher dislocation density and higher local plastic strain compared to the outside. As larger strain in the band is contributing to the total creep strain of the specimen, it explains why the strain rate at 950 °C / 300 MPa is faster for all the creep deformation periods of the specimen with PD (AM1-RTPD-HT1). The conjecture of local lattice misorientation contributing to the overall creep strain is also supported by the misorientation profile along the gauge section shown in Figure 4.17. Misorientation along the gauge section is smaller (or comparable) in Figure 4.17(b) than in Figure 4.17(a), but overall creep strain is by far larger at 950 °C / 300 MPa (Figures 4.2 and 4.4). Lattice rotation is a common characteristic of high-temperature creep deformation especially for specimens whose orientation is far from [001] and [111] [40,61,62]. Therefore, creep damage mechanisms inside the band during creep at 950 °C / 300 MPa is similar to the microstructure without an effect of pre-deformation but accelerated by the locally disordered microstructure with a higher dislocation density from the beginning of the creep test. This leads the specimen with PD to behave like a composite material with a two-scale failure mechanism consisting of a typical precipitate coarsening “matrix” (outside the bands and occupying most of the volume) and rotating plates “fibers” (the microstructure coarsened bands). On the other hand, the absence of lattice rotation in the bands during creep tests at 1050 °C / 140 MPa means no kinematical contribution of the bands to the overall strain, overall explaining the flat secondary creep stage.

Another interpretation resulting from the differences in misorientation profiles is a very strong damage localization in creep at 1050 °C / 140 MPa compared to that at 950 °C / 300 MPa. The internal diffusion rate, determined by the material’s chemistry, creep temperature, and the initial dislocations in the bands, is important to discuss the tendency of strain localization. At high temperature (AM1 at 1050 °C in the present case), the faster diffusion helps all the steps from microstructure coarsening, the formation of the γ′ rafts connected along {111} planes, climb of dislocations with vacancy transportation, void growth, and recrystallization at the end. These processes can easily localize to the place with the best preference which should be a larger void created during heat treatment. At the lower temperature (AM1 at 950 °C in the present case), the capability of internal transportation is less because of a lower diffusion rate. Hence, strain accumulation in the bands, shown as lattice misorientation in Figure 4.16(b, d), is necessary to increase dislocations density and to create diffusion paths for void nucleation/growth. This damaging event occurs in widely distributed areas in the bands, and therefore, damage accumulation is less localized compared to the creep at 1050 °C. Because damage can easily be stored in the most critical region, creep tests at 1050 °C has very good reproducibility regardless of macro plastic strain introduced during pre-deformation. On the other hand, when the contribution of internal strain accumulation is necessary to trigger the failure, creep life is possibly determined by the initial local plastic strain from pre-deformation. Local plastic and elastic strains in one single slip band cannot be controlled in tensile PD. This is possibly a reason for a larger scatter in creep life and minimum strain rate during creep tests at 950 °C/300 MPa (Figures 4.4 and 4.5(b)).

4P-RTPD-HT2 at 1050 °C / 200 MPa did not show strong impact of pre-deformation in terms of creep life. This is different from AM1 at 950 °C that has similar deformation behavior to CMSX-4 Plus at 1050 °C if pre-

deformation was not introduced. These differences between AM1 at 950 °C and CMSX-4 Plus at 1050 °C can be explained by the intrinsic creep behavior of CMSX-4 Plus at 1050 °C and the microstructure before creep tests.

Dislocation networks and precipitate edges observed in the microstructure of CMSX-4 Plus (Figure 3.28) are the main difference when it is compared with that of AM1 (Figures 3.10 and 3.11). As discussed in the previous chapter, this is suggesting the higher magnitude of γ/γ′ interfacial coherency is remaining in CMSX-4 Plus after pre-deformation and heat treatments, which blocks dislocations entering into γ′ phase during creep deformation. It is worth recalling that CMSX-4 Plus has lower yield stress compared to AM1. This led to higher density of slip bands (with smaller elastic strain energy for each band) accumulated in CMSX-4 Plus at the same macro plastic strain. Because CMSX-4 Plus has smaller elastic energy in slip bands and higher absolute lattice misfit at the aging temperature, γ/γ′ interfacial coherency in the microstructure coarsened band was retained at higher magnitude compared to AM1.

Creep curve of CMSX-4 Plus at 1050 °C / 200 MPa shows almost no primary stage and gradually increases strain rate. Although γ′-rafts are observed in creep ruptured microstructure (Figures 4.28 and 4.29), rafting may not start immediately in this creep condition. Instead, relatively good creep properties of this alloy among other SX superalloys are possibly owing to slower internal diffusion that retards γ′-rafting even at 1050 °C. With high volume fraction of γ′ phase at 1050 °C, creep deformation is more in the domain of topological inversion [9] which is suggested by the fact that damage is spreading over longer distances (EBSD results in Figure 4.30). Magnitude of γ′-rafting and microstructure coarsening were not so different between inside and outside of the band within the 4P-RTPD-HT2 specimen after the creep test at 1050 °C / 200 MPa. Since thermally activated damaging processes are slow for this material, and high magnitude of γ/γ′ interfacial coherency is retained in the band, creep damage was not localized at 1050 °C / 200 MPa. In addition, smaller initial precipitate size of HT1 specimens is a possible reason of creep properties better than HT2 processed specimens. However, the effect of pre-deformation with this aging treatment conditions was not clear from the obtained results.

From above all, it can be concluded that the damage processes in pre-deformed material is strongly time dependent. The microstructure coarsened bands are affecting diffusion involved creep damage kinetics, and this effect become dominant as temperature increases. Moreover, it was shown in comparison of AM1 with different creep loading at the same temperature (1050 °C / 140 or 200 MPa) that higher stress decreases the creep life gap between pre-deformed and non-pre-deformed materials. When the applied creep load becomes bigger, residual internal strain related to the band becomes relatively smaller, and contribution of thermally activated process becomes smaller. In other words, the impact of pre-deformation on the creep life of SX superalloys becomes smaller as applied stress increases.

4.2.8. Effect of pre-deformation at RT on creep properties at lower temperatures

A) AM1 at 850 °C / 500 MPa and 750 °C / 800 MPa

Results of creep rupture tests on AM1-RTPD-HT1 at 850 °C / 500 MPa are shown in Figure 4.40. Readers can refer to the Figure 1.40(d) for the results at 750 °C / 800 MPa since additional test was not performed. Creep

of pre-deformed specimens at 850 °C / 500 MPa showed higher creep rate during all period after primary stage and decreased ductility (Figure 4.40). At 750 °C / 800 MPa, creep strain rate after secondary stage was similar for all specimens, however, pre-deformed specimens failed at smaller total strain (Figure 1.40(d)). In both conditions at lower temperatures, the pre-deformed specimens showed shorter duration of primary creep and smaller magnitude of primary creep strain compared to the original materials.

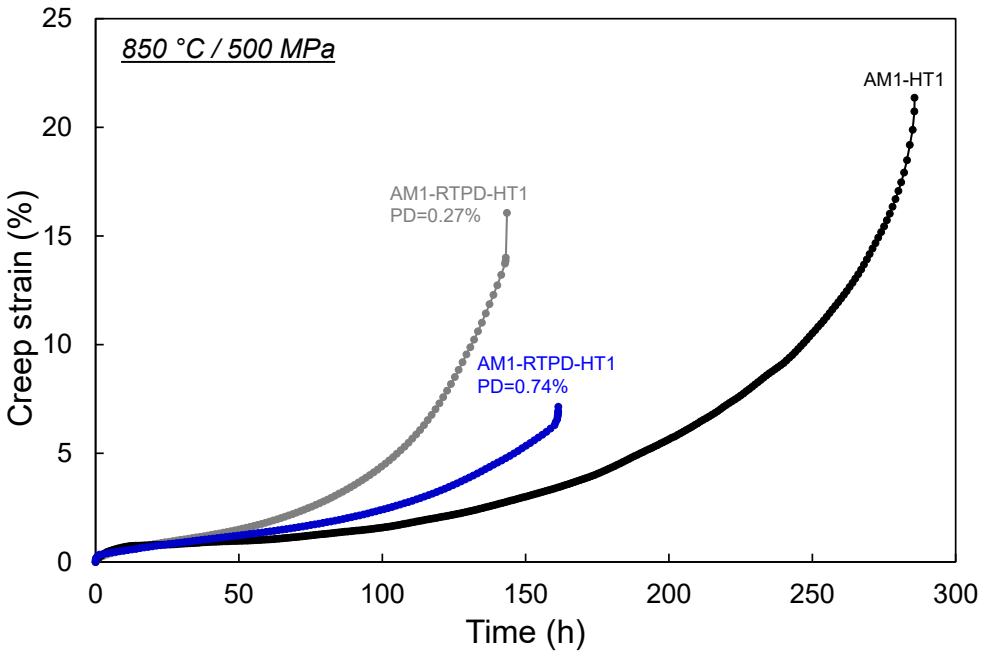

Figure 4.40. Creep curves of AM1 specimens without and with pre-deformation, tested at 850 °C / 500 MPa.

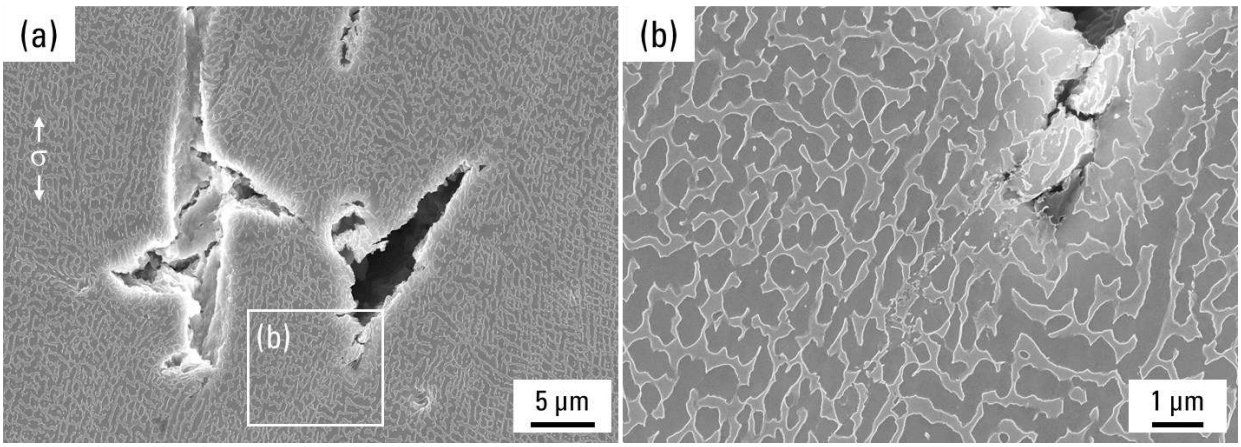

Figure 4.41. Cracks from creep voids near fracture surface of AM1-RTPD-HT1 specimen after creep rupture test at 850 °C / 500 MPa.

Figures 4.41 and 4.42 are voids and cracks observed in AM1-RTPD-HT1 specimen after the creep rupture test at 850 °C / 500 MPa. Cracks in Figure 4. 41 is lying on the band of {111} fracture surface. Disturbed structure is observed at the crack tip in Figure 4. 41(b), but recrystallization was not confirmed in this specimen. Other examples of a crack propagating from a coarsened void lying on the intersection of two different bands are indicated by arrows in Figure 4. 42(a). Microstructure outside the band is similar to that of a specimen without pre-deformation consisting of γ-channel and γ′-particles, but less developed compared to that of AM1-HT1 after creep rupture because of shorter creep time. γ′ precipitates inside the band have further coarsened along

both vertical and horizontal direction from microstructure before creep and a shearing trace is also observed (Figure 4. 42(b)). EBSD analysis was performed close to one of the bands near fracture surface and IPF/KAM maps are shown in Figure 4.43. Lattice misorientation and higher dislocation density were observed within the band, however, recrystallization was not detected. Also, in AM1-RTPD-HT1 after creep rupture at 750 °C / 800 MPa, recrystallization was not present with lower lattice rotation of the band, even near the fracture surface (Figure 4.44).

The original AM1-HT1 performed similarly to other first generation superalloys [33–35]. In the similar creep condition, dislocations fill up matrix during primary and secondary stage, forms dislocation network that surrounds γ′ precipitates, and then precipitates are sheared by dislocations during the tertiary creep stage [34,35]. Although temperature is not so high, microstructure after creep rupture shows that both precipitation coarsening and void formation took place during deformation (Figure 4.42). Coarsened precipitates on AM1-RTPF-HT1 before creep have round edges that suggest dislocations migrating in the matrix side of γ/γ′ interface. STEM observation have proven that already decent amount of dislocations existing in the γ matrix of the microstructure coarsened band. Therefore, dislocation penetration/shearing into the γ′ precipitates are enhanced locally in the band by these native dislocations. In the meantime, crystallographic creep void growth and cracks initiating from this void (Figure 4.42(a)) suggests that faster internal diffusion is also involved in the creep damage localization to the band like the case for creep at higher temperatures, resulting decreased creep life.

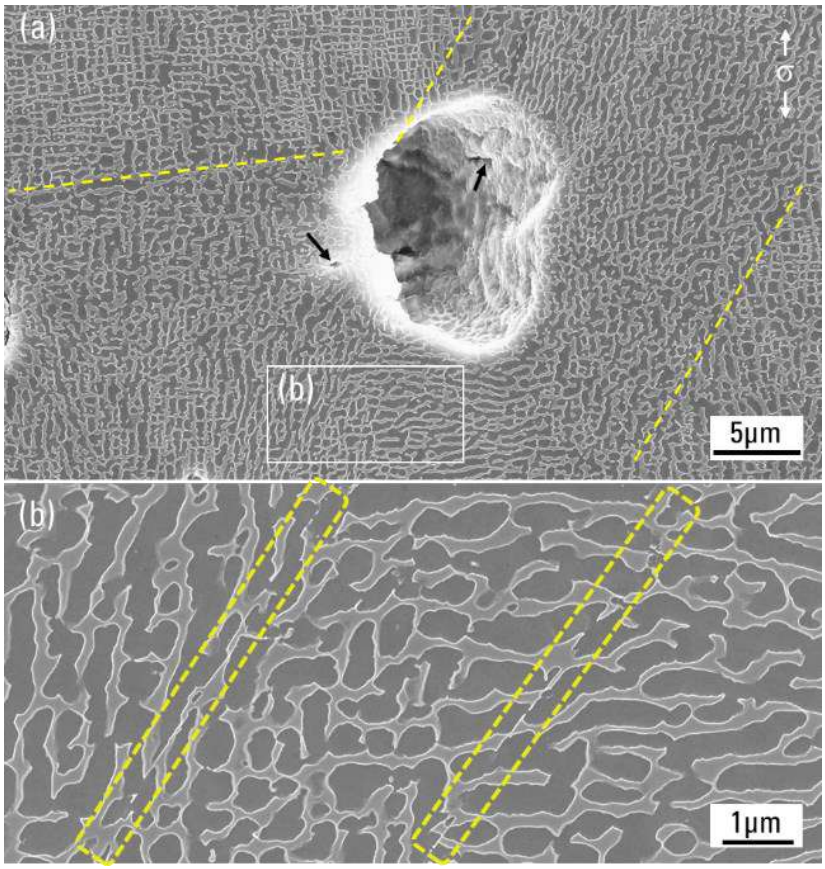

Figure 4.42. Microstructure of AM1-RTPD-HT1 specimen after creep rupture test at 850 °C / 500 MPa. Dotted lines in (a) are showing microstructure coarsened band. Precipitate scale image inside the band is shown in white rectangle, (b) and an area surrounded by dotted line is showing microstructure shearing. Black arrows are indicating cracks initiating from the void.

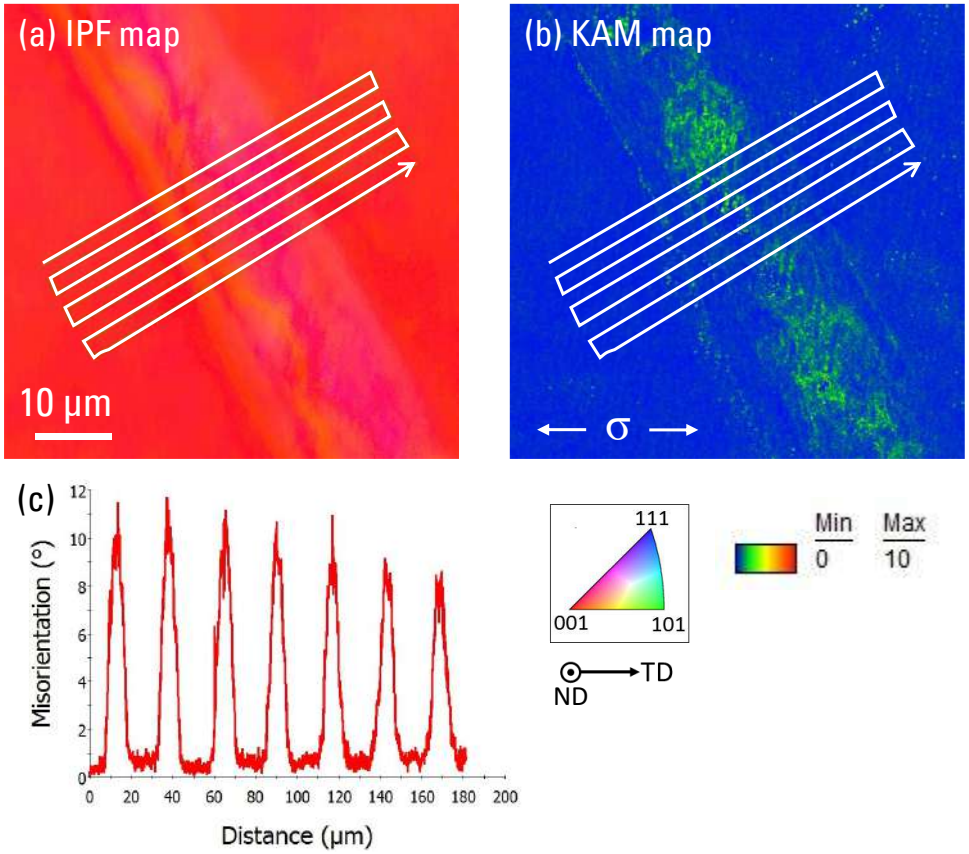

Figure 4.43. IPF color-coded orientation maps referring to the tensile direction (a) and KAM map (b) on AM1-RTPD-HT1 after creep test at 850 °C / 500 MPa. Misorientation profile in (c) is obtained from line analysis following white arrow.

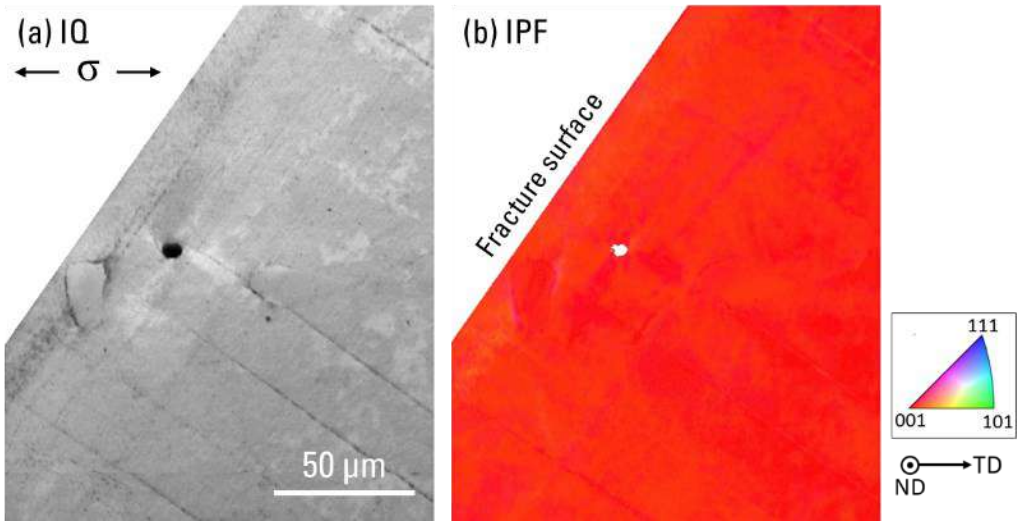

Figure 4.44. IQ map (a) and IPF color-coded orientation maps referring to the tensile direction (b) on AM1-RTPD-HT1 after creep test at 750 °C / 800 MPa obtained at the fracture surface.

As proposed by Drew et al. and explained in the Chapter 1, interfacial dislocation network developed by pre-straining can become “walls” for stacking fault penetration that consequently decrease primary creep strain during creep of CMSX-4 at 750 °C / 750 MPa [36]. Lower primary creep strain in AM1-RTPD-HT1 can be explained by a similar mechanism. Although clear difference was not found from EBSD analyses, the decrease in creep life after the secondary creep stage and fracture surfaces of {111} plane are suggesting that damage localization is still present for the pre-deformed material. Indeed, facilitated microstructure shearing inside the microstructure coarsened band is the most reasonable cause of creep life debit at 750 °C / 750 MPa.

B) CMSX-4 Plus at 950 °C / 390 MPa and 850 °C / 650 MPa

Contrarily to AM1 showing creep life debit in creep at lower temperatures, pre-deformation did not affect creep life of CMSX-4 Plus at lower temperatures. At 950 °C / 390 MPa, 4P-RTPD-HT2 showed creep life, ductility, and fracture morphology similar to 4P-HT2 (Figure 4.45 and 4.46).

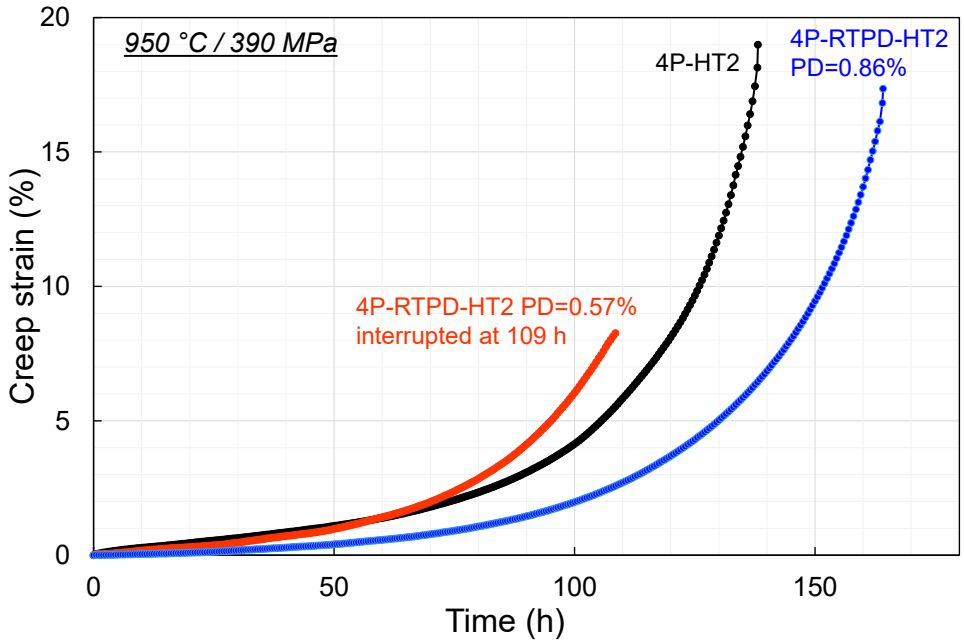

Figure 4.45. Creep curves of CMSX-4 Plus without and with pre-deformation tested at 950 °C / 390 MPa.

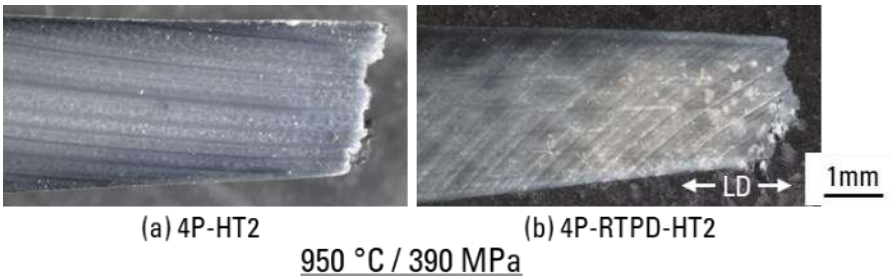

Figure 4.46. Longitudinal cross sections of CMSX-4 Plus creep specimens tested at 950 °C / 390 MPa prepared for microstructure observations.

Fracture surface (Figure 4.47(a)), microstructure shearing (Figure 4.47(b)), and crack propagation from creep void (Figure 4.47(c)) in 4P-RTPD-HT2 were not necessarily related to the microstructure coarsened bands. γ/γ′ microstructure inside the band has faster coarsening rate compared to the outside of the band (Figure 4.47(d)), but overall, γ/γ′ microstructure was not so different from that of 4P-HT2 (Figure 4.48).

EBSD analyses of an area around creep voids is shown in Figure 4.49. The area with the band intersecting with creep voids was chosen for the analyses. GROD map shows strong lattice rotation around the voids. The lattice rotation is showing stress concentration area and it is not following the bands. Therefore, the microstructure degradation by the pre-deformation has almost no effect on the creep deformation mechanisms at this creep condition. The bands in the creep test interrupted specimen (shorter creep life, Figure 4.47(d)) are thicker compared to those observed in ruptured specimen. Individual differences, such as longitudinal misorientation and number of metallurgical defects in specimens, may develop such thicker band (also shown in Figure 3.31) and can slightly enhance the damage localization as explained in creep of AM1 at 950 °C / 300 MPa.

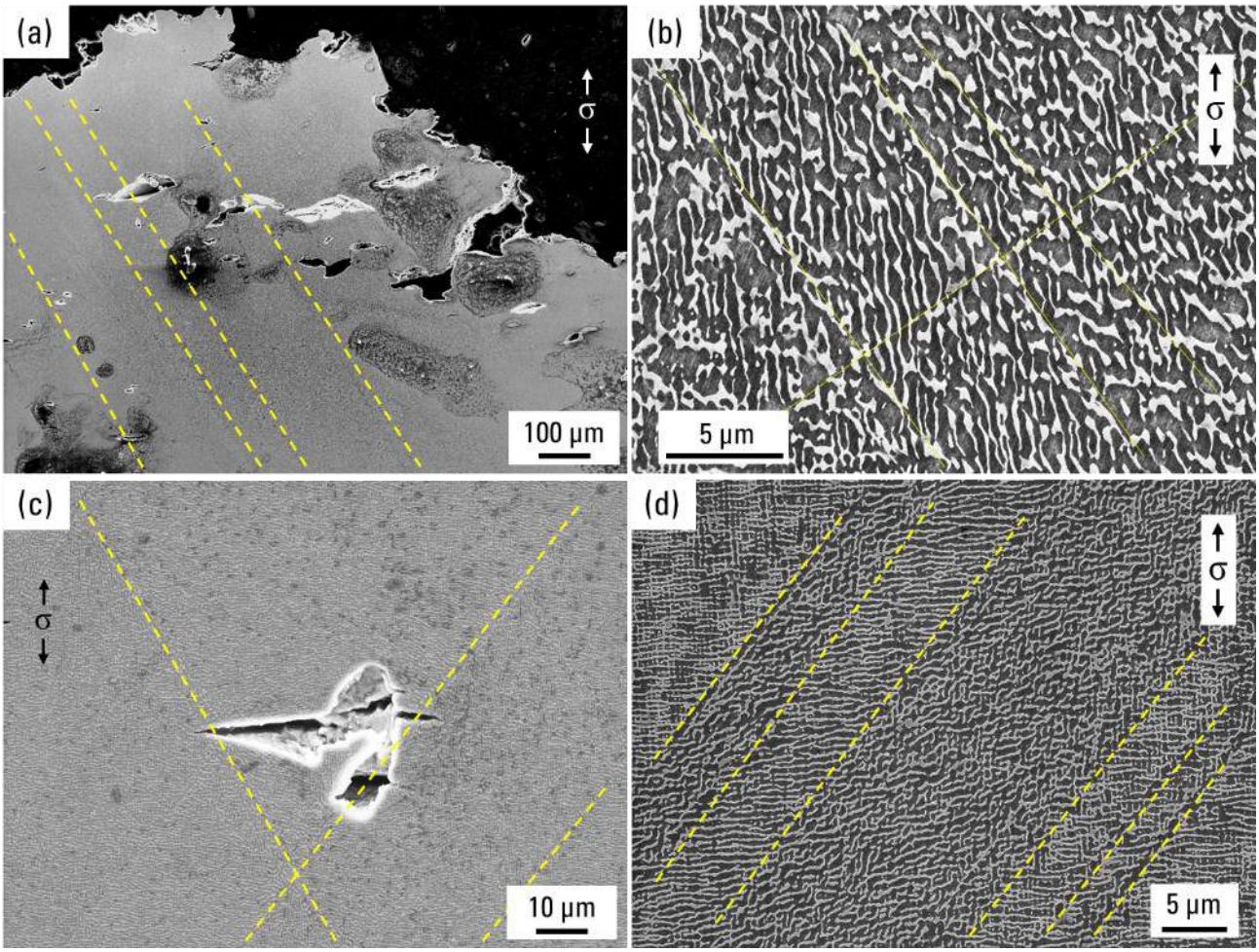

Figure 4.47. Microstructures of 4P-RTPD-HT2 after creep tests at 950 °C / 390 MPa. Near fracture surface (a), microstructure shearing (shown by dotted lines) inside the microstructure coarsened band near fracture surface (b), and crack initiating from creep void observed at 3 mm away from fracture surface (c). Typical microstructure observed in the creep interrupted specimen is shown in (d). Dotted lines in (a, c, d) are indicating the microstructure coarsened bands.

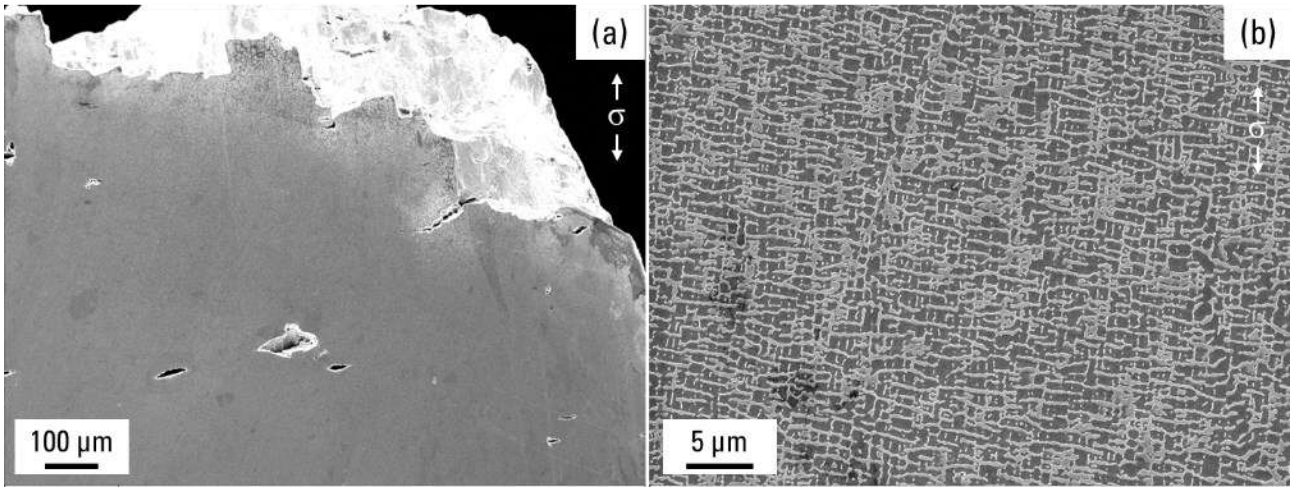

Figure 4.48. Microstructures of 4P-HT2 after creep rupture test at 950 °C / 390 MPa. (a) is low-magnification image showing fracture surface and (b) is typical microstructure 3 mm away from fracture surface.

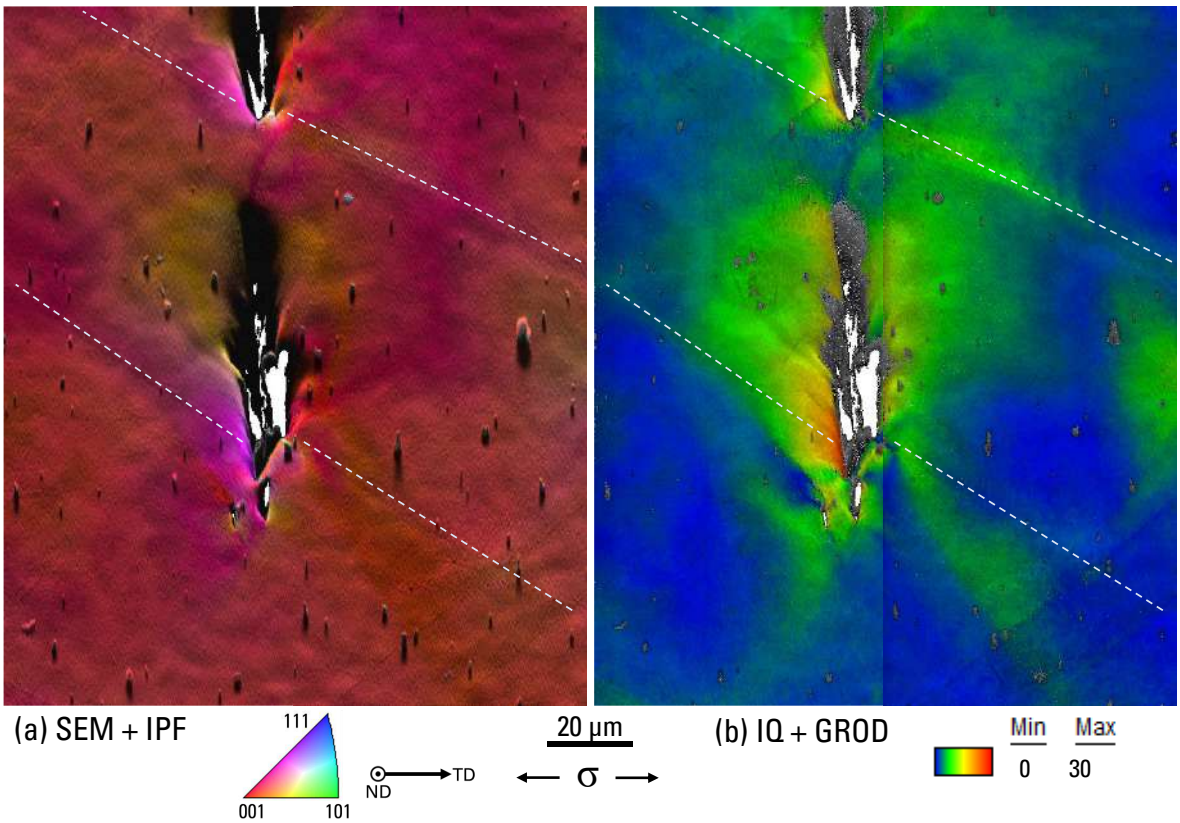

Figure 4.49. SEM image + IPF color-coded orientation maps referring to the tensile direction (a) and IQ + GROD map (b) on 4P-RTPD-HT2 after creep test at 950 °C / 390 MPa. Dotted lines are drawn on the center of the microstructure coarsened bands.

Creep life of 4P-RTPD-HT2 at the lowest tested temperature 850 °C / 650 MPa was much shorter than the reference result (Figure 4.50). This is probably a result of the effect of crystal orientation which is by far the dominant factor compared to the initial microstructural characteristics in these creep conditions [37,38]. The yield strength of this 4P-RTPD-HT2 specimen during pre-deformation was one of the lowest among all specimens (this specimen was machined from SX plate and exact misorientation is not available), which supports an assumption that the specimen was not perfectly aligned to [001] crystallographic orientation.

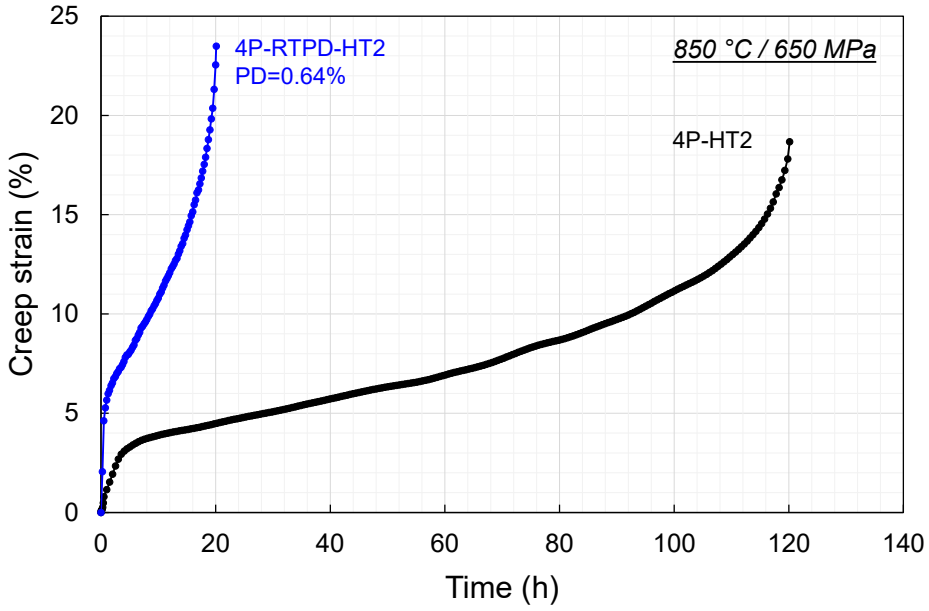

Figure 4.50. Creep curves of CMSX-4 Plus without and with pre-deformation tested at 850 °C / 650 MPa.

Ni-based SX superalloys with lower yield strength (generally the alloys of newer generations [39,40]) has shown to have higher density of slip bands after tensile deformation (Figure 3.2). When pre-deformed CMSX-4 Plus and AM1 with the same macro strain are compared, CMSX-4 Plus stores less internal elastic strain during pre-deformation and experiences less effect on the strengthen mechanism at lower temperature creep. Yet, when it is tested with lower stress for longer duration and contribution of thermally activated mechanism increases, creep life gap between pre-deformed and non-pre-deformed materials may appear.

4.2.9. Ultra-high temperature creep (≥ 1200 °C)

At the ultra-high temperature creep condition of 1200 °C / 80 MPa for AM1 in Figure 4.51, pre-deformation effect showed a trend similar to the creep at 1050 °C for all creep stages except that creep ductility was not affected. 4P-RTPD-HT2 showed earlier tertiary stage, shorter creep life, and slightly decreased ductility from 4P-HT2 at 1250 °C / 60 MPa (Figure 4.52).

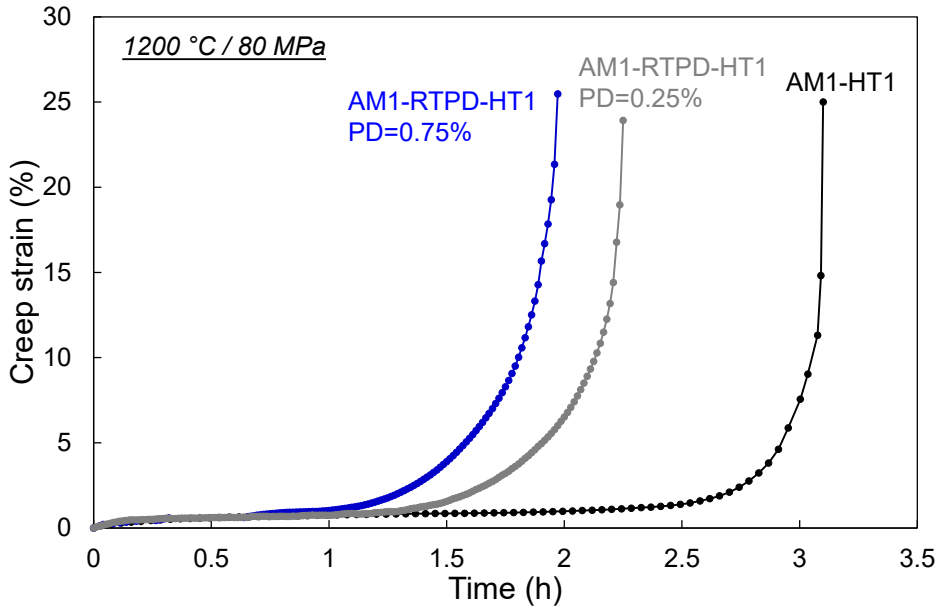

Figure 4.51. Creep curves of AM1 without and with pre-deformation tested at 1200 °C / 80 MPa.

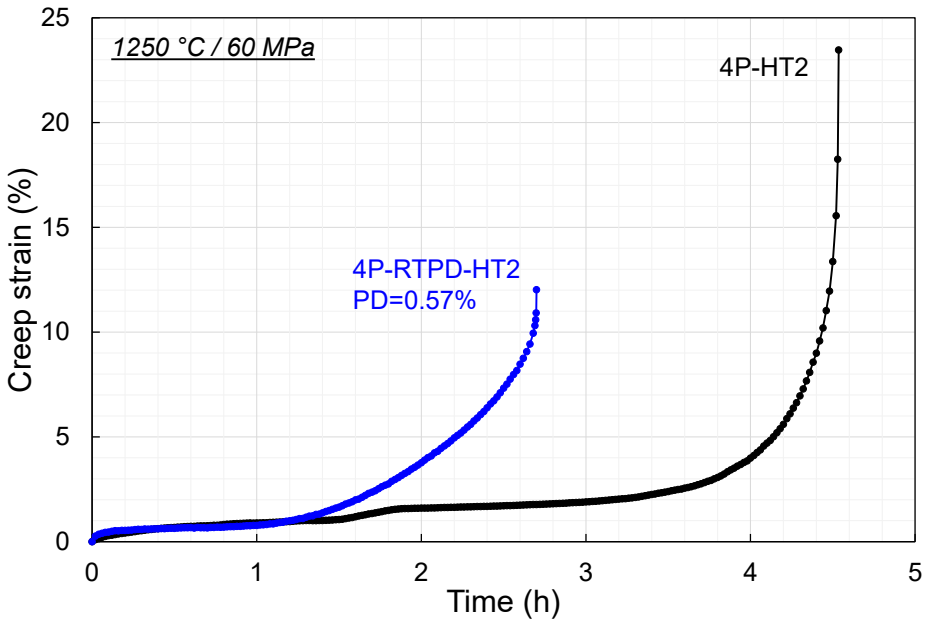

Figure 4.52. Creep curves of CMSX-4 Plus tested at 1250 °C / 60 MPa.

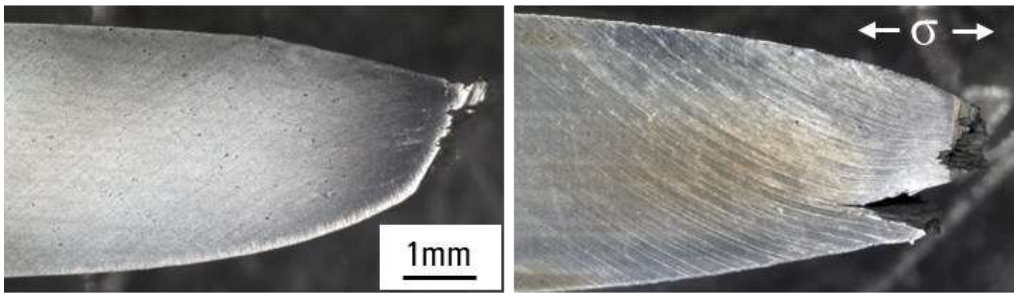

Figure 4.53. Longitudinal cross sections of AM1 creep specimens tested at 1200 °C / 80 MPa prepared for microstructure observations.

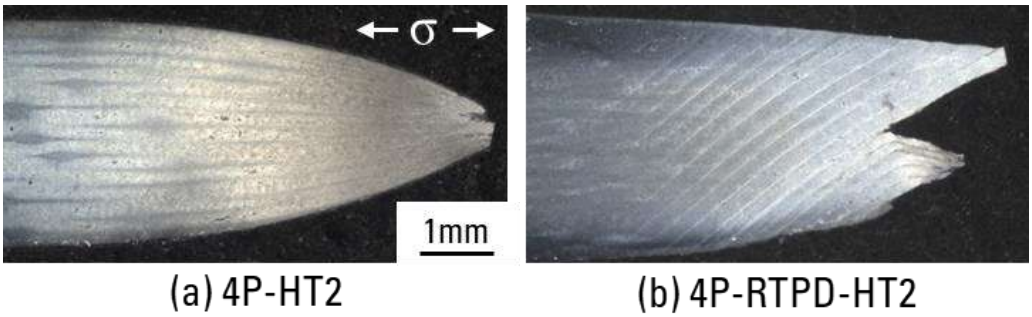

Figure 4.54. Longitudinal cross sections of CMSX-4 Plus creep specimens tested at 1250 °C / 60 MPa prepared for microstructure observations.

Both AM1 at 1200 °C / 80 MPa and CMSX-4 Plus at 1250 °C / 60 MPa have shown creep fracture morphologies affected by the microstructure coarsened band (Figures 4.53 and 4.54). The fracture started from the former {111} plane, but it showed more capability of plastic flow compared to the creep at 1050 °C for AM1 and at 1150 °C for CMSX-4 Plus.

Figure 4.55(a) is the area with deep crack connected to the fracture surface of AM1-RTPD-HT1 and Figure 4.55(b) is a precipitation scale image of the band which is extending from the deep crack. Grain boundaries are clearly visible within γ′ precipitates and they were filling all width of the band. Near fracture surface of 4P-HT2, microstructure was distorted with recrystallized grains due to a large plastic deformation and extremely high temperature (Figure 4.56). In the microstructure of 4P-RTPD-HT2, deep crack was observed like for AM1 (Figure 4.57(a)). The band connected to this deep crack has voids and inclined γ′-rafting elongated along the band (Figure 4.57(b)). Figure 4.57(c) is an example of recrystallization within the same band, obtained near the fracture surface. As can be seen from low-mag image in Figure 4.54(b) and higher magnification in Figure 4.57(d), sliding occurred at the microstructure bands.

It is obvious that initial dislocations in the microstructure coarsened band caused damage localization and affected creep life of both materials. However, AM1-RTPD-HT1 showed ductility and tertiary creep stage similar to the non-pre-deformed one. With very short creep duration, the overall difference of the creep properties is not large in AM1. On the other hand, 4P-RTPD-HT2 has early initiation of the tertiary stage, slower creep rate acceleration, and lower ductility compared to 4P-HT2.

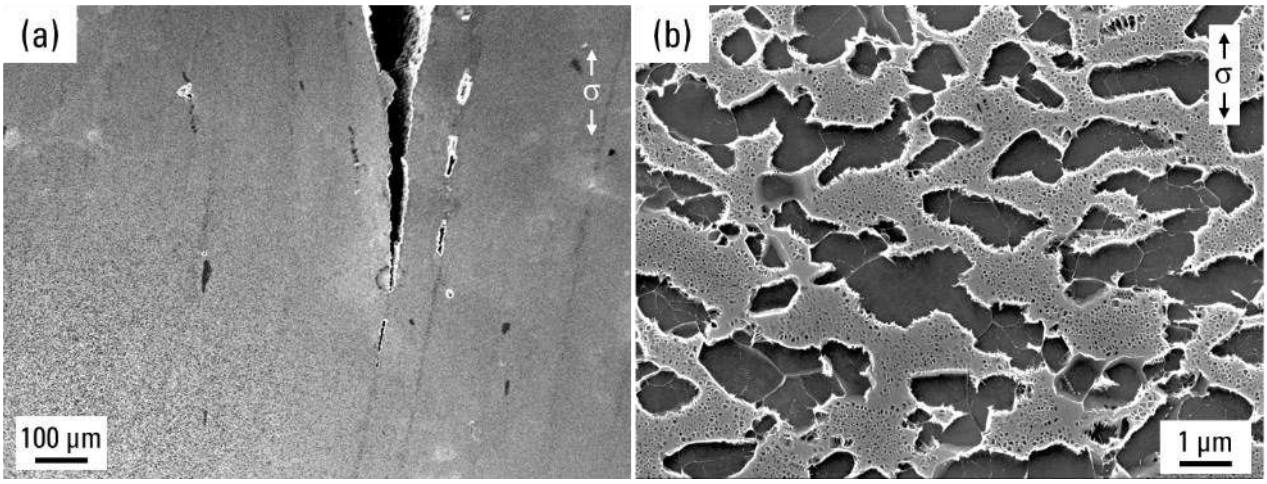

Figure 4.55. Microstructures of AM1-RTPD-HT1 specimen after creep rupture test at 1200 °C / 80 MPa. Recrystallization (b) is observed inside the microstructure coarsened band near the fracture surface (a).

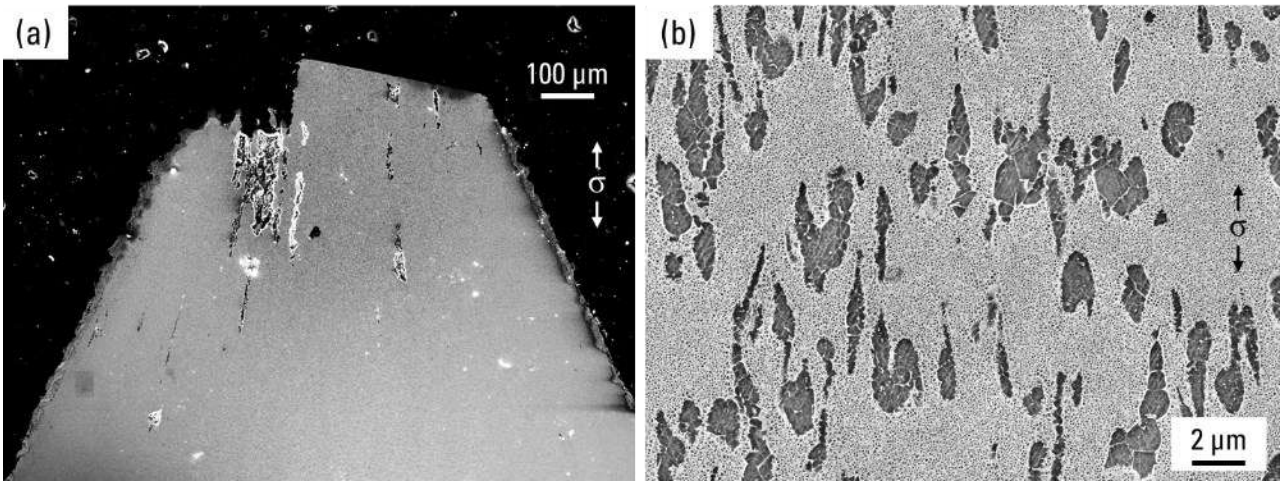

Figure 4.56. Microstructures of 4P-HT2 specimen after creep rupture test at 1250 °C / 60 MPa. (b) is taken from dendrite core in the area near the fracture surface (a).

The creep life at ultra-high temperatures can be partly explained by volume fraction of γ′ phase [41,42]. γ′ volume fraction was measured for AM1-RTPD-HT1 (Figure 4.55(b)), 4P-HT2 (Figure 4.56(b)), and 4P-RTPD-HT2 (Figure 4.57(c)) and values were 38%, 30%, and 48%, respectively. According to Figure 3.9, γ′ volume fraction of AM1 at 1200 °C and CMSX-4 Plus at 1250 °C are 35-40% and 30-35%, respectively. AM1-RTPD-HT1 and 4P-HT2 after creep rupture tests have reasonable value to Figure 3.9. These two specimens have their microstructure stabilized at the exposed temperature. However, 4P-RTPD-HT2 has much higher value of γ′ volume fraction at this temperature.

Tertiary creep stage is assumed to be activated when the γ′ volume fraction reduced to certain value that accepts faster deformation because of no γ′ strengthening contribution [43]. Since 4P-RTPD-HT2 had not reached equilibrated volume fraction, pre-deformation should have accelerated damaging mechanisms at the band. Damage localization (faster strain accumulation) at the band is a reason for lower ductility at failure and slower creep acceleration at tertiary creep stage. Overall, creep damaging mechanisms for pre-deformed material at ultra-high temperature creep conditions follow the relationship (diffusion dependent damage is accelerated at the band) that have been presented above.

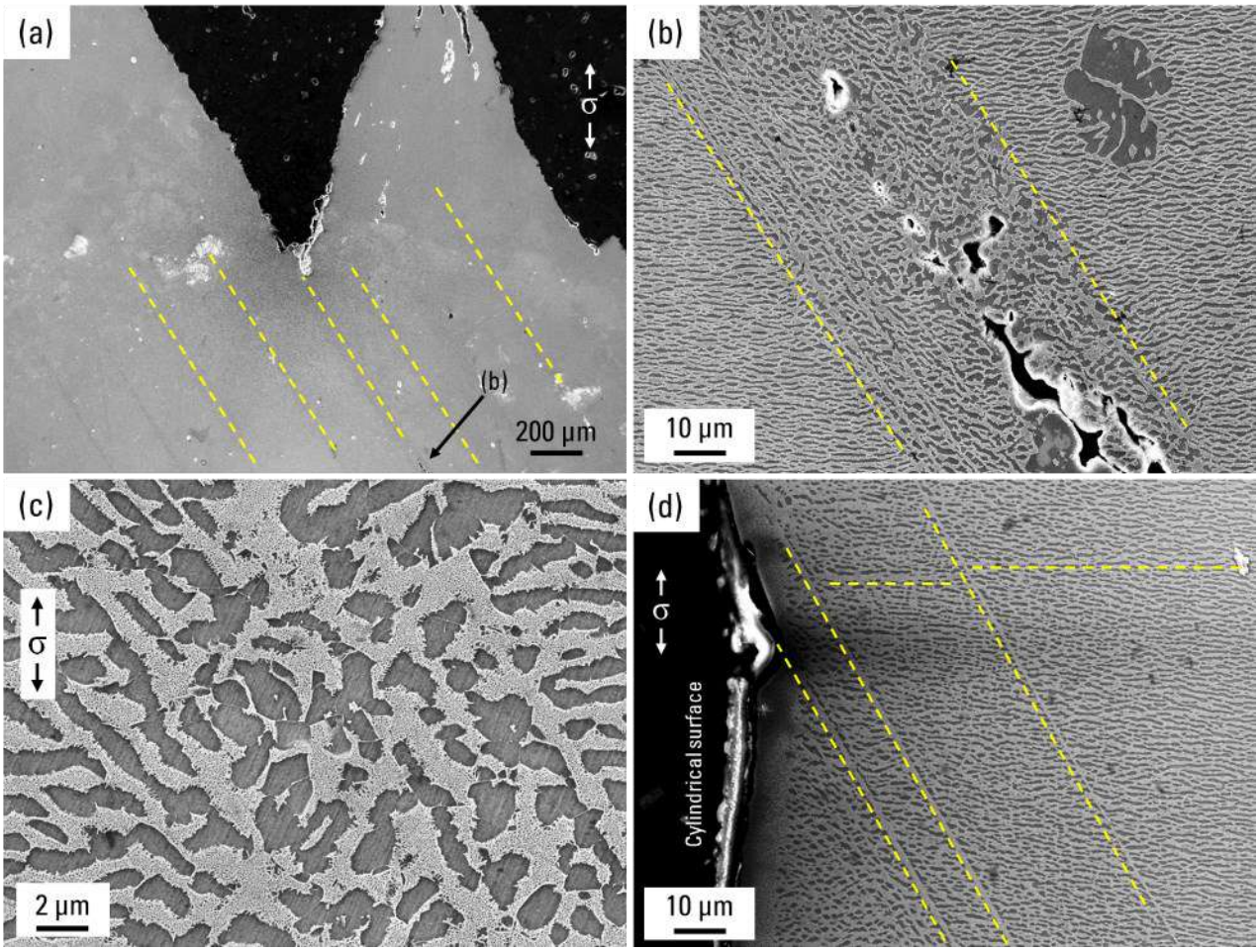

Figure 4.57. Microstructures of 4P-RTPD-HT2 specimen after creep rupture test at 1250 °C / 60 MPa. (b) Voids and cracks on the main band, area is indicated by arrow in (a). (c) Precipitation scale image showing recrystallized grains. (d) Intersection of the bands and cylindrical surface. Dotted lines are showing microstructure coarsened bands.

4. 3. Examination of damage localization using different material histories and test conditions

As presented in Table 4.1, different preparation methods were applied to AM1 and creep tests were performed at 1050 °C / 140 MPa, 950 °C / 300 MPa, and 850 °C / 500 MPa. This section analyzes effect of different material histories on the creep behavior of Ni-based SX superalloys. Results are discussed in comparison with the previous chapter and the previous section. Thermal cycling creep test results are also discussed here to further understand effect of pre-deformation between heat treatments.

4.3.1. Pre-deformation at higher temperature and rejuvenation effect

In the Chapter 3, γ/γ′ pre-rafted microstructure of AM1-PD950-HT1 (pre-deformation at 950 °C) was discussed. Creep tests were performed at 1050 °C / 140 MPa (Figure 4.58) and 850 °C / 500 MPa (Figure 4.59) on the specimen with the same microstructure shown in Figure 3.22(e). Rejuvenated specimens (AM1-RTPD-Rejuv-HT1) were also tested in the same two conditions. Rejuvenation condition for creep specimens was at 1290 °C for 20 min. CMSX-4 Plus with pre-deformation was also rejuvenated at 1330 °C for 1 h and tested at 1150 °C / 110 MPa.

Additional rejuvenation treatment is shown to be very effective to restore original creep properties of AM1 for

both creep testing conditions (Figure 4.58). This is clearly owing to restored microstructure by rejuvenation after pre-deformation (Figure 3.34(h-j)). Specimen with pre-deformation at 950 °C (AM1-PD950-HT1) also performed well at 1050 °C with smaller primary creep strain (Figure 4.58). However, it showed very poor creep durability at 850 °C (Figure 4.59), even shorter than the specimen pre-deformed at RT (AM1-RTPD-HT1). Rejuvenation of CMSX-4 Plus was demonstrated to be applicable by 4P-RTPD-Rejuv-HT2 creep tested at 1150 °C / 110 MPa (Figure 4.18). Other curves shown in Figures 4.58 and 4.59 are explained and discussed later in this section.

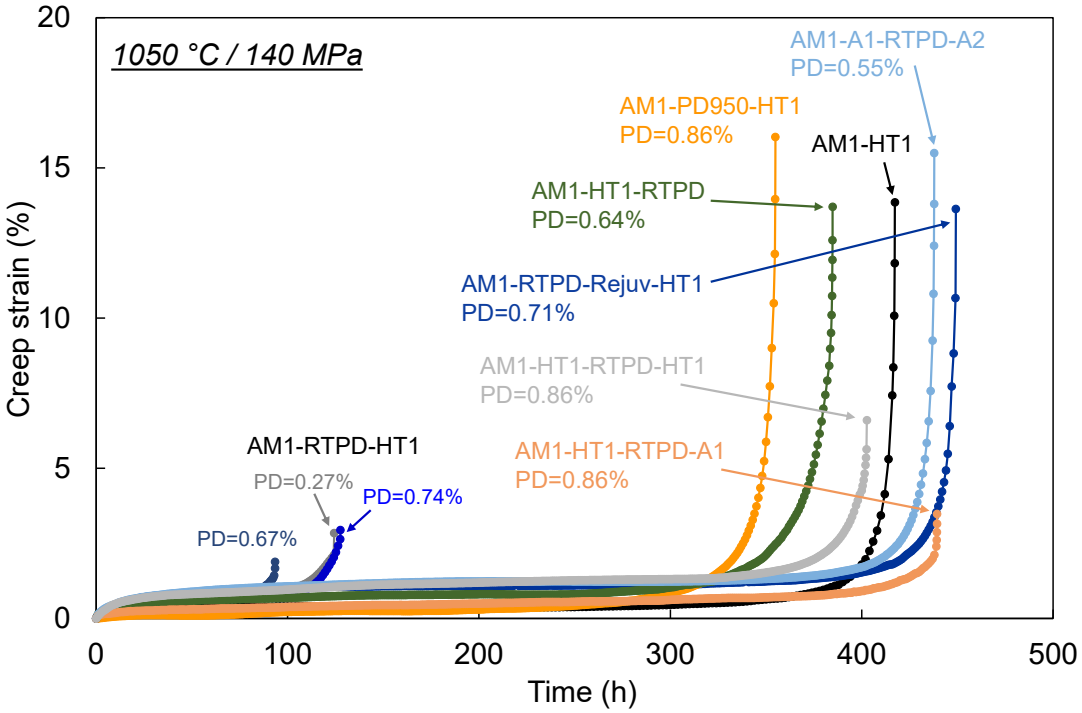

Figure 4.58. Creep curves of AM1 specimens with various preparation conditions tested at 1050 °C / 140 MPa

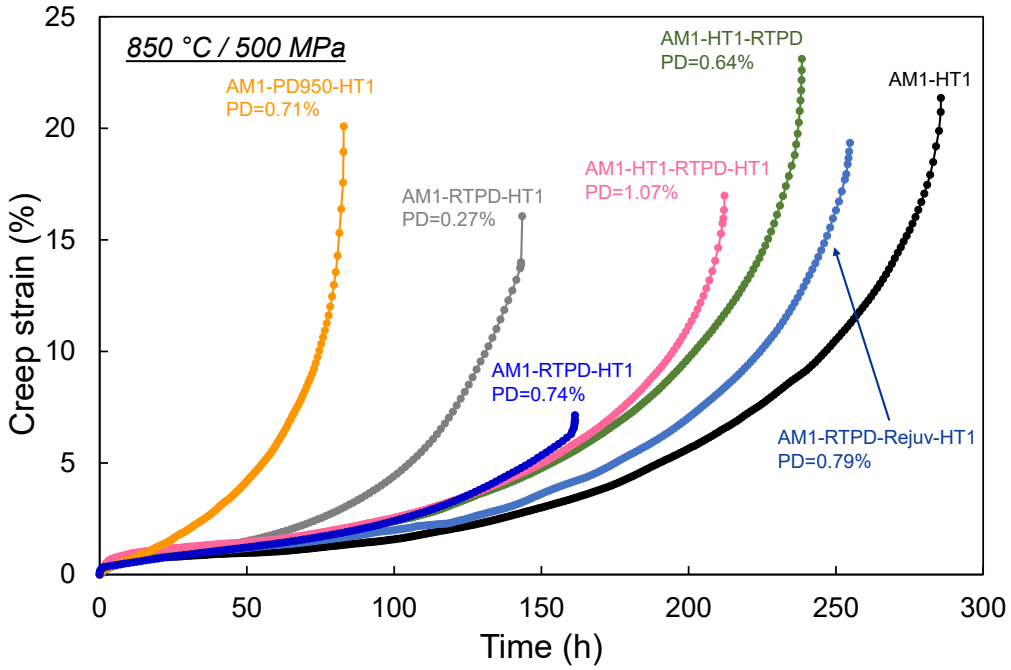

Figure 4.59. Creep curves of AM1 specimens with various preparation conditions tested at 850 °C / 500 MPa

Both AM1-PD950-HT1 (Figure 5.60(a)) and AM1-RTPD-Rejuv-HT1 (Figure 5.60(b)) specimens showed ductile fracture similar to the original AM1-HT1 after creep rupture test at 1050 °C / 140 MPa (Figure 4.6(a)). However, γ′-rafts in dendrite cores far from the fracture surface are coarser in AM1-PD950-HT1 (Figure 4.61(a)) compared to AM1-RTPD-Rejuv-HT1 (Figure 4.61(b)). AM1-RTPD-Rejuv-HT1 has microstructure similar to that observed in AM1-HT1. On the other hand, failure characteristics of AM1-PD950-HT1 at 850 °C / 500 MPa were clearly different. AM1-RTPD-Rejuv-HT1 has directional coarsening with former-matrix γ-particles structure in the area far from fracture surface (Figure 4.61(d)) which is again similar to AM1-HT1 and AM3 after creep test at the same condition [33]. In comparison, AM1-PD950-HT1 has less and smaller creep voids with wavy γ′-rafts (Figure 4.61(c)).

If a target creep life for application is determined to be ±10% of an original material, creep life of AM1-PD950-HT1 with pre-rafted microstructure (Figure 3.22(e)) is acceptable under creep condition of 1050 °C / 140 MPa. This mild γ′-rafting is assumed to continue after applying creep load at 1050 °C to have the microstructure shown in Figure 4.61(a). During creep deformation, this specimen showed very small primary creep strain compared to other three specimens. Decreased primary creep strain by interfacial dislocations introduced during pre-straining was also reported by Drew et al. [36]. This suggests that the plasticity involved during directional coarsening is not so active, resulting in degraded γ′-raft (Figure 4.61(a)) and decreased creep life compared to AM1-HT1. Although it was not well developed like in Figure 4.61(b), this homogeneous microstructure helped avoiding very intense localized damage accumulation in the microstructure coarsened band that was observed in AM1-RTPD-HT1 at the same creep condition 1050 °C / 140 MPa.

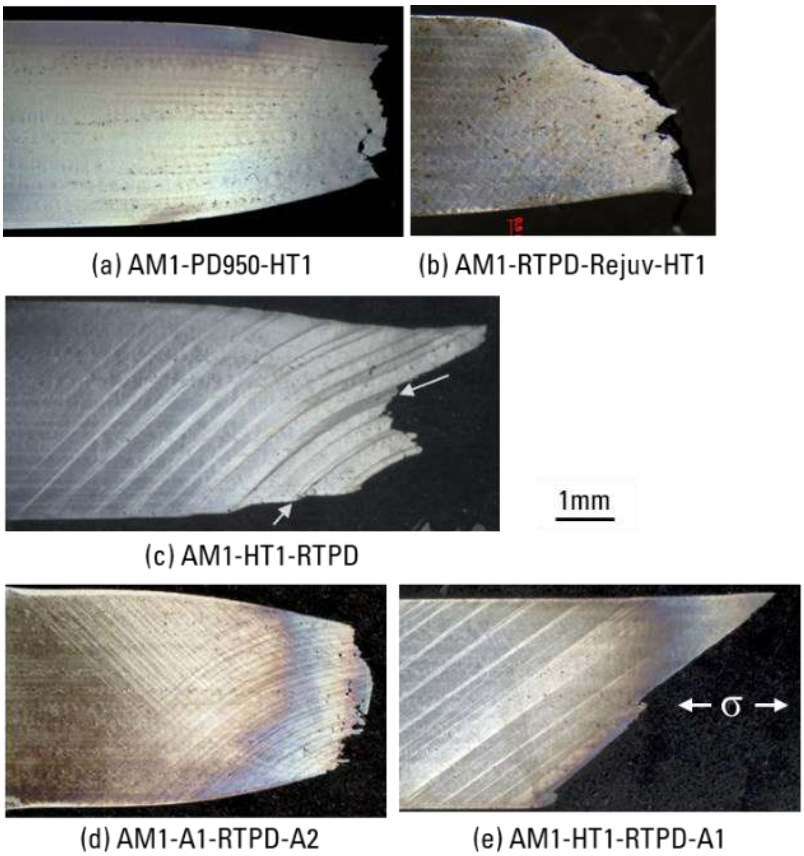

Figure 4.60. Longitudinal cross sections of specimens with various preparation conditions tested at 1050 °C / 140 MPa, prepared for microstructure observations. Arrows are pointing at the microstructure coarsened bands observed by SEM.

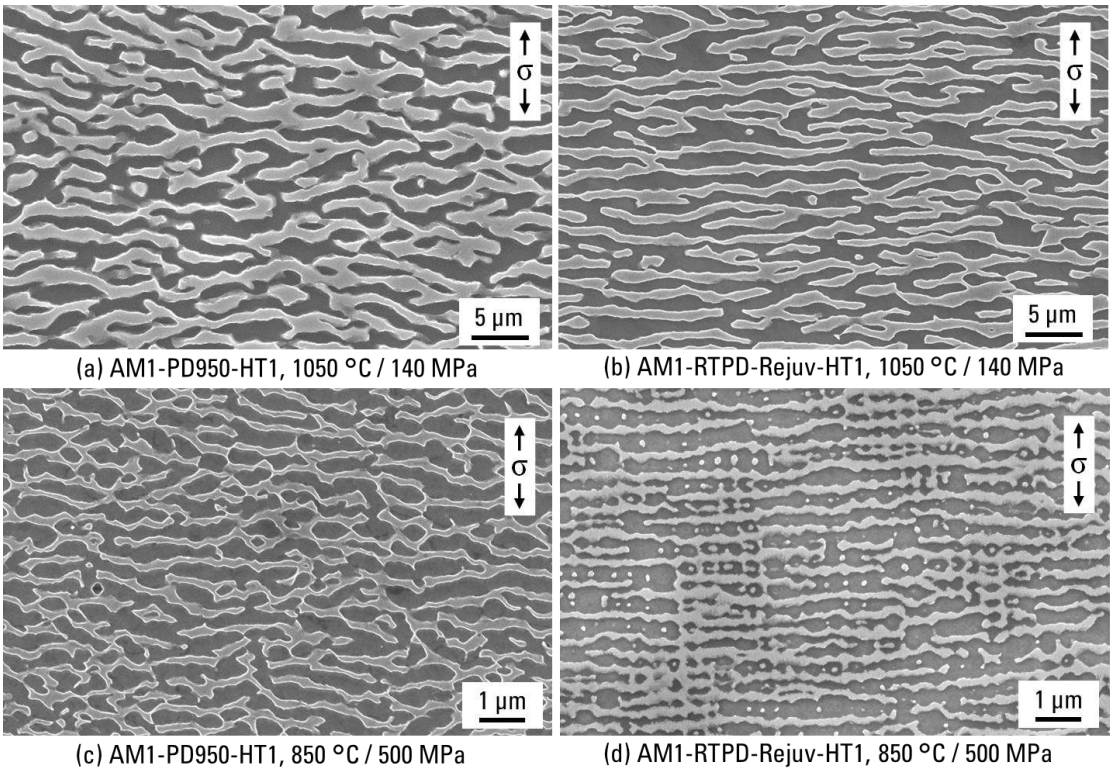

Figure 4.61. Typical microstructure of AM1-PD950-HT1 (a, c) and AM1-RTPD-Rejuv-HT1 (b, d) specimens after creep test at 1050 °C / 140 MPa (a, b) and at 850 °C / 500 MPa (c, d). All observations were made at least 3 mm away from fracture surface

Similarly, very short creep life of AM1-PD950-HT1 in this higher stress creep at 850 °C / 500 MPa can be explained from microstructures both before and after the creep test. This is like the pre-rafted CMSX-2 with very high density of particle shearing dislocations [34], or like AM3 with very slow cooling from the solution treatment temperature that exhibits irregular and larger precipitates [33]. As discussed previously in the Chapter 3, existence of dislocations in γ matrix after full aging treatments is predicted. Creep curve of AM1-PD950-HT1 in Figure 4.59 does not have primary creep stage and creep rate is accelerating from the beginning. Therefore, dislocation shearing assumed to start at very early stage of creep deformation and easily transitioned into the failure. Despite decreased creep life, AM1-PD950-HT1 maintained its ductility at similar level to AM1-HT1 meaning that this deformation occurred homogenously in the gauge section.

From a practical point of view, the rejuvenation treatment was successfully demonstrated, and this is a very useful process to put pre-deformed component back into production line. However, some remarks can be made from the experimental results. As presented in Figures 3.34 and 3.41, pronounced microstructure coarsening can occur if the rejuvenation temperature is too low and dissolution of γ′ phase is incomplete. This is a result of very high-temperature annealing (where diffusion and plasticity are extremely active) leading to a very fast microstructure evolution during rejuvenation treatment. Because creep life of SX superalloys can be significantly reduced [4,33], this situation is much worse compared to the one without rejuvenation. Another risk is a surface recrystallization which has been observed in rejuvenated specimens AM1-RTPD-Rejuv-HT1 tested at 850 °C / 500 MPa (Figure 4.62(a)) and 4P-RTPD-Rejuv-HT2 tested at 1150 °C / 110 MPa (Figure 4.62(b)). Plastic strain is locally higher at the specimen surface since it acts as free surface during PD and locally higher stored energy can activate recrystallization. The rejuvenation treatment was performed in air and this can also assist the surface recrystallization by Al-depletion and γ′ dissolution. Although it did not give

huge debit in the creep tests of cylindrical specimen, it may have an impact for actual turbine component that has thin aerodynamic profiles.

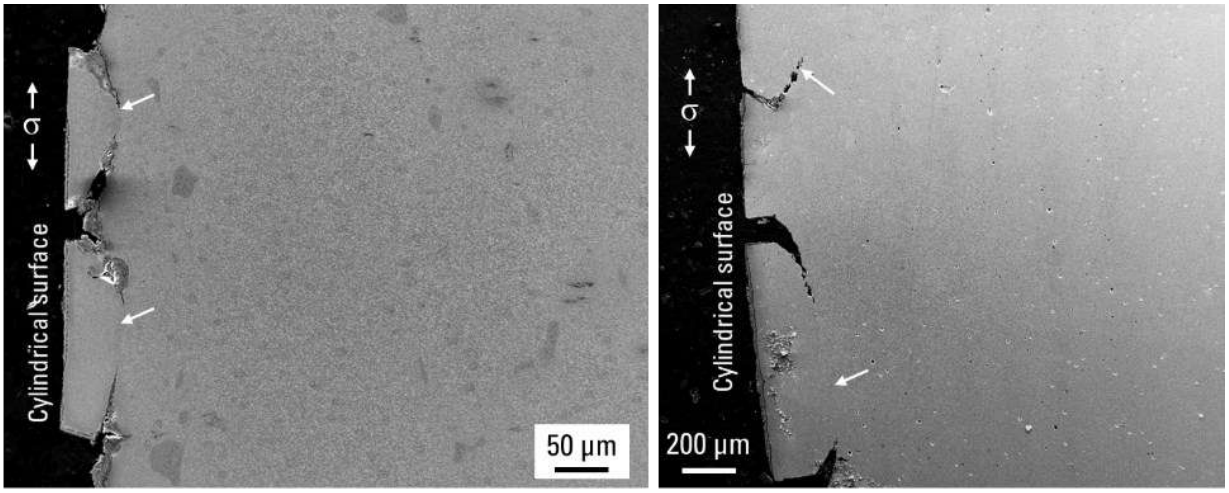

(a) AM1-RTPD-Rejuv-HT1 850 °C / 500 MPa (b) 4P-RTPD-Rejuv-HT2 1150 °C / 110 MPa

Figure 4.62. Surface recrystallization (pointed by arrows) of rejuvenated specimens AM1-RTPD-Rejuv-HT1 (a) and 4P-RTPD-HT2 (b) tested at 850 °C / 500 MPa and 1150 °C / 110 MPa, respectively.

4.3.2. Pre-deformation after aging treatment

Pre-deformation was applied at different stages of preparation procedures to understand how the introduced local strain can affect creep performance. AM1-HT1-RTPD is a specimen with pre-deformation applied at RT after full aging treatment HT1. AM1-HT1-RTPD specimens showed relatively good creep properties for all creep conditions, 1050 °C / 140 MPa (Figure 4.58), 950 °C / 300 MPa (Figure 4.63), and 850 °C / 500 MPa (Figure 4.59).

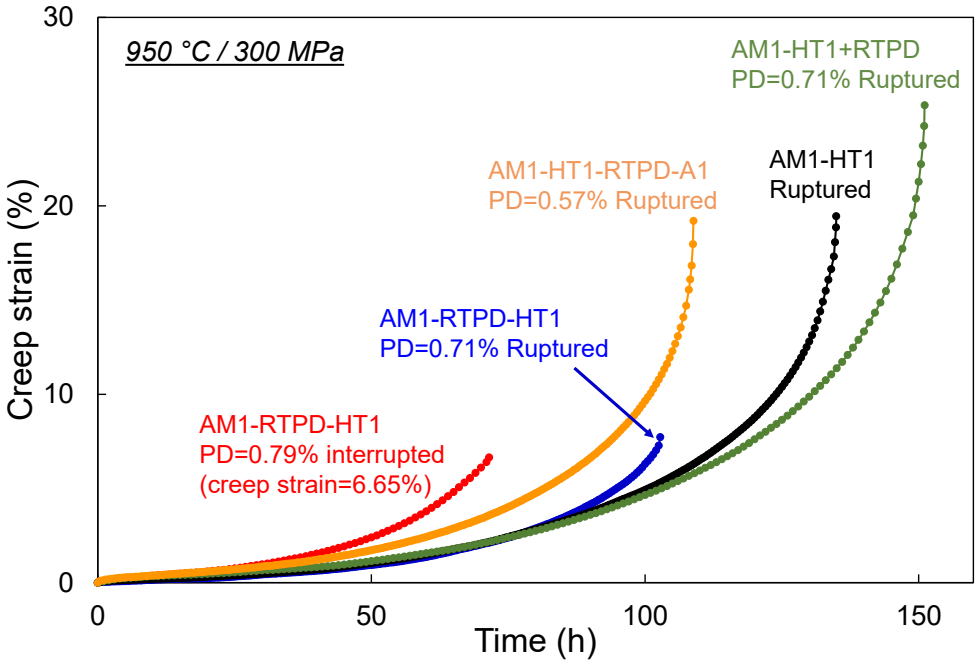

Figure 4.63. Creep curves of AM1 specimens with various preparation conditions tested at 950 °C / 300 MPa

Although the creep life of AM1-HT1-RTPD at 1050 °C / 140 MPa was comparable to AM1-HT1, its fracture morphology was completely different from that of AM1-HT1 as shown in Figure 4.60(c). Two arrows in Figure 4.60(c) are indicating observed area near cylindrical surface (Figure 4.64(a)) and the thickest band (Figure 4.64(b)). Large and high density of voids were observed in the bands with severe deformation (Figure 4.64(a)). The same band was analyzed using EBSD and the obtained results are shown in Figure 4.65. Recrystallized grains are present along the band between voids, and KAM map is showing that area with high dislocation density is spreading over distance of more than 20 µm from the center of the band. This is totally different from AM1-RTPD-HT1 tested at the same condition that recrystallization and lattice rotation is limited in the vicinity of the band (Figure 1.42). Microstructure coarsening occurred faster in the band, but γ′-rafts in the band of Figure 4.64(b) was not connected to form long γ/γ′ planes compared to that observed in (AM1-RTPD-HT1 (Figure 4.10(b)).

After the creep tests at 950 °C / 300 MPa and 850 °C / 500 MPa, the microstructure coarsened bands were almost impossible to locate regardless of the magnification (see example in Figure 4.66). After the pre-deformation, macro pre-strain is the sum of local strain in each slip band. When only one slip band is considered, elastic strain field in its vicinity is not homogeneous because of the shape and elastic misfit of γ matrix/γ′ cuboid structure. Under lower applied load (i.e. 1050 °C / 140 MPa), remaining elastic anisotropy can affect microstructure evolution during creep deformation which resulted in faster coarsening and inclination of γ′-raft (Figure 4.64(b)). On contrary, it the applied load is higher (950 °C / 300 MPa and 850 °C / 500 MPa), residual elastic factor becomes negligible level that microstructure evolution associated with creep deformation is more dominated by the macro creep stress. Moreover, lattice misfit of AM1 at these temperatures is close to zero (-0.1% at 850 °C and -0.22% at 950 °C [44,45]). Therefore, influence of internal residual stresses on the γ′-rafting becomes smaller. Consequently, the creep properties were not affected by pre-deformation introduced after the aging treatments.

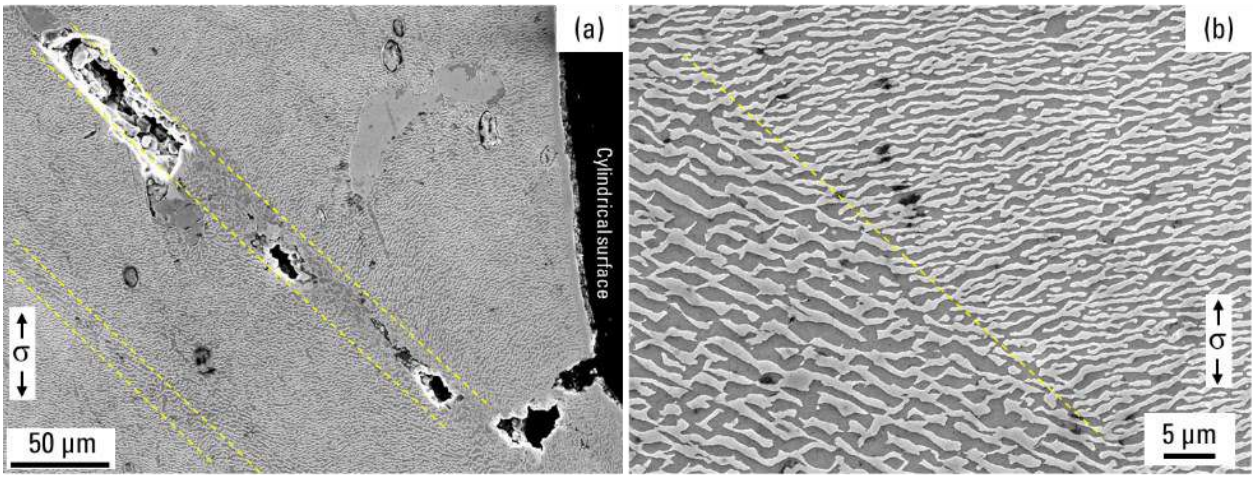

Figure 4.64. Microstructure of AM1-HT1-RTPD specimen after creep rupture test at 1050 °C / 140 MPa. Area near cylindrical surface with major recrystallized band that has voids and cracks (a). Interface of inclined and horizontal rafts (b).

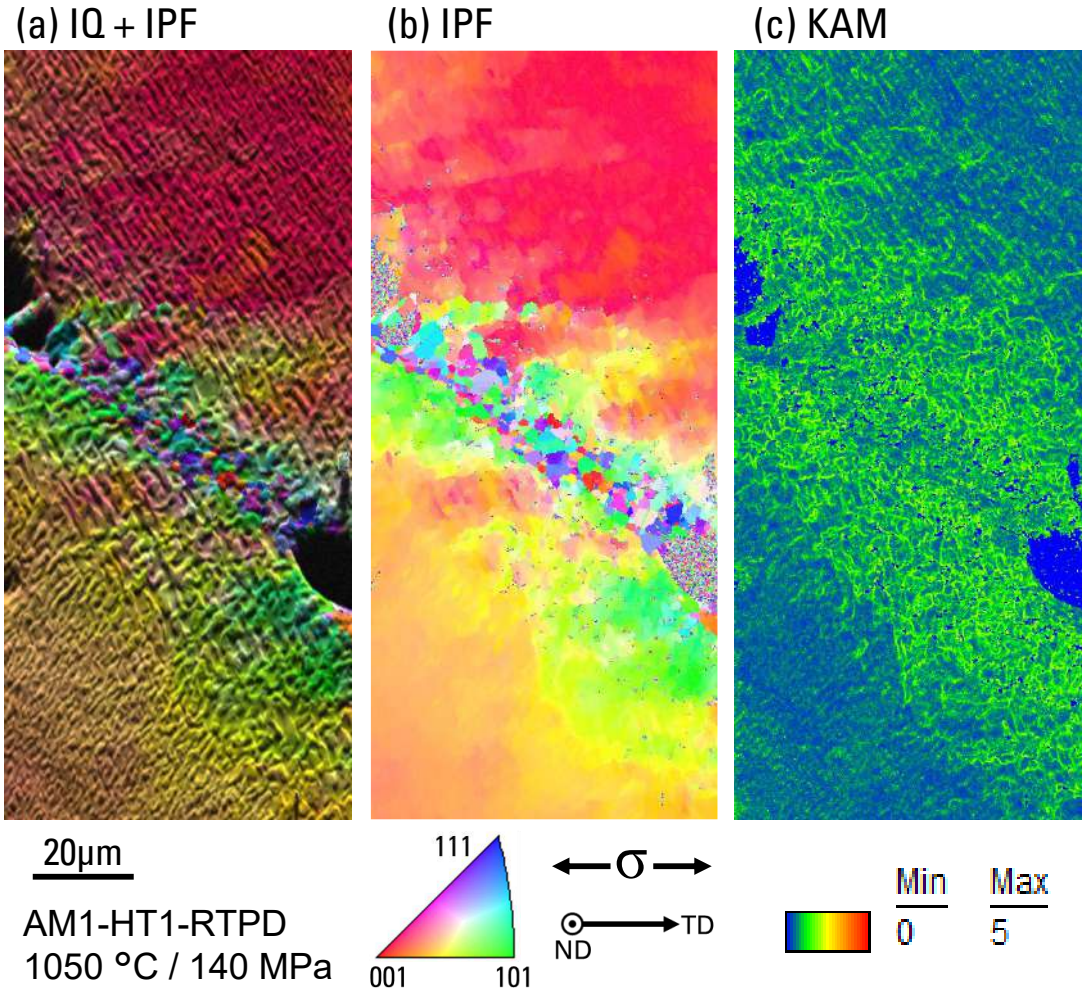

Figure 4.65. IQ + IPF color-coded orientation maps referring to the tensile direction (a), IPF map (b), and KAM map (b) on AM1-HT1-RTPD after creep test at 1050 °C / 140 MPa. Analysis was made on the same band shown in the Figure 4.65(a).

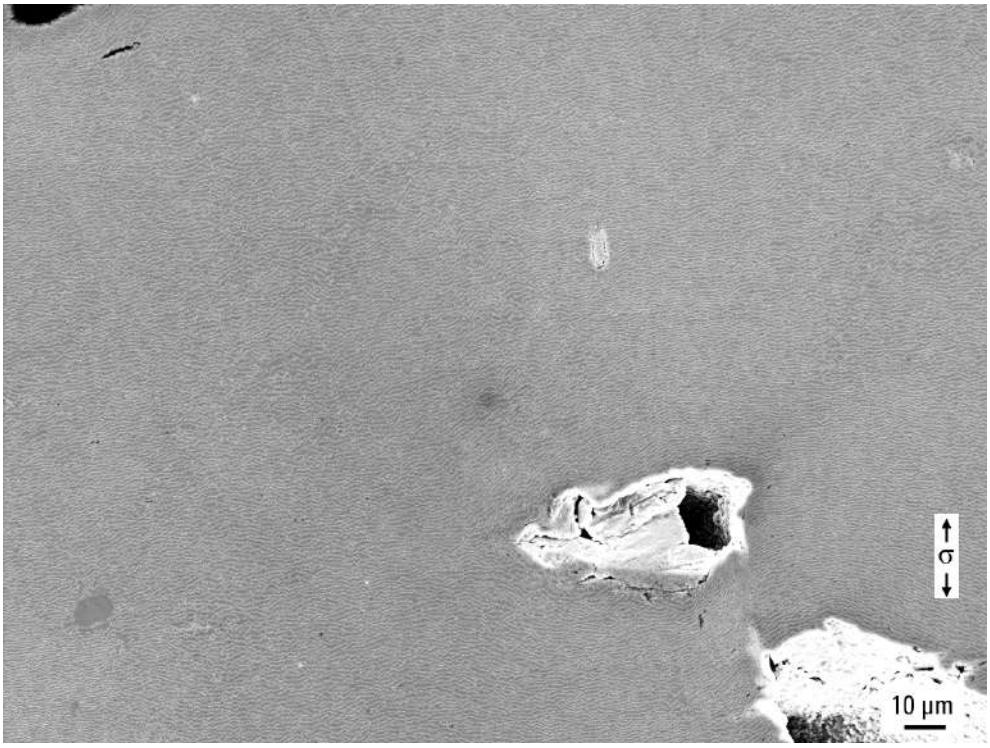

Figure 4.66. Area near fracture surface of AM1-HT1-RTPD after creep rupture test at 950 °C / 300 MPa.

Other preparation variations are AM1-A1-RTPD-A2, AM1-HT1-RTPD-A1, and AM1-HT1-RTPD-HT1. An idea for the first one is pre-deformation between first aging (at 1100 °C for 5 h) and second aging (at 870 °C for 16 h). The second one is pre-deformation after full heat treatment and another aging treatment at the same condition as the first aging treatment at 1100 °C for 5 h. The third one is full heat treatment followed by pre-deformation, and another full heat treatment at the end.

In AM1-A1-RTPD-A2, band traces were observed in low-mag image (Figure 4.60(d)) but they are much thinner compared to AM1-HT1-RTPD and creep life was not affected (Figure 4.58). Void nucleation and coarsening at the intersection of the bands were also the case in this specimen (Figure 4.67(b)). Despite damaging sites were selectively appearing inside the band, fracture surface was not influenced by the microstructure coarsened bands. Near fracture surface, almost all γ′-rafts are irregularly deformed and bands are difficult to locate (Figure 4.67(a)). Cuboidal microstructure was not affected drastically by the secondary aging at 870 °C for 16 h, however, it possibly contributed to reduce internal elastic strain to suppress heavy microstructure evolution of the band observed in Figure 4.64(b).

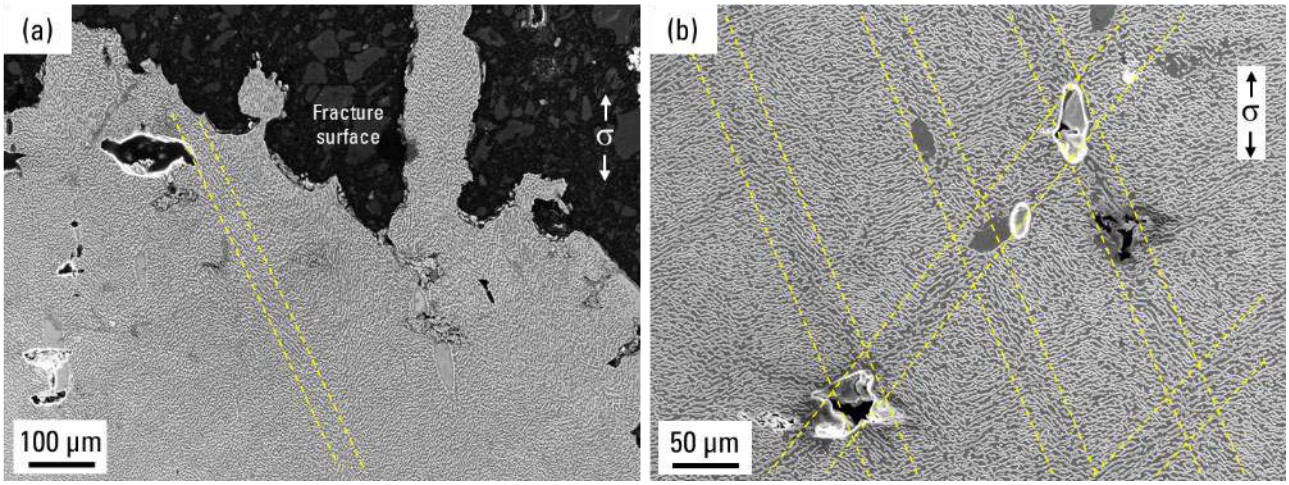

Figure 4.67. Microstructure of AM1-A1-RTPD-A2 specimen after creep rupture test at 1050 °C / 140 MPa. Area near the fracture surface (a) and 1 mm away from the fracture surface (b). Dotted lines are showing the microstructure coarsened bands.

Characteristic planar fracture surface of former slip plane (Figure 4.60(e)) appeared in AM1-HT1-RTPD-A1 with low ductility but maintained creep life at 1050 °C / 140 MPa. In Figure 4.60(e), very thick microstructure coarsened bands are identified. These bands were inherited from the microstructure before creep test (Figures 3.19 and 3.35(c)). Multiple creep voids and cracks were observed in the band of the fracture plane (Figure 4.68(a)). In the same band, very long and connected inclined γ phase was observed with very high density of dislocation traces and recrystallized grain boundaries (Figure 4.69(b)). Coarsening mechanism inside the band and failure mechanism with decreased ductility seem similar to what have been discussed earlier in this chapter. In the microstructure before the creep tests, AM1-HT1-RTPD-A1 has clearly coarser precipitates inside the band (Figure 3.19) compared to that in AM1-RTPD-HT1 (Figure 3.11(d)). This means that the γ′ precipitate size is not an important factor here during creep at 1050 °C / 140 MPa. Dislocation structure evolution was discussed in the previous chapter and the evolution mechanism is possibly similar to typical one during the γ′-rafting process at high temperature/low stress creep. But the precipitate size scale had not been considered deeply. In AM1-RTPD-HT1, precipitates are very fine before applying aging treatment that not only the dislocation climb/glide occur in the matrix, but also distributed site of those dislocations are later taken over

by the evolved γ′ precipitates. Therefore, possibility of dislocations already existing inside the coarsened γ′ precipitates in AM1-RTPD-HT1 should be considered. It may enhance raft inclination and evolution during high-temperature creep. Another difference is decreased interfacial dislocation density in AM1-RTPD-HT1 compared to that in AM1-HT1-RTPD-A1. Lower interfacial dislocation density should ease dislocations to penetrate into γ′ phase during creep of AM1-RTPD-HT1. Finally, void nucleation and coarsening proceeded by dislocation climb in the aging process (mechanism explained in Section 4.2.6) is probably easier in case of AM1-RTPD-HT1 because of the absence of larger γ′ cuboids that blocks dislocation mobility. Based on the discussions above, higher density of metallurgical defects is expected in AM1-RTPD-HT1 compared to AM1-HT1-RTPD-A1, that consequently created a huge gap in creep life despite the similar fracture characteristics between two specimens. In addition, AM1-HT1-RTPD-HT1 performed similarly to AM1-HT1-RTPD-A1 in terms of creep life, ductility, and planar {111} fracture surface. Therefore, the second aging treatment at 870 °C does not affect creep life of the material. Preparation process in order of "solution treatment → PD at RT → aging treatment at 1100 °C" is the situation that pre-deformation induces the most detrimental effect to the creep properties of AM1 at 1050 °C / 140 MPa.

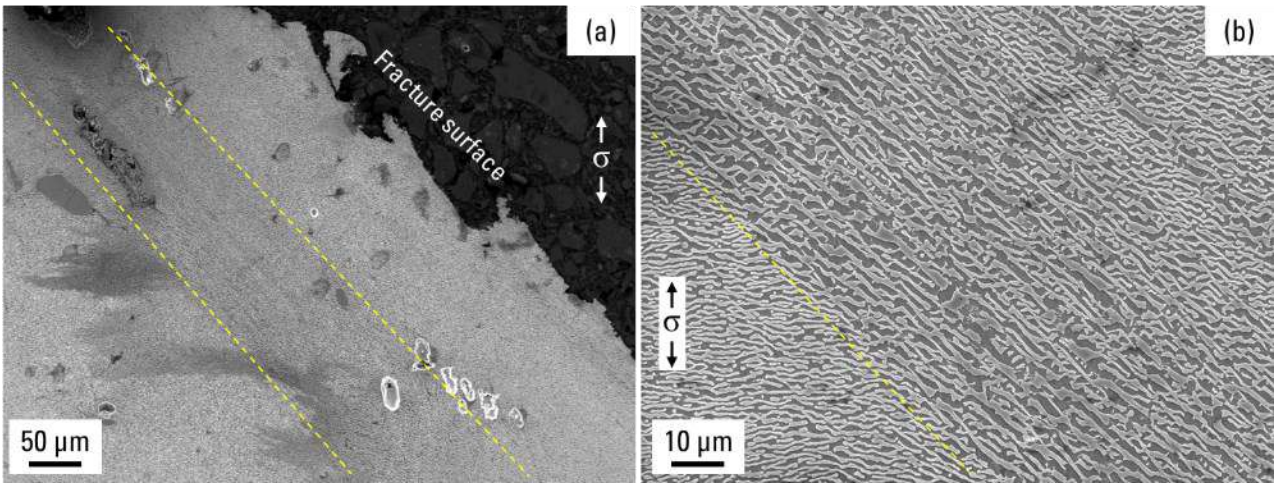

Figure 4.68. Microstructure of AM1-HT1-RTPD-A1 specimen after creep rupture test at 1050 °C / 140 MPa. Area near the fracture surface (a) and magnified image of the same band highlighted by the dotted lines (b).

Combination of full heat treatment + pre-deformation + additional aging treatment was also evaluated by creep tests at 950 °C / 300 MPa (AM1-HT1-RTPD-A1, Figure 4.63) and 850 °C / 500 MPa (AM1-HT1-RTPD-HT1, Figure 4.59). Slight decrease in creep life and retained ductility were observed for both tests in comparison with AM1-HT1 without pre-deformation. Probably the coarsened microstructure is the reason for small creep life debit, but damage localization with {111} fracture was avoided in these specimens. Detailed analyses are necessary for determining the exact effect of pre-deformation. However, it is clear that PD at RT between solution and aging treatments is the most detrimental one for these creep conditions as well. Again, dislocation structure development and void nucleation/growth from as-solutioned microstructure are important processes for accelerating creep damaging mechanisms that drastically decreases creep properties of the material.

4.3.3. Thermal cycling creep tests

Figure 4.69 shows thermal cycling creep (1050 °C / 15 min → 1110 °C / 1 min → 1050 °C / 15 min → 1160 °C / 15 min, 120 MPa) results on AM1 and CMSX-4 Plus without and with PD between solution and aging

treatments. Strain drop shown in 4P-RTPD-HT2 is accidental interruption of the creep test. The test was resumed by keeping weights all period including interruption and re-heating. AM1 did not have impact of pre-deformation on its thermal cycling creep properties. Decreased creep life was shown for 4P-RTPD-HT2, but such scatter may occur in this type of test, and at least, drastic effect was not triggered by pre-deformation. Figure 4.70 is longitudinal cross sections of specimens after SEM sample preparation. Both specimens have traces of microstructure coarsened band. However, they are not linked to the morphology of the fracture surface.

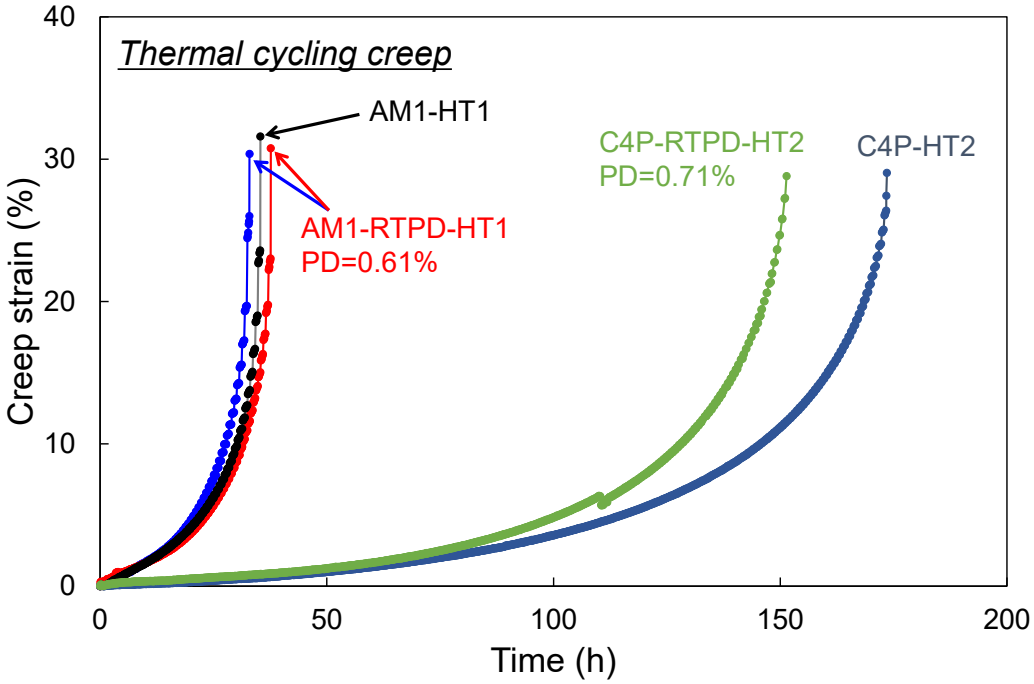

Figure 4.69. Result of thermal cycling creep tests on AM1 and CMSX-4 Plus consist of 1050 °C for 15 min → 1105 °C for 1 min → 1050 °C for 15 min → 1160 °C for 1 min with applied stress of 120 MPa.

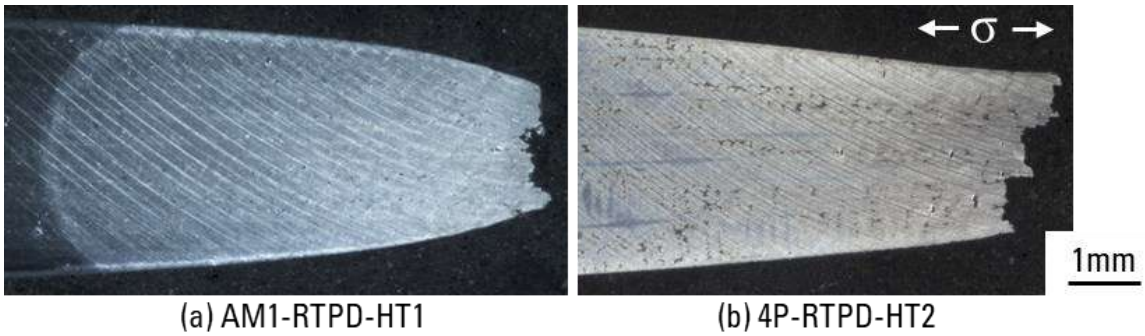

Figure 4.70. Longitudinal cross sections of AM1 and CMSX-4 Plus creep specimens tested in thermal cycling creep tests, prepared for microstructure observations.

In microstructures of both AM1-RTPD-HT1 and 4P-RTPD-HT2, the microstructure coarsened bands were possible to locate as indicated by dotted lines in Figures 4.71 and 4.72. However, all areas near the fracture surface presented disturbed microstructure and wide distribution of creep voids. In CMSX-4 Plus, TCP phases connected to creep voids were observed and this probably became an initiation site of crack propagation.

During thermal cycling of Ni-based SX superalloys, rapid transition of γ′ volume fraction moves γ/γ′ interface back-and-forth and accelerates dislocation shearing into γ′ phase [2,3,46]. Such creep conditions can erase prior microstructure degradation, which is the microstructure coarsened band created by a combination of pre-

deformation at RT and subsequent aging treatments. Therefore, the pre-deformation did not accelerate damaging process in the creep loading with non-isothermal temperature condition.

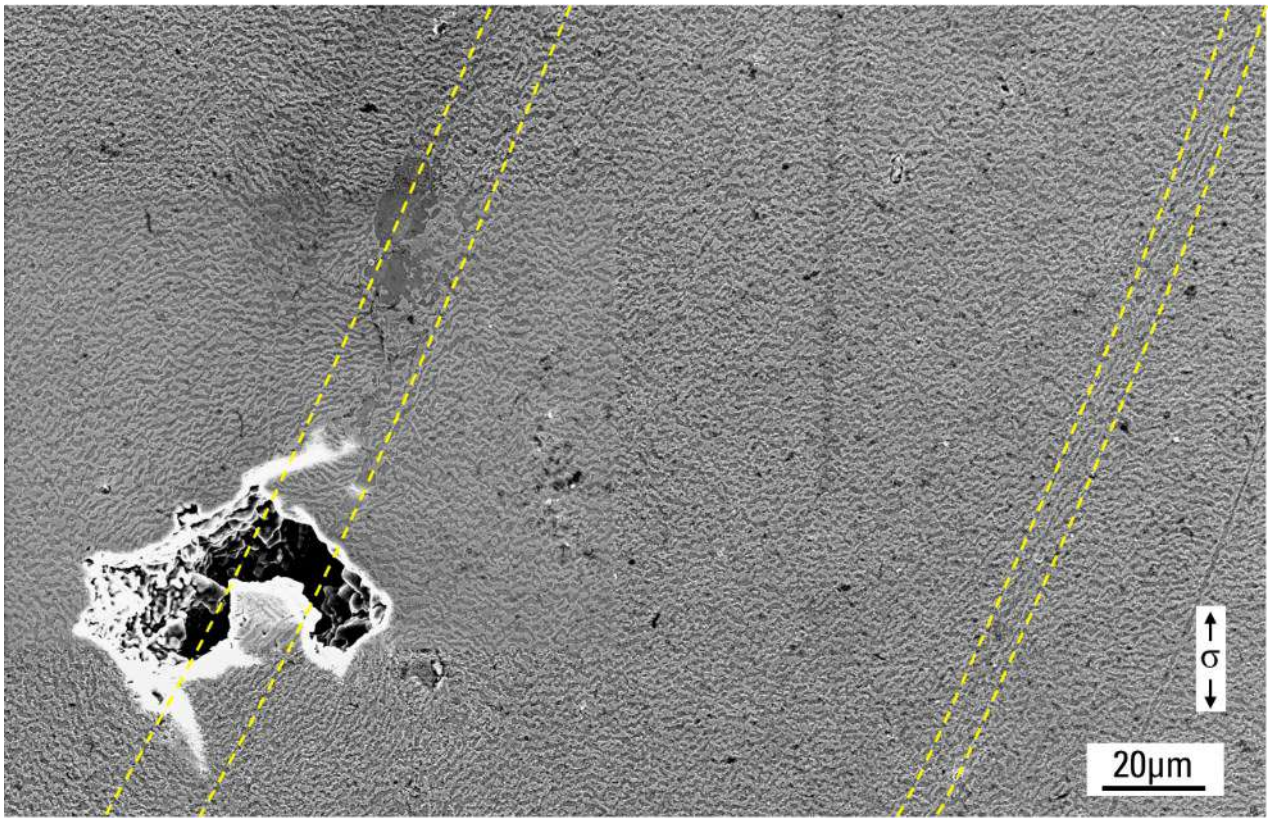

Figure 4.71. Microstructure of AM1-RTPD-HT1 specimen after thermal cycling creep test, observed at 0.5 mm away from the fracture surface and the microstructure coarsened bands are shown by the dotted lines.

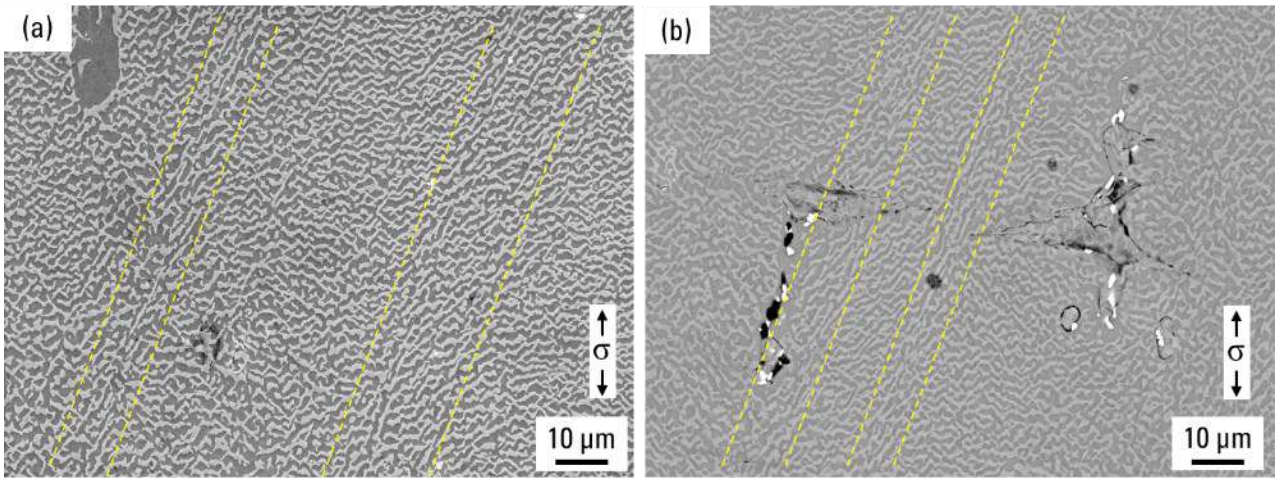

Figure 4.72. Microstructure of 4P-RTPD-HT2 specimen after thermal cycling creep test. Observed at 2 mm away from the fracture surface (a). BSE image taken near the fracture surface (b). The microstructure coarsened bands are indicated by dotted lines.

4. 4. Summary

The objective of this chapter was to understand the effect of different types of pre-deformation on the creep properties of Ni-based single crystal superalloys. Creep rupture tests were performed on AM1 and CMSX-4 Plus single crystal superalloys having microstructures presented in the previous chapter. Important remarks made in this chapter are summarized.

If a plastic deformation is introduced in as-solutioned AM1 at room-temperature, it decreases isothermal creep properties in all test conditions performed: 1200 °C / 80 MPa, 1050 °C / 140 MPa, 1050 °C / 200 MPa, 950 °C / 300 MPa, 850 °C / 500 MPa, and 750 °C / 800 MPa. Same processes were applied to CMSX-4 Plus and creep tests were performed at 1250 °C / 60 MPa, 1150 °C / 110 MPa, 1050 °C / 200 MPa, 950 °C / 390 MPa, and 850 °C / 500 MPa. Pre-deformation decreased creep life of CMSX-4 Plus at higher temperatures (≥ 1150 °C), but not strongly affected the creep properties at lower temperatures (≤ 1050 °C). Followings are the mechanisms behind creep life debits.

- During aging heat treatments, γ/γ′ microstructure coarsens around slip bands which has been explained in the Chapter 3. Simultaneously, deformation-pore nucleation and growth of pores are enhanced in the vicinity of slip planes by vacancy transportation associated with dislocation climb.

- At 1050 °C and 950 °C for AM1 and at 1150 °C for CMSX-4 Plus, microstructure coarsened bands evolve into the inclined γ′-rafted structure during creep deformation by facilitated shearing of {111} dislocations in γ′ phase. The rapid damage accumulation in inclined γ′-rafting accelerates creep void nucleation and growth, leading to a stress concentration around voids that further triggers recrystallization in the bands in the very last stages of creep deformation, resulting in earlier failure featuring a very planar fracture surface.

- In AM1, creep damage localization is much higher at 1050 °C / 140 MPa compared to 950 °C / 300 MPa. Since vacancies' transportation and condensation are the roots of damage localization, a higher creep temperature favors this diffusion-controlled damaging process. Because those thermally activated processes are slower in CMSX-4 Plus, creep damage at 1050 °C / 200 MPa and 950 °C / 390 MPa did not present drastic localization and impact of pre-deformation was not pronounced.

- As creep temperature decreases or applied load increases, diffusion induced damaging process is suppressed and microstructure shearing by slip activation become dominant factor that determines creep life. Because coherency between γ matrix and γ′ precipitates in the band is lost by microstructure evolution during aging treatment after pre-deformation, creep life of AM1 is more sensitive to the pre-deformation compared to CMSX-4 Plus.

To examine different cases that causes fatal damage localization, different preparation methods were applied, and creep tests were performed to those specimens. Procedures were: 1) pre-deformation at 950 °C between solution and aging treatments, 2) pre-deformation after solution followed by rejuvenation and aging treatments, 3) pre-deformation after full heat treatment, 4) pre-deformation between first and second aging treatment, 5) pre-deformation after full heat treatment followed by another first aging treatment. Thermal cycling creep tests were also performed to gain a deeper understanding of creep damage localizing situation.

- Creep deformation proceeded homogeneously within the specimens with the mild pre-rafted microstructure which was obtained after pre-deformation at 950 °C with subsequent aging treatments. Creep properties of this specimen at 1050 °C / 140 MPa was comparable to the reference without pre-deformation. However, the pre-rafted microstructure showed very poor creep life at 850 °C / 500 MPa, in a good agreement with previous literatures.

- Whatever the creep conditions, both AM1 and CMSX-4 Plus specimens with additional rejuvenation treatment showed equivalent properties to the reference materials without pre-deformation.
- Introduction of a room-temperature pre-deformation to AM1 at different preparation stages did not gave drastic impact on creep life at 1050 °C / 140 MPa. However, when specimen with pre-deformation after full heat treatment was aged with additional treatment at 1100 °C for 5 h, localized damage inside the band created planar {111} fracture surface without creep life debit. Dislocation structure developed during high temperature aging by stress relaxation is a possible reason for this unique fracture characteristic.
- Pre-deformation did not affect the creep properties of both AM1 and CMSX-4 Plus in non-isothermal creep condition. Damage localization did not occur in thermal cycling condition which has frequent and rapid transition of γ′ volume fraction. Because thermally activated damage localization is caused by initial dislocation structure, this does not contribute to the damaging process when dislocations can easily enter the γ′ phase.

References

[1] A. Epishin, T. Link, Mechanisms of high-temperature creep of nickel-based superalloys under low applied stresses, Philos. Mag. 84 (2004) 1979–2000. doi:10.1080/14786430410001663240.

[2] C. Schwalbe, J. Cormier, C.N. Jones, E. Galindo-Nava, C.M.F. Rae, Investigating the Dislocation-Driven Micro-mechanical Response Under Non-isothermal Creep Conditions in Single-Crystal Superalloys, Metall. Mater. Trans. A. 49 (2018) 3988–4002. doi:10.1007/s11661-018-4764-3.

[3] S. Antonov, W. An, S. Utada, X. Guo, C. Schwalbe, W. Zheng, C.M.F. Rae, J. Cormier, Q. Feng, Evaluation and comparison of damage accumulation mechanisms during non-isothermal creep of cast Ni-based superalloys, in: S. Tin, M. Hardy, J. Clews, J. Cormier, Q. Feng, J. Marcin, C. O'Brien, A. Suzuki (Eds.), Superalloys 2020, Springer International Publishing, 2020. doi:10.1007/978-3-030-51834-9_22.

[4] P. Caron, T. Khan, Improvement of Creep strength in a nickel-base single-crystal superalloy by heat treatment, Mater. Sci. Eng. 61 (1983) 173–184. doi:10.1016/0025-5416(83)90199-4.

[5] R.N. Ghosh, R. V Curtis, M. McLean, Creep deformation of single crystal superalloys—modelling the crystallographic anisotropy, Acta Metall. Mater. 38 (1990) 1977–1992. doi:10.1016/0956-7151(90)90309-5.

[6] N. Matan, D.C. Cox, P. Carter, M.A. Rist, C.M.F. Rae, R.C. Reed, Creep of CMSX-4 superalloy single crystals: effects of misorientation and temperature, Acta Mater. 47 (1999) 1549–1563. doi:10.1016/S1359-6454(99)00029-4.

[7] R.C. Reed, N. Matan, D.C. Cox, M.A. Rist, C.M.F. Rae, Creep of CMSX-4 superalloy single crystals: effects of rafting at high temperature, Acta Mater. 47 (1999) 3367–3381. doi:10.1016/S1359-6454(99)00217-7.

[8] A. Epishin, T. Link, P.D. Portella, U. Brückner, Evolution of the γ/γ′ microstructure during high-temperature creep of a nickel-base superalloy, Acta Mater. 48 (2000) 4169–4177. doi:10.1016/S1359-6454(00)00197-X.

[9] A. Epishin, T. Link, U. Brückner, P.D. Portella, Kinetics of the topological inversion of the γ/γ′-microstructure during creep of a nickel-based superalloy, Acta Mater. 49 (2001) 4017–4023. doi:10.1016/S1359-6454(01)00290-7.

[10] P. Caron, C. Ramusat, F. Diologent, Influence of the γ′ fraction on the γ/γ′ topological inversion during high temperature creep of single crystal superalloys, in: Superalloys 2008, TMS Warrendale, PA, 2008: pp. 159–167.

[11] S.J. Moss, G.A. Webster, E. Fleury, Creep deformation and crack growth behavior of a single-crystal nickel-base superalloy, Metall. Mater. Trans. A. 27 (1996) 829–837. doi:10.1007/BF02649750.

[12] J. Komenda, P.J. Henderson, Growth of pores during the creep of a single crystal nickel-base superalloy, Scr. Mater. 37 (1997) 1821–1826. doi:10.1016/S1359-6462(97)00341-2.

[13] J.-B. le Graverend, J. Adrien, J. Cormier, Ex-situ X-ray tomography characterization of porosity during high-temperature creep in a Ni-based single-crystal superalloy: Toward understanding what is damage, Mater. Sci. Eng. A. 695 (2017) 367–378. doi:10.1016/j.msea.2017.03.083.

[14] S.H. Ai, V. Lupinc, M. Maldini, Creep fracture mechanisms in single crystal superalloys, Scr. Metall. Mater. 26 (1992) 579–584. doi:10.1016/0956-716X(92)90287-O.

[15] L. Agudo Jácome, P. Nörtershäuser, C. Somsen, A. Dlouhý, G. Eggeler, On the nature of γ′ phase cutting and its effect on high temperature and low stress creep anisotropy of Ni-base single crystal superalloys, Acta Mater. 69 (2014) 246–264. doi:10.1016/j.actamat.2014.01.021.

[16] P. Kontis, Z. Li, D.M. Collins, J. Cormier, D. Raabe, B. Gault, The effect of chromium and cobalt segregation at dislocations on nickel-based superalloys, Scr. Mater. 145 (2018) 76–80. doi:10.1016/j.scriptamat.2017.10.005.

[17] J.R. Mianroodi, P. Shanthraj, P. Kontis, J. Cormier, B. Gault, B. Svendsen, D. Raabe, Atomistic phase field chemomechanical modeling of dislocation-solute-precipitate interaction in Ni–Al–Co, Acta Mater. 175 (2019) 250–261. doi:10.1016/j.actamat.2019.06.008.

[18] J. Cormier, M. Jouiad, F. Hamon, P. Villechaise, X. Milhet, Very high temperature creep behavior of a single crystal Ni-based superalloy under complex thermal cycling conditions, Philos. Mag. Lett. 90 (2010) 611–620. doi:10.1080/09500839.2010.489887.

[19] B. Ruttert, D. Bürger, L.M. Roncery, A.B. Parsa, P. Wollgramm, G. Eggeler, W. Theisen, Rejuvenation of creep resistance of a Ni-base single-crystal superalloy by hot isostatic pressing, Mater. Des. 134 (2017) 418–425. doi:10.1016/j.matdes.2017.08.059.

[20] H. Buck, P. Wollgramm, A.B. Parsa, G. Eggeler, A quantitative metallographic assessment of the evolution of porosity during processing and creep in single crystal Ni-base super alloys, Materwiss. Werksttech. 46 (2015) 577–590. doi:10.1002/mawe.201500379.

[21] L. Mujica Roncery, I. Lopez-Galilea, B. Ruttert, S. Huth, W. Theisen, Influence of temperature, pressure, and cooling rate during hot isostatic pressing on the microstructure of an SX Ni-base superalloy, Mater. Des. 97 (2016) 544–552. doi:10.1016/j.matdes.2016.02.051.

[22] W.W. Milligan, S.D. Antolovich, Yielding and deformation behavior of the single crystal superalloy PWA 1480, Metall. Trans. A. 18 (1987) 85–95. doi:10.1007/BF02646225.

[23] M. Feller-Kniepmeier, T. Link, I. Poschmann, G. Scheunemann-Frerker, C. Schulze, Temperature dependence of deformation mechanisms in a single crystal nickel-base alloy with high volume fraction of γ′ phase, Acta Mater. 44 (1996) 2397–2407. doi:10.1016/1359-6454(95)00354-1.

[24] D.L. Anton, A.F. Giamei, Porosity distribution and growth during homogenization in single crystals of a nickel-base superalloy, Mater. Sci. Eng. 76 (1985) 173–180. doi:10.1016/0025-5416(85)90091-6.

[25] T. Link, S. Zabler, A. Epishin, A. Haibel, M. Bansal, X. Thibault, Synchrotron tomography of porosity in single-crystal nickel-base superalloys, Mater. Sci. Eng. A. 425 (2006) 47–54. doi:10.1016/j.msea.2006.03.005.

[26] A. Epishin, T. Link, I.L. Svetlov, G. Nolze, R.S. Neumann, H. Lucas, Mechanism of porosity growth during homogenisation in single crystal nickel-based superalloys, Int. J. Mater. Res. 104 (2013) 776–782. doi:10.3139/146.110924.

[27] A.I. Epishin, I.L. Svetlov, Evolution of pore morphology in single-crystals of nickel-base superalloys, Inorg. Mater. Appl. Res. 7 (2016) 45–52. doi:10.1134/S2075113316010056.

[28] M. Sakaguchi, M. Ike, M. Okazaki, Microstructural changes in a single crystal Ni-base superalloy induced by plastic straining, Mater. Sci. Eng. A. 534 (2012) 253–259.

doi:10.1016/J.MSEA.2011.11.066.

[29] L. Agudo Jácome, P. Nörtershäuser, J.-K. Heyer, A. Lahni, J. Frenzel, A. Dlouhy, C. Somsen, G. Eggeler, High-temperature and low-stress creep anisotropy of single-crystal superalloys, Acta Mater. 61 (2013) 2926–2943. doi:10.1016/j.actamat.2013.01.052.

[30] A. Cervellon, S. Hémery, P. Kürnsteiner, B. Gault, P. Kontis, J. Cormier, Crack initiation mechanisms during very high cycle fatigue of Ni-based single crystal superalloys at high temperature, Acta Mater. 188 (2020) 131–144. doi:10.1016/j.actamat.2020.02.012.

[31] S. Antonov, Y. Zheng, J.M. Sosa, H.L. Fraser, J. Cormier, P. Kontis, B. Gault, Plasticity assisted redistribution of solutes leading to topological inversion during creep of superalloys, Scr. Mater. 186 (2020) 287–292. doi:10.1016/j.scriptamat.2020.05.004.

[32] J. He, C.H. Zenk, X. Zhou, S. Neumeier, D. Raabe, B. Gault, S.K. Makineni, On the atomic solute diffusional mechanisms during compressive creep deformation of a Co-Al-W-Ta single crystal superalloy, Acta Mater. 184 (2020) 86–99. doi:10.1016/j.actamat.2019.11.035.

[33] S. Steuer, Z. Hervier, S. Thabart, C. Castaing, T.M. Pollock, J. Cormier, Creep behavior under isothermal and non-isothermal conditions of AM3 single crystal superalloy for different solutioning cooling rates, Mater. Sci. Eng. A. 601 (2014) 145–152. doi:10.1016/j.msea.2014.02.046.

[34] P. Caron, P.J. Henderson, T. Khan, M. McLean, On the effects of heat treatments on the creep behaviour of a single crystal superalloy, Scr. Metall. 20 (1986) 875–880. doi:10.1016/0036-9748(86)90458-8.

[35] T.M. Pollock, A.S. Argon, Creep resistance of CMSX-3 nickel base superalloy single crystals, Acta Metall. Mater. 40 (1992) 1–30. doi:10.1016/0956-7151(92)90195-K.

[36] G.L. Drew, R.C. Reed, K. Kakehi, C.M.F. Rae, Single Crystal Superalloys: The transition from Primary to Secondary Creep, in: Superalloys 2004, 2004: pp. 127–136. doi:10.7449/2004/Superalloys_2004_127_136.

[37] R.A. MacKay, R.D. Maier, The influence of orientation on the stress rupture properties of nickel-base superalloy single crystals, Metall. Trans. A. 13 (1982) 1747–1754. doi:10.1007/BF02647830.

[38] C.M.F. Rae, M.A. Rist, D.C. Cox, R.C. Reed, N. Matan, On the primary creep of CMSX-4 superalloy single crystals, Metall. Mater. Trans. A. 31 (2000) 2219–2228. doi:10.1007/s11661-000-0139-6.

[39] L.M. Bortoluci Ormastroni, S. Utada, J. Rame, L. Mataveli Suave, K. Kawagishi, H. Harada, P. Villechaise, J. Cormier, Tensile, low cycle fatigue and very high cycle fatigue characterizations of advanced single crystal nickel-based superalloys, in: S. Tin, M. Hardy, J. Clews, J. Cormier, Q. Feng, J. Marcin, C. O'Brien, A. Suzuki (Eds.), Superalloys 2020, Springer International Publishing, 2020: pp. 341–351. doi:10.1007/978-3-030-51834-9_33.

[40] P. Caron, F. Diogolent, S. Drawin, Influence of chemistry on the tensile yield strength of nickel-based single crystal superalloys, in: Adv. Mater. Res., Trans Tech Publ, 2011: pp. 345–350.

[41] Y. Ru, H. Zhang, Y. Pei, S. Li, X. Zhao, S. Gong, H. Xu, Improved 1200°C stress rupture property of single crystal superalloys by γ′-forming elements addition, Scr. Mater. 147 (2018) 21–26. doi:10.1016/j.scriptamat.2017.12.023.

[42] J. Cormier, S. Utada, Ultra-high temperature creep of Ni-based SX superalloys at 1250°C, Metals. (2021) To be submitted.

[43] A. Epishin, B. Fedelich, G. Nolze, S. Schriever, T. Feldmann, M.F. Ijaz, B. Viguier, D. Poquillon, Y. Le Bouar, A. Ruffini, A. Finel, Creep of Single Crystals of Nickel-Based Superalloys at Ultra-High Homologous Temperature, Metall. Mater. Trans. A. 49 (2018) 3973–3987. doi:10.1007/s11661-018-4729-6.

[44] L. Dirand, J. Cormier, A. Jacques, J.-P. Chateau-Cornu, T. Schenk, O. Ferry, P. Bastie, Measurement of the effective γ/γ′ lattice mismatch during high temperature creep of Ni-based single crystal superalloy, Mater. Charact. 77 (2013) 32–46. doi:10.1016/J.MATCHAR.2012.12.003.

[45] A. Royer, P. Bastie, M. Veron, In situ determination of γ′ phase volume fraction and of relations between lattice parameters and precipitate morphology in Ni-based single crystal superalloy, Acta Mater. 46 (1998) 5357–5368. doi:10.1016/S1359-6454(98)00206-7.

[46] J.-B. le Graverend, A. Jacques, J. Cormier, O. Ferry, T. Schenk, J. Mendez, Creep of a nickel-based single-crystal superalloy during very high-temperature jumps followed by synchrotron X-ray diffraction, Acta Mater. 84 (2015) 65–79. doi:https://doi.org/10.1016/j.actamat.2014.10.036.

CHAPTER 5
VHCF PROPERTIES OF PRE-DEFORMED AM1 SX SUPERALLOY

Table of contents

Résumé : Propriétés VHCF du superalliage monocristallin AM1 avec pré-déformation 169

5. 1. Introduction 170

5. 3. Fractographic observations 170

5. 4. Microstructure characterization of specimen's longitudinal section 173

5. 5. Effect of pre-deformation in fully reversed condition $R = -1$ 175

5. 6. Enhanced shearing and recrystallization at positive stress ratio condition, $R = 0.5$ 177

5. 7. VHCF life restoration by rejuvenation heat treatment 179

5. 8. Summary 179

References 180

RÉSUMÉ : PROPRIÉTÉS VHCF DU SUPERALLIAGE MONOCRISTALLIN AM1 AVEC PRÉ-DÉFORMATION

Les propriétés en fatigue à très grand nombre de cycles (VHCF) du superalliage monocristallin AM1 en présence d'une pré-déformation plastique ont été étudiées à 1000 °C en utilisant une machine de fatigue ultrasonique fonctionnant à 20 kHz. La pré-déformation a été appliquée entre les traitements thermiques de mise en solution et de revenu pour le matériau (AM1-RTPD-HT1).

Le matériau pré-déformé n'a pas montré de chute de la durée de vie dans des conditions fatigue pure ($R = -1$). Dans le chapitre précédent, l'augmentation du nombre de pores de déformation (D-pores) a été explorée comme conséquence de la pré-déformation et des traitements de revenu suivants. Les ruptures par fatigue ont été provoquées par les pores de solidification (S-pores) et ces petits D-pores n'ont pas affecté la durée de vie en VHCF. Ce résultat est en accord avec les études précédentes qui montrent qu'un traitement thermique prolongé n'affecte pas la durée de vie du VHCF en condition de fatigue pure [1]. Des observations fractographiques et microstructurales sur des matériaux pré-déformés ont montré de multiples pores de solidification présentent les premiers stades d'amorçage de fissures associé à une recristallisation locale autour d'eux. Ce mécanisme a également été proposé pour l'amorçage des fissures de fatigue. [2]. Par conséquent, le mécanisme de rupture par fatigue dans cette condition peut être déterminé comme le même que celui rapporté dans les études précédentes [2,3].

Sous charge moyenne appliquée, la pré-déformation réduit la durée de vie du VHCF dans des conditions de charge moyenne élevé ($R = 0{,}5$, $\sigma_{max} = 551$ MPa). La recristallisation de surface et l'amorçage de fissures de surface en mode I à partir de la zone recristallisée ont été observés dans le spécimen pré-déformé. La rupture en fatigue par des fissures de mode I a été observée uniquement dans l'AM1-RTPD-HT1. Toutes les autres éprouvettes (AM1-HT1 et AM1-RTPD-Rejuv-HT1) présentaient des fissures de fatigue s'amorçant à partir de pores internes comme dans l'étude précédente [1,4]. Les bandes à microstructure grossière sur les plans {111} facilitent le cisaillement de la microstructure sous forte charge moyenne en fatigue ultrasonore. Cela a conduit à relief de surface très marqué sur les génératrices de normales <110> des échantillons de par le glissement sur les plans {111} débouchant en surface. Cette plus forte rugosité de la surface locale a conduit en une concentration locale des contraintes et à l'augmentation de la densité de dislocations. La recristallisation de la surface a été activée dans cette zone de concentration des contraintes. Des fissures s'amorcent alors en mode I à partir de la zone recristallisée, ce qui a conduit à la rupture pour une très faible durée de vie comparativement aux échantillons sans pré-déformation.

Les échantillons avec un traitement thermique de restauration additionnelle après la pré-déformation ont également été préparés pour les tests VHCF. Le traitement de restauration permet restaurer la durée de vie en fatigue gigacylique à fort rapport de charge. Cette restauration ne présente aucun impact sur la durée de vie quelles que soient les conditions testées dans cette étude. L'efficacité du traitement de restauration a été démontrée sur les propriétés en fatigue gigacylique.

5. 1. Introduction

It has been shown in the previous chapter that if a PD is introduced in a Ni-based SX superalloy after the solution heat treatment, γ/γ' microstructure evolution, growth of S-pores [2,3] and H-pores [2,4], and nucleation of D-pores [5] are all enhanced along with introduced slip bands during aging treatments. Moreover, during creep loading at high temperature (≥ 950 °C), faster microstructure coarsening along the former slip band accelerates creep damage accumulation at nucleated and enlarged pores, ultimately leading to faster creep failure. During creep test at lower temperatures with higher applied stresses (e.g. 850 °C / 500 MPa), γ/γ' microstructure shearing from creep void was observed locally in the microstructure coarsened band. Considering these microstructure evolution and high-temperature behaviors of pre-deformed AM1 Ni-based SX superalloy, coarsened pores lying in the microstructure coarsened band with lower resistance to shearing may decrease the high temperature fatigue life of the material.

Within this context, this chapter aims to investigate the influence of microstructural defects induced by a prior PD on the VHCF lifetime and to improve the understanding of fracture mechanisms in the VHCF regime at 1000 °C both in fully reversed ($R = -1$) and with the application of high mean stress ($R = 0.5$). Because pre-deformation can be introduced to a turbine blade during production [6], and since high cycle fatigue properties have been imposed as turbine airfoil design criteria by the airworthiness authorities (FAA, EASA), evaluating fatigue properties of pre-deformed material is an essential matter. Rejuvenation heat treatment, which has been demonstrated to restore microstructure and creep life after pre-deformation, is also tested in this chapter to evaluate its efficiency in restoring VHCF life.

5. 2. VHCF tests results

VHCF tests were performed on pre-deformed AM1 at 1000 °C with stress ratio of $R = -1$ (Figure 5.1) and $R = 0.5$ (Figure 5.2). Under fully reversed condition ($R = -1$), both AM1-RTPD-HT1 and AM1-RTPD-Rejuv-HT1 have a similar lifetime compared to the reference "AM1 Bridgman" which was taken from the previous research and was processed with standard heat treatments (same as HT1) without prior deformation [7]. In the tests with a positive stress ratio of $R = 0.5$, AM1-RTPD-Rejuv-HT1 performed similarly to the reference AM1-HT1. AM1-RTPD-HT1 exhibited a shorter lifetime at a higher maximum stress condition of $\sigma_{max} = 551$ MPa, with a debit in fatigue life of nearly one decade. At lower stress condition of $\sigma_{max} = 413$ MPa, a similar life to the reference was however obtained after pre-deformation.

5. 3. Fractographic observations

Fracture surfaces of AM1-RTPD-HT1 are shown in Figures 5.3(a) and 5.4(a). The fracture plane parallel to the {111} slip system appeared in all specimens. At $R = -1$ conditions, the fatal crack started from S-pore close to the cylindrical surface and it was surrounded by the rough zone (Figure 5.3(b)) regardless of applied stress and lifetime up to ~10^9 cycles. This observation is consistent with previous results from the literature [7]. Also, traces of the microstructure coarsened band were apparent in all AM1-RTPD-HT1 specimens tested at $R = -1$ (see white arrows in Figures 5.3(b, c)). In AM1-RTPD-HT1 tested with $R = -1$ and $\sigma_a = 209$ MPa, multiple and isolated S-pores having features similar to the main crack initiating pore (i.e. presence of a rough zone) were observed on the fracture surface (Figure 5.3(c)). Multiple S-pores were exposed in the fracture

surface of specimens failed at lower stresses as well. Aside from one exception, all fatigue specimens after R = 0.5 and maximum stress lower than 600 MPa also presented an internal crack initiation feature with the major fracture plane lying on {111} plane, in good agreement with the previous studies [1,7].

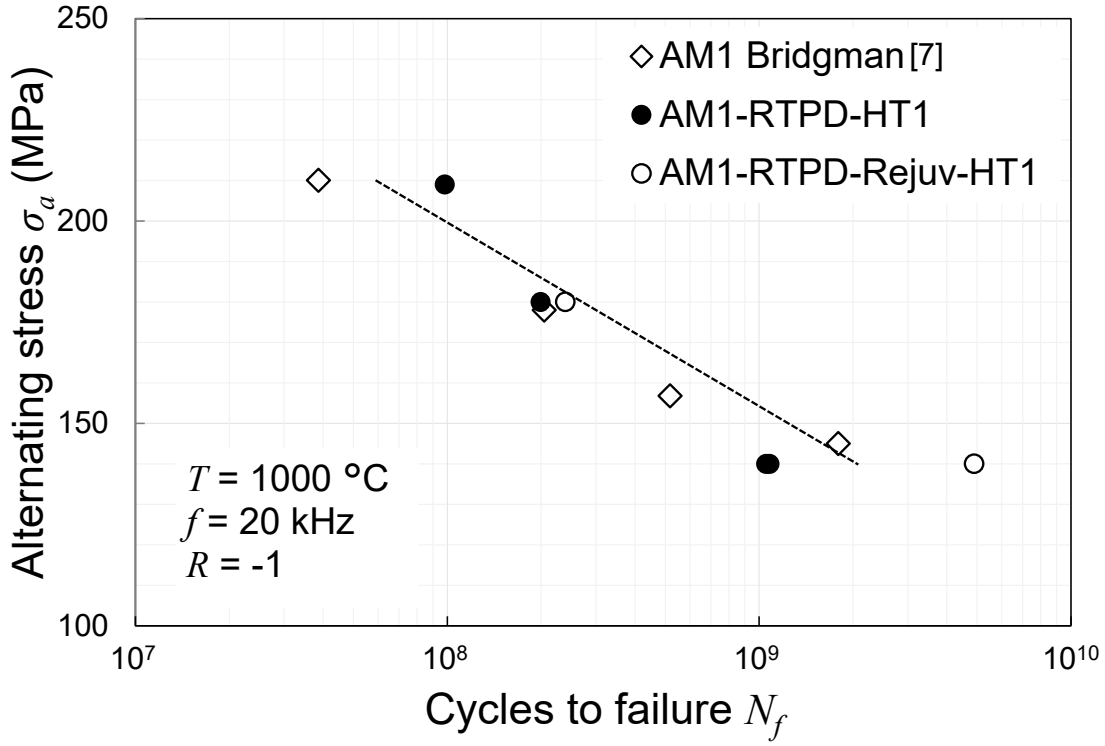

Figure 5.1. Results of VHCF tests at 1000 °C / f = 20 kHz / R = −1 in S-N diagram. The alternating stress is plotted as a function of the number of cycles to failure. Data for Bridgman in (a) are taken from the reference [7].

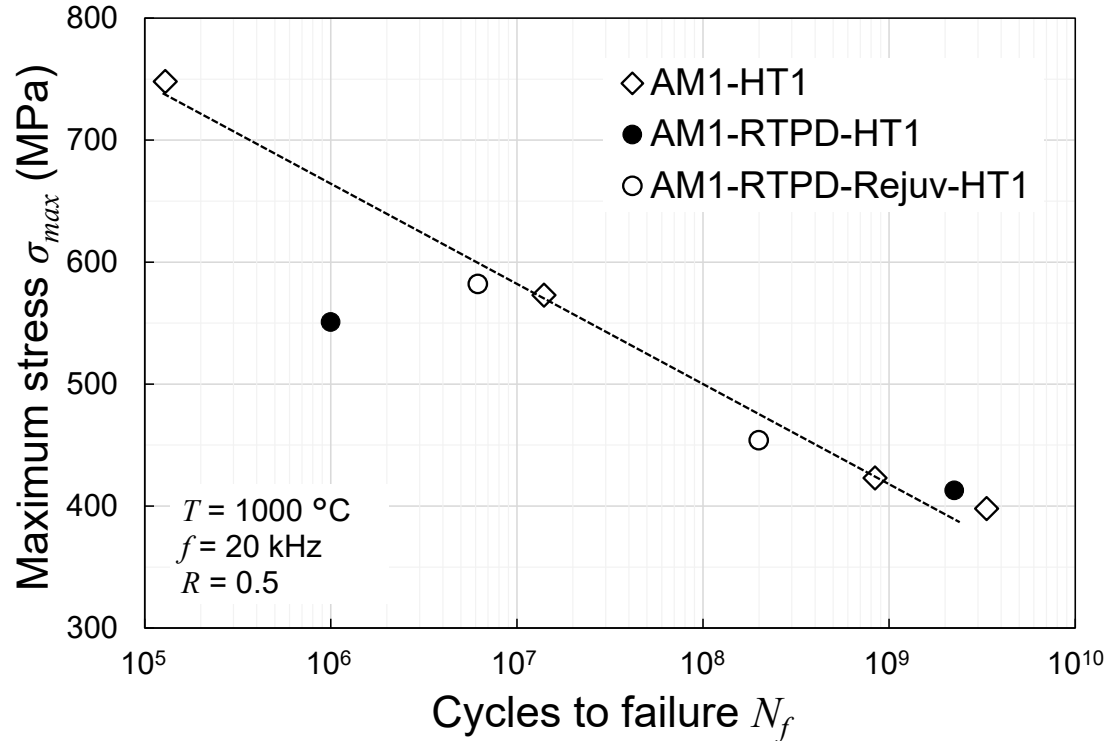

Figure 5.2. Results of VHCF tests at 1000 °C / f = 20 kHz / R = 0.5 in S-N diagram. The maximum stress is plotted as a function of the number of cycles to failure

The only exception to these trends with a failure starting from the surface was the test performed with the conditions of 1000 °C, f = 20 kHz, R = 0.5, and σ_{max} = 551 MPa (Figure 5.4(a)). Mode I cracks are initiating from the surface of the specimen at locations with an external normal to the specimen's gauge surface of <110> type, as indicated by black arrows in Figures 5.4(a, b). Apart from the cracks, line traces transverse to the specimen's longitudinal direction were observed at the same locations as the mode I cracks (white arrows in Figures 5.4(b, c)) which is mentioned above. In the same specimen viewed from other direction, slip marks parallel to the {111} plane were observed on the surface (black arrows in Figure 5.4(c)). Such slip traces are similar to the ones previously observed at the surface of the specimen just after pre-deformation or after creep tests at temperatures above 950 °C. The transverse line traces and {111} slip bands also appeared on the surface of AM1-HT1 (R = 0.5 and σ_{max} = 582 MPa) and AM1-RTPD-Rejuv-HT1 (R = 0.5 and σ_{max} = 573 MPa), but the number of slip bands was by far lower compared to AM1-RTPD-HT1. Surface cracks were also observed in those specimens at the intersection of two slip bands, however, the failure came from an internal crack initiation site (i.e. an S-pore).

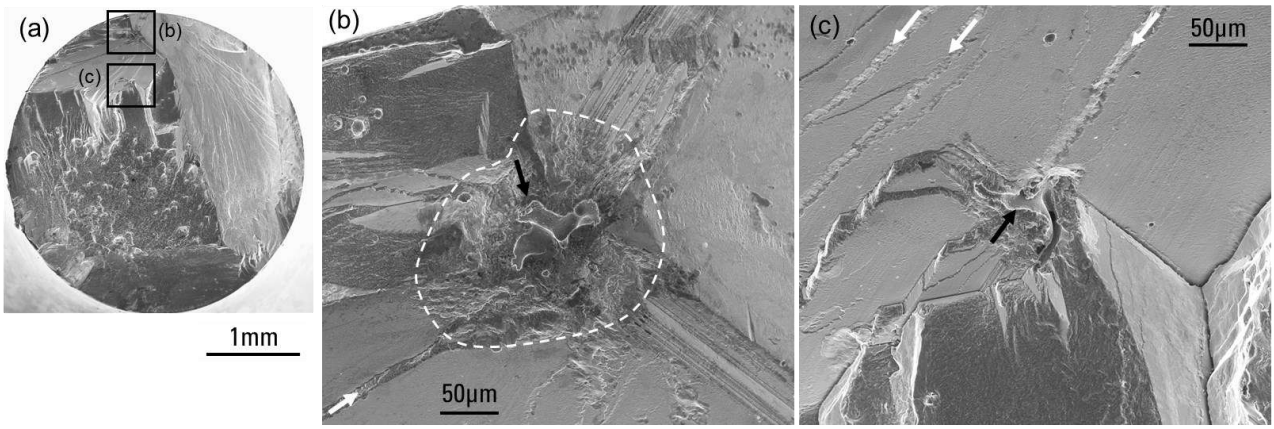

Figure 5.3. (a) Fractography of VHCF specimen (AM1-RTPD-HT1) tested at 1000 °C, f = 20 kHz. R = −1, σ_a = 209 MPa. (b) Magnified image showing the main crack initiation site indicated by a black arrow and the rough zone indicated by the dotted line. (c) Magnified image showing another solidification pore on the fracture surface. White arrows are indicating microstructure coarsened bands.

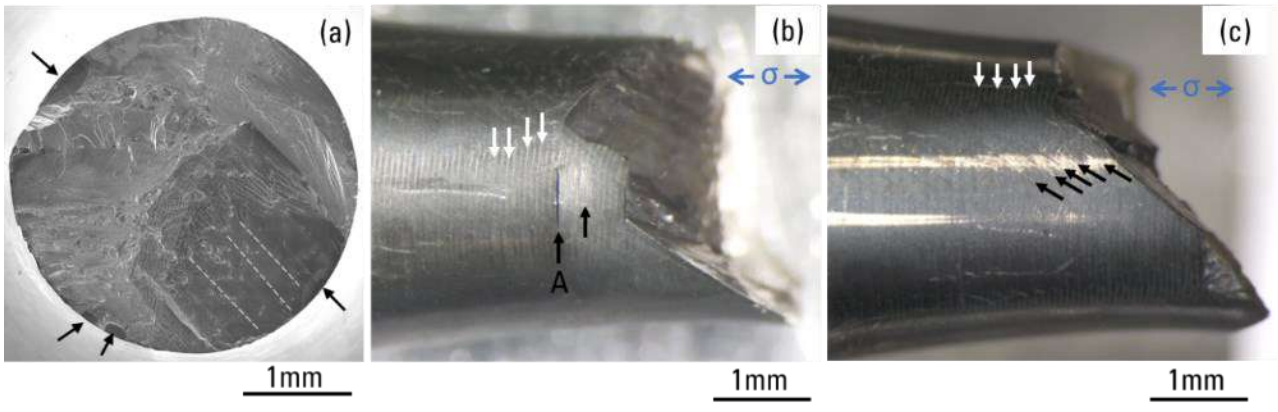

Figure 5.4. (a) Fractography of VHCF specimen (AM1-RTPD-HT1) tested at 1000 °C, f = 20 kHz, R = 0.5, σ_{max} = 551 MPa. (b, c) Appearances of the same specimen. Arrows in (a) are failure initiating sites from the cylindrical surface. Black arrows in (b) are surface cracks and the microstructure of crack A is presented in Figures 5.7 and 5.8. Black arrows in (c) are {111} slip traces appearing on the cylindrical surface. White arrows in (b, c) are line traces transverse to the loading direction.

5. 4. Microstructure characterization of specimen's longitudinal section

Precipitate scale images of the microstructure coarsened band are shown in Figure 5.5. γ′ precipitates in the specimen tested at $R = -1$ / $\sigma_a = 209$ MPa had coarsened more than the ones in the specimen tested in $R = 0.5$ which is simply because the overall duration of this test was longer. Although microstructure evolution had not proceeded much, dislocation traces were observed in the microstructure coarsened band of the specimen tested with $R = 0.5$ / $\sigma_{max} = 551$ MPa (magnified image in Figure 5.5(b)), whereas they were not observed in $R = -1$ / $\sigma_a = 209$ MPa. Close to the specimen's surface, microstructure coarsening proceeded much faster inside the band with shear traces. Intermetallic phases other than γ matrix and γ′ precipitates (i.e. TCP phases) were not observed in these specimens. AM1 is indeed known to be an alloy with a very stable microstructure without TCP precipitation after over 400 h of creep test at 1050 °C (see Chapter 4).

Figures 5.6(a, b) are showing γ/γ′ microstructure around an S-pore on the fracture surface associated with the rough zone. Like in previous studies [1,8], a high density of shear traces and disturbed γ/γ′ microstructure were observed below the rough zone (Figure 5.6(b)). Figure 5.6(c) is an example of an S-pore where cracks are propagating along recrystallized grains (see Figure 6(d)), which will become the rough zone and can be considered as an intermediate stage before failure.

Figures 5.7(a) is showing the low magnification microstructure at the surface of AM1-RTPD-HT1 specimen tested at 1000 °C, $f = 20$ kHz, $R = 0.5$, $\sigma_{max} = 551$ MPa. Despite a very short test duration (~ 50 s), multiple surface cracks were observed, as well as the microstructure coarsened bands indicated by dotted lines in the same figure to help the reader. Figure 5.7(b) is a crystallographic orientation map obtained by EBSD analyses. In this IPF map, three surface recrystallization areas are observed. Two areas on the right and left are associated with initiated cracks and one located in the middle is a potential third crack initiation site. A darker area in an image quality (IQ) map is corresponding to an area with a higher dislocation density that decreases the quality of diffraction. In Figure 5.7(b), dark areas and lines are observed in the surface layer of the specimen with a thickness of ~30 µm. The bands with disturbed microstructure like the one shown in Figure 5.5(c) are observed in this layer. In the crack shown in Figure 5.7(c), oxide and the γ′-depleted zone were observed all along the crack path and up to the tip.

Other cracks marked as A and B in Figure 5.7(a) are presented in Figure 5.8 with higher magnification and IPF maps. These cracks have a greater opening (> 3µm) and crack tips were not filled with oxides when they are compared with the one in Figure 5.7(c) having a smaller opening (~1 µm). The crack on the right in Figure 5.7(b) is also of the same type with a large opening and without an oxide layer at the crack tip. Recrystallized grain was not observed around crack A with the largest opening (Figure 5.8(c)). Lattice rotation at the tip of this crack A indicates the existence of very strong stress concentration. The IPF map in Figure 5.8(d) shows recrystallized grains surrounding crack B. At the tips of both cracks A and B, slip bands can be observed in secondary electron images and IPF maps. When these IPF maps are shown with an IQ map, slip bands appear as dark lines as previously explained in Figure 5.7(b). It should be noted that slip bands observed in the sub-surface layer and at the crack tips are different from the slip bands introduced during pre-deformation and from the microstructure coarsened bands that formed during aging treatments.

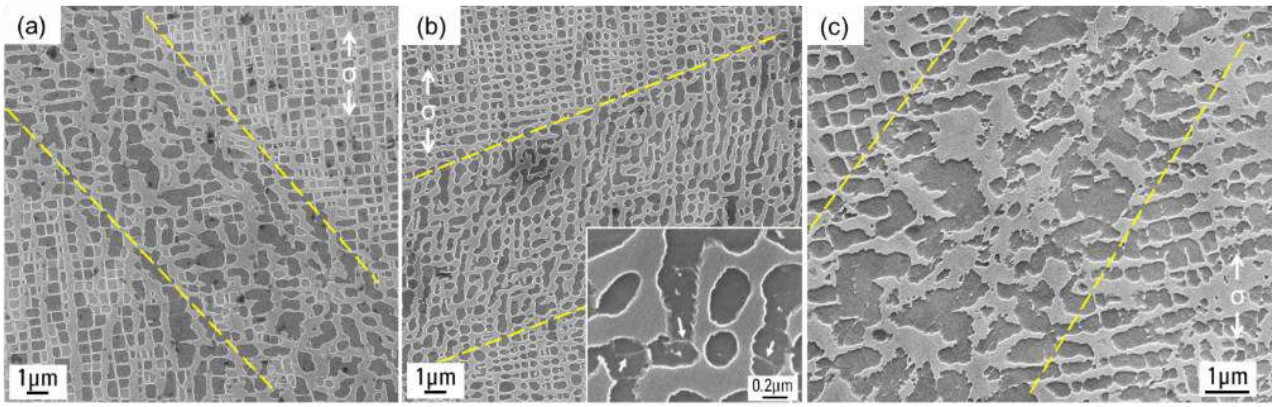

Figure 5.5. Precipitate scale microstructure observed in longitudinal cross section of AM1-RTPD-HT1 VHCF specimens after tests at 1000 °C, f = 20 kHz. (a) R = −1, σ_a = 209 MPa, failed at 9.8 × 10^7 cycles, (b) R = 0.5, σ_{max} = 551 MPa, N_f = 1.0 × 10^6 cycles and magnified image of precipitates inside the band is on the bottom right. Arrows are indicating dislocation traces in the γ′ phase. (c) R = 0.5, σ_{max} = 551 MPa, N_f = 1.0 × 10^6 cycles, microstructure close to the specimen's surface. Dotted lines are indicating the microstructure coarsened bands.

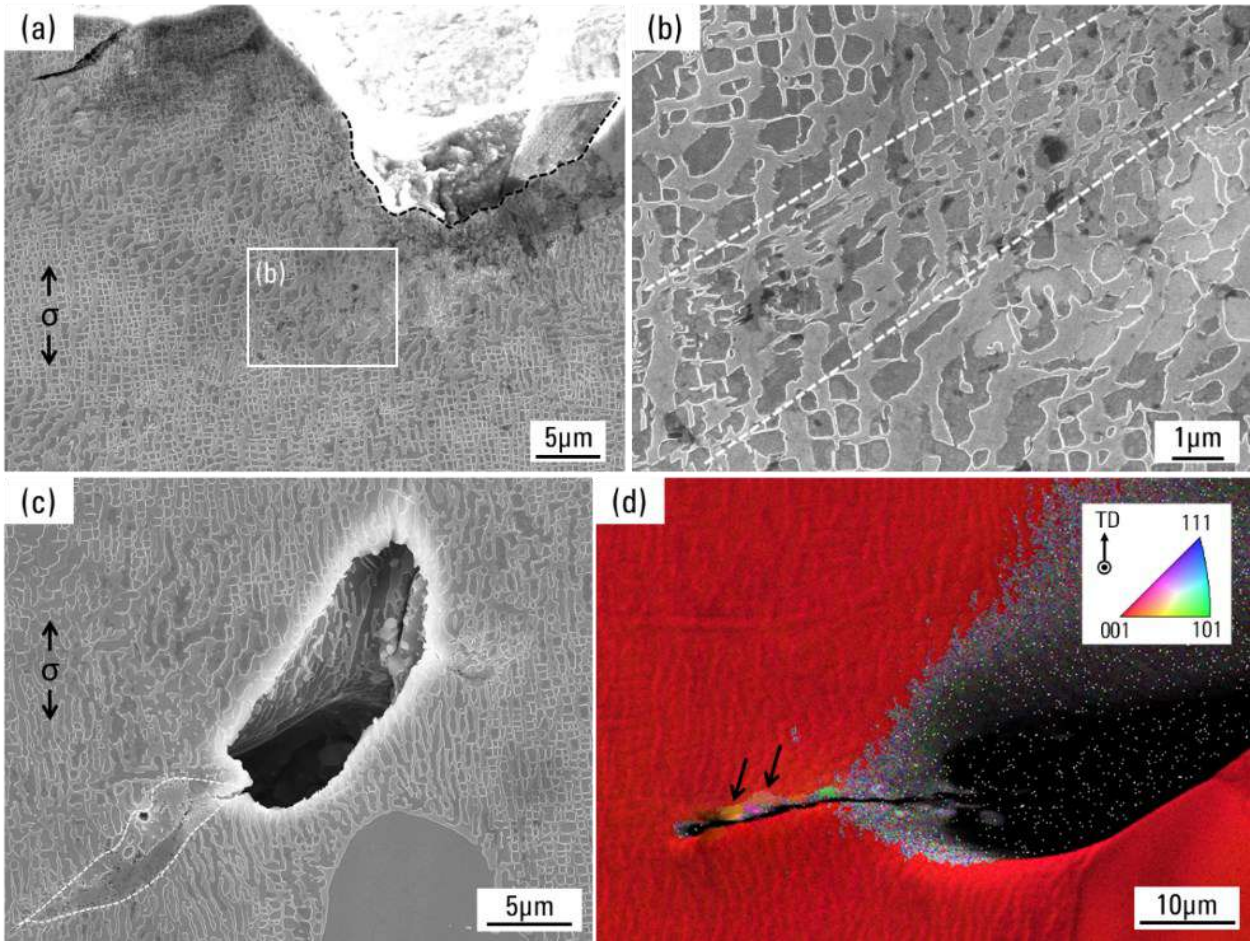

Figure 5.6. Microstructure observed along longitudinal cut of AM1-RTPD-HT1 specimen tested at 1000 °C, f = 20 kHz, R = −1, σ_a = 209 MPa. (a) The area near the fracture surface with S-pore exhibiting the rough zone indicated by the dotted curve. (b) Magnification of the rectangle in (a) showing microstructure shearing in between dotted lines. (c) S-pore inside the specimen and evolved microstructure with crack propagation are surrounded by the dotted curve. (d) IPF map of the area around the crack in (c) superimposed on forward scatter detector signal. Arrows are showing recrystallized grains along the crack path.

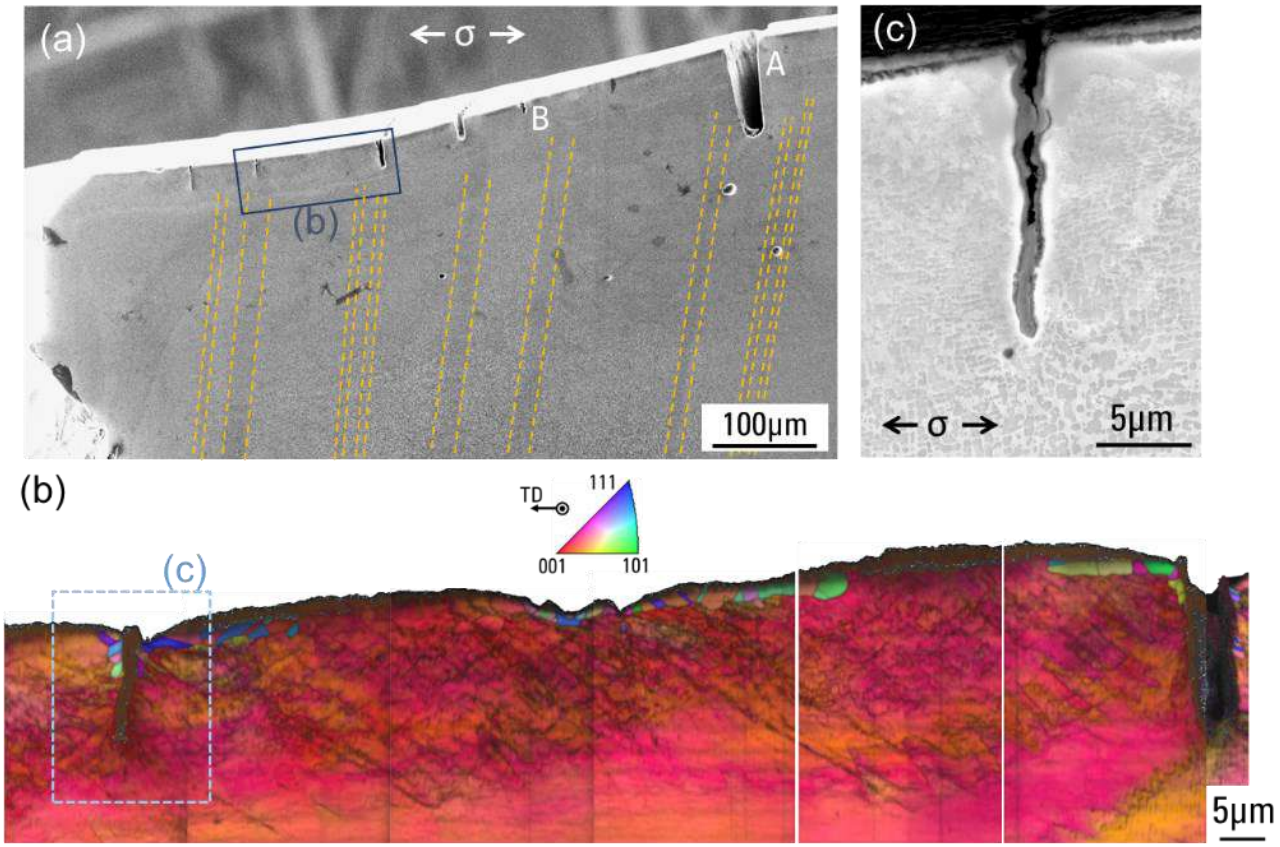

Figure 5.7. Microstructure observed along longitudinal cross-section of AM1-RTPD-HT1 specimen tested at 1000 °C, f = 20 kHz, R = 0.5, σ_{max} = 551 MPa. (a) The area including cylindrical surface and dotted lines are indicating the microstructure coarsened bands. (b) Merged IPF + IQ maps at the surface layer indicated by the rectangle in (a). (c) Backscatter electron image of the area indicated by the rectangle in (b).

5. 5. Effect of pre-deformation in fully reversed condition $R = -1$

In the previous chapter, stereological analyses were performed on void/pore size and counts in AM1-RTPD-HT1. Increase in void size and density induced by pre-deformation before aging treatments has been evidenced. Since void/pore size is the most important factor controlling the VHCF durability in the Ni-based SX superalloys under fully reversed condition [7,9], the pre-deformed material having a lifetime similar to non-pre-deformed material seems contradictory.

Recalling that both reference and AM1-RTPD-HT1 are produced by the Bridgman SX casting method with similar casting parameters, primary dendrite arm spacings, S-pores, and eutectics are assumed to be comparable in these materials in the as-solutioned state. Thus, the probability of having a critical S-pore within the gauge center section of the VHCF specimens are equivalent. In comparison, specimens prepared by LMC or with HIP methods have far better VHCF lives, due to smaller S-pores or absence of remaining S-pores, respectively [7]. In the previous chapter, counts and size distribution of larger voids are not so different among two materials, AM1-HT1 and AM1-RTPD-HT1. Moreover, it has already been shown that increased void size by over-aging did not affect the VHCF life of CMSX-4 tested under similar testing conditions [1]. An increased number of smaller voids by pre-deformation is not an essential factor controlling the VHCF life of Ni-based SX superalloys under fully reversed conditions, in good agreement with a previous analysis by Cervellon et al. [1].

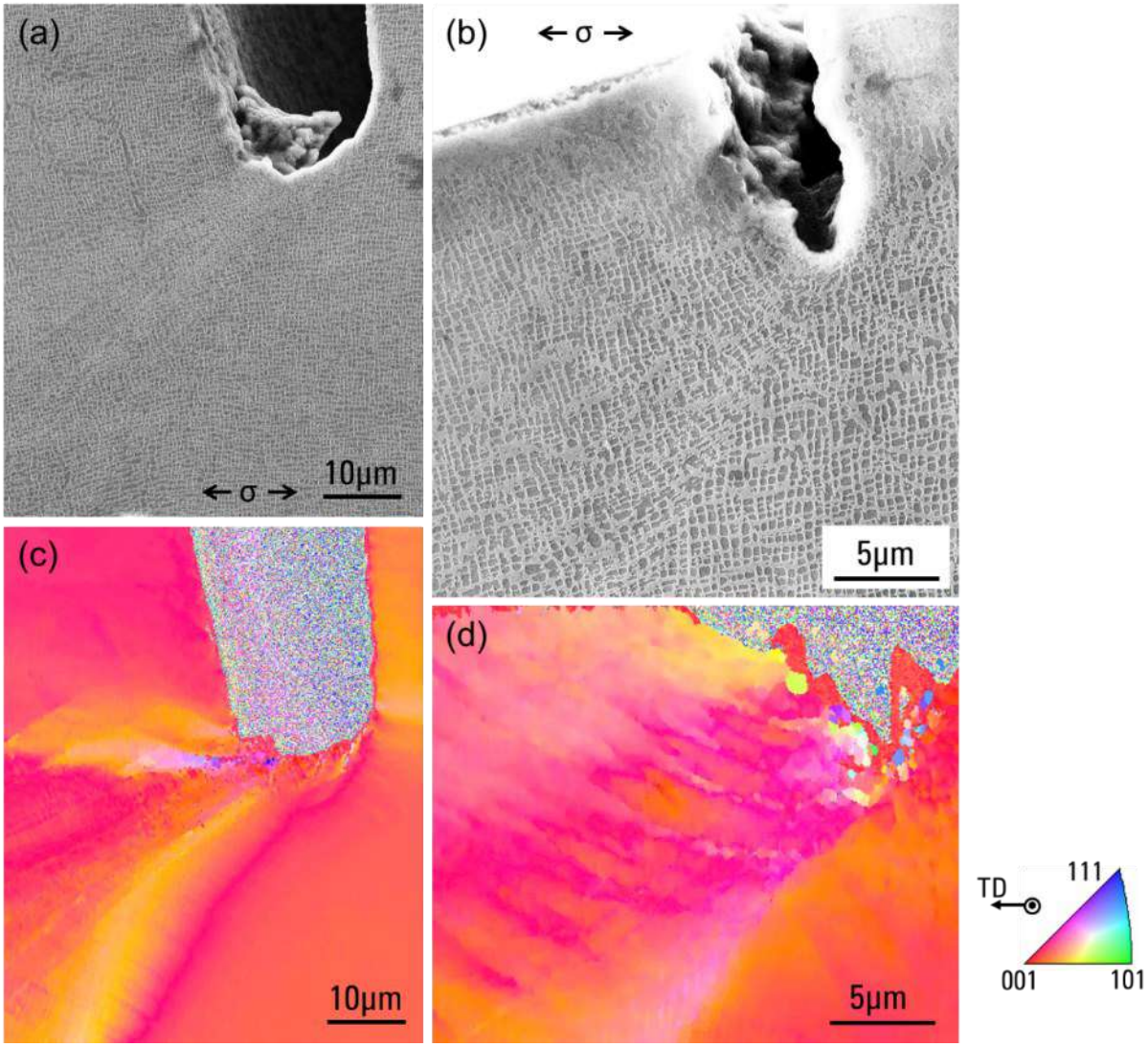

Figure 5.8. Microstructure observed along longitudinal cross-section of AM1-RTPD-HT1 specimen tested at 1000 °C, f = 20 kHz, R = 0.5, σ_{max} = 551 MPa, failed at 1.0 × 10^6 cycles. (a, b) Secondary electron images showing γ/γ′ microstructure. (c, d) IPF maps at the same area as (a, b). (a, c) and (b, d) are corresponding to the cracks indicated as A and B in Figure 7(a), respectively.

The fracture surface of all AM1-RTPD-HT1 specimens after VHCF tests exhibited either {111} plane or pattern of the microstructure coarsened band. Moreover, in the fully reversed VHCF conditions, multiple S-pores were exposed on the fracture surface with the surrounding rough zone and were connected to microstructure coarsened bands. These imply that, although pre-deformation may not affect the initiation of the fatal crack and overall durability in these conditions, the microstructure coarsened bands and pores lying on the bands remained as preferable damaging sites that assists crack propagation up to the final fracture. By increasing the duration of VHCF tests at $R = -1$ (tests in excess of 10^{10} cycles), an effect of pre-deformation on VHCF life might be observed, resulting from a longer time to allow sufficient microstructure evolution within the coarsened bands.

Compared to previous studies performed at Institut Pprime during which it was almost impossible to identify secondary cracks outside of the main crack initiation site of specimen tested at $R = -1$ [1,7–11], several pores triggering recrystallization like in Figure 5.6(c) were observed in the same specimen. Those pores were mostly connected to the microstructure coarsened band. The γ/γ′ microstructure around this pore and the recrystallized

area is coarser compared to the other areas. The micro shearing is suggested to be starting from the pore that creates a local intense strain field. This accelerates the microstructure evolution and activates the recrystallization once it reaches a certain amount of plastic deformation. This mechanism has been presented by Cervellon et al. in the same VHCF conditions [8]. In the non-pre-deformed specimen, S-pore with surrounding recrystallized area was only present at the fracture surface [7]. Therefore, the number of cycles required to initiate a fatal crack is the same regardless of pre-deformation; however, the number of potential primary crack initiating pore is possibly higher in the pre-deformed material, due to these coarsened bands.

5. 6. Enhanced shearing and recrystallization at positive stress ratio condition, $R = 0.5$

It has been shown in a previous study from Cervellon et al. that the γ/γ′ microstructure (morphology and size) controls the VHCF life at 1000 °C of Ni-based SX superalloys when high mean stress is superimposed to the alternating stress [1,11]. As the material is exposed at high-temperature and tensile stress for all testing periods, creep damage is also taking place [11,12]. At a very high strain rate in the tensile deformation, a degraded γ/γ′ microstructure is known to have lower yield stress compared to the optimal cuboidal microstructure [1,13–16]. In the present study, a higher dislocation density in the microstructure coarsened band was observed both inside (Figure 5.5(b)) and especially at the surface layer (Figure 5.5(c)). In addition, during creep at 850 °C / 500 MPa (Figure 4.42), 950 °C / 300 MPa (Figure 4.13), or 1050 °C / 200 MPa (Figure 4.12), microstructure shearing occurred much more frequently inside the microstructure coarsened band. Therefore, fatigue damage mechanisms can proceed faster inside the microstructure coarsened bands when the creep damage is active, and the VHCF life of pre-deformed AM1 may decrease at high mean stress conditions. Furthermore, initial dislocations introduced by a combination of pre-deformation and subsequent aging treatments can enhance dislocation penetration from the matrix into the precipitates that accelerate the damaging processes.

The shorter VHCF lifetime of AM1-RTPD-HT1 compared to AM1-HT1 at the conditions $R = 0.5$ / $\sigma_{max} = 551$ MPa is clearly the consequence of pre-deformation. However, unlike other specimens that exhibited internal crack initiation, AM1-RTPD-HT1 presented multiple cracks from the surface and did not have an internal crack from the creep void. This is because fatigue loading time (~ 50 s) was so short that the γ′-rafting and creep void growth did not have sufficient time to occur (Figure 5.5(b)). The unique feature of this specimen is a greater number of the {111} slip band traces shown in Figure 5.4 compared to that in AM1-HT1, despite the fact that the test duration of AM1-RTPD-HT1 was by far shorter. With a very high density of dislocations at the surface layer shown in Figure 5.7(b), and high density of the slip band traces on the surface, the surface condition can be determined as the key in the fatigue failure of this specimen.

The average spacing between transverse traces in Figure 5.4(b) is 66 μm and that of cracks observed in Figure 5.7(a) is 71 μm if the recrystallized area in the middle of Figure 5.7(b) is counted as a “close-to-initiated-crack”. Recrystallized layers in Figure 5.7(b) are located at two cracks in the right and left of the figure and the possible crack initiation site in the middle. These three points are observed as the transverse traces at lower magnification. Therefore, the surface recrystallizations in the pre-deformed specimen are linked to the transverse traces. Recalling that the transverse band traces are observed along generatrices of ~ <110> type for all specimens tested at $R = 0.5$ / σ_{max} = 550-600 MPa, they formed as consequences of preferential slip accumulation and stress concentration created by the alternating stress, and possibly because of elastic

anisotropy of SX specimen [17,18]. In the pre-deformed material, stress concentration can be strongly enhanced because of the surface roughness at the intersection of slip traces and transverse traces, accordingly, triggering surface recrystallization.

The recrystallized layer in Figure 5.7(b) is limited to only one-grain thickness. Two deeper cracks in Figure 5.7(b) and the largest one in Figure 5.8(c) do not have recrystallized grains up to their crack tips. In the same two cracks observed in Figure 5.7(b), the recrystallized layer below the surface along the crack path has a depth of ~10 μm. This recrystallization depth is the same as the depth of the crack shown in Figure 5.8(d) which has recrystallized grains at its tip. This suggests that recrystallization is causing crack initiation at the surface, but it is not necessary for cracks to further propagate. Crack tip plasticity shown as slip bands in Figure 5.8(a, c) is typical of mode I crack [19,20] and it is enough to ensure further crack propagation.

Figure 5.9 schematically represents the crack initiation mechanism that occurred in AM1-RTPD-HT1 at 1000 °C, f = 20 kHz, R = 0.5, σ_{max} = 551 MPa. The microstructure coarsened bands lying on {111} plane facilitates shearing (see microstructure in Figure 5.5(c) and schematic illustration in Figure 5.9(b)). This consequently leads to {111} slip traces at the specimens' surface as observed in Figure 5.4(c). Slip trace intersection with the specimen's <110> generatrices leads to a greater stress concentration due to the creation of a locally greater roughness resulting from slip accumulation (Figures 5.9(b, c)). The deformed layer is created underneath the stress concentration area and a high density of dislocations is accumulated at the transverse trace (Figure 5.9(d)). Recrystallization is subsequently triggered at the surface layer (Figure 5.9(e)), which can be assisted by oxidation (there is also 45 min of soak before the test for emissivity stabilization) leading to an Al depletion and very local γ′ dissolution [21,22]. Finally, mode I crack starts at the recrystallized area and propagates like other typical fatigue mode I cracks (Figure 5.9(f)). Bifurcation to a mode II crack propagation can be reached once these mode I micro-cracks become long enough (see fracture surface in Figure 5.4(a)).

During isothermal creep tests, local microstructure shearing in the band was in fact more apparent in the creep conditions with higher stress. This is consistent with the fact that shearing inside the band was facilitated in the pre-deformed material during the VHCF test at a positive ratio condition with high maximum stress. On the other hand, time-dependent creep damage should be accumulated faster inside the band and causes earlier failure. However, at the lower maximum stress condition (~400 MPa), the VHCF lifetime was not affected by the pre-deformation in the S-N diagram (Figure 5.2). Here again, fatigue tests with a lower applied mean stress can be an option to clarify the possibility of localized creep damage accumulation within the bands. Decreasing the testing frequency can be another option to check this possibility, however, a lower strain rate may change the active deformation and damage mechanisms [11]. Overall, the difference in VHCF life between pre-deformed and non-pre-deformed specimens at this condition (σ_{max} ~400 MPa) remains within the standard variability observed among all the data generated at Institut Pprime using different Ni-based SX superalloys and this machine (over 200 VHCF test results at 1000 °C, including different R ratios).

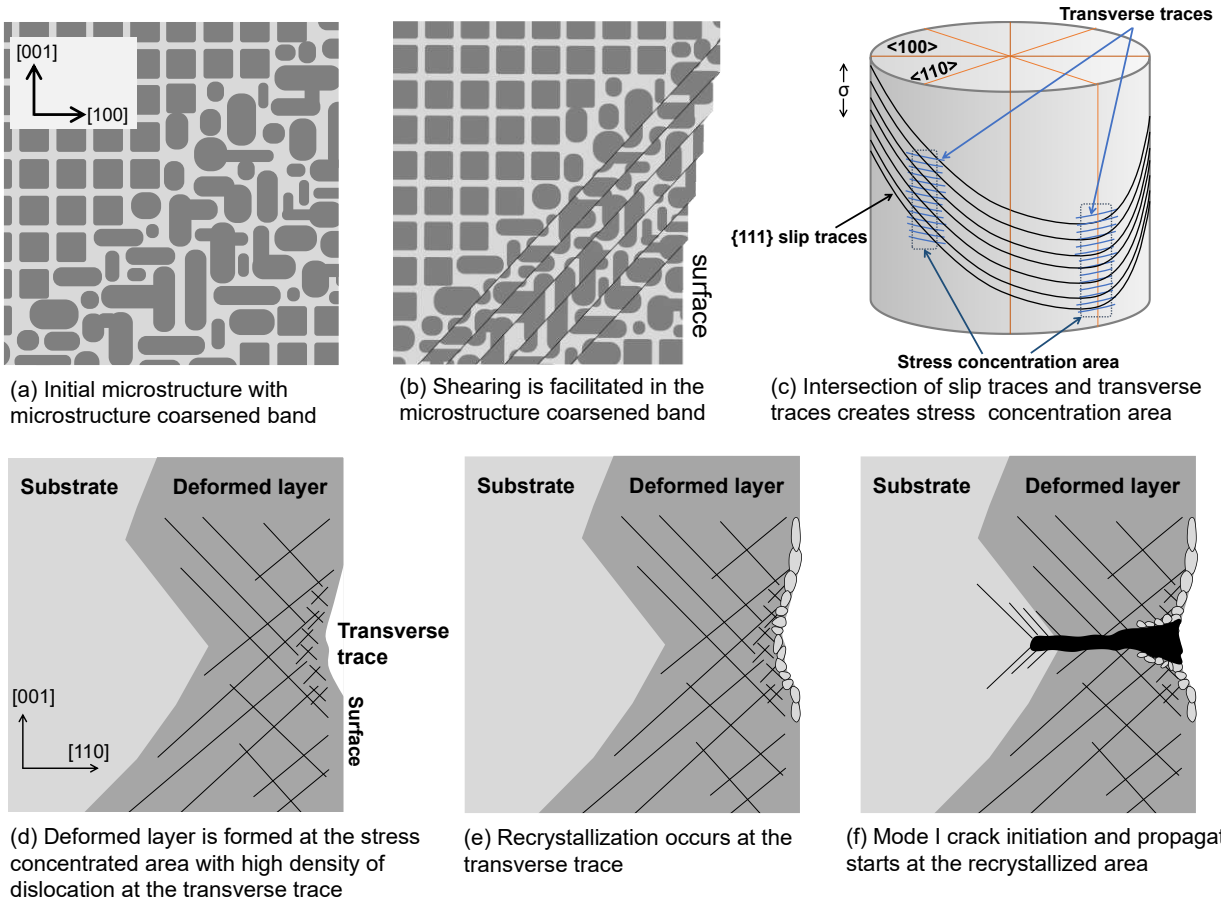

(a) Initial microstructure with microstructure coarsened band

(b) Shearing is facilitated in the microstructure coarsened band

(c) Intersection of slip traces and transverse traces creates stress concentration area

(d) Deformed layer is formed at the stress concentrated area with high density of dislocation at the transverse trace

(e) Recrystallization occurs at the transverse trace

(f) Mode I crack initiation and propagation starts at the recrystallized area

Figure 5.9. Schematic illustration of the crack initiation mechanisms in pre-deformed Ni-based SX superalloys at high temperature and high applied mean stress VHCF test.

5. 7. VHCF life restoration by rejuvenation heat treatment

Like creep properties presented in the previous chapter, rejuvenation treatment after pre-deformation successfully restored VHCF properties in all conditions tested in this study. It was especially effective in the positive stress ratio condition where pre-deformation leads to a debit in VHCF lifetime at higher maximum stress. This result supports the fact that the coarsened microstructure affects fatigue life when high mean stress is applied at high temperatures [1]. On the other hand, the results under fully reversed condition suggest that one of the risks using a rejuvenation treatment, namely, further S-pore growth by additional high-temperature re-solution treatment and stress relaxation, is not an issue since no impact on VHCF life is observed after rejuvenation. Indeed, the risk of recrystallization during the rejuvenation remains and it can cause severe VHCF life debit. Since the rejuvenation condition is properly determined in Chapter 3, the effectiveness of the rejuvenation treatment is successfully demonstrated in VHCF behavior in addition to the creep properties.

5. 8. Summary

Fatigue properties of AM1 Ni-based single crystal superalloy with prior plastic deformation applied between solution and aging treatment has been tested in the very high cycle domain at 1000 °C using an ultrasonic fatigue machine. The main conclusions established in this study are:

- VHCF lifetime and primary crack initiation in fully reversed ($R = -1$) conditions were not affected by either the microstructure coarsened band or the increased density of smaller pores in pre-deformed

material. Fractographic and microstructural observations on pre-deformed material showed multiple pores presenting the primary process of crack initiation associated with local recrystallization around them.

- Pre-deformation decreased the VHCF lifetime by more than a decade at a positive stress ratio (R = 0.5) and high mean stress condition. The microstructure coarsened band in the pre-deformed material facilitated γ/γ′ microstructure shearing at a very high strain rate in the ultrasonic fatigue test, resulting in {111} slip traces appearing on the specimens' surface. The accumulated slip along <110>-type generatrices of the specimens led to a locally higher density of dislocations and stress concentration, hence triggering surface recrystallization. Mode I surface cracks were initiated from the recrystallized area, leading to the earlier failure compared to the specimen without pre-deformation.

- Rejuvenation treatment can restore VHCF lifetime at a positive stress ratio condition and does not affect fatigue life in all the other conditions tested in this study.

References

[1] A. Cervellon, J. Cormier, F. Mauget, Z. Hervier, VHCF life evolution after microstructure degradation of a Ni-based single crystal superalloy, Int. J. Fatigue. 104 (2017) 251–262. doi:10.1016/j.ijfatigue.2017.07.021.

[2] D.L. Anton, A.F. Giamei, Porosity distribution and growth during homogenization in single crystals of a nickel-base superalloy, Mater. Sci. Eng. 76 (1985) 173–180. doi:10.1016/0025-5416(85)90091-6.

[3] T. Link, S. Zabler, A. Epishin, A. Haibel, M. Bansal, X. Thibault, Synchrotron tomography of porosity in single-crystal nickel-base superalloys, Mater. Sci. Eng. A. 425 (2006) 47–54. doi:10.1016/j.msea.2006.03.005.

[4] A. Epishin, T. Link, I.L. Svetlov, G. Nolze, R.S. Neumann, H. Lucas, Mechanism of porosity growth during homogenisation in single crystal nickel-based superalloys, Int. J. Mater. Res. 104 (2013) 776–782. doi:10.3139/146.110924.

[5] A. Epishin, T. Link, Mechanisms of high-temperature creep of nickel-based superalloys under low applied stresses, Philos. Mag. 84 (2004) 1979–2000. doi:10.1080/14786430410001663240.

[6] S. Pierret, T. Etter, A. Evans, H. Van Swygenhoven, Origin of localized rafting in Ni-based single crystal turbine blades before service and its influence on the mechanical properties, Acta Mater. 61 (2013) 1478–1488. doi:10.1016/j.actamat.2012.11.024.

[7] A. Cervellon, J. Cormier, F. Mauget, Z. Hervier, Y. Nadot, Very High Cycle Fatigue of Ni-Based Single-Crystal Superalloys at High Temperature, Metall. Mater. Trans. A. 49 (2018) 3938–3950. doi:10.1007/s11661-018-4672-6.

[8] A. Cervellon, S. Hémery, P. Kürnsteiner, B. Gault, P. Kontis, J. Cormier, Crack initiation mechanisms during very high cycle fatigue of Ni-based single crystal superalloys at high temperature, Acta Mater. 188 (2020) 131–144. doi:10.1016/j.actamat.2020.02.012.

[9] L.M. Bortoluci Ormastroni, S. Utada, J. Rame, L. Mataveli Suave, K. Kawagishi, H. Harada, P. Villechaise, J. Cormier, Tensile, low cycle fatigue and very high cycle fatigue characterizations of advanced single crystal nickel-based superalloys, in: S. Tin, M. Hardy, J. Clews, J. Cormier, Q. Feng, J. Marcin, C. O'Brien, A. Suzuki (Eds.), Superalloys 2020, Springer International Publishing, 2020: pp. 341–351. doi:10.1007/978-3-030-51834-9_33.

[10] L.M. Bortoluci Ormastroni, L. Mataveli Suave, A. Cervellon, P. Villechaise, J. Cormier, LCF, HCF and VHCF life sensitivity to solution heat treatment of a third-generation Ni-based single crystal superalloy, Int. J. Fatigue. 130 (2020) 105247. doi:10.1016/j.ijfatigue.2019.105247.

[11] A. Cervellon, J.Z. Yi, F. Corpace, Z. Hervier, J. Rigney, P.K. Wright, C.J. Torbet, J. Cormier, J.W. Jones, T.M. Pollock, Creep, Fatigue, and Oxidation Interactions During High and Very High Cycle

Fatigue at Elevated Temperature of Nickel-Based Single Crystal Superalloys, in: S. Tin, M. Hardy, J. Clews, J. Cormier, Q. Feng, J. Marcin, C. O'Brien, A. Suzuki (Eds.), Superalloys 2020, Springer International Publishing, 2020: pp. 185–195. doi:10.1007/978-3-030-51834-9_18.

[12] P.K. Wright, M. Jain, D. Cameron, High Cycle Fatigue in a Single Crystal Superalloy: Time Dependence at Elevated Temperature, in: Superalloys 2004 (Tenth Int. Symp., TMS, 2004: pp. 657–666. doi:10.7449/2004/Superalloys_2004_657_666.

[13] A. Epishin, T. Link, M. Nazmy, M. Staubli, H. Klingelhöffer, G. Nolze, Microstructural degradation of CMSX-4: Kinetics and effect on mechanical properties, in: Superalloys 20082, 2008: pp. 725–731. doi:10.7449/2008/Superalloys_2008_725_731.

[14] T. Tinga, W.A.M. Brekelmans, M.G.D. Geers, Directional coarsening in nickel-base superalloys and its effect on the mechanical properties, Comput. Mater. Sci. 47 (2009) 471–481. doi:10.1016/j.commatsci.2009.09.013.

[15] D. Leidermark, J.J. Moverare, S. Johansson, K. Simonsson, S. Sjöström, Tension/compression asymmetry of a single-crystal superalloy in virgin and degraded condition, Acta Mater. 58 (2010) 4986–4997. doi:10.1016/j.actamat.2010.05.032.

[16] B. Fedelich, A. Epishin, T. Link, H. Klingelhöffer, G. Künecke, P.D. Portella, Experimental characterization and mechanical modeling of creep induced rafting in superalloys, Comput. Mater. Sci. 64 (2012) 2–6. doi:10.1016/j.commatsci.2012.05.071.

[17] D. Leidermark, J.J. Moverare, K. Simonsson, S. Sjöström, S. Johansson, Room temperature yield behaviour of a single-crystal nickel-base superalloy with tension/compression asymmetry, Comput. Mater. Sci. 47 (2009) 366–372. doi:10.1016/j.commatsci.2009.08.012.

[18] W. Hermann, H.G. Sockel, J. Han, A. Bertram, Elastic properties and determination of elastic constants of nickel-base superalloys by a free-free beam technique, in: R.D. Kissinger, D.J. Deye, D.L. Anton, A.D. Cetel, M. V. Nathal, T.M. Pollock, D.A. Woodford (Eds.), Superalloys 1996, The Minerals, Metals, & Materials Society, 1996. doi:10.7449/1996/Superalloys_1996_229_238.

[19] S. Flouriot, S. Forest, G. Cailletaud, A. Köster, L. Rémy, B. Burgardt, V. Gros, S. Mosset, J. Delautre, Strain localization at the crack tip in single crystal CT specimens under monotonous loading: 3D Finite Element analyses and application to nickel-base superalloys, Int. J. Fract. 124 (2003) 43–77. doi:10.1023/B:FRAC.0000009300.70477.ba.

[20] P.A. Sabnis, S. Forest, J. Cormier, Microdamage modelling of crack initiation and propagation in FCC single crystals under complex loading conditions, Comput. Methods Appl. Mech. Eng. 312 (2016) 468–491. doi:10.1016/j.cma.2016.04.018.

[21] A. Srivastava, S. Gopagoni, A. Needleman, V. Seetharaman, A. Staroselsky, R. Banerjee, Effect of specimen thickness on the creep response of a Ni-based single-crystal superalloy, Acta Mater. 60 (2012) 5697–5711. doi:10.1016/j.actamat.2012.06.043.

[22] J.J. Moverare, S. Johansson, Damage mechanisms of a high-Cr single crystal superalloy during thermomechanical fatigue, Mater. Sci. Eng. A. 527 (2010) 553–558. doi:10.1016/j.msea.2009.08.023.

GENERAL CONCLUSIONS AND PERSPECTIVES

This thesis research was aimed to understand the effects of pre-deformation introduced during the production of the Ni-based single crystal superalloys. Plastic deformation was introduced to the first-generation AM1 and the third-generation CMSX-4 Plus single crystal superalloys to mimic possible issues occurring during cooling operations and subsequent heat treatment sequences. Mechanical tests such as isothermal creep tests, thermal cycling creep tests, and very high cycle fatigue tests were performed on pre-deformed superalloy specimens

In Chapter 1, the fundamentals of Ni-based single crystal superalloys were introduced with studies related to the pre-straining of single crystal superalloys. The literature on the effect of plastic deformation between the processing of turbine blade material, specifically a pre-deformation between solution and aging treatment, was limited. Preceding experiments showed that this pre-deformation drastically decreases creep properties of AM1 single crystal superalloy. The mechanism of the creep life debit became the major question to investigate in this thesis research. Basic experimental procedures were presented in Chapter 2.

Microstructure evolution after pre-deformation

Analyses of microstructural behaviors after pre-deformation were the main subject of Chapter 3. Tensile plastic deformation was introduced to AM1 at room-temperature, 750 °C, and 950 °C, and to CMSX-4 Plus at room-temperature. Aging treatments were applied subsequently and microstructures of obtained specimens were analyzed.

Regardless of the material and pre-deformation temperature, faster microstructure evolution similar to directional coarsening was triggered by the residual elastic strain introduced by the pre-deformation. Pre-deformation at temperatures below 750 °C proceeded by precipitation shearing mechanism and the microstructure evolution occurred locally at the vicinity of former slip band during aging treatment at 1100 °C. 1/2⟨101⟩{111} type dislocations were mainly observed in the γ matrix of the microstructure coarsened band after the aging heat treatments.

Dislocation by-passing was the deformation mechanism at 950 °C and the microstructure evolution occurred homogeneously in the gauge section, resulting in a mild γ′-rafted structure. The magnitude of directional coarsening decreased and become sluggish as plastic strain increases. The decreased size of pre-rafts with increasing plastic strain in pre-deformation at 950 °C is probably due to the higher dislocation density stored in the γ matrix during plastic deformation. The interfacial dislocations suppressed precipitation coarsening during aging treatments.

The microstructure of CMSX-4 Plus evolved in the vicinity of slip bands after aging treatments. However, it was less anisotropic compared to that of AM1 after room-temperature pre-deformation. Overall, the pre-deformation effect on the material's microstructure was minor in CMSX-4 Plus. Because yield stress of CMSX-4 Plus is lower than that of AM1, lower strain energy was stored in a single slip band during pre-deformation. CMSX-4 Plus presented a higher density of slip bands after room temperature tensile deformation for the same macroscopic pre-strain magnitude. Therefore, internal elastic and plastic energy stored on each

slip band was smaller for CMSX-4 Plus which resulted in less effect of pre-deformation on its microstructure.

Creep damaging mechanisms after pre-deformation

Creep tests at different temperatures on specimens with different preparation methods were presented and creep damaging mechanisms for each test condition were discussed in Chapter 4.

Largest creep life debit appeared at 1050 °C / 140 MPa for AM1 and 1150 °C / 110 MPa for CMSX-4 Plus which are the condition that consists of primary creep stage, flat secondary stage, and very rapid tertiary stage in the creep curve. In these conditions, specimens showed very low ductility with inclined γ′-rafts along with the former {111} slip plane that ultimately became a fracture plane. By the stereological analyses on void size distribution at different stages (ex: after solution treatment, before creep test, creep interrupted, and after creep rupture), it was demonstrated that void nucleation and growth were enhanced by dislocation climb occurring at the vicinity of slip band. The nucleated pores became a site that intensively accumulates creep damage through inclined rafts and lead to very early failure associated with recrystallization starting from damage concentrated void. As creep temperature decreases or applied stress increases, the thermally activated mechanism became less prominent to stress-induced creep damage by microstructure shearing.

The pre-deformation effect becomes negligible for creep properties of CMSX-4 Plus when the shearing of {111} slip system is dominant, whereas creep life debit remained in AM1. This is because the strengthening mechanisms of AM1 are mostly relying on the shear resistance of cuboidal γ′ precipitates. Pre-deformation causes γ′ precipitate coarsening that leads to disruption of the cubic structure and decrease in interfacial coherency, hence directly affecting shear resistance. As for the same mechanism, creep life at 850 °C / 500 MPa had drastically reduced in AM1 pre-deformed at 950 °C that has “pre-rafted” γ/γ′ structure.

Moreover, pre-deformation at different stages (such as after full heat treatment, between first and second aging, and after full heat treatment with additional aging at 1100 °C) did not impact the creep life of AM1. However, when additional aging at 1100 °C was applied after the pre-deformation of a fully treated specimen, a ruptured specimen presented a planar fracture surface on the {111} plane. This implies that the dislocation structure formed during aging at 1100 °C is causing the inclination of γ′-rafts during creep loading.

During thermal cycling creep at temperatures above 1000 °C, neither thermally activated damage localization nor stress-induced microstructure shearing damages involves in creep damaging mechanisms. Therefore, creep life debit was not observed in the thermal cycling creep tests of the pre-deformed materials.

Very high cycle fatigue

Fatigue tests in the very high cycle domain were performed on pre-deformed AM1 and results were discussed in Chapter 5. Pre-deformed material has a VHCF lifetime in a fully reversed fatigue condition comparable to the original material. Although the pre-deformation causes void nucleation and growth during aging treatment, it did not change time to initiate fatal crack from a solidification pore. Multiple pores were observed in fractography of pre-deformed specimens that suggest that the number of possible initiation sites may have increased due to the enhanced void growth mechanism.

With the high mean stress, microstructure shearing becomes the main damage source, and hence, the VHCF lifetime decreased in the pre-deformed material. Slip bands at the specimen's surface increased the surface roughness, which led to the local stress concentration and accumulation of high density of dislocations near the surface. Surface recrystallization was triggered at this stress concentrated area. Mode I surface cracks initiated from the recrystallized area, leading to the failure at a very short lifetime compared to the specimen without pre-deformation.

Rejuvenation after pre-deformation

The microstructure of both AM1 and CMSX-4 Plus was successfully restored by additional rejuvenation treatment applied after pre-deformation at room-temperature. Rejuvenated specimens of both AM1 and CMSX-4 Plus showed mechanical properties (creep and VHCF) comparable to the original material without pre-deformation. The applicability of rejuvenation treatment to unintentionally deformed Ni-based single crystal superalloy components has been demonstrated.

Perspectives

After all these conclusions, there are still some missing points that can be deepened in future research works. The development of dislocation structures was discussed using deeply-etched SEM images and one STEM diffraction contrast image on AM1 specimen after pre-deformation and aging treatment. These are very big clues for discussing how the initial microstructure affected microstructure evolution and damaging mechanism during subsequent creep tests. However, as discussed in the main chapters, a sequential explanation of dislocation structure development remains unknown. The difference between two alloys, AM1 and CMSX-4 Plus, is another interesting topic. High-temperature in-situ TEM/STEM analyses are possible ways to understand dislocation behavior during aging treatments after pre-deformation. These understandings should help to develop a model to predict pre-deformed material's mechanical properties.

The pre-deformation at different stages was only tested for AM1. Because pre-deformation affected the creep properties of AM1 and CMSX-4 Plus differently, it is highly possible that CMSX-4 Plus shows a different response to the different types of pre-deformation. Considering the difference in damage localization shown in isothermal creep tests for these two alloys, CMSX-4 Plus showing different behavior is highly possible. This would give suggestions to material composition design for new alloys and defect tolerance design for an application.

The effect of pre-deformation on the mechanical properties of bulk material was studied in this research. In the experiments, the surface condition effect was eliminated by mechanical polishing. Considering the application, the surface condition is an important topic to study. The microstructure coarsened band is considered as a diffusion path. Therefore, oxidation/corrosion can be accelerated at the intersection of the band and the material's surface. The adhesiveness of the turbine blade coating system can also be affected by the band (formation of irregularly deep secondary reaction zone).

In the rejuvenation experiments, recrystallization occurred in the specimens pre-deformed at 950 °C even at a smaller magnitude of plastic strain compared to the other superalloys after creep straining. Macro strain is

generally used to evaluate rejuvenation capability in other studies. Instead, rejuvenation capability should be discussed with micromechanics that strongly relates to how the material is “damaged” locally at the scale of γ/γ′ structure and how the recrystallization is triggered at subsolvus temperatures. Types and migrating sites of dislocations should affect the γ′ dissolution path and they may change recrystallization sensitivities at elevated temperatures.

APPENDIX

Test results

Creep test results of AM1 SX superalloy are summarized in Tables A.1-A.6.

Table A.1. Results of creep tests at 1050 °C / 140 MPa

Specimen	Reference	Misorientation from ⟨001⟩ (°)	Pre-deformation				Creep			
			Pre-strain (%)	Strain rate (/s)	Young's modulus (GPa)	Yield stress / 0.05% (MPa)	Duration (h)	Strain (%)	Minimum strain rate (/s)	Area reduction (%)
AM1-HT1	53_11	2	/	/	/	/	417.4	13.85	1.39E-11	44.45
AM1-RTPD-HT1	41K3	1.5	0.79	/	/	/	24.8	0.24	/	/
	41F1	2.7	0.27	/	/	/	124.4	2.84	5.30E-09	1.30
	41F2	2.7	0.74	/	/	/	127.6	2.94	5.33E-09	2.50
	53F3	5	0.61	5.0E-04	111	1041	93.5	1.88	1.61E-09	4.34
	53-3	2	0.79	5.0E-04	126	1032	105.0	1.09	1.56E-09	2.12
AM1-PD950-HT1	53-13	2	0.86	5.0E-04	81	752	354.9	17.22	1.39E-10	53.11
AM1-RTPD-Rejuv-HT1	53_10	2	0.71	5.0E-04	113	1062	449.2	13.63	1.11E-10	38.66
AM1-HT1-RTPD	2409_1	10	0.64	5.0E-04	110	1123	384.8	13.71	1.39E-10	30.91
AM1-AT1-RTPD-AT2	53N1	6	0.55	5.0E-04	138	1057	437.9	15.49	9.44E-10	53.35
AM1-HT1-RTPD-A1	54D2	8	0.86	5.0E-04	120	1092	439.4	3.48	2.43E-08	3.15
AM1-HT1-RTPD-HT1	54B5	8	0.86	5.0E-04	122	1075	402.7	6.60	1.36E-07	6.40

Table A.2. Results of creep tests at 1050 °C / 200 MPa

Specimen	Reference	Misorientation from ⟨001⟩ (°)	Pre-deformation				Creep			
			Pre-strain (%)	Strain rate (/s)	Young's modulus (GPa)	Yield stress / 0.05% (MPa)	Duration (h)	Strain (%)	Minimum strain rate (/s)	Area reduction (%)
AM1-HT1	53_12	2	/	/	/	/	30.1	19.16	4.94E-08	46.06311646
AM1-RTPD-HT1	53_8	2	0.85714285	5.0E-04	116	1061	18.4	5.01	1.80E-07	9.443288241

Table A.3. Results of creep tests at 950 °C / 300 MPa

Specimen	Reference	Misorientation from ⟨001⟩ (°)	Pre-deformation				Creep			
			Pre-strain (%)	Strain rate (/s)	Young's modulus (GPa)	Yield stress / 0.05% (MPa)	Duration (h)	Strain (%)	Minimum strain rate (/s)	Area reduction (%)
AM1-HT1	53F5	5	/	/	/	/	138.7	19.45	2.22E-08	38.68
AM1-RTPD-HT1	53-2	2	0.86	5.0E-04	118	1066	71.5	6.65	4.15E-08	7.20
	53-15	2	0.71	5.0E-04	115	1029	102.8	7.73	3.06E-09	7.54
AM1-HT1-RTPD	2409-3	<10	0.71	5.0E-04	112	1082	151.1	25.34	2.67E-08	38.44
AM1-HT1-RTPD-A1	54D3	5	0.57	5.0E-04	123	1082	108.8	19.20	3.97E-06	39.23

Table A.4. Results of creep tests at 850 °C / 500 MPa

Specimen	Reference	Misorientation from ⟨001⟩ (°)	Pre-deformation				Creep			
			Pre-strain (%)	Strain rate (/s)	Young's modulus (GPa)	Yield stress / 0.05% (MPa)	Duration (h)	Strain (%)	Minimum strain rate (/s)	Area reduction (%)
AM1-HT1	53F4	5	/	/	/	/	285.6	21.37	7.56E-09	31.50
AM1-RTPD-HT1	41C1	2.2	0.27	/	/	/	143.5	16.07	5.70E-08	22.00
	41C2	2.2	0.76	/	/	/	161.4	7.14	4.41E-08	10.90
	53F1	5	0.67	5.0E-04	111	1033	143.0	4.02	2.96E-08	3.68
AM1-PD950-HT1	53-21	2	0.71	5.0E-04	82	757	82.9	20.09	9.20E-08	38.17
AM1-RTPD-Rejuv-HT1	53F2	5	0.79	5.0E-04	121	1038	254.9	20.05	1.59E-06	26.85
AM1-HT1-RTPD	2409-2	<10	0.64	5.0E-04	118	1100	238.4	23.12	5.33E-09	29.27
AM1-HT1-RTPD-HT1	54D1	5	1.07	5.0E-04	119	1078	212.2	16.98	2.10E-06	27.00

Table A.5. Results of creep tests at 1200 °C / 80 MPa

Specimen	Reference	Misorientation from ⟨001⟩ (°)	Pre-deformation				Creep			
			Pre-strain (%)	Strain rate (/s)	Young's modulus (GPa)	Yield stress / 0.05% (MPa)	Duration (h)	Strain (%)	Minimum strain rate (/s)	Area reduction (%)
AM1-HT1	106049	5	/	/	/	/	3.10	25.00	2.66E-07	85.9
AM1-RTPD-HT1	41C1	2.2	0.25	/	/	/	2.25	23.92	2.86E-07	79.9
	41C2	2.2	0.76	/	/	/	1.97	25.48	2.90E-07	88.8

Table A.6. Results of creep tests at 750 °C / 800 MPa

Specimen	Reference	Misorientation from ⟨001⟩ (°)	Pre-deformation				Creep			
			Pre-strain (%)	Strain rate (/s)	Young's modulus (GPa)	Yield stress / 0.05% (MPa)	Duration (h)	Strain (%)	Minimum strain rate (/s)	Area reduction (%)
AM1-HT1	105982	<10	/	/	/	/	602.0	10.98	5.49E-09	/
AM1-RTPD-HT1	41K1	1.5	0.25	/	/	/	450.5	5.73	2.09E-08	6.70
	41K2	1.5	0.76	/	/	/	387.8	6.90	1.93E-08	8.60

Table A.7. Results of creep tests at 1250 °C / 60 MPa

Specimen	Reference	Misorientation from ⟨001⟩ (°)	Pre-deformation				Creep			
			Pre-strain (%)	Strain rate (/s)	Young's modulus (GPa)	Yield stress / 0.05% (MPa)	Duration (h)	Strain (%)	Minimum strain rate (/s)	Area reduction (%)
4P-HT2	4P06	<10	/	/	/	/	4.54	23.46	1.99E-07	93.20
4P-RTPD-HT2	4P11	<10	0.64	5.0E-04	124	869	2.70	12.02	9.92E-07	22.69

Table A.8. Results of creep tests at 1150 °C / 110 MPa

Specimen	Reference	Misorientation from ⟨001⟩ (°)	Pre-deformation				Creep			
			Pre-strain (%)	Strain rate (/s)	Young's modulus (GPa)	Yield stress / 0.05% (MPa)	Duration (h)	Strain (%)	Minimum strain rate (/s)	Area reduction (%)
4P-HT2	4P04	<10	/	/	/	/	126.7	11.54	1.28E-09	49.48
4P-RTPD-HT2	4P07	<10	0.64	5.0E-04	130	882	25.7	6.95	7.78E-09	8.30
4P-HT1	4P15	<10	/	/	/	/	125.3	15.59	3.78E-07	41.99
4P-RTPD-HT1	4P16	<10	0.64	5.0E-04	119	808	31.5	15.88	9.01E-07	17.79
4P-RTPD-Rejuv-HT2	4P14	<10	0.57	5.0E-04	121	879	111.5	12.61	1.56E-09	31.78

Table A.9. Results of creep tests at 1050 °C / 200 MPa

Specimen	Reference	Misorientation from ⟨001⟩ (°)	Pre-deformation				Creep			
			Pre-strain (%)	Strain rate (/s)	Young's modulus (GPa)	Yield stress / 0.05% (MPa)	Duration (h)	Strain (%)	Minimum strain rate (/s)	Area reduction (%)
4P-HT2	4P03	<10	/	/	/	/	106.3	28.57	8.91E-09	48.7
4P-RTPD-HT2	4P01	<10	0.64	5.0E-04	147	772	95.2	22.45	2.34E-08	45.0
4P-HT1	4P13	<10	/	/	/	/	141.0	22.44	5.56E-10	39.0
4P-RTPD-HT1	4P09	<10	0.57	5.0E-04	128	761	102.9	20.41	3.56E-09	48.1

Table A.10. Results of creep tests at 950 °C / 390 MPa

Specimen	Reference	Misorientation from ⟨001⟩ (°)	Pre-deformation				Creep			
			Pre-strain (%)	Strain rate (/s)	Young's modulus (GPa)	Yield stress / 0.05% (MPa)	Duration (h)	Strain (%)	Minimum strain rate (/s)	Area reduction (%)
4P-HT2	4P05	<10	/	/	/	/	138.1	18.99	4.37E-08	29.97
4P-RTPD-HT2	4P08	<10	0.57	5.0E-04	118	854	108.1	8.26	1.38E-08	10.67
4P-RTPD-HT2	4P12	<10	0.86	5.0E-04	125	909	164.2	17.36	3.89E-08	29.48

Table A.11. Results of creep tests at 850 °C / 650 MPa

Specimen	Reference	Misorientation from ⟨001⟩ (°)	Pre-deformation				Creep			
			Pre-strain (%)	Strain rate (/s)	Young's modulus (GPa)	Yield stress / 0.05% (MPa)	Duration (h)	Strain (%)	Minimum strain rate (/s)	Area reduction (%)
4P-HT2	BE	<10	/	/	/	/	120.1	18.67	1.24E-05	/
4P-RTPD-HT2	19A4	<10	0.64	5.0E-04	138	779	20.1	23.49	3.17E-05	10.67

Table A.12. Results of thermal cycling creep tests

Specimen	Reference	Misorientation from ⟨001⟩ (°)	Pre-deformation				Creep			
			Pre-strain (%)	Strain rate (/s)	Young's modulus (GPa)	Yield stress / 0.05% (MPa)	Duration (h)	Overheat cycles	Strain (%)	Area reduction (%)
AM1-HT1	53R6	7	/	/	/	/	35.3	125	31.59	61.6
AM1-RTPD-HT1	53R1	7	0.61	5.0E-04	117	973	32.9	117	30.38	69.3
	53R2	7	0.61	5.0E-04	114	990	37.6	133	30.77	69.0
4P-HT2	19A2	<10	/	/	/	/	173.4	611	27.43	45.2
4P-RTPD-HT2	19A3	<10	0.71	5.0E-04	126	793	151.4	517	28.81	48.8

Results of VHCF tests are summarized in Tables A.13 and A.14.

Table A.13. Results of VHCF tests (R = -1)

Specimen	Reference	Misorientation from ⟨001⟩ (°)	Pre-deformation				VHCF						
			Pre-strain (%)	Strain rate (/s)	Young's modulus (GPa)	Yield stress / 0.05% (MPa)	R	σ_a (MPa)	σ_{min} (MPa)	σ_{max} (MPa)	N_f	Duration (h)	Failure
AM1 (Cervellon, 2018)	X8155H-1	<10	/	/	/	/	-1	178	0	178	2.04E+08	2.84	Pore
	X8155C-1	<10	/	/	/	/	-1	210	0	210	3.86E+07	0.54	Pore
	X8155C-2	<10	/	/	/	/	-1	157	0	157	5.18E+08	7.19	Pore
	X8155H-2	<10	/	/	/	/	-1	145	0	145	1.80E+09	24.93	Rough zone
AM1-RTPD-HT1	X8253P-1	1	0.50	5.0E-04	119	949	-1	140	0	140	1.08E+09	14.99	Pore
	X8253P-2	1	0.42	5.0E-04	124	944	-1	140	0	140	1.05E+09	14.62	Pore
	X8254K-1	2	1.00	5.0E-04	114	1025	-1	180	0	180	1.99E+08	2.77	Pore
	X8254K-2	2	0.50	5.0E-04	120	1019	-1	209	0	209	9.82E+07	1.36	Pore
AM1-RTPD-Rejuv-HT1	X8254X-1	2	0.75	5.0E-04	121	988	-1	180	0	180	2.39E+08	3.32	Pore
	X8254X-2	2	0.58	5.0E-04	116	1017	-1	140	0	140	4.89E+09	67.92	Pore

Table A.14. Results of VHCF tests (R = 0.5)

Specimen	Reference	Misorientation from ⟨001⟩ (°)	Pre-deformation				VHCF						
			Pre-strain (%)	Strain rate (/s)	Young's modulus (GPa)	Yield stress / 0.05% (MPa)	R	σ_a (MPa)	σ_{min} (MPa)	σ_{max} (MPa)	N_f	Duration (h)	Failure
AM1-HT1	/	5	/	/	/	/	0.4	128	295	423	8.39E+08	11.657	Pore
	/	6.5	/	/	/	/	0.5	150	423	573	1.40E+07	0.194	Pore
	/	3.1	/	/	/	/	0.5	190	558	748	1.29E+05	0.002	Surface
	/	3.1	/	/	/	/	0.4	125	273	398	3.34E+09	46.388	Pore
AM1-RTPD-HT1	X8254A-1	1	0.58	5.0E-04	120	951	0.4	124	289	413	2.24E+09	31.108	Pore
	X8254A-2	1	0.75	5.0E-04	115	951	0.5	145	406	551	9.97E+05	0.014	Surface
AM1-RTPD-Rejuv-HT1	X8253S-1	1	1.08	5.0E-04	123	932	0.5	145	437	582	6.17E+06	0.086	Pore
	X8253S-2	1	0.75	5.0E-04	121	952	0.5	114	340	454	1.99E+08	2.767	Pore

Effet d'une pré-déformation plastique au cours des traitements thermiques sur les propriétés mécaniques des superalliages base Ni pour l'application d'aubes de turbine

Les superalliages monocristallins base Ni sont utilisés pour la conception des aubes de turbines en raison de leur excellente durabilité à haute température. Lors de la production d'une aube de turbine, une déformation plastique (DP) inattendue peut être introduite dans le matériau. Dans cette étude, les matériaux monocristallins ont été pré-déformés entre les traitements thermiques de mise en solution et de revenu pour simuler la DP pouvant être rencontrée lors des étapes de production. Des tests mécaniques sur les matériaux pré-déformés ont été effectués pour comprendre l'effet de cette DP.
Au cours des traitements thermiques de revenu du superalliage monocristallin AM1 pré-déformé, un grossissement des précipités γ′ plus rapide et une nucléation accélérée de pores ont été observés à proximité des bandes de glissement introduites lors de la DP à température ambiante. Au cours de la déformation par fluage de l'AM1 pré-déformé dans des conditions de haute température/basse contrainte (≥ 950 °C), les bandes à microstructure grossière sont des sites préférentiels d'accumulation du dommage de fluage induit par diffusion, induisant de la recristallisation et une réduction drastique des propriétés de fluage. Dans des conditions de basse température/haute contrainte (≤ 850 °C), le cisaillement de la microstructure est facilité dans les bandes à microstructure grossière et il réduit également les propriétés de fluage. La recristallisation n'est pas été observée dans des ces conditions de fluage à basse température car les mécanismes diffusifs sont ralentis. Ces résultats ont été confirmés via des essais de fluage sur des matériaux pré-déformés suivant différent chemin de pré-déformation (température, position de la DP dans le cycle thermique…).
Le superalliage monocristallin CMSX-4 Plus a été testé de manière similaire à l'AM1 pour comprendre l'effet de la composition chimique. L'effet de la DP sur la microstructure de l'alliage est plus limité pour cet alliage par rapport à celui sur l'AM1. Par conséquent, la pré-déformation n'a pas montré de chute de la durée de vie pour le CMSX-4 Plus à des températures inférieures à 1050 °C. Par contre, pendant le fluage de CMSX-4 Plus à 1150 °C, la pré-déformation a montré un impact spectaculaire sur la durée de vie et la ductilité via les mêmes mécanismes que ceux observés pour l'AM1 à 1050 °C.
Afin de régénérer les propriétés des superalliages monocristallins pré-déformés, un traitement thermique de restauration a été ajouté après la DP. Le traitement de restauration a permis de restaurer la microstructure après la DP à température ambiante avec succès, et les propriétés de fluage des matériaux restaurés sont équivalentes à celles de l'AM1 et du CMSX-4 Plus vierges de pré-déformation.

Mots-clés: Alliages réfractaires, Déformations (mécanique), Durée de vie (ingénierie), Matériaux—Détérioration, Matériaux—Effets des hautes températures, Matériaux—Fluage, Métaux—Traitement thermique, Microstructure (physique), Nickel—Alliages, Plasticité, Superalliages monocristallins base Ni, Pré-déformation, Pores, Restauration, VHCF

Effect of a prior plastic deformation during heat treatments on the mechanical properties of Ni-based superalloys for turbine blade application

Ni-based single crystal (SX) superalloys are used for turbine blade applications because of their high-temperature durability. During the production of a turbine blade, unexpected plastic deformation (PD) can be introduced to the material. In this study, SX materials were pre-deformed in between solution and aging heat treatments to mimic PD during production. Mechanical tests on the pre-deformed materials have been performed to understand the effect of the prior PD.
During aging treatments of pre-deformed AM1 SX superalloy, faster coarsening of γ′ precipitates and enhanced void nucleation were observed in the vicinity of slip bands which were introduced by PD at room-temperature. During creep deformation of pre-deformed AM1 at high temperature/low stress conditions (≥ 950 °C), the microstructure coarsened bands act as diffusion induced creep damage accumulating paths, further triggering recrystallization and resulting in drastic reduction of creep properties. At low temperature/high stress conditions (≤ 850 °C), microstructure shearing was facilitated in the microstructure coarsened band and it decreased creep properties. Recrystallization was not observed at lower temperature creep because the diffusion damage was suppressed. These relationships have been explained by creep tests on pre-deformed materials prepared by different pre-deformation temperatures and heat treatment procedures.
CMSX-4 Plus SX superalloy was tested similarly to AM1 to understand the effect of the chemical composition. Effect of pre-deformation on alloy's microstructure was mild in CMSX-4 Plus compared to that in AM1. Therefore, the pre-deformation did no exhibit large creep life debit in CMSX-4 Plus at temperatures lower than 1050 °C. However, during creep of CMSX-4 Plus at 1150 °C, pre-deformation presented huge impact on creep life and ductility by the same mechanisms as the ones observed for AM1 at 1050 °C.
In order to restore properties of pre-deformed SX superalloys, rejuvenation heat treatment was added after PD. Rejuvenation treatment successfully restored microstructure after PD at room-temperature, and creep properties of rejuvenated specimens were shown to be equivalent to that of original AM1 and CMSX-4 Plus without PD.

Keywords: Heat resistant alloys, Deformations (Mechanics), Service life (Engineering), Materials—Deterioration, Materials at high temperatures, Materials—Creep, Meatal—Heat treatment, Microstructure, Nickel alloys, Plasticity, Ni-based single crystal superalloy, Pre-deformation, Voids, Rejuvenation, VHCF